

π^0 Production in
Au+Au Collisions at $\sqrt{s_{NN}} = 130$ GeV

Ken Oyama

Doctoral Thesis

*Department of Physics,
Graduate School of Science,
University of Tokyo,
7-3-1 Hongo, Bunkyo, Tokyo 113-0033, JAPAN*

Abstract

The measurement of π^0 production from Au+Au collisions at $\sqrt{s_{NN}}=130$ GeV has been carried out at the PHENIX detector system of Relativistic Heavy Ion Collider at Brookhaven National Laboratory. The results presented here are based on the data taken during the first physics run from the middle of July to the end of August 2000. π^0 was reconstructed from two photons measured with segmented electromagnetic calorimeters of PHENIX. The kinematic region of measured π^0 's were approximately from 1.0 GeV/ c to 5.0 GeV/ c in the transverse momentum, and from -0.35 to 0.35 in rapidity.

Motivation of this analysis is to investigate the jet quenching effect in the matter of deconfined quarks and gluons that is produced in the extremely high energy density as predicted by the Quantum chromodynamics. Jets are produced by initial hard scattering of partons in the colliding nuclei. If the deconfined matter is formed by Au+Au collisions, it is expected that the scattered parton loses its energy by gluon bremsstrahlung while the parton traverse in the matter, and productions of high- p_T particles are quenched.

In this thesis, the centrality dependence of yield and shape of transverse momentum distribution of π^0 are measured. Quite differently to the measurement at lower energy at CERN SPS, it is observed that π^0 yield strongly depends on the centrality. While it is consistent to the Glauber model for the peripheral collisions, the yield is suppressed to about a half for the central events. The data are compared with theoretical calculations which consider several medium effects.

Contents

1	Introduction	1
1.1	Quark Gluon Plasma	1
1.2	Relativistic Heavy Ion Collisions Experiment	2
1.3	Jet Quenching	4
1.4	Thesis Outline	7
2	Theoretical and Experimental Background	9
2.1	Overview	9
2.2	Space-time Evolution of the Colliding System	9
2.2.1	Initial Energy Density and QGP formation	12
2.3	Hard Process and Jet	12
2.4	Hard Particle Production in Au+Au Collisions	15
2.4.1	Binary Scaling	15
2.4.2	Modification Factor	16
2.4.3	Known Nuclear Effects	16
2.4.4	Jet Quenching	20
2.5	Past Experiments Concerned to Jet Quenching	23
2.5.1	WA80 Experiment	23
2.5.2	WA98 Experiment	24
3	Experimental Setup	27
3.1	Overview	27
3.2	AGS-RHIC Accelerator Complex	27
3.3	PHENIX	31
3.3.1	PHENIX Global Coordinate System	34
3.4	Electromagnetic Calorimeter	35
3.4.1	Overview	35
3.4.2	Structure	36
3.4.3	Performances from Test Beam	38

3.4.4	Monitoring System	41
3.4.5	Energy Calibration	43
3.5	Other Devices in the Central Arms	43
3.5.1	Drift Chamber	44
3.5.2	Pad Chambers	45
3.5.3	RICH	46
3.6	Trigger and Event Characterization Devices	47
3.6.1	ZDC's: Zero-degree Calorimeters	47
3.6.2	BBC's: Beam-Beam Counters	51
3.7	Data Acquisition System	54
3.7.1	Front-end Modules	56
4	Run Conditions	61
4.1	Overview	61
4.2	Beam Conditions	61
4.3	Detector Conditions	63
4.3.1	EMCal	63
4.3.2	ZDC	63
4.3.3	BBC	63
4.4	Trigger Settings	64
4.4.1	Raw Level Trigger	64
4.4.2	BBC Local Level 1 Trigger	64
4.5	Statistics	66
5	Data Analysis	69
5.1	Overview	69
5.2	Invariant Yield	69
5.3	Vertex and Collision Time Determination	71
5.3.1	Measurement of the Event Vertex Position	71
5.3.2	Measurement of the Collision Time	72
5.3.3	Event Selection	73
5.4	Event Classification	74
5.4.1	Participant-Spectator Model	75
5.4.2	Glauber Model	75
5.4.3	BBC and ZDC Responses	76
5.4.4	Centrality	77
5.4.5	Systematic Fluctuations of N_{part} and N_{coll}	79
5.5	EMCal Clustering and Photon Measurement	82

5.5.1	Clustering Algorithm	83
5.5.2	Multiplicity	85
5.5.3	Hit Position Correction	87
5.5.4	E_{core} Variable	87
5.5.5	MIP Observation	91
5.5.6	Electron Observation	92
5.5.7	Time of Flight Measurement with EMCal	93
5.5.8	Shower Shape Parameter Cut	99
5.5.9	Summary of γ PID	104
5.6	π^0 Reconstruction	105
5.6.1	Invariant Mass and p_T of Photon Pair	105
5.6.2	Combinatorial Background Calculation by Event Mixing	106
5.6.3	Asymmetry Cut	109
5.6.4	Opening Angle Cut	110
5.6.5	Fiducial Area Cut	113
5.6.6	Counting π^0 's	117
5.6.7	Energy Scale Correction Using π^0 Peaks	119
5.6.8	Raw Number of π^0 's	124
5.7	Corrections and Systematic Uncertainties	124
5.7.1	Acceptance and Efficiency Corrections	125
5.7.2	Systematic Uncertainty in the Efficiency Correction	127
5.7.3	Shower Overlapping Effect	130
5.7.4	Other Corrections	132
5.7.5	Summary of Corrections and Systematic Uncertainties	134
6	Experimental Results	137
7	Discussions	143
7.1	Overview	143
7.2	Comparison to the $N+N$ Data	143
7.3	Comparison to the Peripheral Data	147
7.4	ε_0 Dependence of $R_{AA/NN}$	150
7.5	Result from STAR Experiment	152
7.6	Comparison with the Theoretical Calculations	153
7.6.1	Perturbative QCD Calculation	153
7.6.2	Hydrodynamical Calculation	154
7.6.3	Comparison to a Simple Toy-Model	157
8	Summary and Conclusions	161

Acknowledgments	163
A QGP signatures	165
A.1 Overview	165
A.2 J/Ψ suppression	165
A.3 Jet quenching	167
A.4 Chiral Symmetry Restoration	167
A.4.1 Disoriented Chiral Symmetry Restoration	168
A.5 Thermal photon enhancement	168
A.6 Strangeness enhancement	169
B Hadron Spectra in $N+N$ Collisions at $\sqrt{s} = 130$ GeV	171
C Supplements	173
C.1 Natural Units	173
C.2 Kinematic Variables	173
D Results of π^0 Extraction	175
D.1 Raw numbers, Mass, and Widths of π^0 's	175
D.2 Figures of π^0 Peaks	175
E Correction Factors	189

List of Figures

1.1	Phase diagram of nuclear matter.	2
1.2	The estimated energy densities for AGS, SPS, RHIC and LHC	3
1.3	A schematic picture of Au+Au collision and jet quenching.	5
1.4	π^0 distribution predicted by Wang.	6
2.1	Space-time diagram of longitudinal evolution of QGP.	10
2.2	Inclusive cross section of hadrons.	13
2.3	The ratios of quark structure functions by EMC.	17
2.4	p_T v.s. α	19
2.5	Modification factor calculated by pQCD.	20
2.6	Ratio of π^0 yield in S+Au to $p+p$ at WA80.	23
2.7	WA98 π^0 distribution and parton model calculations.	24
2.8	Ratios of π^0 yields in Pb+Pb at WA98	25
3.1	The AGS-RHIC accelerator complex.	28
3.2	The air-scape of the PHENIX detector system.	31
3.3	PHENIX experimental setup in the Year-2000 run.	32
3.4	Definition of global coordinates system.	34
3.5	Collision point view of a PbSc EMCAL sector.	36
3.6	A module of PbSc calorimeter.	37
3.7	Test result of the energy spectra measured in the EMCAL.	39
3.8	PbSc timing resolution for electrons, pions, and protons.	41
3.9	Schematic diagram of EMCAL monitoring system.	42
3.10	Structure of the Drift Chamber.	43
3.11	The layout of DC wire position within one DC sector.	44
3.12	Pad Chamber pad and pixel geometry.	46
3.13	A cutaway view of one arm of the RICH detector.	47
3.14	Cross section of the ZDC module.	48
3.15	Overview of RHIC intersection region.	49
3.16	ZDC response line shapes for 100 and 160 GeV incident protons.	50

3.17	Energy distribution measured by a ZDC.	51
3.18	Pictures of BBC.	52
3.19	BBC timing deviation and profile.	54
3.20	Schematic view of PHENIX DAQ system.	55
3.21	The block diagram of Integrator Chip of EMCal	57
3.22	Detailed block diagram of the AMU/ADC ASIC.	58
3.23	FEM timing diagram.	59
4.1	First successful ramp of both RHIC beams to 65 GeV/u.	62
4.2	Schematic view of PHENIX trigger devices.	64
4.3	Schematics of PHENIX trigger logic.	66
4.4	Final integrated trigger rates.	67
5.1	Vertex distribution measured by BBC's.	71
5.2	BBC t_0 distribution.	72
5.3	A schematic figure of the participant-spectator model.	74
5.4	ZDC energy v.s. BBC charge.	76
5.5	Relation between centrality and impact parameter.	77
5.6	Simulated ZDC and BBC response.	78
5.7	Systematic fluctuations of N_{part} and N_{coll}	80
5.8	Fluctuation of central to peripheral ratio of $\langle N_{\text{part}} \rangle$ and $\langle N_{\text{coll}} \rangle$	83
5.9	Example of event.	84
5.10	Multiplicity distributions for selected centrality cuts.	86
5.11	Definitions of impact angles and impact position correction way.	87
5.12	An example of predicted shower energy fraction in towers.	88
5.13	Number of towers in E_{core} and fraction of E_{core}	89
5.14	Effect of E_{core} algorithm.	90
5.15	$E_{\text{core}}/E_{\text{org}}$ distribution.	91
5.16	E_{core} distribution.	92
5.17	Observed minimum ionization peak.	93
5.18	E/p ratio of electrons identified by RICH.	94
5.19	EMCal timing distribution.	95
5.20	EMCal-TOF run-by-run fluctuations before corrections.	96
5.21	Simulated time of flight distribution.	97
5.22	Timing Cut Efficiency.	100
5.23	δ^2 distribution of clusters.	101
5.24	δ^2 cut threshold v.s. survival ratio.	102
5.25	δ^2 cut efficiency calculated from number of π^0	103

5.26	E_{core} distributions of the selected clusters.	104
5.27	Schematic of π^0 reconstruction method.	105
5.28	Typical Invariant mass spectra.	107
5.29	The combinatorial background shapes.	108
5.30	Simulated asymmetry distribution.	109
5.31	Asymmetry distributions of several p_T regions.	110
5.32	Before and after opening angle cut.	111
5.33	p_T v.s. opening angle.	112
5.34	A schematic of idea of fiducial volume calculation.	113
5.35	A schematic of one tower rejection.	114
5.36	Tower inspection plots.	115
5.37	EMCal dead tower map.	116
5.38	Efficiency of fiducial area cut.	117
5.39	Example of counting π^0 's	118
5.40	p_T resolution of PbSc calculated by GEANT simulation.	119
5.41	Measured π^0 peak position and width before the correction.	120
5.42	Centrality v.s. π^0 peak position and width.	121
5.43	Raw p_T distributions of π^0	123
5.44	Geometrical Acceptance of PbSc.	125
5.45	EMCal pure acceptance v.s. p_T	126
5.46	Calculated PbSc efficiency.	128
5.47	Efficiency fluctuation.	129
5.48	Conception of raw data mixing.	130
5.49	Cluster multiplicity distribution before/after mixing.	131
5.50	Summed v.s. mixed cluster multiplicity.	132
5.51	The amount of off vertex π^0 's.	133
6.1	Corrected p_T distributions of π^0	138
7.1	Comparison to scaled $p+p$ collisions.	144
7.2	R_{AA} v.s. p_T	146
7.3	R_{AA} v.s. centrality.	147
7.4	$R_{C/m.p.}$ v.s. p_T	148
7.5	$R_{C/m.p.}$ v.s. centrality.	149
7.6	E_T distribution measured from PHENIX EMCal.	150
7.7	Calculation of the transverse area S	151
7.8	R_{AA} v.s. Bjorken's energy density.	153
7.9	Comparison between PHENIX data and STAR data.	154

7.10	Comparison to the pQCD calculations.	155
7.11	Comparison to Hydro+Jet calculation.	156
7.12	R_{AA} v.s. Bjorken's energy density.	159
A.1	The observed J/Ψ suppression in CERN SPS.	166
A.2	Inclusive e^+e^- mass spectrum from CERES experiment.	167
A.3	WA98 direct photon data.	169
B.1	Inclusive charged particle production for $N+N$ collisions.	172
D.1	Fitting results of π^0 peaks for $C=0-10$ % events ($p_T=0.5-3.0$ GeV/ c).	179
D.2	Fitting results of π^0 peaks for $C=0-10$ % events ($p_T=3.0-5.0$ GeV/ c).	180
D.3	Fitting results of π^0 peaks for $C=10-20$ % events ($p_T=0.5-3.0$ GeV/ c).	181
D.4	Fitting results of π^0 peaks for $C=10-20$ % events ($p_T=3.0-5.0$ GeV/ c).	182
D.5	Fitting results of π^0 peaks for $C=20-40$ % events ($p_T=0.5-3.0$ GeV/ c).	183
D.6	Fitting results of π^0 peaks for $C=20-40$ % events ($p_T=3.0-5.0$ GeV/ c).	184
D.7	Fitting results of π^0 peaks for $C=40-60$ % events ($p_T=0.5-3.0$ GeV/ c).	185
D.8	Fitting results of π^0 peaks for $C=40-60$ % events ($p_T=3.0-5.0$ GeV/ c).	186
D.9	Fitting results of π^0 peaks for $C=60-80$ % events ($p_T=0.5-2.5$ GeV/ c).	187
D.10	Fitting results of π^0 peaks for $C=60-80$ % events ($p_T=2.5-4.0$ GeV/ c).	188

List of Tables

3.1	Summary of RHIC parameters.	29
3.2	Summary of the PHENIX Detector Subsystems.	33
3.3	Summary of PbSc EMCAL parameters.	35
4.1	RHIC Beam Conditions in Year-2000 run	63
4.2	Trigger logic definitions.	65
5.1	Statistics of the analyzed events.	73
5.2	The estimated $\langle N_{\text{part}} \rangle$ and $\langle N_{\text{coll}} \rangle$ in each centrality class.	81
5.3	Expected particle contamination.	98
5.4	Result of fitting data by the power-law function.	127
5.5	$\langle M_{\text{obs}} \rangle / M_{\text{max}}$ and $\epsilon_{\text{overlap}}$ for five centrality classes.	133
5.6	Materials between vertex and center of PbSc sector.	134
5.7	Summary of corrections and errors.	135
6.1	Fit results for π^0 invariant yields.	139
6.2	Corrected π^0 yield for $C=0-10$ % events.	140
6.3	Corrected π^0 yield for $C=10-20$ % events.	140
6.4	Corrected π^0 yield for $C=20-40$ % events.	141
6.5	Corrected π^0 yield for $C=40-60$ % events.	141
6.6	Corrected π^0 yield for $C=60-80$ % events.	141
7.1	Summary of centrality and ϵ_0	152
A.1	Some of the typical signature of QGP and its observables.	165
B.1	$N+N$ collision data used for comparisons.	171
D.1	Raw π^0 numbers detected in $C=0-10$ % events.	176
D.2	Raw π^0 numbers detected in $C=10-20$ % events.	176
D.3	Raw π^0 numbers detected in $C=20-40$ % events.	177
D.4	Raw π^0 numbers detected in $C=40-60$ % events.	177
D.5	Raw π^0 numbers detected in $C=60-80$ % events.	178

E.1	Correction factors for each p_T and centrality bin.	189
-----	---	-----

Chapter 1

Introduction

1.1 Quark Gluon Plasma

Quantum chromodynamics (QCD) is the theory which describes the system of particles have the strong interactions. The strong interaction has different characteristics from other forces such as electromagnetic interactions.

In the electromagnetic interactions, atoms are easily broken into electrons and nuclei. But quarks are confined into hadrons by the color force and can not be observed as naked particles. Even in high energy experiments, only their evidences are observed. For example, the ratio of cross sections of $e^+ + e^- \rightarrow \text{hadrons}$ and $e^+ + e^- \rightarrow \mu^+ + \mu^-$ is described by assuming quarks and color degree of freedom[1].

The next remarkable characteristic of QCD is “asymptotic freedom”. In the low energy region, the strong interaction coupling constant α_s is large and no perturbative treatment is possible. In the large momentum transfer, however, the interaction between quarks becomes weak ($\alpha_s < 1$). This is called asymptotic freedom where quarks and gluons interact weakly and perturbative handling is possible.

The confinement and the asymptotic freedom imply the possibility of non-ordinary nuclear matter. It is predicted that highly excited and dense hadronic matter might undergo a phase transition into a matter of weakly interacting quarks and gluons, a Quark Gluon Plasma (QGP) [2, 3]. The phase diagram of hadronic matter including the QGP can be schematically drawn as shown in Figure 1.1. The horizontal axis is baryon density in the unit of density of normal nuclear: $\sim 0.15 \text{ GeV}/\text{fm}^3 (= 2.7 \times 10^{14} \text{ g}/\text{cm}^3)$ and vertical axis is temperature. The QGP may exist at very high temperature and/or high baryon density conditions.

In high temperature, the system consists of deconfined quarks and gluons freely move and weakly interact (hot QGP). The transition temperature from the ordinary matter to the hot QGP is calculated to be $T_c \sim 150 \pm 10 \text{ MeV}$ from the lattice QCD [4]. In high density, if the distances between baryons become smaller than their size, they connect each other (cold QGP). No theoretical calculations for high baryon density is completed

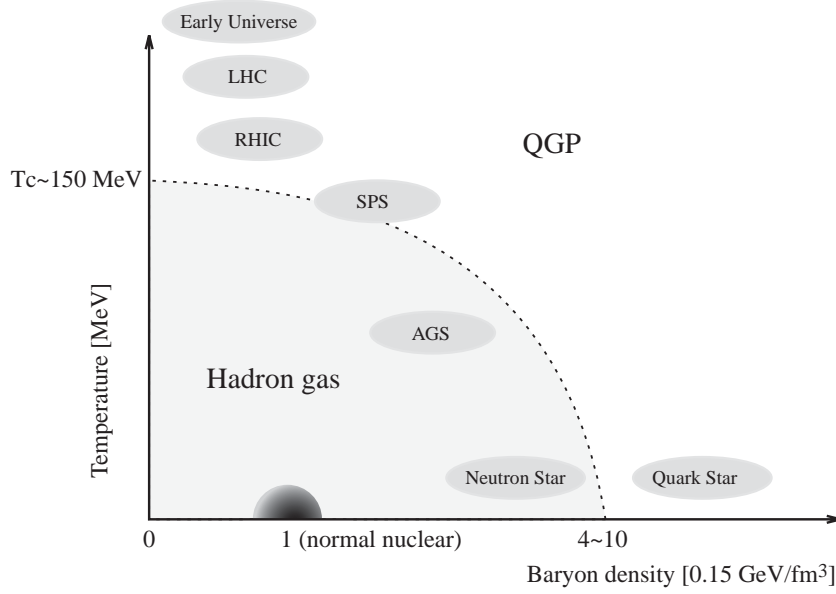


Figure 1.1: Phase diagram of nuclear matter. Horizontal axis is the baryon density in the unit of normal nuclear and vertical axis is the temperature. QGP might exist in nature. For example, the early universe was in the phase of the hot QGP. Cold high baryon density QGP may exist inside the neutron star or quark star. By heavy ion collisions experiments, QGP phase is realized artificially.

yet, to predict the critical density for the cold QGP.

In the universe, there are two cases which may be related to the QGP phase transition. One is in the “early universe” and the other is “neutron star”. The very hot and baryon free state of QGP is thought to exist in the early stage of the universe after a few μs from the Big-Bang. The universe expands and cools down, and freezes out into ordinary hadrons at $\sim 10 \mu\text{s}$ after the Big-Bang. The cold QGP may exist in the center of cold neutron stars where the baryon density is many times larger than normal nuclear matter. Some theories predict phenomena such as quark condensation, color superconductivity, and kaon condensation [5, 6, 7] in the high baryon density cold matter.

1.2 Relativistic Heavy Ion Collisions Experiment

By colliding relativistically accelerated ions with each other, an extremely high energy or high baryon density system can be achieved. If the energy and baryon density are high enough, the QGP state might be achieved. In this case, the system passes through the phase transition and different aspects from ordinary nucleus+nucleus collisions will

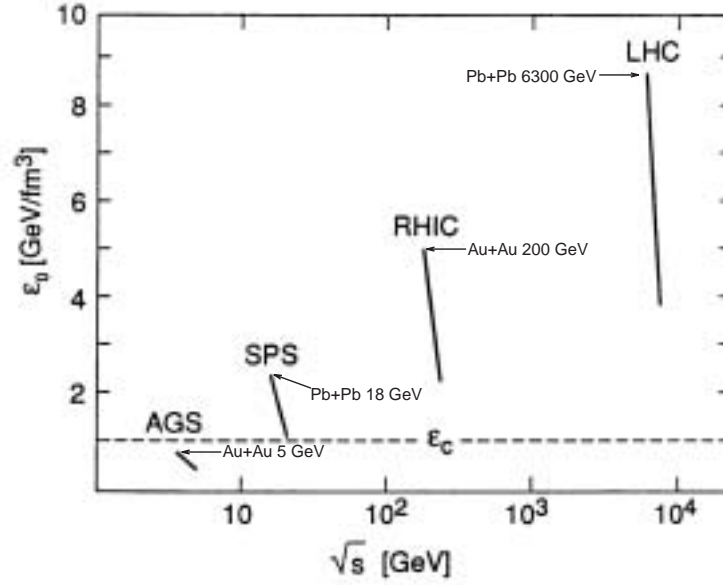


Figure 1.2: The estimated energy densities for AGS, SPS, RHIC and LHC as function of the incident energies. The constant formation time $\tau_0 \sim 1 \text{ fm}/c$ is assumed.

be observed.

Experimental studies with heavy ion collisions had began in Bevalac at Lawrence Berkeley Laboratory in 1970's. The beam energy at Bevalac was 2 GeV per nucleon. In the middle of 1980's, experiments at Alternating Gradient Synchrotron (AGS) at Brookhaven National Laboratory (BNL) and at Super Proton Synchrotron (SPS) at European Organization for Nuclear Research (CERN) started. At AGS, $11 \sim 15A$ GeV ions were collided on targets and collisions with center-of-momentum energy per nucleon-nucleon pair of $\sqrt{s_{NN}} \sim 5$ GeV were achieved. At SPS, with up to $200A$ GeV beams, $\sqrt{s_{NN}} \sim 18$ GeV collisions were achieved.

The experiments at Relativistic Heavy Ion Collider (RHIC) at BNL started in 2000. At RHIC, Au+Au collisions at $\sqrt{s_{NN}} = 130$ GeV and 200 GeV have been achieved. Sufficiently high energy density might be realized for QGP formation at RHIC.

As a future plan, an experiment at the Large Hadron Collider (LHC) is being prepared. A Large Ion Collider Experiment (ALICE) group at the LHC is planning to observe the Pb+Pb collisions at $\sqrt{s_{NN}} = 6.3$ TeV. The expected energy density reaches $\sim 9.0 \text{ GeV}/\text{fm}^3$.

Figure 1.2 shows the energy density achieved in the experiments at AGS, SPS, RHIC, and expected at the LHC as an extrapolations from AGS and SPS data. Details to estimate the energy density will be discussed in the next chapter. In the AGS, the initial

energy density was lower than the critical energy density ($\varepsilon_c \sim 1 \text{ GeV}/\text{fm}^3$) predicted from the lattice calculations. In the SPS, it is believed to be larger than ε_c and there were claims that QGP was possibly observed [14]. In the LHC, probably longer life-time and much higher initial energy density will be achieved.

The QGP state can not be measured directly as well as ordinary nuclear matter. Therefore, the only way to identify the QGP is to study a suite of observables that are sensitive to the collision dynamics. Such observables are still controversial things as they are indirect probes of the QGP formation. Even though, many possible signatures of the QGP have been proposed and detectors were designed for suitable measurement of observables resulted from the signals[15].

Some of representatives of currently proposed signals, and signatures of deconfined matter observed at CERN SPS are explained in Appendix A. Jet quenching is one of the strong candidates of evidences of the QGP. The amount of data recorded by PHENIX in the first year RHIC run was enough to discuss about this subject. This effect was not observed in CERN SPS. This thesis is to study the jet quenching through the measurements of π^0 production yield in Au+Au collisions at $\sqrt{s_{NN}} = 130 \text{ GeV}$ taken at the PHENIX experiment performed at the RHIC.

1.3 Jet Quenching

After a jet is created by parton-parton collisions at the initial stage of a heavy ion collision, it loses energy during passing through the QGP medium. Energy loss of the jet parton is primary due to gluon radiation, as similar to the electromagnetic bremsstrahlung radiation.

Figure 1.3 shows the schematic picture of jet energy loss in the created medium by the central Au+Au collision with impact parameter $b = 0$. In the Au+Au collisions, according to the Bjorken's scenario[17], the medium has the size of (nuclear diameter of) $\sim 10 \text{ fm}$ so that the high- p_T jet parton produced at the initial stage have flight length of $\sim 5 \text{ fm}$ in average in the medium. If the system is at the QGP phase, the energy loss causes significant modification in p_T spectra of high- p_T hadrons originated from the jet. Since the jet cross section has a power-law dumping shape, higher p_T jet is crushed in the lower momentum region, and buried under lower momentum hadrons, and the energy loss result in the jet quenching and suppression. At lower momentum $p_T < 2 \text{ GeV}/c$ region, the hadrons originated from soft particle production is dominant compared to the jet originated hadrons. Experimental observation of the jet quenching effect is possible through the measurement of inclusive high- p_T hadrons.

In this thesis, the p_T distribution of neutral pions are measured. The π^0 measurements

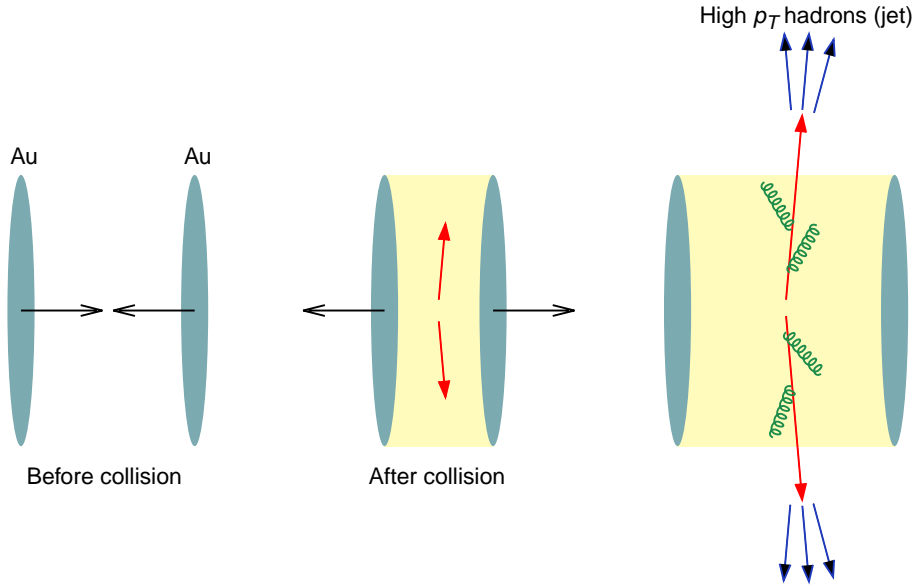


Figure 1.3: A schematic picture of Au+Au collision and jet quenching for central ($b = 0$) collision. Jet partons generated by nucleon+nucleon collisions traverse in the medium, and lose its energy by gluon bremsstrahlung.

have a statistical advantage due to its large production cross section. As π^0 is identified from the invariant mass peak of the daughter two photons, the purity of the signal is high without extra particle identifications, compared to charged π 's.

There are several theoretical calculations which qualitatively describe the jet quenching and its effect to the high- p_T hadron spectra. In the most simplified picture, the energy loss mechanism is regarded as the multiple scattering of partons in the medium. The energy loss is expressed by $-dE/dx = \varepsilon_a/\lambda_a$ where ε_a is the average radiative energy loss per scattering and λ_a is the mean free path of parton in the medium. Figure 1.4 shows inclusive spectra of hadrons and π^0 's in the model for $\sqrt{s_{NN}} = 130$ GeV and 200 GeV Au+Au collisions with and without the constant energy loss[18, 16].

The energy loss can depends on the energy density of the medium and parton energy, and the longitudinal and transverse developments of the medium could affect the total energy loss. Such dependencies were vigorously studied by Baier *et al.*[19]. In their calculations, the coherent gluon radiation may suppress the bremsstrahlung radiation (LPM effect), and the parton energy loss is proportional to \sqrt{E} where E is the parton energy.

There are no theoretical calculations which quantitatively describe the strength of the jet quenching effect. It is, therefore, important to find a procedure to probe the energy loss as a function of an experimental observable. The measurement of “centrality”

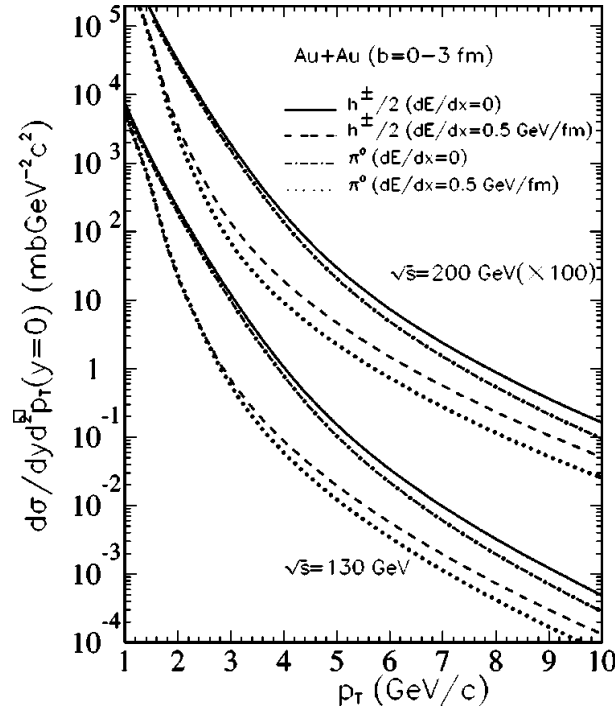


Figure 1.4: Prediction of transverse momentum spectra of charged hadrons (solid lines) and π^0 (dotted lines) in Au+Au collisions at $\sqrt{s_{NN}} = 130$ and 200 GeV without energy loss, calculated by Wang[16]. Dashed lines and dotted lines are results with $-dE/dx = 0.5$ GeV/fm for charged hadrons and π^0 , respectively.

dependence of high- p_T neutral pion yield is the way applied in this thesis where the centrality is the quantity determined experimentally and concern the impact parameter b of the collision. The detailed explanation of the centrality is given in Section 5.4. If the jet quenching effect depends on the size and energy density of the medium, it depends on the centrality of the collision. In the central (small impact parameter) collisions, the size and initial energy density of the medium is large. Stronger modification in the p_T spectrum is expected in the central collisions than peripheral (large impact parameter) collisions.

To measure the modification of p_T spectra of π^0 's in the given centrality event, the reference spectra of π^0 is indispensable. If the Au+Au collision is the superposition of nucleon+nucleon ($N+N$) collisions (binary collisions) of their constituent nucleons, and no medium effect exist, high- p_T hadron yield is proportional to the number of binary collisions in a Au+Au collision. This scaling idea is called “binary scaling”, and the π^0 yield predicted by the binary scaling is usable as the reference spectra. The number of binary collisions depends on the centrality. The smaller impact parameter event has the

larger number of binary collisions, and has the larger number of initial jet productions. But if jet energy loss exists, a proportional tendency breaks. The goal of this thesis is to discuss about the dependency of modification of π^0 spectra on the centrality as well as the initial energy density.

1.4 Thesis Outline

The thesis consists of the following chapters.

Chapter 2 Theoretical and experimental background concerned to the high energy heavy ion collision experiment and jet energy loss is given.

Chapter 3 The RHIC accelerator and PHENIX detector complex is introduced and the precise explanations about detectors used to measure π^0 are given. Especially, electromagnetic calorimeter of the PHENIX play the most important role to reconstruct $\pi^0 \rightarrow \gamma\gamma$.

Chapter 4 Conditions of accelerators and detectors while the data taking, and event statistics obtained in the experiment are shown.

Chapter 5 Explanations of analysis method is presented. In the analysis stage, the good Au+Au events are extracted and separated into several class of centralities. By using Monte Carlo, the number of binary collision is estimated for each event class. Clustering method is applied to the data of the electromagnetic calorimeter. After extracting photon samples, the π^0 is reconstructed and per event yield of π^0 is finally calculated. At every stage of analysis, detector acceptance, reconstruction efficiency of photon and π^0 , and concerned systematic errors are always accounted.

Chapter 6 The obtained experimental data are shown for each centrality class.

Chapter 7 Discussions are given using the obtained π^0 yield. First, π^0 yield is compared to the estimation based on the binary scaling assumption. Also the data is compared to past experiments and theoretical calculations. For example the data is compared to WA98 results at CERN and several models which is considering the jet energy loss.

Chapter 8 Thesis is concluded in this chapter.

Chapter 2

Theoretical and Experimental Background

2.1 Overview

In this chapter, theoretical and experimental background concerned to the high energy heavy ion collision and jet energy loss are given. First, Bjorken's scenario of space-time evolution of the collision system is explained. The initial energy density of the system is estimated. Next, the explanations about hard process and jet are provided. The concept of "binary scaling" which gives extrapolation from the $N+N$ elementary collisions to the Au+Au collisions is given. After that, several nuclear effects (Cronin effect and shadowing effect) which are already known to break the binary scaling and new effect from the jet quenching are described. Finally, the past experimental data concerned to the jet quenching are shown.

2.2 Space-time Evolution of the Colliding System

J. D. Bjorken proposed a scenario on the space-time evolution in the relativistic heavy ion collisions[17]. This scenario gives the way to estimate the initial energy density of the medium.

Figure 2.1(a) shows the system at the time t after the collision. In the relativistic heavy ion collisions, nuclei look like thin disks due to the Lorentz contraction in the center-of-momentum (c.m.) frame of the collision. The collision is defined to happen at $z = 0$ position. Rapidity y of each nucleon is ± 4.9 in the c.m. frame at $\sqrt{s} = 130$ GeV collision¹. By a collision, the leading baryons in the nucleus lose their energy. In high energy heavy ion collisions, the energy loss of leading baryons is $\Delta y = 2 \sim 3$. The rapidity of leading baryons after collision are still large ($y = 2 \sim 3$), and pancakes still remaining the after collision.

¹The definition of rapidity variable y is found in Appendix C.

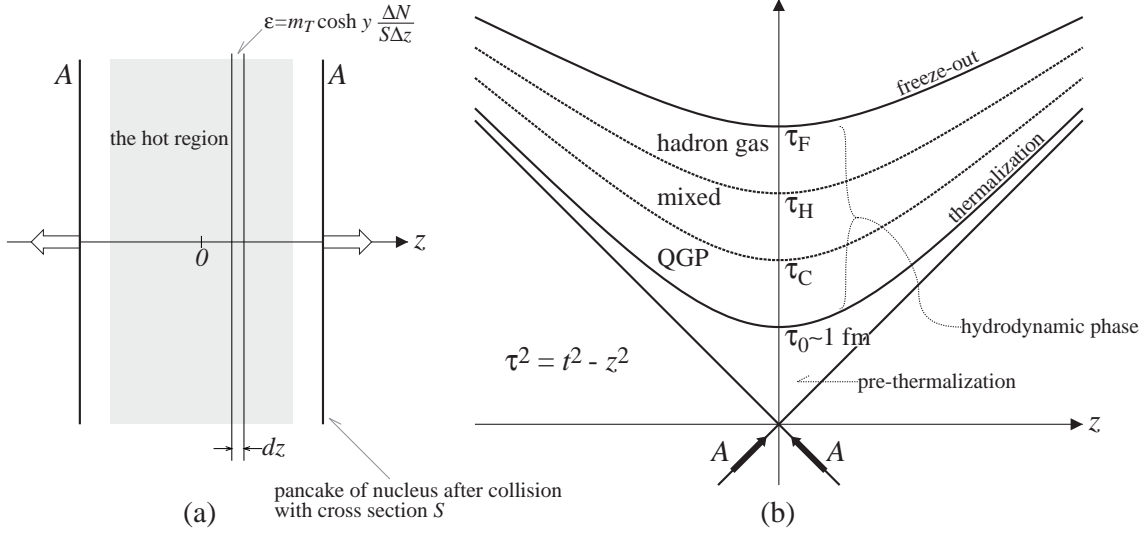


Figure 2.1: (a) The initial state of centrally produced medium in $A+A$ collisions. (b) Space-time diagram of longitudinal evolution of the medium.

After the collision, the leading baryons in both nucleus pass through each other and a large energy is deposited in the region between two nuclei. The matter created in the central region has a very high energy density, but a small net baryon content.

The amount of energy in the central region and how it evolves is estimated by extending the $N+N$ collisions. In $p+p$ reactions at $\sqrt{s} > 23$ GeV in CERN Inter Section Ring (ISR), rapidity distribution dN/dy of produced charged particle has plateau with $\Delta y \sim 4$ with \sqrt{s} dependent height[20]. The rapidity plateau is naturally reproduced by the string model[21]. According to the model, the status of local system is uniformly described by the proper time $\tau = \sqrt{t^2 - z^2}$. Every positions of particle formation lie on the $\tau = \tau_0$ line. This model gives the constant rapidity distribution of the particles with the magnitude expressed by

$$\frac{dN}{dy} = \frac{\kappa \tau_0}{\langle m_T \rangle} \quad (2.1)$$

where κ is the string tension (1 GeV/fm) and $\langle m_T \rangle$ is the mean transverse momentum of the produced particles².

If a $A+A$ collision is the superimpose of the $N+N$ collisions, the evolution of system is also described by the proper time. Figure 2.1(b) schematically shows the space-time evolution of the $A+A$ collision system. At $\tau = 0$, the free partons due to the initial collision exist. The system begins expansion in space and the evolution of system is described by τ . If the deposited energy is large enough and exceeds the critical energy

²See Appendix C for the definition of m_T . $m_T \simeq p_T$ in the p_T range discussed in this thesis.

density, the strongly interacting system is expected, and it is assumed that the system equilibrates. The equilibration of the system is, like at the formation time of particles in $N+N$ collision, achieved at the constant τ_0 line in space-time diagram. The formation time in $N+N$ collisions is estimated to be $0.5 \sim 1.0$ fm/ c , and QGP formation time is, although not known, expected to be around this value.

After the QGP formation, the system expands and cool down. At τ_C , the system will reach the critical temperature between QGP gas and ordinary hadron gas, and after mixed phase, the system becomes the ordinary hadron gas at τ_H . At τ_F , the hadron gas freeze-out and finally produced particles are scattered.

The achieved energy density at the formation time is estimated as follows. From the definition of the rapidity, the space-time position of the particle with rapidity y at τ is represented by

$$z = \tau \sinh y \quad (2.2)$$

$$\text{and } t = \tau \cosh y. \quad (2.3)$$

This indicates that the particle's position at proper time τ_0 is estimated from its observed rapidity. The smaller rapidity associated with the smaller longitudinal position z . On the other hand, the interaction area at τ_0 is a cylindrical shape with the transverse surface of S defined from the overlap region of the colliding ions (see Figure 2.1(a)). If ΔN particles with a mean transverse energy $\langle m_T \rangle$ are in the volume defined by the transverse area S and z -directional thickness of Δz , the energy density is written as

$$\varepsilon_0 = \langle m_T \rangle \cosh y \frac{\Delta N}{S \Delta z}, \quad (2.4)$$

where $\langle m_T \rangle \cosh y$ is the particle's mean energy (see Appendix C). From Eq. (2.2), the number density is related to the rapidity density:

$$\frac{\Delta N}{S \Delta z} = \frac{1}{S} \cdot \frac{dN}{dy} \cdot \frac{dy}{dz} = \frac{1}{S} \cdot \frac{dN}{dy} \cdot \frac{1}{\tau_0 \cosh y}. \quad (2.5)$$

This means that energy density can be deduced from the rapidity and transverse momentum of the final state particles by

$$\varepsilon_0 = \langle m_T \rangle \frac{dN}{dy} \cdot \frac{1}{\tau_0 S}. \quad (2.6)$$

Sometime the transverse energy flow is measured instead of dN/dy , and energy density is, in this case, expressed by

$$\varepsilon_0 = \frac{dE_T}{dy} \cdot \frac{1}{\tau_0 S}, \quad (2.7)$$

where E_T is the transverse (perpendicular to the collision axis) energy flow directly measured in the experiment.

2.2.1 Initial Energy Density and QGP formation

How much energy density ε_0 is required to form the QGP? For the pion gas at the predicted critical temperature $T_c \sim 150$ MeV, the Stephan-Boltzmann energy density is

$$\varepsilon_{c(H.G.)} = \frac{d\pi^2}{30} T_c^4 \sim 65 \text{ MeV/fm}^3, \quad (2.8)$$

where $d = 3$ is the iso-spin degree of freedom of the pion. For the QGP at the same temperature, the energy density is significantly large since d should be considered for both gluons and quarks. For the gluons, $d_g = 2 \times 8 = 16$ where 2 and 8 are the degree of freedom of spin and color, respectively. For the quarks, since it is fermion, $d_q = 2 \times 2 \times 3 \times 2 = 24$ where the numbers are degree of freedom of the spin, particle/anti-particle, the colors, and the flavors (u and d). The energy density for the QGP gas is, therefore,

$$\varepsilon_c = \frac{(d_g + \frac{7}{8}d_q)\pi^2}{30} T_c^4 = \frac{37\pi^2}{30} T_c^4 \sim 1 \text{ GeV/fm}^3, \quad (2.9)$$

where a factor $\frac{7}{8}$ is due to difference of the Fermi-Dirac statistics and the Bose-Einstein statistics.

In the Au+Au collisions at $\sqrt{s_{NN}} = 200$ GeV, $dN/dy \sim 1000$ and $\langle m_T \rangle \sim 500$ MeV are expected by the extrapolation from the past experiments. If $\tau_0 = 1$ fm/ c and $S \sim 110$ fm² are assumed, the expected energy density calculated by Eq.(2.6) is ~ 5 GeV/fm³. This is larger than previously estimated ε_0 and might be enough for the QGP phase transition.

2.3 Hard Process and Jet

Before explaining the jet quenching effect, a little more in detail about the characteristics of the jet production in the parton-parton initial hard scattering is given below.

In the $N+N$ collisions, the p_T distribution of produced particles is described approximately by $\exp(-\alpha p_T)$ in the low- p_T region below $p_T \sim 2$ GeV/ c . Processes which produces these particles, are called ‘‘soft process’’. They are associated with a length scale that is large in the context of QCD and belong to the realm of non-perturbative QCD. A successful model to describe the soft process is a string model. The exponentially dumping particle production yield is derived from a similar mechanism to Schwinger’s particle production mechanism.

At higher p_T , the production rate of hadrons significantly increases than the expected yield from the soft process. This is called ‘‘hard process’’. Figure 2.2 shows the inclusive invariant cross section as functions of p_T at from $\sqrt{s} = 63$ to 1800 GeV $p+p$ and $p+\bar{p}$ collisions measured by British-Scandinavian collaboration at ISR[26], UA1 collaboration[23, 24, 25] at $Spp\bar{S}$, and CDF (Collider Detector at Fermilab) collaboration[22]. The hadron

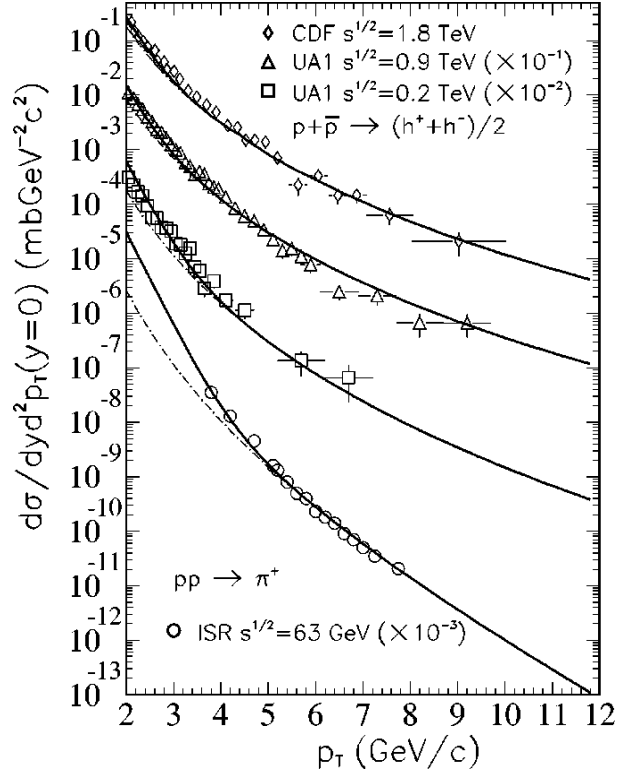


Figure 2.2: The p_T spectra of charged hadrons $(h^+ + h^-)/2$ and π^+ in $p+p$ and $p+\bar{p}$ collisions. The experimental data are from CDF collaboration[22], UA1 collaboration[23, 24, 25], and British-Scandinavian collaboration at ISR[26]. The dot-dashed lines are from jet fragmentation only and solid lines include also soft production parametrized in an exponential form. Comparisons were made in Ref. [18].

production rate at $p_T > 2$ GeV/ c region is not described by the exponential fall off typical of the soft process. The hard production exceeds the soft production already at $p_T \sim 2$ GeV/ c in the collisions above $\sqrt{s} = 200$ GeV. The hadron yield in $p_T > 2$ GeV/ c region is then sensitive to the hard production.

The hard process involves a large momentum transfer which is associated with a small coupling constant in QCD. It corresponds to parton+parton scattering with short distance, and the techniques of perturbative QCD is applicable. Production rate of such partons is considered to be independent from the soft process and proportional to the number of parton+parton collisions.

A remarkable characteristic of hard process is “jet” production. Jet is one of the aspects of the confinement of QCD vacuum. It had been observed more than 25 years ago and its characteristics were well studied in $e^+ + e^-$ and $p + p$ (or \bar{p}) collisions. In

the $e^+ + e^-$ collisions, jet partons are produced by $e^+ + e^- \rightarrow \gamma^* \rightarrow q + \bar{q}$ process. In $p+p$ collisions, the quarks and gluons in each nucleons collide by $q(g)+q(g) \rightarrow q(g)+q(g)$ at high momentum transfer. These scattering produces the high momentum partons (quarks or gluons), and each parton fragments into hadrons due to the confinement. The fragmentation of jet is governed by the non-perturbative QCD, and the parametrized fragmentation function is experimentally determined. Since a scattered parton has high momentum, associated hadrons are emitted to the similar direction of the parton. Then, jets are identified as directive particle productions of hadrons. Those scattered hadrons concentrates into a cone of relatively small solid angles, and the total momentum of hadrons in a jet has strong correlation to the original momentum of scattered partons. The mean lateral momentum of jet hadrons with respect to the direction of original parton is small ($\sim 0.3 \text{ GeV}/c$).

Jets are usually identified by observing directive particle production. It is, however, very difficult for the PHENIX to identify “jet”. One reason is because PHENIX geometrical acceptance is limited. It is impossible to capture entire particles from a jet. The other reason is a little more fundamental. Even if PHENIX has enough geometrical acceptance, directivity of particle production due to a jet production is disturbed because of high particle multiplicity environment at RHIC, and jet could not be identified event-by-event.

Even though, study of jets is still possible without identifying each jet but through the inclusive particle p_T measurement. This is because the production cross section of hard process component is larger than the soft process at $p_T > 2 \text{ GeV}/c$ as already shown in Figure 2.2.

Without any medium effect, jet production is independent of the QGP formation. The productions of high- p_T partons take place well before the formation time of hadronic medium. Particles at $p_T > 2 \text{ GeV}/c$ are mainly the fragments of partons with much higher p_T so that such partons traverse to the lateral direction with respect to the z -axis. If the formation time of fragment hadron is the same order of soft particle production $\sim 1 \text{ fm}/c$ in proper time, the actual formation time is even later than QGP phase due to Lorentz boost ($\gamma > 20$ for 3 GeV pions). The partons fragment at the place enough far from the medium. Therefore, the factorization is applicable for the Au+Au collisions so that the production of partons and fragmentation of jets can be separated.

Without nuclear effects, production rate of hard hadrons in a single Au+Au collision is estimated to be simple superposition of binary scattering of nucleons.

In the CERN ISR, a succession of data of hadron productions in $N+N$ collisions were accumulated[26, 27, 20]. Hard particle productions in $A+A$ collisions are estimated from those $N+N$ data.

2.4 Hard Particle Production in Au+Au Collisions

In this section, it is first described how the π^0 yields in Au+Au collisions are predicted from those of $N+N$ collisions. There are some known “nuclear effects” caused by the medium produced by $A+A$ collisions, such as shadowing and Cronin effects. They are described in Section 2.4.3.

2.4.1 Binary Scaling

Because an Au nucleus is composed of 197 nucleons, the Au+Au collision can be regarded as multiple $N+N$ binary scatterings. The number of $N+N$ collisions (N_{coll}) is a key parameter to estimate the hadron yield in the Au+Au collision. The N_{coll} is estimated by the Glauber model[28] which will be extensively discussed in Section 5.4. If each $N+N$ collision is completely independent of other binary collisions, the π^0 yield per Au+Au collision is proportional to the N_{coll} and expressed by

$$\frac{d^2n_{AA}}{2\pi p_T d\eta dp_T} = \langle N_{\text{coll}} \rangle \cdot \frac{d^2n_{NN}}{2\pi p_T d\eta dp_T}, \quad (2.10)$$

where n_{NN} is the π^0 production yield per $N+N$ collision. This prediction is experimentally practical because an abundance of $p+p$ and $p+\bar{p}$ collision data are accumulated in the past experiments at SPS and Tevatron.

In the perturbative QCD (pQCD) calculation, the factorization theorem is applied to calculate hard component of the particle production spectra in each $N+N$ collision. π^0 yield at high- p_T is represented by superposition of $q(g) + q(g) \rightarrow q(g) + q(g)$ initial scatterings, and fragmentations of scattered partons.

The yield in the $N+N$ collision is expressed by a sum of all possible leading order parton-parton scatterings:

$$\begin{aligned} \frac{d^2n_{NN}}{2\pi p_T d\eta dp_T} &= \frac{K}{2\pi} \sum_{abcdh} \int dx_a \int dx_b f_{a/N}(x_a, Q^2) f_{b/N}(x_b, Q^2) \\ &\times \frac{D_{h/c}(z_c, Q^2)}{\pi z_c} \frac{d\sigma}{d\hat{t}}(ab \rightarrow cd), \end{aligned} \quad (2.11)$$

where factor $K \simeq 2$ accounts for higher order corrections, $a \sim d$ denotes the parton species, h is the hadron species, $f_{a/N}(x_a, Q^2)$ is the parton distribution function in a nucleon with momentum fraction x_a , $D_{h/c}(z_c, Q^2)$ is the parton fragmentation function, and $d\sigma/d\hat{t}(ab \rightarrow cd)$ is the cross sections of the parton+parton scatterings.

The particle production in each $A+A$ collision with impact parameter $b = 0$ is given by

$$\frac{d^2n_{AA}}{2\pi p_T d\eta dp_T} = \frac{K}{2\pi} \int d^2r t_A^2(r) \sum_{abcdh} \int dx_a \int dx_b f_{a/A}(x_a, Q^2) f_{b/A}(x_b, Q^2)$$

$$\times \frac{D_{h/c}(z_c, Q^2)}{\pi z_c} \frac{d\sigma}{dt}(ab \rightarrow cd), \quad (2.12)$$

where $t_A(r)$ is the nuclear thickness function and it is normalized to $\int d^2r t_A(r) = A$. The thickness function effectively represents the number of nucleons in the region $r \sim r + \Delta r$. A generalized expression of Eq. (2.12) for non-central collisions is available but not shown here because it is complicated[16]. The parton distribution function is, at the first approximation, the mean of parton distribution functions in proton and neutron:

$$f_{a/A}(x, Q^2) = \frac{Z}{A} f_{a/p}(x, Q^2) + \left(1 - \frac{Z}{A}\right) f_{a/n}(x, Q^2), \quad (2.13)$$

where Z and A are the atomic number and atomic mass of nucleus, respectively.

The calculation was vigorously performed by X.-N. Wang and M. Gyulassy. For example, in their HIJING Monte Carlo calculation[29], the hard scattering components are described by Eq. (2.12). Their Monte Carlo also simulates the nuclear effects by modifying the fragmentation functions and parton distribution functions as explained below. If no nuclear effect is considered in Eq. (2.12), it is equivalent to Eq. (2.10).

2.4.2 Modification Factor

For convenience, the ‘‘modification factor’’ is defined to express the strength of nuclear effects. The modification factor is defined by the ratio of yields:

$$R_{AA/NN}(p_T) = \frac{\overline{d^2n^c}}{2\pi p_T d\eta dp_T} \cdot \frac{1}{\langle N_{\text{coll}} \rangle^c \cdot \frac{d^2n_{NN}}{2\pi p_T d\eta dp_T}}, \quad (2.14)$$

where a denominator is the expected yield of hadron by binary scaling assumption which is the same as Eq.(2.10), and a numerator is the obtained yield by experiment or some calculation considering nuclear effects. If the binary scaling assumption is correct, $R_{AA/NN}$ should be unity. $R_{AA/NN}(p_T) > 1$ (or < 1) indicates enhancement (or suppression) is seen at the certain transverse momentum.

2.4.3 Known Nuclear Effects

The prediction by binary collision scaling represented by Eq. (2.10) is quite simplified and based on the assumptions that each binary collision is independent of others, and produced matter does not affect to the traveling partons as well as its fragmentations. In the past experiments of $p+A$ and $A+A$ collisions, this assumption is violated due to several nuclear effects.

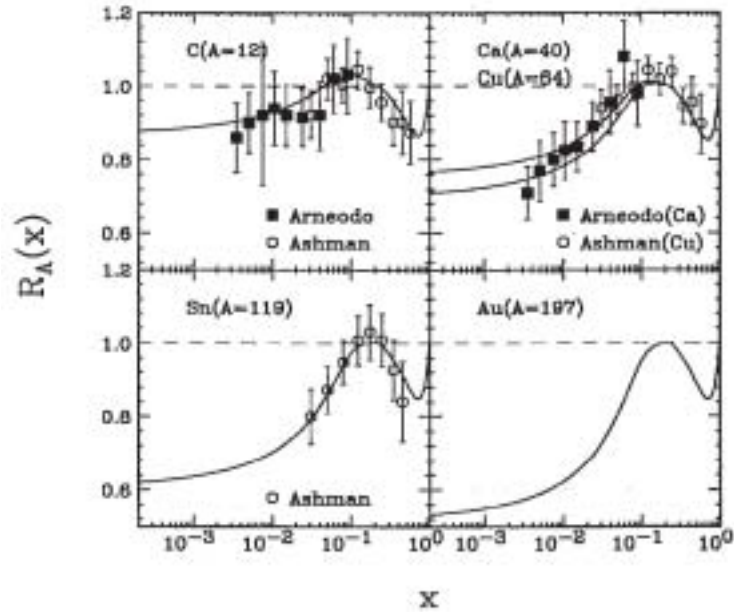


Figure 2.3: The ratios of quark structure functions $R_A(x) = f_{a/A}(x, Q^2)/Af_{a/N}(x, Q^2)$ as a function of x for different nuclear mass number A measured by EMC[30, 31] (points) and parametrization used in HIJING Monte Carlo[29](curves).

The known nuclear effects which affect to the high- p_T π^0 yield are, (1) nuclear shadowing and (2) Cronin effect. Brief explanations about these nuclear effects are given in the following.

Nuclear Shadowing

It was found in the measurement of parton distribution function by EMC (European Muon Collaboration) that $f_{a/A}(x, Q^2)$ of partons in the nucleus deviates from Eq. (2.13) and decrease at low- x region[30, 31]. This is called “nuclear shadowing effect” or “EMC effect”. The results from the EMC indicate that the effect is roughly Q^2 independent.

Figure 2.3 shows the ratios of the quark structure functions of nuclei with mass number A divided by the scaled structure function of a nucleon:

$$R_A(x) = \frac{f_{a/A}(x, Q^2)}{Af_{a/N}(x, Q^2)}, \quad (2.15)$$

for the several nuclei from carbon to tin measured by the EMC. The curves are the parametrization used in the HIJING[29].

Several mechanisms have been proposed to explain this effect based on the parton model. One interpretation is a destructive interference effect which causes suppression

of flux at low- x . Interaction probability that an incident parton is scattered inside the nucleus then scattered at back face of the nucleus again is suppressed due to the coherence effect[32] and causes shadowing effect.

The effect of nuclear shadowing was phenomenologically implemented in HIJING by replacing the parton distribution function in Eq. (2.13) by

$$f_{a/A}(x, Q^2, r) = S_{a/A}(x, r) \left[\frac{Z}{A} f_{a/p}(x, Q^2) + \left(1 - \frac{Z}{A}\right) f_{a/n}(x, Q^2) \right], \quad (2.16)$$

where $S_{a/A}(x, r)$ is the parton shadowing factor, parametrized to account for the $p+A$ data.

In Au+Au collisions, the shadowing effect reduces the averaged inclusive jet cross section. For partons with momentum p_T , x is roughly $\sim 2p_T/\sqrt{s_{NN}}$. In $\sqrt{s_{NN}}=130$ GeV collisions, $p_T = 2$ GeV/ c hadron correspond to $x \sim 0.03$. From Figure 2.3, the modification factor at this x is approximately 70 %, and it is still not in the deep-shadowed region. For higher p_T , the modification factor reaches unity. For sufficiently high energy collisions, such as LHC with $\sqrt{s_{NN}} = 6.3$ TeV, most of jets associated to $p_T \sim$ few GeV come from $x < 0.01$ region so that the shadowing effect become apparent.

Cronin Effect

It was first observed by Cronin *et al.*, in 1975 at Fermilab that there is an enhancement in the production cross section of hadrons in $p+A$ collisions compared to the simple scaling of $N+N$ data in $p_T > 2$ GeV/ c region[34, 33]. This is called ‘‘Cronin effect’’. The production cross section of hadrons in $p+A$ collision is represented by

$$\sigma_{pA}(p_T) = \sigma_{pp}(p_T)A^\alpha, \quad (2.17)$$

where $\sigma_{pp}(p_T)$ is the cross section of particle production in $p+p$ collisions. If the binary scaling is correct, $\alpha = 1$. By the Cronin effect, α is larger than unity. Figure 2.4 shows the measured α as a function of p_T for 400 GeV proton incident on A (corresponds to $\sqrt{s_{NN}} \sim 28$ GeV). The value α significantly larger than unity for $p_T > 2$ GeV/ c hadrons. In the case of gold nuclei, enhancement factor of pions relative to the scaled cross section by mass number is $A^\alpha/A \sim 1.7$.

The theoretical interpretation of the Cronin effect is the increase of average transverse momentum (k_T) of partons due to intrinsic k_T of partons in nucleon and multiple scatterings.

Even in $p+p$ collisions, the intrinsic $\langle k_T^2 \rangle_p$ has finite value due to uncertainty principle and higher order pQCD processes. The value of $\langle k_T^2 \rangle_p$ is measured by comparing deep inelastic $e+p$ collisions and $p+p$ collisions. Systematic study of Drell-Yan lepton pair production, heavy quark pair production, and direct photon production resulted the value of $\langle k_T^2 \rangle_p$ is ~ 1 GeV[35]. In $p+p$ collision at $\sqrt{s} = 20$ GeV, the p_T slope of invariant

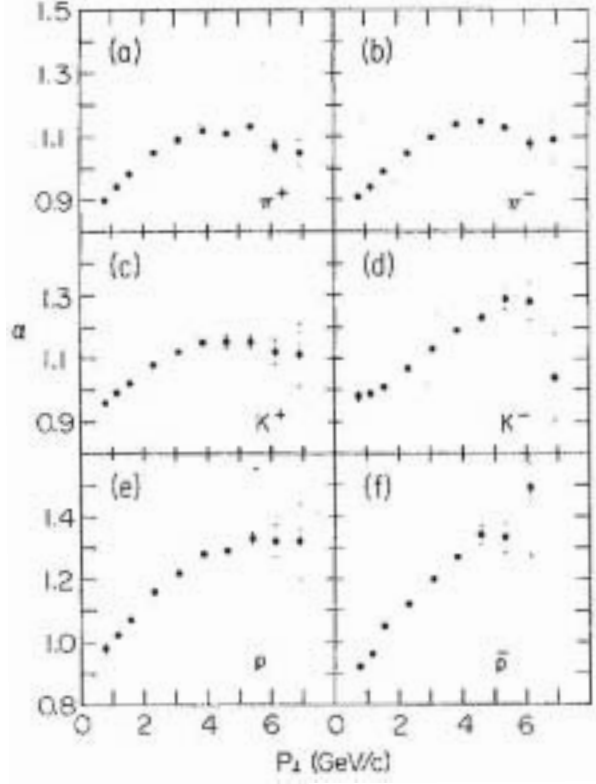


Figure 2.4: α as a function of p_T of produced hadrons by 400 GeV proton to nucleus measured at Fermilab[33].

yield of produced hadrons is decreasing steeply as p_T increases. If there are the initial k_T , final state hadrons could have the higher momentum so that strong enhancement is seen. In higher energy collisions, though, the effect of k_T kick becomes less important because the p_T slope becomes gentle.

In the case of $p+A$ collision, it is considered that additional multiple scattering occur in prior to the hard scattering. The total k_T value is usually expressed by the linear combination of intrinsic $\langle k_T^2 \rangle_p$ and multiple scattering effect:

$$\langle k_T^2 \rangle_A = \langle k_T^2 \rangle_p + \delta^2 (N_A(b) - 1), \quad (2.18)$$

where $N_A(b)$ is the number of target nucleons swept by the incoming proton at impact parameter b and δ^2 is the average momentum square added by one nucleon+nucleon collision. Eq. (2.18) represents that the incident proton has multiple scatterings by $(N_A(b) - 1)$ and increases its transverse momentum, before the hard scattering occurs. Values of $\langle k_T^2 \rangle_p$ and δ^2 are Q^2 dependent. For $Q = 2 \sim 3$ GeV, $k_T^2 = 1.4 \sim 1.7$ GeV²/c² and $\delta^2 = 0.064 \sim 0.129$ GeV²/c².

Since the direction of transverse kick and direction of parton momentum emitted

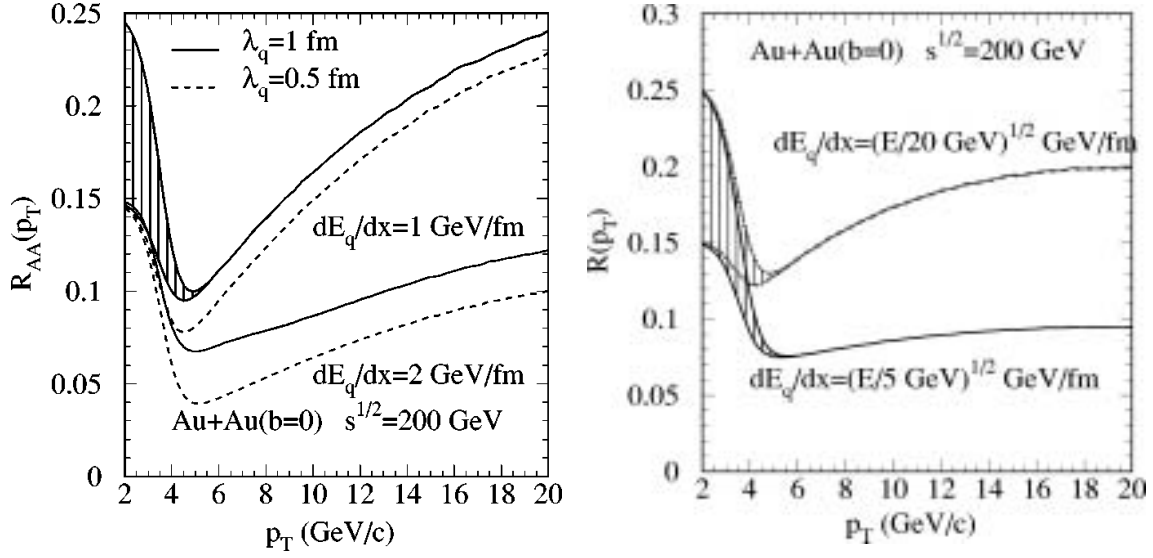


Figure 2.5: Modification factor v.s. p_T demonstrated by Wang[18]. Left panel shows result of calculation assuming constant dE/dx and mean free path. Shaded area indicates the uncertainty of the effective A scaling of low- p_T spectra depending on the interplay of soft and hard processes. Right panel shows result of calculation assuming energy dependent dE/dx . If higher energy parton has larger energy loss, the modification factor get flat. In both calculations, central ($b = 0$) Au+Au collisions at $\sqrt{s_{NN}} = 200$ GeV is considered.

by inelastic collision are independent of each other, k_T broaden the p_T distribution of fragment hadrons, and results in the enhancement of high- p_T hadron yields because the p_T distributions of hadrons are steeply decreasing with respect to p_T .

In pQCD calculation by Wang, the Cronin effect is implemented as a modification in the parton distribution function by

$$dx_a f_{a/A}(x, Q^2) \rightarrow dx_a d^2 k_{aT} \frac{1}{\pi \langle k_T^2 \rangle} e^{-k_T^2 / \langle k_T^2 \rangle} f_{a/A}(x, Q^2), \quad (2.19)$$

where the Gaussian function is assumed. The comparison between data and actual result of calculation is performed in later section.

2.4.4 Jet Quenching

Different from the nuclear shadowing and Cronin effect, jet quenching is an effect newly predicted to occur only in the high energy heavy ion collisions. Jet quenching effect implies the suppression of hadrons at high- p_T region above 2 GeV/c. On the other

hand, the nuclear shadowing predicts suppressions of hadrons at low momentum region ($p_T < 2 \text{ GeV}/c$) and Cronin effect predicts enhancement at ($p_T > 2 \text{ GeV}/c$) region.

The quantitative prediction of the parton energy loss is still under investigation. When parton energy loss is incorporated in the pQCD calculation, the parton fragmentation function is modified. As an example of implementation by Wang[18], the jet energy loss is assumed to depends on pass length ΔL that the parton traverse in the medium and fragmentation function is replaced by

$$D_{h/c}(z_c, Q^2) \rightarrow D_{h/c}(z_c, Q^2, \Delta L). \quad (2.20)$$

The parton energy loss is, in one of their options, $-dE/dx = 0.25 \sim 2 \text{ GeV}/\text{fm}$. In the case of $b = 0$ collision, the path length of parton ΔL is the length that the parton travels in the cylindrical medium with the nucleus radius.

The idea of constant dE_a/dx of parton a is obtained by considering bremsstrahlung radiation of gluons emission, and calculated by

$$-\frac{dE_a}{dx} = \frac{\varepsilon_a}{\lambda_a}, \quad (2.21)$$

where ε_a is the mean energy loss per gluon emission, and λ_a is the mean free path of a parton in the medium. The parton with reduced energy hadronize outside the deconfined medium according to the fragmentation function.

The left panel of Figure 2.5 shows the modification factor by the pQCD calculation. In this calculation, $-dE/dx = 1 \text{ GeV}/\text{fm}$ and $2 \text{ GeV}/\text{fm}$ are used and mean free path of 1 fm and 0.5 fm are assumed. Although the collision energy $\sqrt{s_{NN}} = 200 \text{ GeV}$ is different from the present experiment, the behavior might be almost same. The modification factor takes minimum at $p_T \sim 5 \text{ GeV}/c$ and increasing with respect to p_T . This is because the effect of constant dE/dx become relatively smaller for higher momentum partons.

Landau-Pomeranchuk-Migdal Effect in QCD

There is a model where the energy loss will depends on the parton energy, and energy density or parton density of the medium. There is a calculation considering a similar effect to electromagnetic interference of bremsstrahlung photons. In the case of high energy electrons (typically $> 100 \text{ GeV}$ electrons), electron loses its energy by bremsstrahlung in material. By the same reason, high energy γ causes e^+e^- pair creation near the nucleus. It was proposed by L. Landau and I. Ya. Pomeranchuk in 1953 that the interaction probability of bremsstrahlung is smaller for higher density medium than low density medium. And it is precisely calculated by Migdal[36]. This effect is called Landau-Pomeranchuk-Migdal (LPM) effect. This density effect is explained by

quantum mechanical interference, and high energy bremsstrahlung photon radiation is suppressed and energy loss of incident electron become weak.

It is probable that the same effect as LPM in electromagnetism will be in QCD system. In the QCD system, the electromagnetic field is replaced by the color field and partons have role of electrons in the QED framework.

The systematic analysis of the LPM effect in QCD medium was performed by Baier *et al.*[19, 37]. According to their analysis, the energy loss experienced by a fast parton propagating in an infinite large medium has an energy dependence expressed by

$$-\frac{dE}{dx} \propto N_c \alpha_s \sqrt{E \frac{\mu^2}{\lambda}} \ln \frac{E}{\lambda \mu^2} \quad (\text{for } E < \frac{\mu^2 L^2}{\lambda}), \quad (2.22)$$

where $N_c = 3$, E is parton energy, μ^2 is the Debye screening mass for the effective parton scattering, λ is parton's mean free path in the medium. For the QGP gas of $T = 200$ MeV temperature, Debye screening length is $\lambda_D \sim 0.36$ fm. Therefore, corresponding Debye mass is $1/\lambda_D \sim 0.56$ GeV, and Eq. (2.22) is effective for $E < 8$ GeV partons, if $\lambda = 1$ fm and $L = 5$ fm are assumed. If $N_c = 3$ and $\alpha_s = 0.3$ is given and the logarithmic factor is neglected, Eq. (2.22) become approximately $-dE/dx = \sqrt{E[\text{GeV}]/4}$.

For more energetic partons traveling through a medium with finite length, the energy loss becomes almost independent of E and can be related to the total transverse momentum broadening acquired by the parton through multiple scatterings, and given by

$$-\frac{dE}{dx} = \frac{N_c \alpha_s}{8} \Delta p_T^2 = \frac{N_c \alpha_s}{8} \delta p_T^2 \frac{\Delta L}{\lambda}, \quad (2.23)$$

where δp_T^2 is the transverse momentum kick per scattering the parton acquire during the propagation in the medium and ΔL is the total length that the parton travels. Since the energy loss per unit length is proportional to ΔL , the total energy loss of the parton is proportional to ΔL^2 .

Because above two cases are extreme cases of parton energy and the medium length, and involving two unknown parameters λ and μ^2 , it is difficult to apply it to a realistic case. In Wang's pQCD calculation, it was treated phenomenologically. The right panel in Figure 2.5 shows the result of his calculation. In this calculation, it is assumed that the energy loss is proportional to $\sqrt{E/E_0}$, where the factor E_0 is taken to be $20 \text{ fm}^2/\text{GeV}$ or $5 \text{ fm}^2/\text{GeV}$, and quark's mean free path λ_q was assumed to be 1 fm. Different from the constant dE/dx assumption in the left panel, the modification factor become flat at high- p_T .

Unfortunately, as it is seen in Figure 2.5, the LPM effect and energy dependence of dE/dx is seen if the modification factor is measured for p_T range larger than 10 GeV. As the maximum transverse momentum of observed π^0 's is 5 GeV/ c in this thesis, it is

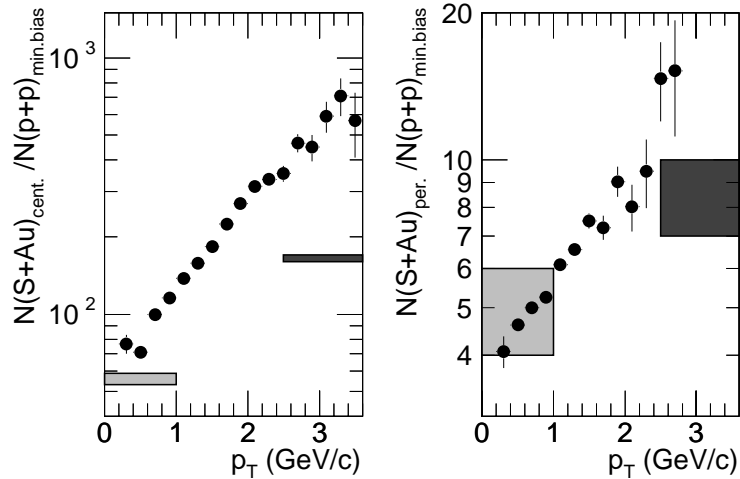


Figure 2.6: Ratio of central (left) and peripheral (right) 200A GeV S+Au to scaled $p+p$ π^0 production yield as a function of p_T measured from WA80 experiment. Indicated as shaded areas are the ratio of the number of participants at low p_T and the ratio of the number of binary collisions at high p_T .

difficult to compare the functional form of the modification factor between experiment and theory.

2.5 Past Experiments Concerned to Jet Quenching

Several attempts to measure the jet energy loss had been done but no evidence was found yet. Two experimental results of neutral pion yields at high- p_T region are available in high energy heavy ion collisions at CERN. One is WA80 experiment and the other is WA98 experiment.

2.5.1 WA80 Experiment

In the WA80 experiment, π^0 productions in 200A GeV S+S and S+Au collisions were measured. It corresponds to $\sqrt{s_{NN}} = 19.4$ GeV[38].

Figure 2.6 shows the results of π^0 measured from the WA80 experiment. Left panel shows the π^0 yield in central S+Au collisions divided by the yield in $p+p$ collision. Right panel shows the π^0 yield in peripheral S+Au collisions divided by the yield in $p+p$ collision. In both cases, at $p_T < 1$ GeV/c region, the π^0 yields are smaller than binary scaling prediction (dark shaded box) and the yield is close to $\langle N_{\text{part}} \rangle$ scaling (light shaded box). For higher p_T , the π^0 yields increasing as a function of p_T and reach to the binary

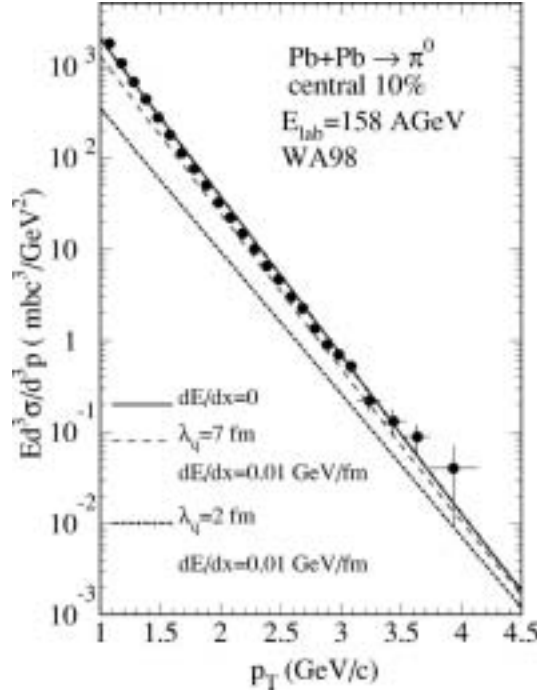


Figure 2.7: Measured π^0 production by Pb+Pb collision at $E_{lab} = 158$ GeV per nucleon[39]. Data is compared to the parton model calculations of single inclusive spectra of π^0 with different values of dE/dx and mean free path λ_q [35].

scaling at $p_T = 1.5 \sim 2.0$ GeV/c . At $p_T > 2.5$ GeV/c region, π^0 is enhanced significantly than binary scaling. These characteristics are same for both central and peripheral events. This enhancement of hadron yield at the WA80 experiment is explained by the Cronin effect.

2.5.2 WA98 Experiment

In the WA98 experiment, π^0 productions in 158A GeV Pb+Pb collisions were measured. It corresponds to $\sqrt{s_{NN}} = 17.8$ GeV[40, 39].

Figure 2.7 shows the invariant p_T distribution of inclusive π^0 . The data is available in the p_T region from 1 to 4 GeV/c . Data were compared to the theoretical calculations by Wang considering the jet energy loss[35]. According to Wang, the energy loss is limited to less than $-dE/dx = 0.01$ GeV/fm[41].

A left panel in Figure 2.8 shows the modification factor measured by the WA98 experiment[40]. The ratio is ~ 0.3 at low m_T and increases exponentially as large as 10 at $m_T = 4$ GeV/c² . A forceful explanation of this enhancement is due to the Cronin

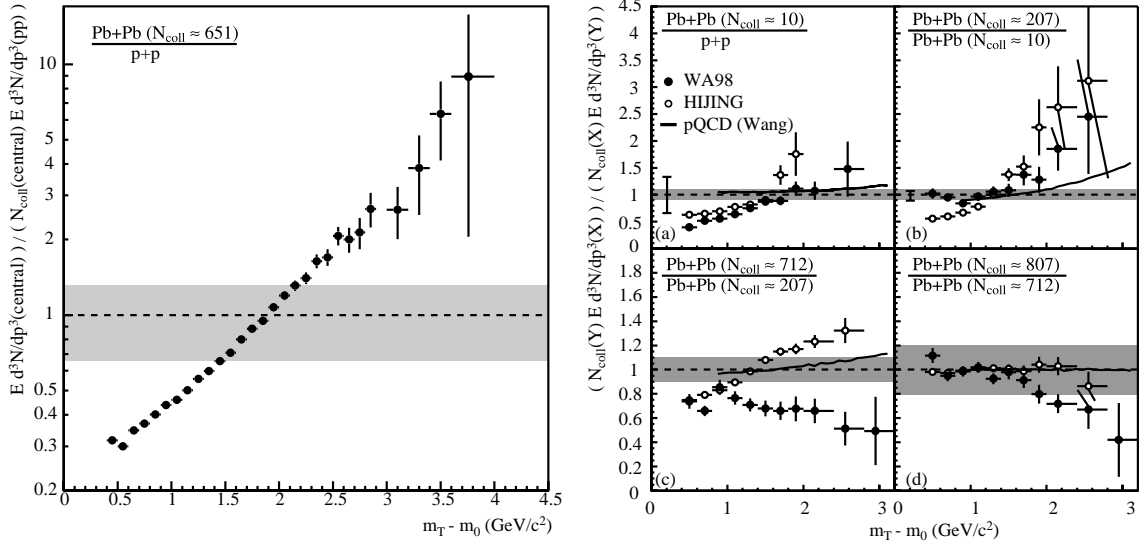


Figure 2.8: Left: Ratios of invariant multiplicity distributions of neutral pions for central (top 12.7 %) Pb+Pb reactions to the parametrization of $p+p$ reactions normalized to the number of binary collisions measured from WA98 experiment[40]. The gray band shows the estimate of the systematic error due to the calculation of the number of collisions and the absolute cross section normalization relative to $p+p$. Right: Ratios of π^0 yields in Pb+Pb collisions among several centralities.

effect.

WA98 collaboration reported the result of further analysis. They reported that although the enhancement is seen, the strength of enhancement of π^0 is weaker for central collisions than expected enhancement by the Cronin effect. A right panel in Figure 2.8 shows the ratios of π^0 yields measured from the WA98 experiment compared to the theoretical calculations using pQCD and HIJING by Wang including Cronin effect. In the plot (a) to (b), the WA98 data at $p_T > 1.5$ GeV/c agree to the theoretical calculations or higher than both calculation. But obviously the experimental data in (c) and (d) are below the theories and behavior is different from (a) and (b). It may suggest some suppression mechanism is in the large volume system.

Chapter 3

Experimental Setup

3.1 Overview

In this chapter, descriptions about the AGS-RHIC accelerator complex and the PHENIX detector system are given. Detailed explanations of detectors used for the π^0 measurement are provided.

3.2 AGS-RHIC Accelerator Complex

Figure 3.1 shows the AGS-RHIC high energy heavy ion accelerator complex[42, 43] at Brookhaven National Laboratory (BNL) in Upton, New York, United States of America.

At the beginning of an acceleration cycle of the beam, the negatively charged (-1) heavy ions generated by a pulsed sputter ion source are injected to Tandem Van de Graaff. The ions are accelerated in the Tandem Van de Graaff with the static field up to 15 MeV and pass a stripping foil in the high voltage terminal. The ions are stripped off its electrons to be positively multi-charged (Q_T) ions. The stripped ions are accelerated back to ground potential and increase their energy by $15 \times Q_T$ MeV. For gold beam, a charge state of Au^{12+} is selected for further acceleration, and an energy at the exit of Tandem Van de Graaff is 1.0 MeV per nucleon. Exiting from the Tandem Van de Graaff, the ions are further stripped to charge state Au^{32+} . The ions are then transferred to the Booster Ring via the Heavy Ion Transfer Line (HITL) and the Heavy Ion Bypass Line (HITB). The Booster Ring increases the beam energy up to 95 MeV per nucleon. Then the Au^{32+} beam is stripped to charge state of Au^{77+} by a foil (only K-shell electrons are remaining) and injected to the Alternating Gradient Synchrotron (AGS). The AGS accelerates the beam to 10.8 GeV per nucleon. In one cycle of acceleration from the Tandem to the AGS, AGS has four bunches and each bunch has approximately 1×10^9 ions and 12 ns length. Then the heavy ions are fully stripped (Au^{79+}) and injected to the RHIC through the AGS to RHIC Transfer Line.

The brief summary of parameters of RHIC is shown in the Table 3.1. RHIC is the

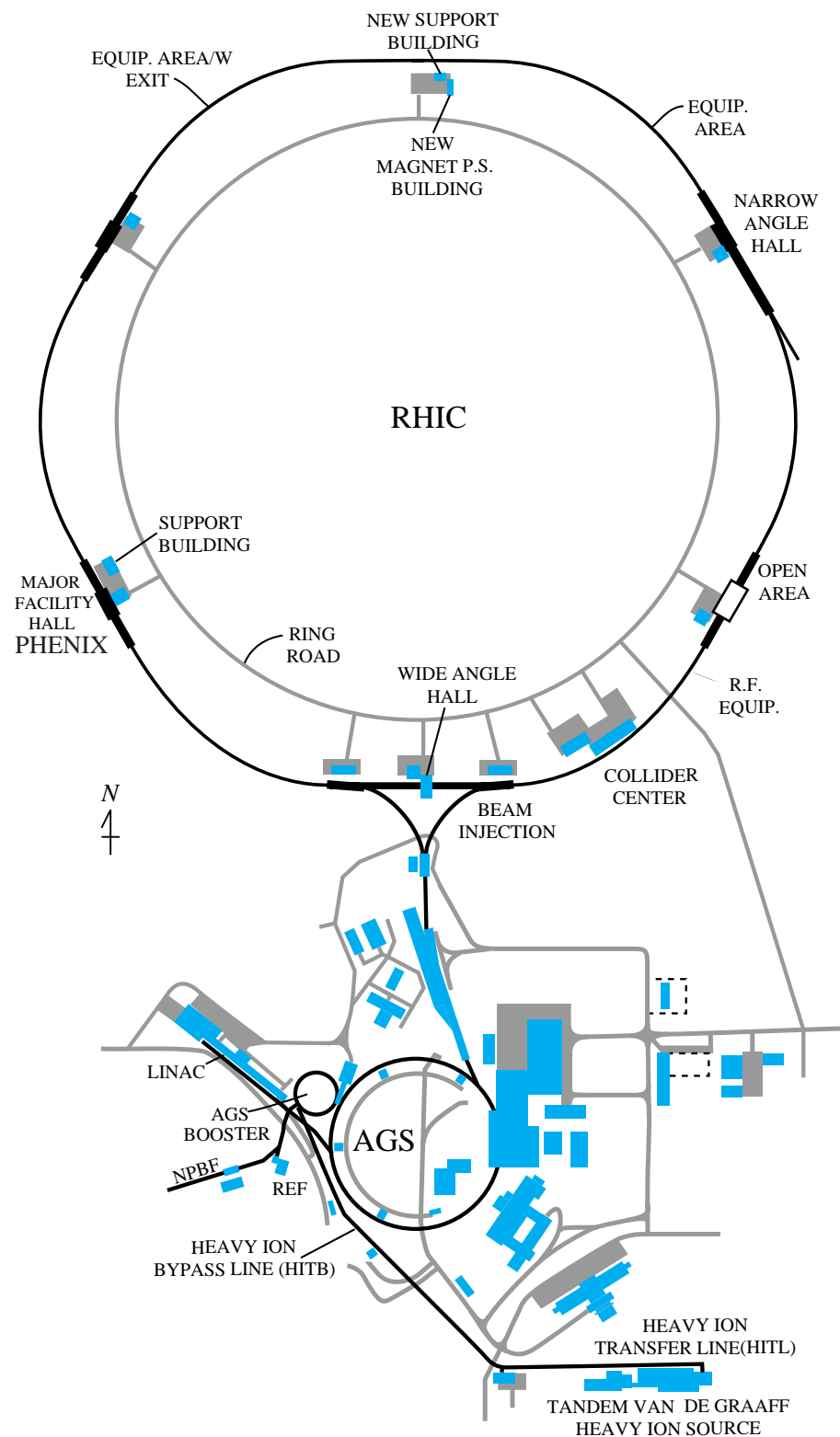


Figure 3.1: The AGS-RHIC accelerator complex.

Number of accelerator rings	2	
Circumference of each ring	3.834 km	
Number of bunches per ring	60	
Bunch spacing	213 ns	
Number of interaction regions	6	
Beam life time	~ 10 hours	
Collision angle	< 1.7 mrad	
Number of dipole	192 (per ring) \times 2 + 12 common = 396	
Number of quadrupoles	276 arc + 216 insertion = 492	
Number of other magnets	72 trim quadrupoles 288 sextupoles 492 correctors	
Dipole field	3.458 T @ 100 GeV/u, Au	
Arc dipole length	9.45 m (effective) , 9.728 m (physical)	
Operating temperature	< 4.9 K	
Filling time	< 1 minute	
Acceleration time	75 seconds	
	for Au+Au collisions	for $p+p$ collisions
Number of particles per bunch	1×10^9	1×10^{11}
Energy spread	$\pm(1.49 \sim 1.78) \times 10^{-3}$	$\pm(0.83 \sim 1.25) \times 10^{-3}$
Normalized emittance at top energy	43π mm·mrad	29π mm·mrad
rms bunch length	0.19 \sim 0.22 m	0.10 \sim 0.14 m
Kinetic energy	11 \sim 100 GeV/u	30 \sim 250 GeV
Design Luminosity (10 hours average at top energy)	2×10^{26} cm $^{-2}$ s $^{-1}$	1.4×10^{31} cm $^{-2}$ s $^{-1}$
Maximum event rate	~ 1.4 kHz	~ 800 kHz

Table 3.1: Summary of RHIC parameters[42, 43].

colliding type accelerator with the two acceleration rings. Each ring has approximately 3.8 km circumference. A total of 60 bunches are injected into each collider ring. The 2×15 AGS cycles are used to fill two RHIC rings and total of 6×10^{10} ions are injected in each ring sequentially, accelerated simultaneously, and are kept colliding for several to 10 hours until the beams are dumped.

In the RHIC, the 192 superconducting dipole magnets are used in each ring. The maximum magnetic field of the dipole magnets is 3.46 Tesla. Also 12 common dipole magnets, 492 quadrupole magnets and 852 trim or corrector magnets are used. All of these magnets are superconducting magnets and operated in temperature less than 4.9 K. The beams collide at six intersection points. PHENIX detector system is placed at one of the intersection points (8 o'clock position in the Figure 3.1).

RHIC can accelerate any species of stable nuclei from proton to Au. The maximum beam energy of the RHIC is 100 GeV per nucleon for Au ions and the center-of-momentum energy $\sqrt{s_{NN}}$ is 200 GeV. In the case of $p+p$ collisions, the maximum beam energy is 250 GeV and $\sqrt{s}=500$ GeV. It is also to be noted that RHIC can realize anisotropic collisions like $p+A$ and so forth.

For head-on collisions of very short bunches, the beam luminosity (L) is given by

$$L = \frac{f_r}{4\pi} \frac{BN_B^2}{\sigma_H \sigma_V}, \quad (3.1)$$

where $f_r \sim 80$ kHz is the revolution frequency, $B = 60$ is the number of bunches in one ring, N_B is the number of particles in one bunch, and $\sigma_{H,V}$ are horizontal or vertical radius of the beam. N_B is $\sim 1 \times 10^9$ for Au beam and $\sim 1 \times 10^{11}$ for proton beam. Since the $\sigma_{H,V}$ at the crossing point are tuned to be ~ 0.1 mm, the expected L is order of $10^{27} \text{ cm}^{-2}\text{s}^{-1}$ for Au+Au collisions. In realistic case, due to beam-beam collision angle (less than 1.7 mrad) and beam losses, the 10 hours averaged beam luminosity is $2 \times 10^{26} \text{ cm}^{-2}\text{s}^{-1}$ for $\sqrt{s_{NN}}=200$ GeV Au+Au collisions, and $1.4 \times 10^{31} \text{ cm}^{-2}\text{s}^{-1}$ for $\sqrt{s}=500$ GeV $p+p$ collisions.

The beam life time is determined by rf-bucket size limitation, intra-beam interaction, and beam-beam interactions such as bremsstrahlung electron pair production, beam-beam coulomb dissociations, and nuclear interactions. Also interaction between beam and residual gas contributes to the beam life time. Since the intra-beam or beam-beam interaction scattering cross section is proportional to Z^4/A^2 , the beam loss is severe for Au beam. The half life of the Au beam is ~ 14 hours while proton's half life is ~ 400 hours.

The expected rate of the nuclear interaction is estimated from the luminosity L and total nuclear interaction cross section σ_{ntot} by $L \cdot \sigma_{ntot}$. Since $\sigma_{ntot} \sim 7.2$ barn for Au+Au collisions, the expected collision rate is ~ 1.4 kHz. For $p+p$ collisions, the event rate will exceeds 800 kHz where $\sigma_{ntot} \sim 60$ mb at $\sqrt{s}=500$ GeV.

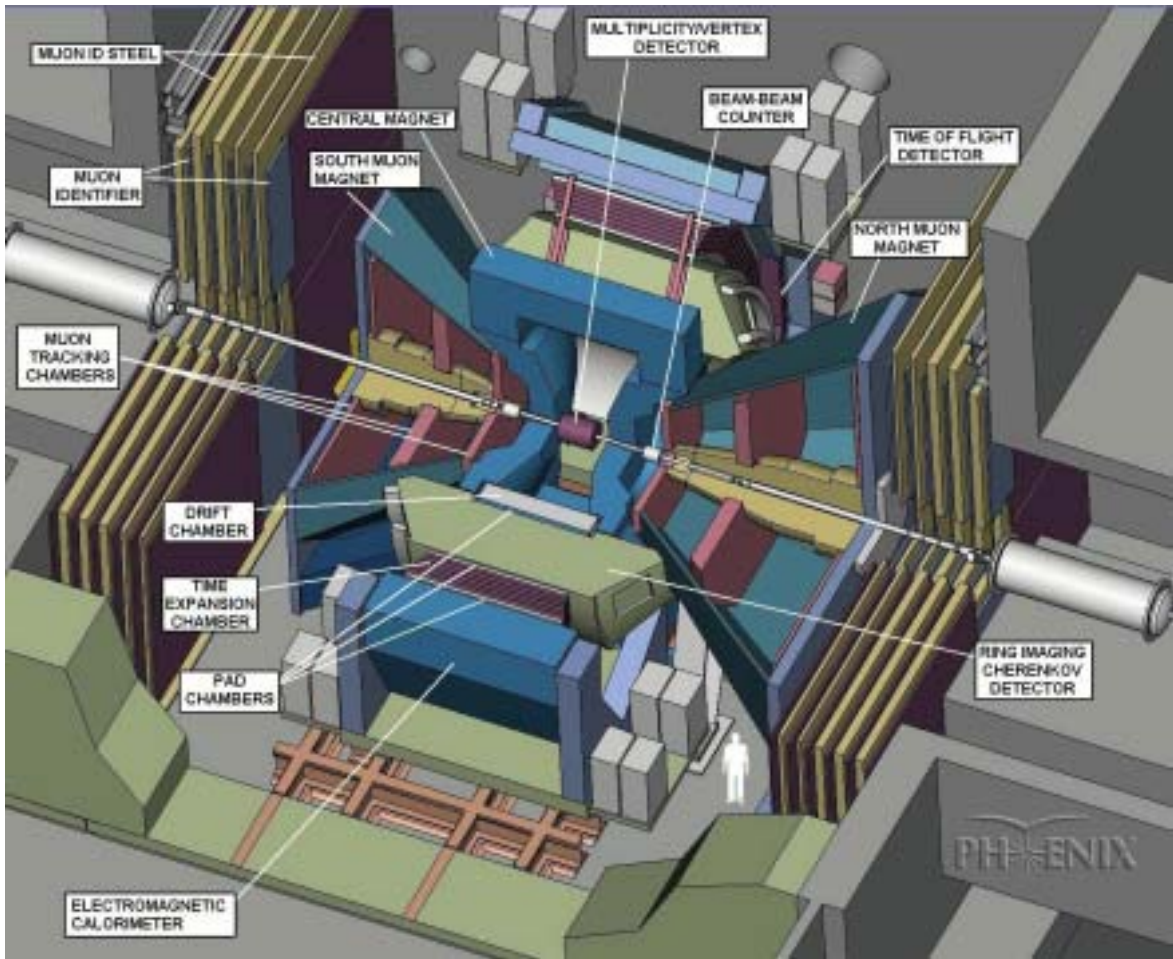


Figure 3.2: The air-scape of the PHENIX detector system.

In the six collision points of the RHIC, there are four detectors designed to study heavy ion collisions, STAR[44], PHOBOS[45], BRAHMS[46, 47] and PHENIX that is explained in the next section. Experiments of polarized $p+p$ collisions at $\sqrt{s} = 500$ GeV are also planned and performed at PHENIX[48] and STAR[49].

3.3 PHENIX

The PHENIX[50] consists of many detector subsystems. Figure 3.2 shows the air-scape drawing of the PHENIX detector system. Detector subsystems are surrounding the beam pipe which is penetrating the PHENIX. The construction of PHENIX has begun in 1995. More than 400 collaborators including scientists and engineers from 51 institutes in 11 countries have participated in the experiment.

The PHENIX detector is designed to perform a broad study of the collision system

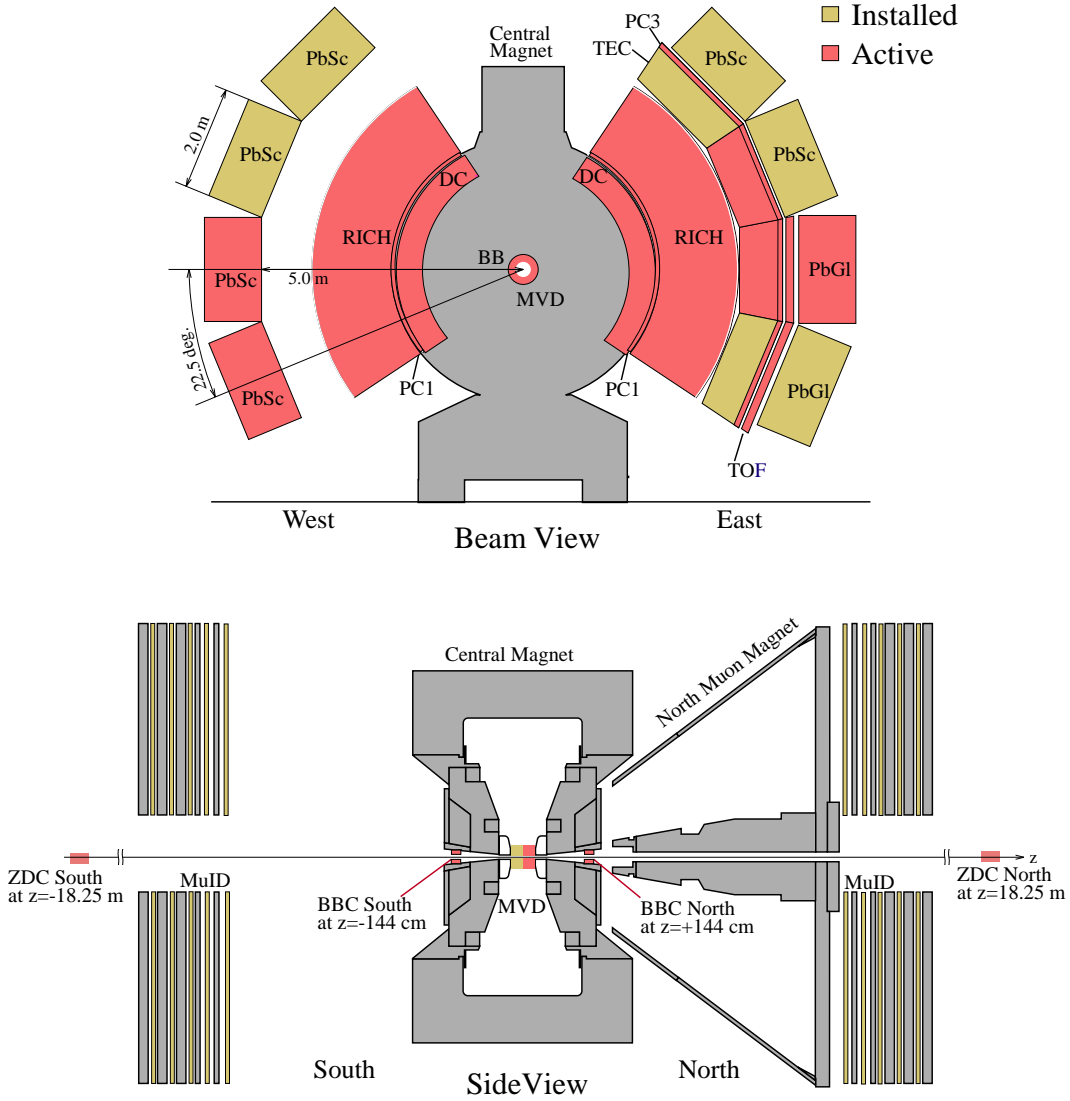


Figure 3.3: PHENIX experimental setup in the Year-2000 run. Only installed detectors in the run are shown. The used (active) detectors in the run and unused detectors are distinguished by different shades. Top: Cross section perpendicular to the beam pipe. Bottom: East side view of the cross section along the beam pipe.

Component	η or θ coverage	$\Delta\phi$ coverage	Purpose and special features
Central Magnet	-	-	$BL(\text{max}) = 1.15 \text{ T}\cdot\text{m}$.
BBC	$3.1 < \eta < 3.9$	360°	Trigger, start time, vertex position measurement, event characterization.
ZDC	$\theta < 2 \text{ mrad}$	360°	Trigger and event characterization.
DC	$-0.35 < \eta < 0.35$	$90^\circ \times 2$	Charged momentum measurement. $\Delta p/p = 0.6 \oplus 3.6 \cdot (p \text{ GeV}/c) \%$.
PC	$-0.35 < \eta < 0.35$	$90^\circ \times 2$	Tracking for non-bend direction.
RICH	$-0.35 < \eta < 0.35$	$90^\circ \times 2$	Electron identification.
PbSc EMCAL	$-0.35 < \eta < 0.35$	$90^\circ \times 1.5$	Photon and electron detection.

Table 3.2: Summary of detector subsystems of the PHENIX experiment. Only components used in the thesis are shown.

from $p+p$, $p+A$ to $A+A$ collisions. In Au+Au collisions, the particle multiplicity per one event is very high ($dN/dy|_{y=0} \sim 1,000$), and the number of charged particles come in the PHENIX aperture is estimated to be more than 300 per event. PHENIX is required to measure many probes, electrons, muons, photons, hadrons, as good as possible resolution in such high multiplicity environment to perform systematic study of quark matter as well as spin structure of the nucleon using polarized proton beam[48].

Figure 3.3 shows the setup of the PHENIX in Year-2000 run¹. Upper half of the figure shows the cross section perpendicular to the beam pipe. Lower half of the figure shows east side view of the cross section along the beam pipe. The PHENIX detector has a central magnet, two central arms in the east and west, and two muon arms in the north and south. The central arms are shown in only upper half of the figure and the muon arms are shown in only lower half for clearness. The muon arms are not used in this thesis.

The central arms are used to measure electrons, photons and charged hadrons. Each central arm covers a pseudo-rapidity range of $-0.35 < \eta < 0.35$ for single particles, and 90 degrees in azimuth. As shown in the Figure 3.3, the configuration of west and east arms are different. The west arm has a drift chamber, a Pad Chamber (PC1)[51], Ring Image Cherenkov (RICH) detector[52, 53], and four Electromagnetic Calorimeter (EMCAL) sectors[54]. While the east arm has a drift chamber, Pad Chambers (PC1 and PC3), RICH detector, Time Expansion Chambers (TEC)[55], Time of Flight (TOF),

¹Year-2000 run was the first period of attempts of data acquisition. The run summaries are given in Chapter4.

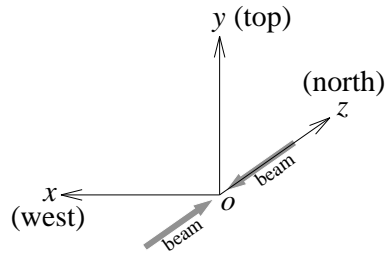


Figure 3.4: Definition of global coordinates system.

and four EMCal sectors.

Independent from the central arms, BBC's (Beam-Beam counters)[56] and ZDC's (Zero-Degree calorimeters)[57, 58] are used for collision vertex determinations, event triggers, and event characterizations.

The geometrical coverages and main purposes of the detectors of PHENIX are summarized in Table 3.2 where only the components used in the thesis are described.

3.3.1 PHENIX Global Coordinate System

In order to describe unambiguously the detector setup, the global coordinates system of the PHENIX is introduced. Figure 3.4 shows the schematic explanation of the global coordinate system. The definition of the coordinates system is as follows:

1. Origin of the coordinate system is the center of interaction region along the center of beam pipe cylinder. Actually it is approximately in the center of Central Magnet.
2. y -axis is defined as altitude relative to the origin's altitude.
3. z -axis is defined as an axis along the center of beam pipe. $z > 1$ directs north side of detector.
4. x -axis is defined as x , y and z axes form right handed coordinate system. Thus the x -axis directs west side of detector.

Each central arm is symmetrical with respect to the $z = 0$ plane.

It should be noted that origin of PHENIX coordinates system is not event vertex (Au+Au collision point) because the Au beam has finite length (~ 20 cm in σ in design value) and collision can happen at any place in the overlapping region of colliding beams.

Item	Parameters
Segment size	$5.54 \times 5.54 \text{ cm}^2$
Sampling cell thickness	5.6 mm (0.277 X_0)
Scintillator	4 mm, Polystyrene (1.5 % PT / 0.01 % POPOP)
Absorber	Pb, 1.5 mm thickness
Active sampling cells	66
Active depth	375 mm, 18 Rad.length, 0.85 Abs.length
WLS fiber	BCF-99-29a, 1 mm
Number of fibers	36 per tower
PMT type	FEU115M, $\phi 30$ mm, MELS, Russia [60]
Photo-cathode	Sb-K-Na-Cs
Quantum Efficiency	15.5 % at 500 nm wavelength
Gain	$4 \sim 6 \times 10^6$
Luminous sensitivity	$\geq 80 \mu\text{A/lm}$
Rise time (20% \rightarrow 80%)	$\leq 5 \text{ ns}$

Table 3.3: Summary of EMCAL parameters.

3.4 Electromagnetic Calorimeter

3.4.1 Overview

The electromagnetic calorimeter (EMCAL) is the system to measure the energy, position, and arrival time of electrons, positrons and photons[59]. Since the EMCAL is the key detector in this thesis, a separate section is prepared for its explanation.

The PHENIX EMCAL consists of two different types of electromagnetic calorimeters[54]. One is the Lead-Scintillator type calorimeter (PbSc), and the other is the Lead-Glass type calorimeter (PbGl). The EMCAL consists of eight sectors and are surrounding the beam pipe. Six sectors (3/4 azimuthal coverage) are PbSc type and the other two sectors are PbGl type. As shown in Figure 3.3, four PbSc sectors were placed in the west arm, and two PbSc and two PbGl sectors were placed in the east arm. In the Year-2000 run, two PbSc calorimeter sectors in the east arm and a PbGl calorimeter sector were operational, as indicated in Figure 3.3. Since the two operational PbSc sectors were used in this thesis, following descriptions are concentrated on the PbSc.

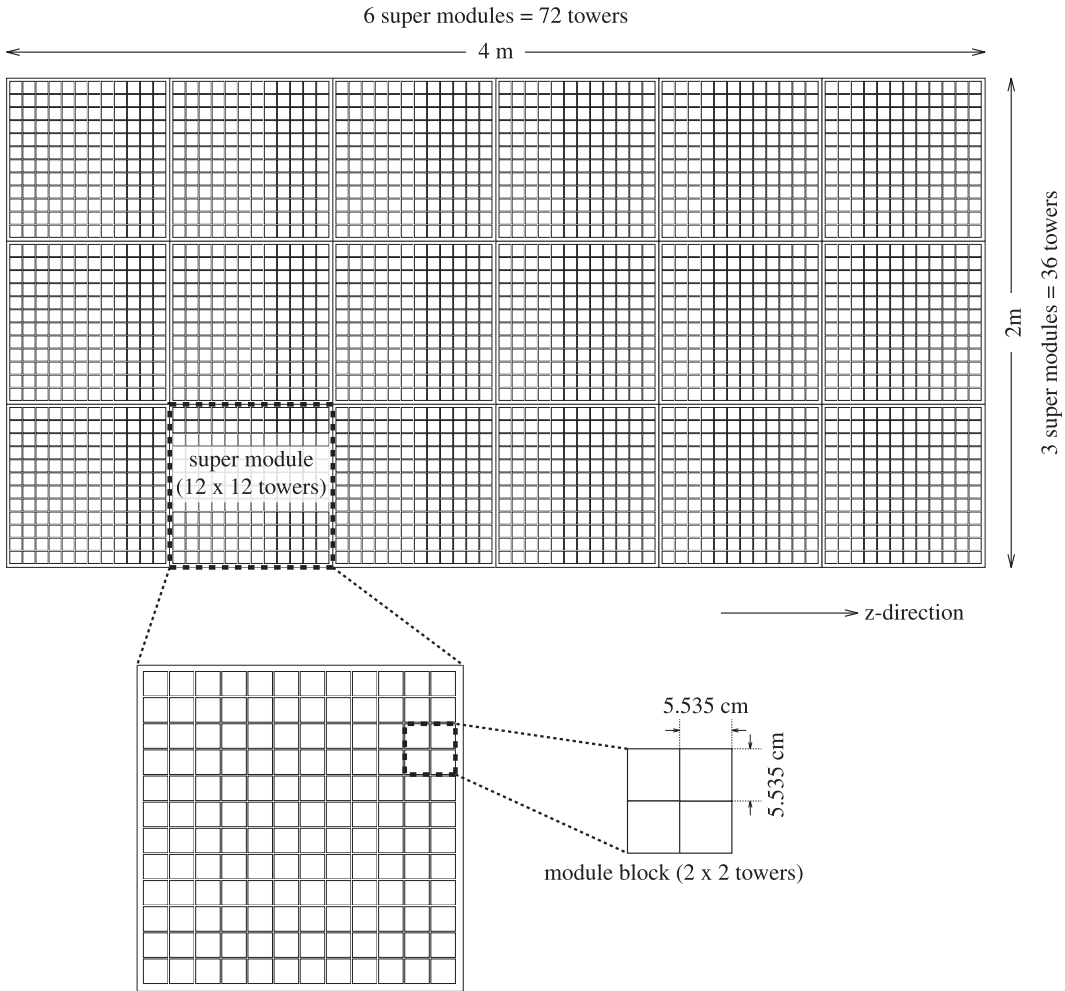


Figure 3.5: Collision point view of a PbSc sector. A sector consists of 6×3 super modules. A super module consists of 12×12 towers. Two sectors were operational in Year-2000 run.

3.4.2 Structure

The EMCal is a sampling calorimeter. One sector consists of 2,592 calorimeter tower elements arrayed so that their heads constitute a flat plane, and covers an area of 4 m in z -direction and 2 m in azimuthal direction. The distance between the nominal collision point to the EMCal surface is 5.0 m at the center of a sector and 5.3 m at edge because the sector has a flat surface. Due to the same reason, the photons from vertex have ~ 20 degrees angle from the perpendicular line to the EMCal surface at the edge. With two sectors active in Year-2000 run, EMCal covers kinematical region of $-0.35 < \eta < 0.35$ and $\Delta\phi = 45^\circ$. A summary of the parameters of PbSc is given in Table 3.3.

The surface size of a tower element is $5.54 \times 5.54 \text{ cm}^2$. As shown in Figure 3.5,

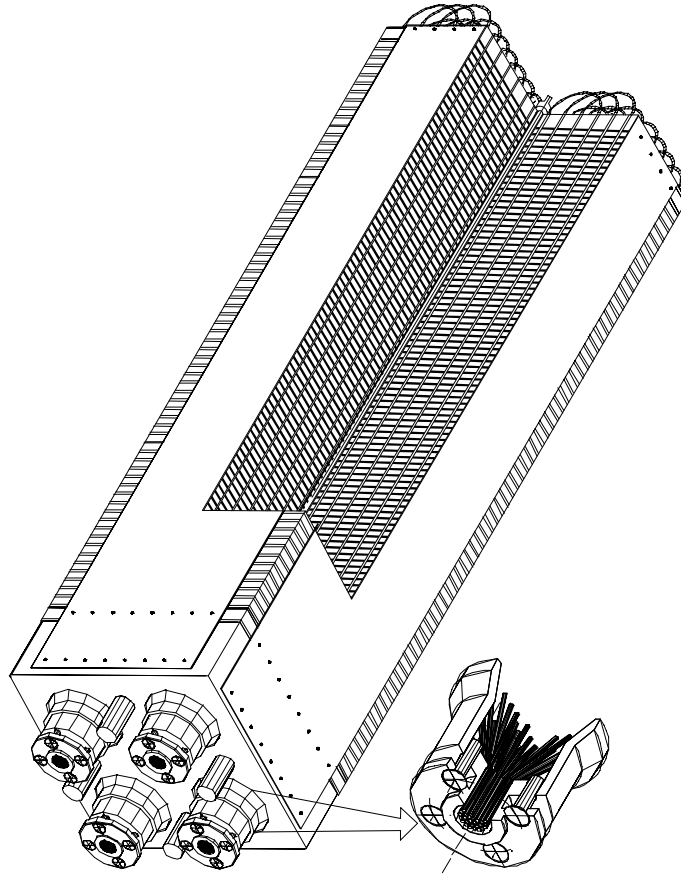


Figure 3.6: A module of PbSc calorimeter. A module consists of four towers. WLS fibers are penetrating scintillator and lead plates, and collected to a PMT.

towers were organized into $6 \times 3 = 18$ “super modules”. A super module consists of 6×6 calorimeter “module blocks”. Each module block has four (2×2) mechanically grouped but optically isolated calorimeter tower elements. Thirty six module blocks are attached to a backbone and held together by welded stainless steel skins on the outside, and one rigid structure of super module is formed.

Figure 3.6 shows the interior view of a module block. Each tower is a sampling type calorimeter composed of 66 sampling cells which consist of alternating lead and scintillator plates. Thirty six wavelength shifting (WLS) fibers are used as the light guide. WLS fibers are longitudinally penetrating the tower and optically connecting each scintillator. Finally the scintillation lights are collected into a photomultiplier tube (PMT) at the bottom of the tower. A PMT has 30 mm diameter and was manufactured in Russia (FEU115M)[60]. The WLS fibers attenuates light yield with the attenuation length of ~ 120 cm. The attenuation length was measured by scanning PbSc tower with

radioactive source and with cosmic muons. Since the tower length is ~ 37.5 cm, the attenuation factor for the lights from farthest position from the PMT is ~ 70 %. Due to light collection efficiency, attenuation in the WLS, quantum efficiency of the PMT, and so on, the nominal number of photoelectrons at PMT is $\sim 1,500$ for 1 GeV electromagnetic particles. A signal from PMT's are readout by the front-end readout electronics system and light yields and flash timings of towers are recorded.

The depth of PbSc is 18 radiation length and Molière radius (ϱ_M) is ~ 6 cm; i.e. 90 % of shower energy is deposited in a cylinder with this radius[59]. Since the tower size is smaller than ϱ_M , the energy of a particle is deposited in multiple towers, and form a “cluster” which is two-dimensional energy distribution. The total energy of a particle is measured by adding energy deposits in towers contributing to such cluster. Also cluster shape (energy distribution) give the important information for particle identification and particle hit position measurement. The analysis method to find the clusters is described in Section 5.5. The energy resolution is measured from test beam experiment.

An intrinsic timing resolution is expected to be better than 200 ps for the electromagnetic showers. The timing information of each tower is used for the measurement of particles arrival time and photon identification.

3.4.3 Performances from Test Beam

The basic performance of PbSc EMCAL had been tested using the particle beams at U-70 (IHEP, Russia), AGS (BNL) and SPS (CERN)[61].

Energy Resolution

Figure 3.7 shows the result of energy measurement. EMCAL was exposed to 0.5, 1.0 and 2.0 GeV/c of electrons, protons and charged pions. The electrons distribution is peaked at the beam energy showing that all its energy was contained in the calorimeter. Charged pions deposit energy of ~ 250 MeV almost independently of the incident energy. It is because $\beta\gamma = p/Mc$ exceeds 3.5 for 0.5 GeV/c or higher momentum pions. For protons at 1 GeV/c momentum, the $\beta\gamma \sim 1$ and an ionization become 3 times larger than minimum ionization. For protons at 2 GeV/c, the minimum ionization peak is seen at the same position as charged pions (~ 250 MeV). Since the depth of PbSc measured in units of absorption length at normal incidence is $0.85 L_{abs}$, ~ 43 % hadrons would have hadronic interaction in the detector. Then the tails of energy distributions for pions spread to the full beam energy as shown in Figure 3.7. Major process for large energy deposition is π^0 production inside the tower where π^0 decays immediately to two photons and cause electromagnetic cascades.

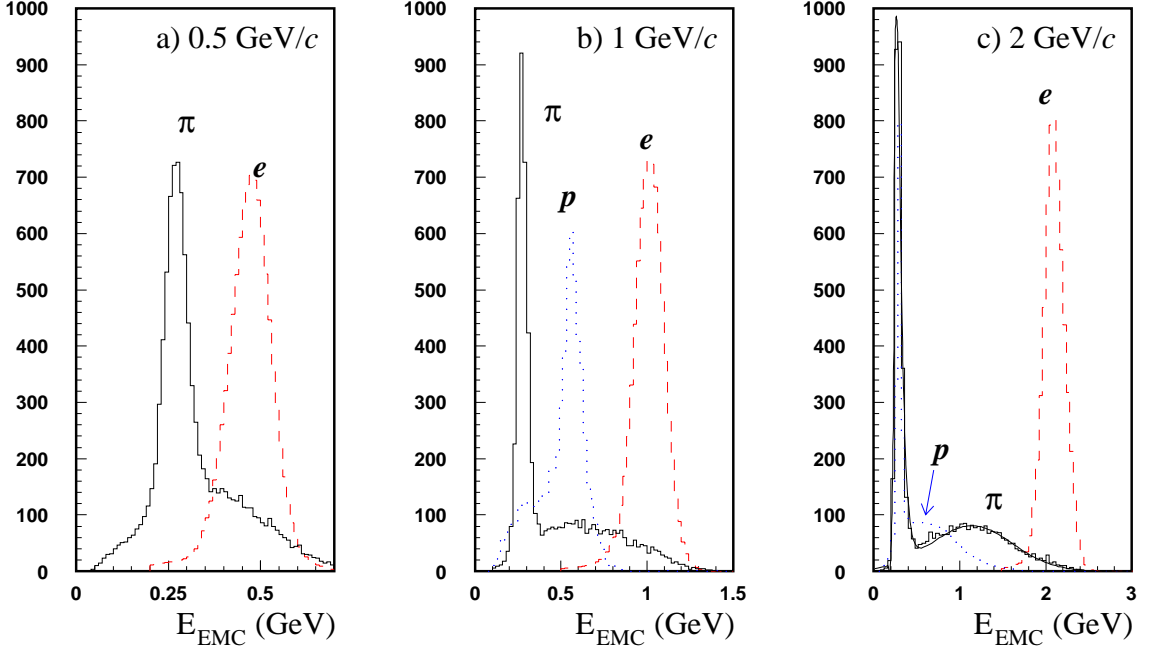


Figure 3.7: Test result of the energy spectra measured in the EMCal. EMCal was exposed to electrons (dashed lines), pions (solid lines) and protons (dotted lines) beams: (a) 0.5 GeV/c , (b) 1 GeV/c and (c) 2 GeV/c .

The nominal energy resolution obtained from the test beam result is approximately given by

$$\frac{\sigma_E}{E} = \frac{8.2}{\sqrt{E}} \oplus 1.9 \%, \quad (3.2)$$

where E is the energy of the incident particle in the unit of GeV, and an operator \oplus represents quadratic sum. The value 8.2 for the stochastic term is close to the expected resolution from sampling as predicted by simulation based on GEANT. The constant term are intrinsic non-uniformities, and contributors include tower boundaries, energy leaking from the calorimeter via the front and back surfaces, hot spots at fiber positions and shower depth fluctuations. Especially, the main contributor is the response inhomogeneity. A particle hitting the corner of the tower causes 8 % smaller output.

Position Resolution

If a particle impacts the detector perpendicularly, the hit position of the particle is measured from the center of gravity of energy distribution in the towers. The measured shower shape depends on the incident angle of the particle on the EMCal. It was checked by test beam experiment and simulation. The position resolution depends on the incident

photon energy (E) and the incident angle (θ) by

$$\sigma_x(E, \theta) = \sigma_0(E) + \Delta \times \sin \theta, \quad (3.3)$$

where

$$\sigma_0(E) = 1.55 + \frac{5.7}{\sqrt{E}} \text{ [mm]} \quad (3.4)$$

is the position resolution for normal incidence, E is represented in the unit of GeV, and $\Delta \sim L_{rad} \sim 19$ mm. Since the maximum incident angle of photons on the PbSc is 20 degrees, $\Delta \times \sin \theta \sim 6.5$ mm and the position resolution for 1 GeV photon is ~ 13 mm.

Time Resolution

Timing information from the EMCal is used for particle identification. In particular, timing information is very useful to reject neutral baryons; anti-neutron is a major contributor to clusters that can ~ 2 GeV energy deposit. Also, a large inconsistency between the measured times in different towers in a cluster often indicates the overlap of two particles with very different arrival time.

The velocity of lights in the WLS fibers is $v \simeq c/1.7$. Therefore, if a relativistic particle penetrates the tower. light produced in the last tile (the tile closest to the PMT) appears ~ 880 ps earlier than light from the first tile. Taking into account the entire shower development and the discriminator threshold, penetrating particles is expected to produce a timing signal ~ 200 ps earlier than electromagnetic particles. However, if an anti-neutron with 2 GeV/ c momentum and a photon are compared, an arrival time of neutron on the PbSc delays 2 ns after the photon arrival. Therefore, timing is useful tool to reject baryons even they vanishes at the last tile.

Particle arrival times measured by exposing the EMCal to electrons, pions and protons at 1 GeV/ c momenta are shown in the three plots at the top of Figure 3.8. The timing distribution for the electrons has a Gaussian shape with a few events in the tails. Both the pion and proton distributions show the presence of tails and shapes are slightly asymmetric.

A bottom plot in Figure 3.8 shows the relations between timing resolution and energy deposit in the tower measured by exposing the calorimeter to the particles in the 0.3 \sim 1.0 GeV/ c momentum range. Away from the discriminator threshold the calorimeter timing resolution is nearly constant at ~ 100 ps for electrons, and ~ 270 ps for hadrons where shower fluctuations are the major contributor to the measured resolution. In general the data can be well fitted by the function:

$$\Delta t = \Delta t_0 + \frac{\Delta t_1}{E - E_{th}}, \quad (3.5)$$

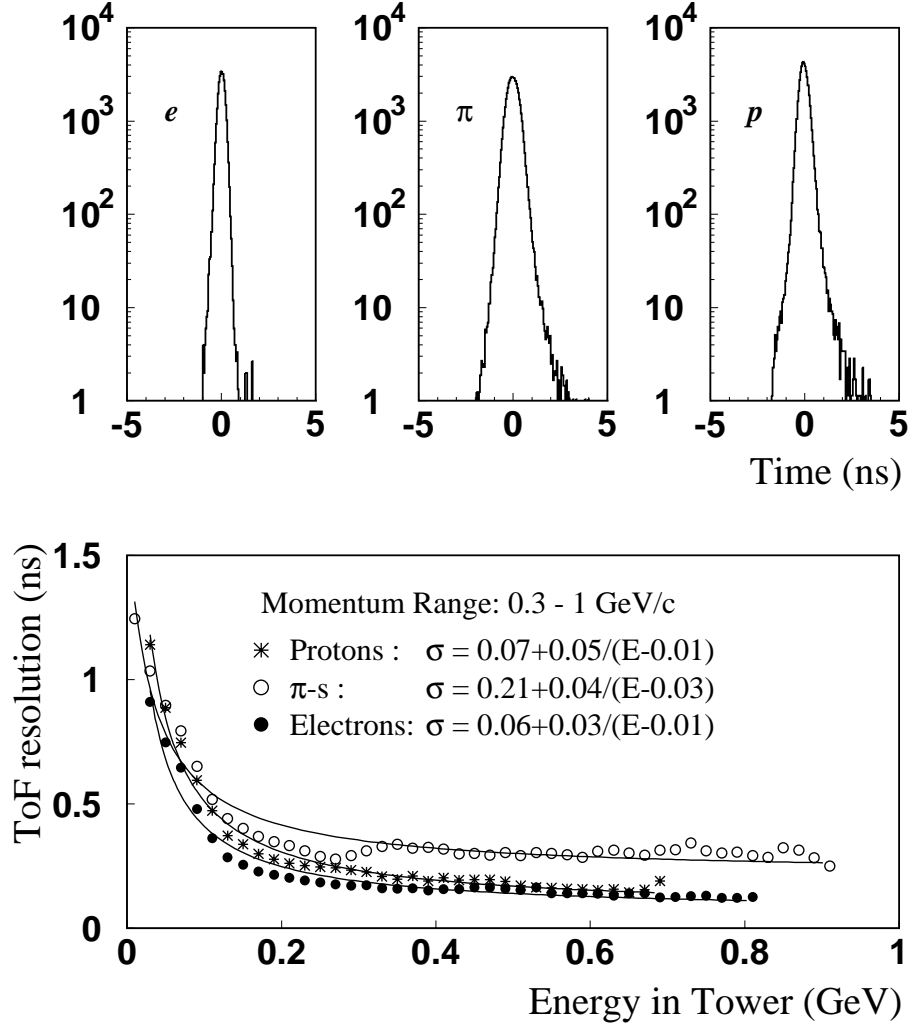


Figure 3.8: PbSc EMCal time of flight resolution for electrons, pions, and protons. Top: Line shape for 1 GeV/c electrons, pions, and protons. Bottom: Resolution v.s. energy in momentum range 0.3 to 1 GeV/c .

where Δt_0 is an intrinsic timing resolution limit due to fluctuations in the localization of the shower, and Δt_1 includes fluctuations of photon statistics as well as pulse shape fluctuations. The latter is dominant near threshold E_{th} .

3.4.4 Monitoring System

The calibration and monitoring system of PbSc EMCal is based on a UV laser which supplies light to the calorimeter through a series of optical splitters and fibers. The block diagram of the monitoring system is shown in Figure 3.9.

Light from a high power YAG laser is initially split into six equal intensity beams by

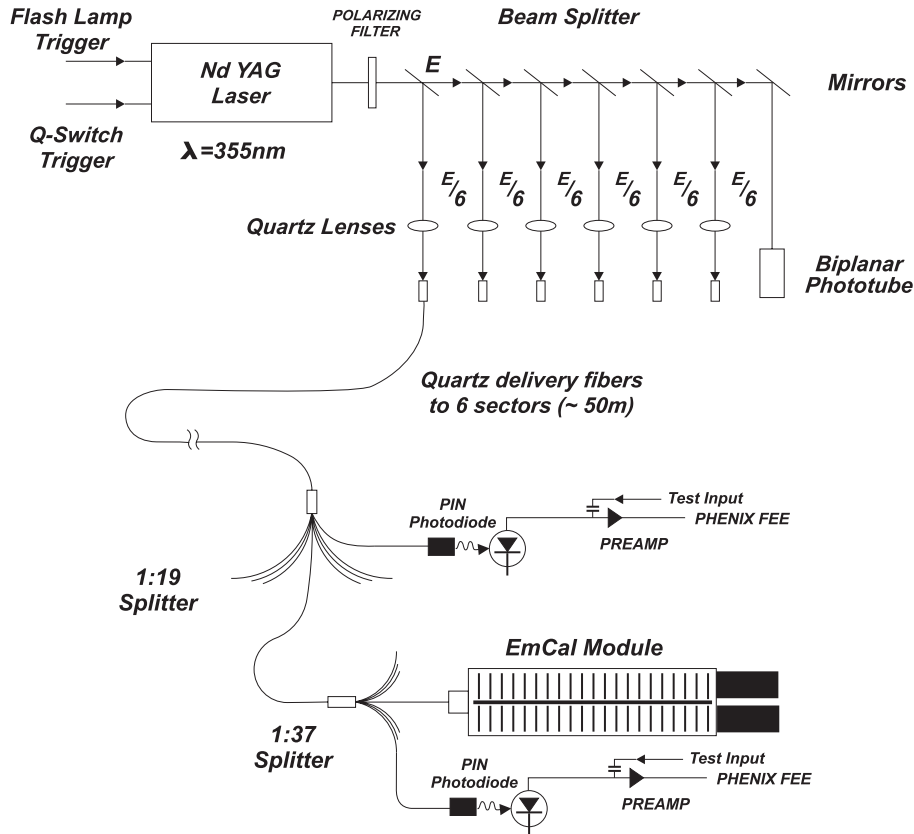


Figure 3.9: Schematic diagram of PbSc EMCAL laser light distribution and monitoring system.

partially reflecting mirrors. The beam from each mirror passes through a quartz lens and is focused to a point just in front of a quartz fiber. The fiber transport the light over a distance of approximately 50 m to each sector of PbSc EMCAL. Optical splitters are used to distribute the light to each of the individual calorimeter module blocks. At the last stage the light is injected into a 38 cm, 2 mm diameter plastic fiber that penetrates the center of the module block (small gap in the optical shield of the towers). This “leaky fiber” is grated such that light exits along it length simulating the depth of profile of a 1 GeV electromagnetic shower in the four surrounding towers in the module block.

The overall efficiency to convert the primary light of the laser to photoelectrons in an individual tower is $\sim 4 \times 10^{-12}$. Approximately 0.2 mJ per pulse from the YAG laser is delivered, to immitate 1 GeV of energy into each tower.

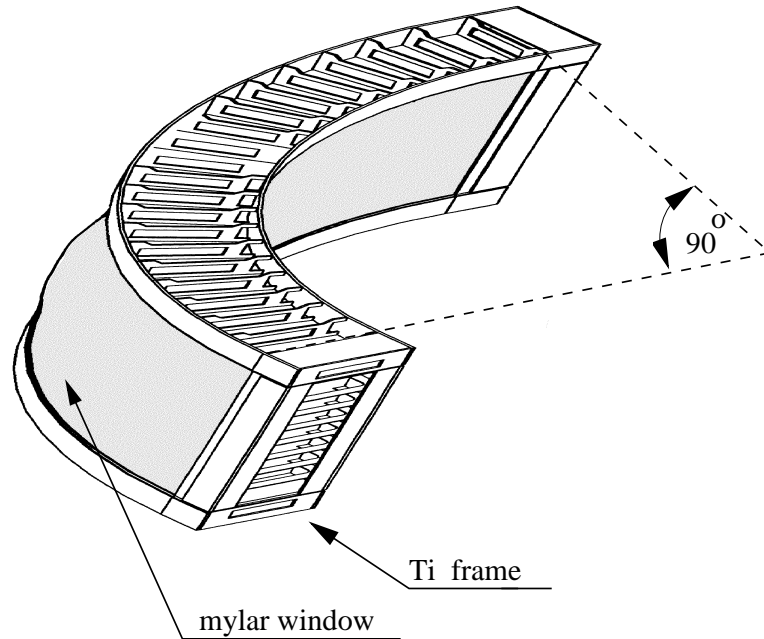


Figure 3.10: Structure of the Drift Chamber.

3.4.5 Energy Calibration

Energy calibrations were performed by measurements of cosmic ray muons and electrons test beam. The PbSc response to the cosmic ray muons penetrating the super module in the direction nearly orthogonal to the tower axis was recorded. With the response to laser pulses, the cosmic muon data was used to minimize relative difference of gains of towers. The absolute energy scale was in turn established by test-beam measurements using electrons of known energy. In the analysis stage, the final energy scale calibration is performed by using invariant mass measurement of π^0 's.

3.5 Other Devices in the Central Arms

Momentum of charged particles were determined by using Pad Chamber 1 and drift chamber. Electron identification was performed by using RICH.

In the analysis the electron sample measured by DC-PC1-RICH combination was used to check the response of EMCal to the electromagnetic particle. Also the charged particle tracks were used to extract the minimum ionization peaks (MIP's) by muons and charged pions. The MIP's were then used to check the energy scale of EMCal.

In the following subsections, the brief summary of these devices are provided.

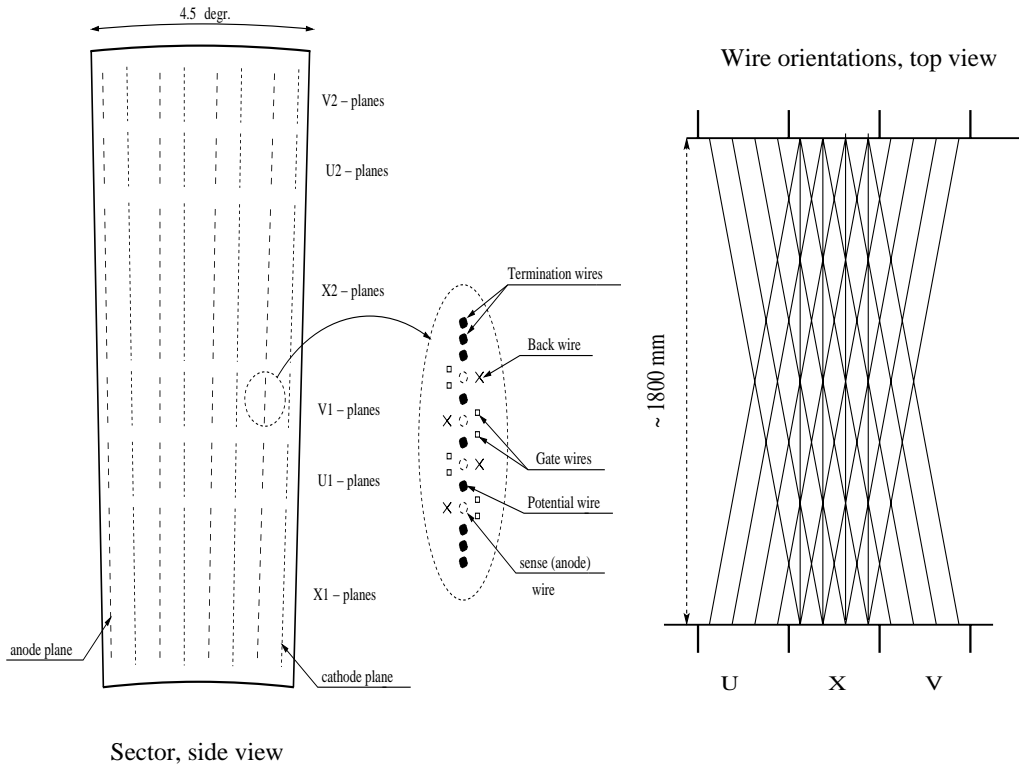


Figure 3.11: The layout of DC wire position within one DC sector. Figure in the right shows stereo wire orientation.

3.5.1 Drift Chamber

The PHENIX drift chamber (DC) system consists of two independent gas volumes located in the west and east arms. The chambers in the east arm and the west arm are symmetric with respect to $x = 0$ plane, as seen in Figure 3.3. Each volume is cylindrically shaped and located in the region from 2.02 to 2.46 m from the beam axis, 2 m along the beam direction, and 90 degrees in azimuth. The DC is in residual magnetic field of 0.6 kG at maximum. Each DC measures charged particle trajectories in the $r - \phi$ direction to determine p_T of each particle. The DC is also used for the pattern recognition at high particle track densities by providing position information that is used to link tracks through the various PHENIX detector sub-systems. To measure invariant mass of ϕ by $\phi \rightarrow e^+e^-$ channel with a resolution better than its natural width ($4.5 \text{ MeV}/c^2$) and have good tracking efficiency under high multiplicities at RHIC, the DC was designed to have (i) single wire resolution better than $150 \mu\text{m}$ in $r - \phi$, (ii) two track separation better than 1.5 mm, (iii) single wire efficiency better than 99 %, and (vi) spatial resolution in the z -direction better than 2 mm.

As shown in Figure 3.10, each DC volume is defined by a cylindrical titanium frame defining the azimuthal and beam-axis limits of the detector volume. 5-mil Al-Mylar window define the limits of the gas volume radially. Each frame is filled with drift chamber modules and is divided in 20 equal sectors each covering 4.5 degrees in ϕ . As shown in Figure 3.11, there are six types of wire modules stacked radially in each sector: X1, U1, V1, X2, U2 and V2. Each wire module contains four sense (anode) planes and four cathode planes forming cells with a 2.0–2.5 cm drift space in the ϕ direction. U1, V1, U2, and V2 wires have stereo angles about 6 degrees relative to the X-wires and measure the z position of the track.

To satisfy the requirement of efficient track recognition for up to 500 tracks per event, each sense wire is separated in the center into two halves. Each half of sense wire is then read out independently. To electrically isolate the two halves of a single sense wire the wire was attached to a low mass central support. The support was made of Kapton with 100 μm thickness and introduces only very little additional mass in the chamber. Each wire plane in a cell has it's own Kapton strip in the center to which the anode wires were attached and then cut in the middle. Since the DC system contains roughly 6,500 anode wires, number of total readout channels of DC is 13,000. The anode wires are separated by potential wires and surrounded by gate wires and back wires. Gate wires limit the track sample length to roughly 3 mm and terminate unwanted drift lines. The back wire has a rather low potential and terminates most of drift lines from it's side, eliminate left-right ambiguity, and decreasing the signal rate by a factor of two. The DC volumes were filled with a gas mixture of 50 % Ar and 50 % Ethane.

3.5.2 Pad Chambers

The PHENIX Pad Chambers (PC) are multi-wire proportional chambers. Each detector contains a single plane of wires inside a gas volume bounded by two cathode planes. One cathode is finely segmented into an array of pixels. The charge induced on a number of pixels when a charged particles starts an avalanche on an anode wire, is read out through specially designed readout electronics.

The PC determines the positions along the straight line particle trajectories outside the magnetic field. As shown in Figure 3.3, the innermost pad chamber plane, called PC1, is located between the DC and the RICH on both the west arm and the east arms. PC1 is essential for determining the three-dimensional momentum vector by providing the z coordinate at the exit of the DC. Also one more PC system (PC3) is mounted just in front of the EMCal only on the east arm.

Figure 3.12 shows the pad pattern of the PC. Each cell contains three pixels and an avalanche must be sensed by all three pixels to form a valid hit in the cell. The interleaved

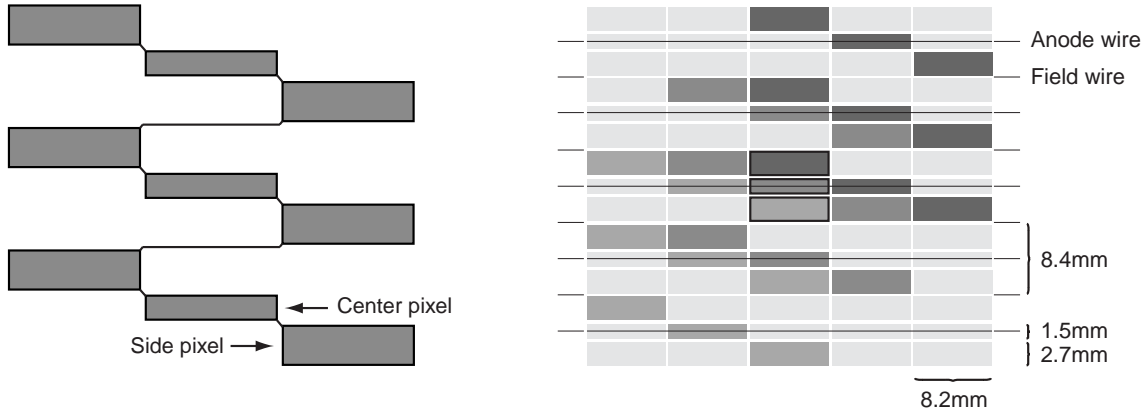


Figure 3.12: The pad and pixel geometry (left). A cell defined by three pixels is at the center of the right picture.

pixels were ganged together, nine-by-nine and connected to a common readout channel, such that the three pixels in a cell are always connected to different but neighboring channels and each cell is defined by its unique channel triplet. So, the information can be broken down to the cell level, by identifying the triplet.

This arrangement saves a factor of nine in readout channels compared to readout of every pixels and a factor of three compared to a readout pad geometry where a cell is the actual electrode connected to an electronics channel. The design goals for the position resolution were ± 4 mm. This motivated an anode wire spacing of about 8 mm. For geometrical reasons, a spacing of 8.4 mm was chosen. Desiring a square cell geometry, a cell area of $8.4 \text{ mm} \times 8.4 \text{ mm}$ was adopted. In the z direction this resulted in a position resolution of ± 1.7 mm which was substantially better than the design goals.

3.5.3 RICH

The RICH (Ring Image CHerenkov) detector is designed for electron identification, and provides e/π discrimination below the π^\pm Cherenkov threshold, which is set at $\sim 4 \text{ GeV}/c$. In combination with the EMCAL, the goal is to limit the false identification of hadrons as electrons to less than 10^{-4} .

Figure 3.13 shows a cutaway drawing of one of the RICH detectors revealing the internal components. Each RICH detector has a volume of 40 m^3 , with a particle entrance window area of 8.9 m^2 and a particle exit window area of 21.6 m^2 , and filled with CO_2 gas (or Ethane gas). The entrance and exit windows are made of $125 \mu\text{m}$ thickness Kapton, and covered by black vinyl coated polyester light shields. Each detector contains 48 composite mirror panels, forming two intersecting spherical surfaces, with a total

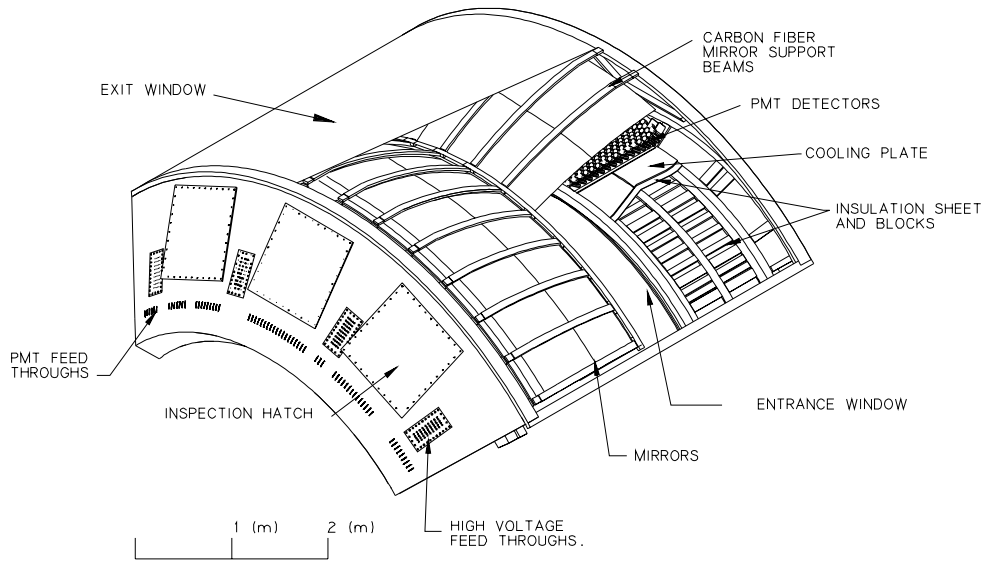


Figure 3.13: A cutaway view of one arm of the RICH detector.

reflecting area of 20 m^2 . The spherical mirrors focus Cherenkov light onto two arrays of 1,280 Hamamatsu H3171 UV sensitive PMT's, each located on either side of the RICH entrance window. The PMT's are fitted with 2" diameter Winston cones and have magnetic shield hats which allow them to operate at up to 100 Gauss. The UV glass of PMT absorb photons of wavelength below 200 nm. The thickness of radiator gas is 87~150 cm. The preamplifiers are mounted directly on the detector.

3.6 Trigger and Event Characterization Devices

In Year-2000 run, PHENIX mainly used two devices, ZDC's and BBC's for triggering events. The minimum bias trigger was made as logical OR of these main trigger devices. In addition, five scintillators were used for temporary test trigger. These are used for trigger bias study of main trigger devices and to trigger cosmic muon which punches through the EMCal. In the following sections, explanations of main trigger devices are presented.

3.6.1 ZDC's: Zero-degree Calorimeters

The main purposes of ZDC's[57, 58] are to determine the collision centrality, to monitor the beam luminosity, and to generate minimum bias event trigger. PHENIX as well as the other three RHIC experiments use a pair of commonly designed ZDC's placed at very forward region; "ZDC North" at north side and "ZDC South" at south side. The

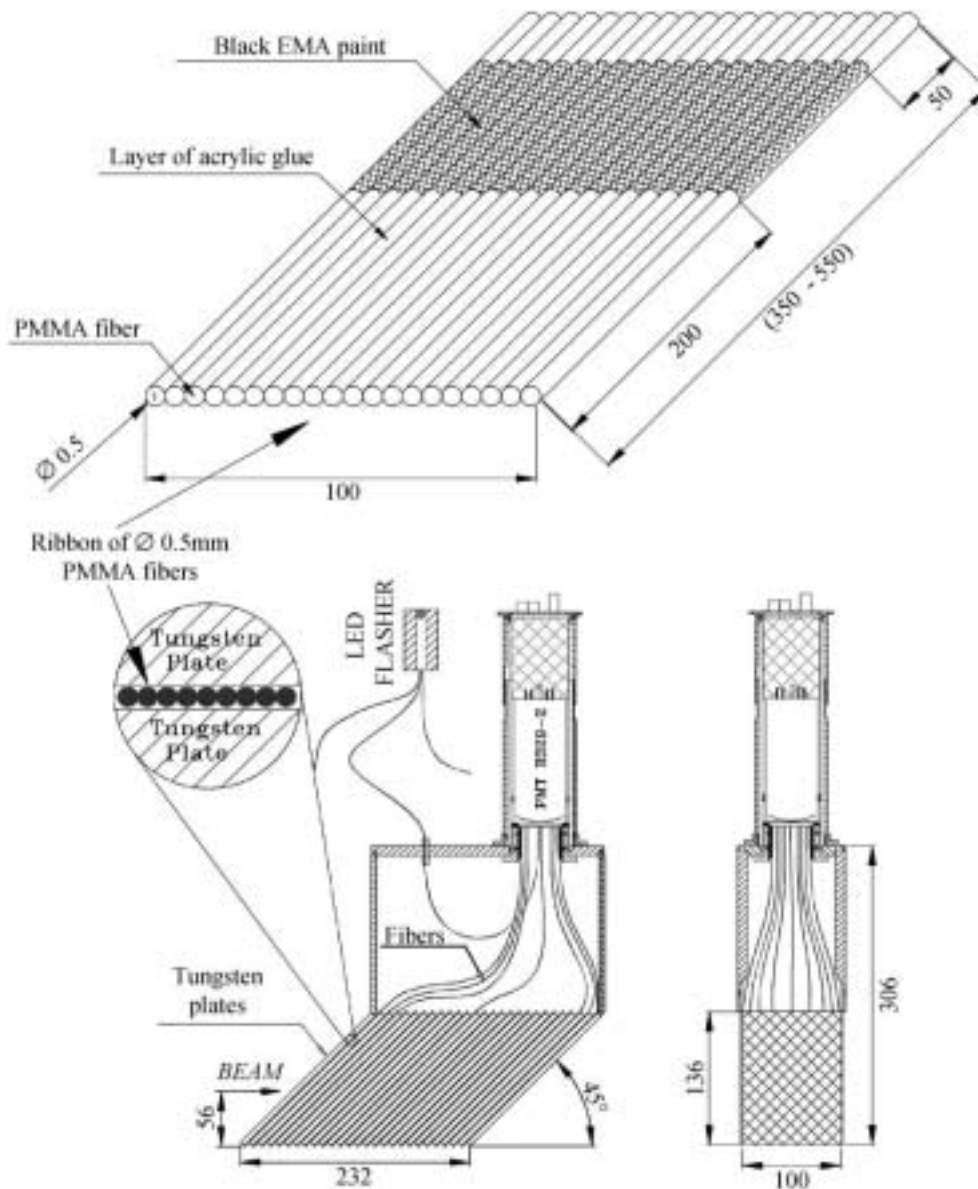


Figure 3.14: Cross section of the ZDC module[57].

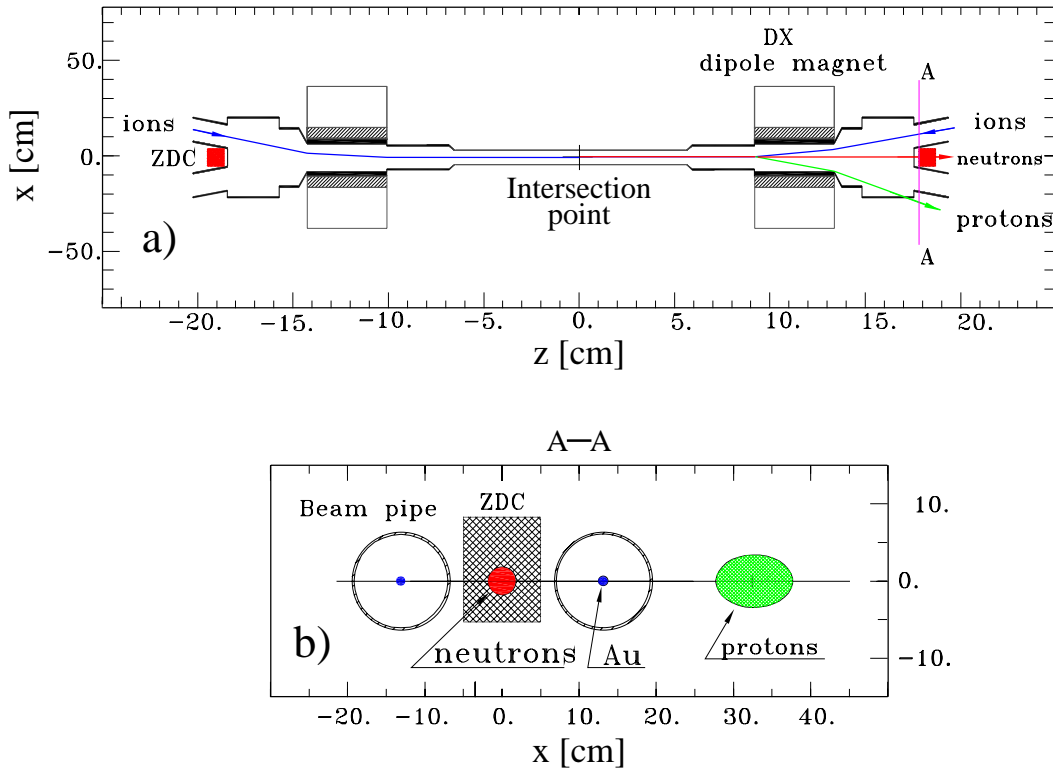


Figure 3.15: Overview of RHIC intersection region. A top figure shows the top view of the intersection region, with arbitrary scales. Au ions from both rings collide at $z = 0$ and produced protons and other charged particles are swept by DX dipole magnets and do not reach to the ZDC's. Only neutral particles arrive ZDC's. A bottom figure shows the cross section at A-A' position in top figure. This shows the position of each fragments or Au beam.

ZDC's are hadron calorimeters. It measure the energy of neutral fragments produced by nuclear+nuclear hadronic reactions and also by Coulomb dissociation process.

A ZDC consists of three modules. Figure 3.14 shows the cross section of one ZDC module. Each ZDC module consists of Tungsten alloy plates and ribbons of commercial optical fibers in the sampling layer. The lights are collected into a PMT via optical fibers and readout. A LED is used for test pulse. The total absorption length of each ZDC is approximately $8 \lambda_{abs}$.

As shown in Figure 3.15, ZDC's are located at $z = \pm 18.25$ m from the center of intersection point. Each ZDC covers 2 mrad of forward angular cone which corresponds to $|\eta| > 6$. At $z \simeq \pm 11$ m from the center of intersection point, there are the dipole magnets to align two circulating beams to match at intersection point. The Au ions beam bended by one dipole magnet is bended again by another dipole magnet in the

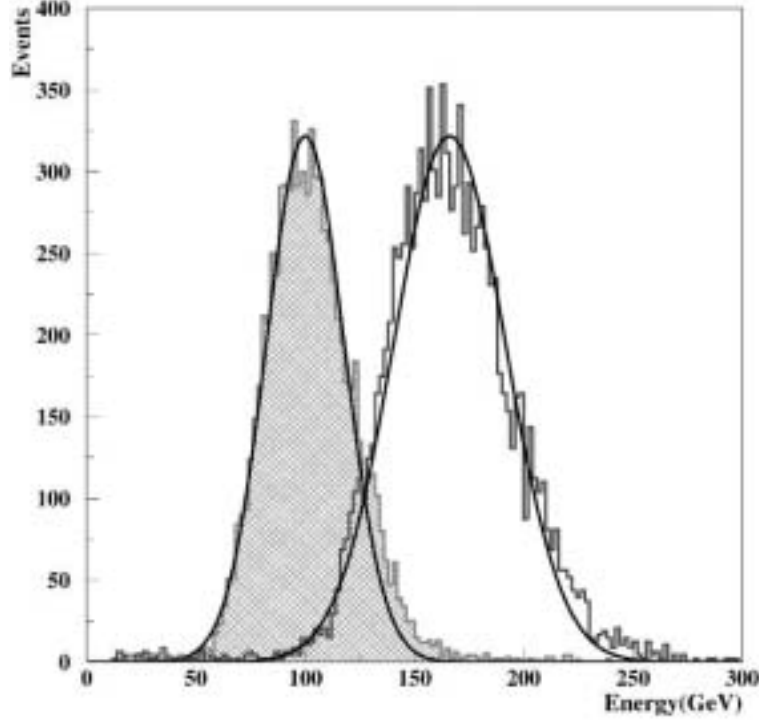


Figure 3.16: ZDC response line shapes for 100 and 160 GeV incident protons[58].

opposite side, and returned to the collider beam line. Fragment protons are swept out as is schematically shown in the bottom figure, and only fragment neutrons emitted in the very narrow angular cone directly hit the ZDC.

The ZDC performance was checked in the test beam experiment. Figure 3.16 shows the response to 100 and 160 GeV incident protons. The energy resolution of ZDC is approximately given by

$$\frac{\sigma_E}{E} \simeq \frac{218}{\sqrt{E}} \%, \quad (3.6)$$

where E is energy of incident hadrons in the unit of GeV.

The normal hadronic interaction cross section of Au+Au collision σ_{geo} is ~ 7.2 barn. It is obtained from geometrical model calculation and corresponds to the maximum impact parameter b_{max} of 15.1 fm. In collisions at $b < b_{max}$, the neutrons toward ZDC that are not bounded in deuterons or heavier fragments are detected by ZDC. For a given impact parameter the number of forward going neutrons is estimated by Monte Carlo calculations. The full discussion is presented in the next chapter.

In the heavy ion collisions, even if the impact parameter b is larger than b_{max} , the colliding Au ions are excited due to the strong Coulomb fields, and neutrons evaporate in case of high excitation. This Coulomb Dissociation (CD) process and mutual CD process

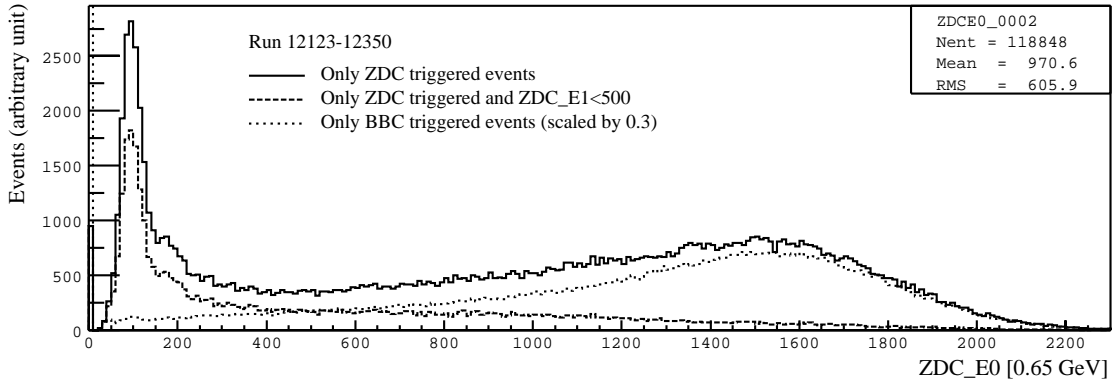


Figure 3.17: Energy distribution measured by a ZDC. A solid line is the North ZDC energy distribution of events triggered by only ZDC coincidence. South ZDC has basically the same shape as it. A gray line is the North ZDC energy distribution if South ZDC energy deposit is gated within 500 GeV. A dotted line shows the ZDC South energy distribution of events triggered by only BBC (scaled by 0.3).

where both Au ions emit neutrons, were studied at RHIC energy[58]. Since as explained in the next chapter, the coincidence of north and south ZDC are used for minimum bias trigger, the mutual CD fulfills the trigger conditions and have cross section σ_{CD} . The total cross section counted with ZDC's coincidence is expressed by

$$\sigma_{tot} = \sigma_{geo} + \sigma_{CD}. \quad (3.7)$$

Since the evaporated neutron has small transverse momentum, and has the longitudinal momentum close to the beam (65 GeV), the neutrons from the mutual CD process is observed as a clear peak at 65 GeV in ZDC energy distribution of both ZDC's, and the event can be clearly distinguished from other processes. Mutual CD process is useful for ZDC's calibration to monitor luminosity.

In addition, as a background process, the interaction between Au beam and remnant gas in the beam pipe (beam-gas interaction) is observed by ZDC's. It is discussed in the next chapter.

3.6.2 BBC's: Beam-Beam Counters

The main roles of Beam-Beam Counters (BBC's)[56] are to determine the collision centrality, to provide the time of the interactions, to measure the collision vertex point along the beam axis (z -axis) and to produce a trigger signal.

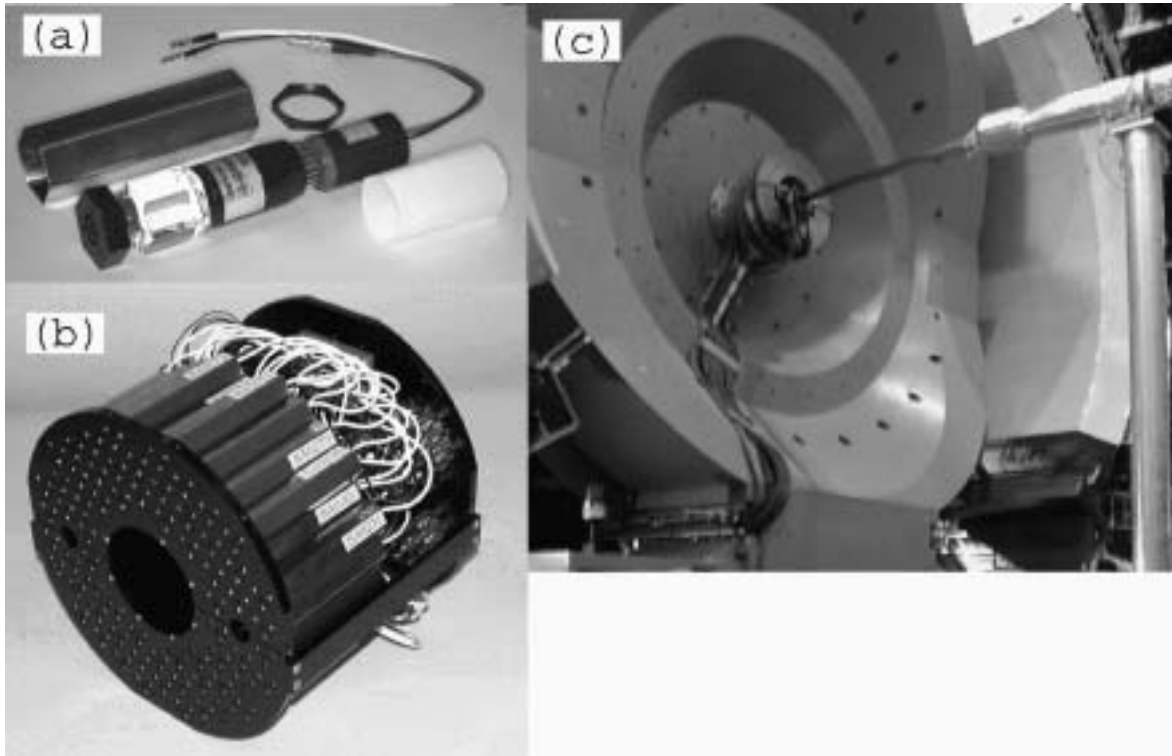


Figure 3.18: (a) A BBC element consist of one-inch mesh dynode photomultiplier tube with 3 cm quartz radiator. (b) 64 BBC elements built into a BBC array. (c) The BBC mounted on the PHENIX detector. The beam pipe is seen in the middle of the picture. The BBC is installed on the mounting structure just behind the central spectrometer magnet.

Since the longitudinal size of the beam bunch at RHIC for Au+Au collisions is designed to be 20 cm in RMS, the time spread of nuclear collisions could be as much as 0.7 ns. In the first year PHENIX run, actual RHIC bunch length is larger than design value and time spreading was larger than 3 ns in RMS. In any case, EMCal intrinsic timing resolution can not be achieved without precise start time measurement by BBC's,

The BBC's are composed of two identical arrays of Cherenkov counters installed on both north and south sides of the collision point along the beam axis and the arrays are named BBC-N and BBC-S, respectively. Each counter array is placed at $z = 144$ cm from the center of the interaction region and surrounding the beam pipe, just outside the poles of central magnet. The rapidity coverage and azimuthal angle coverage are $3.0 < |\eta| < 3.9$ and 2π , respectively.

According to the HIJING[29] model calculation, the number of charged particles within the BBC acceptance is ~ 400 . BBC was designed to work up to thousand charged particles. Furthermore the BBC also needs to operate for $p+p$ collisions. The BBC must

thus have a large dynamic range.

The magnetic field around the BBC is ~ 0.3 T. From beam-beam interactions, albedo particles from materials around detector and beam-associated background, the estimated photon and neutron flux at BBC is 10^{10} and 10^{11} [/cm²/year], respectively. BBC's are designed to ensure full functionality in such hard environment.

Each counter array consists of 64 one-inch diameter mesh-dynode photomultiplier tubes (Hamamatsu R6178) equipped with 3 cm quartz on the head of the PMT as a Cherenkov radiator. Pictures in Figure 3.18 shows (a) a BBC element, (b) a BBC array mounted on the BBC mechanical frame and (c) the BBC installed in the mounting fixture on the magnet. The outer diameter of the BBC is 30 cm and the inner diameter is 10 cm with clearance between the beam pipe and the BBC of 1 cm.

A laser light which is used for EMCAL calibration systems is also delivered to individual BBC elements to monitor and calibrate the timing drift. The BBC system has 8 high voltage channels for each side. A single high voltage supply operates 8 BBC elements. Operational high voltage is set to obtain 75 pC output charge for a minimum ionization particle from each BBC element.

The BBC readout electronics chain consists of discriminators, shaping amplifiers, time-to-voltage converters (TVC), flash ADC's (FADC) and buffer memories. The BBC provides the first level trigger with an input signal thus the timing and pulse height of BBC elements are digitized during each beam crossing by the TVC and FADC and stored at the same time in the buffer memory. Description of the front-end electronics used in the PHENIX detector is given in later sections.

After application of the time calibration to all BBC elements, the time deviation from the average hit time is mostly caused by the time resolution of the particular BBC element, since the average hit time is statistically determined. Figure 3.19(a) shows the distribution of the timing deviations from the BBC average time for a typical BBC element. The standard deviation of this distribution is defined as the time resolution of each BBC element. Figure 3.19(b) shows the distribution of the time resolution over all BBC elements. The time resolution of a single BBC element is 52 ± 4 ps under real experimental conditions.

In the experiment, the collision time is defined as the average arrival time of the BBC's. The time difference between the BBC arrays provides the vertex position along the beam axis. Detailed explanations are given in section 5.3. Combined information from the BBC's and ZDC's is used to define the collision centrality in the analysis.

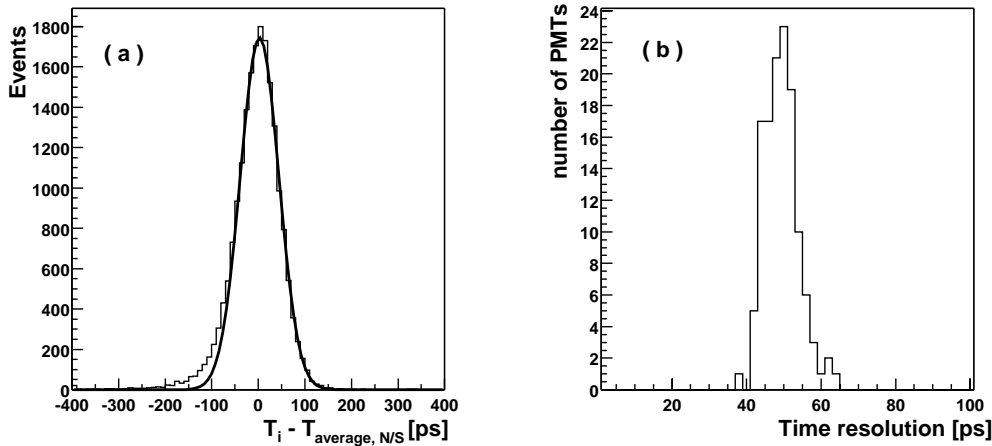


Figure 3.19: (a) Distribution of timing deviation for a typical BBC element from BBC averaged hit timing. (b) Profile of timing resolution for each BBC element.

3.7 Data Acquisition System

In the following, explanation of the PHENIX Data AcQuisition system (PHENIX DAQ) is presented.

Figure 3.20 shows the block diagram of PHENIX DAQ. From the DAQ side view, the detector subsystems are considered to be electronics devices that is called Front End Modules (FEM's) which are shown in the right top of Figure 3.20. The FEM's are located near detectors in the interaction region. Each FEM was developed separately so as to match to the detector characteristics but according to the common pre-defined interfaces for the control and the data transfer. Each FEM is controlled via two sort of control lines. One is a serial control line and the other is a timing fiber line. The ARCNET protocol was used for the serial control line[62]. The ARCNET is the simple industry standard serial network. The FEM setup data such as discriminator threshold and the configuration data of field programmable gate arrays (FPGA's) are downloaded by using the ARCNET before the data taking start. The control via the serial line is also called "slow control" because its speed is up to 1 Mbps. All the ARCNET control lines are managed by a PC located in the counting room.

The control via the timing fiber is the real time fast control which synchronizes to the RHIC bunch crossing at the speed of ~ 10 MHz. The G-LINK hardware level protocol and optical fiber were used for the timing data transfer. These are commercially used for recent high speed computer network. All the data transmission between the counting

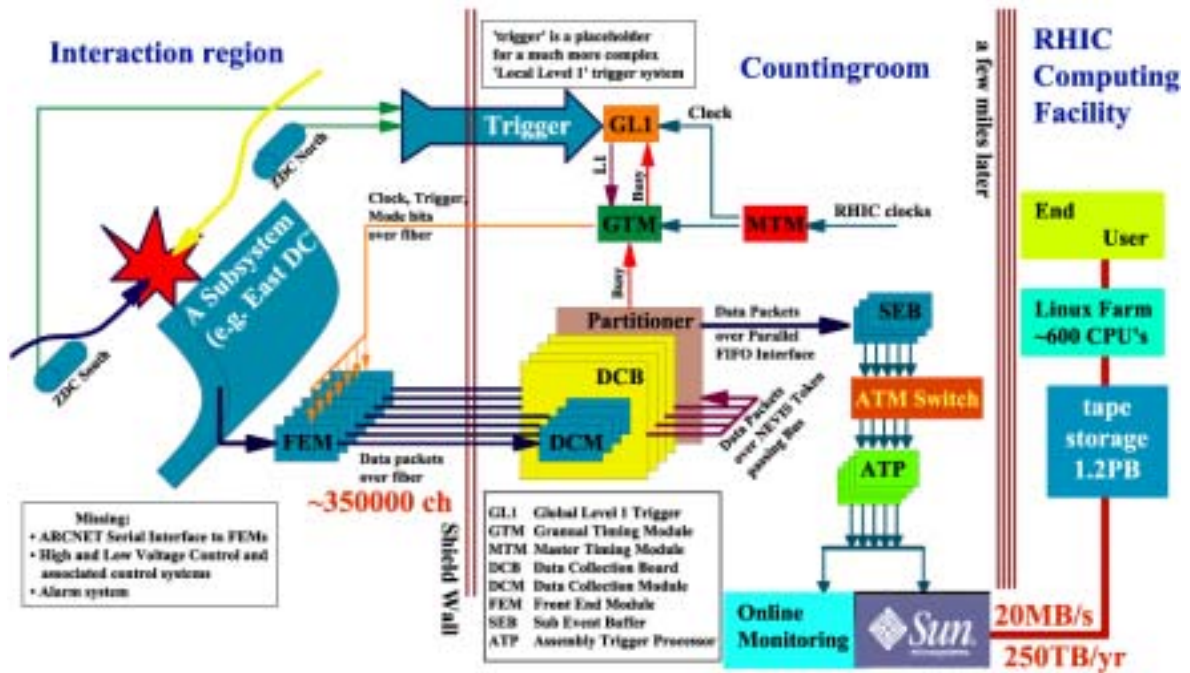


Figure 3.20: Schematic view of PHENIX DAQ system. The system is divided into three sections, (i) the front-end electronics modules near the detector placed inside the shield wall (left), (ii) global trigger, data collection, and event builder components in counting room, and (iii) storage system (right).

room and the interaction region uses the fiber optical cables, so that the two regions are electrically isolated.

The Master Timing Module (MTM) receives the clock from the RHIC, and controls the all electronics via a Granule Timing Module (GTM) installed in a VME crate located in the counting room. The timing and control signals are supplied to each FEM by GTM. The GTM collects trigger data, trims the fine timing (~ 50 ps step), and distributes timing data to FEM's,

FEM's of the trigger detector generates the trigger information and send it to a Local Level 1 trigger system. Local Level 1 signals are collected to the Global Level 1 system. The Global Level 1 system decides whether the event should be recorded or not and generates the final trigger bit. The trigger decision is performed within approximately 30 RHIC clocks. Each FEM keeps the data until the corresponding trigger information arrives. If the kept data is determined to be not recorded, the FEM discards it. There are two sorts of data keeping method; one is to use analog memory units (AMU's) [63] and the other is to use RAM's. The former type keeps the analog data as

charge in capacitors of AMU and the charge is converted to the digital data using analog to digital converter (ADC) when the corresponding event is triggered. The latter type convert analog data from detector using flash ADC's (FADC) or discriminators and keep the digital data in the RAM's. The AMU type FEM's were used for detectors which have many (more than a few thousands) channels, because it is unrealistic to have huge amount of FADC channels. For example the RICH and EMCal use AMU.

The triggered and digitized data at each FEM are sent to the Data Collection Module (DCM) via fiber optical cable. The G-LINK protocol is used here too. At this stage the data of an event exists in different DCM's because one DCM corresponds to one FEM. Event building is performed next.

The collected data by DCM's are processed by Sub-Event Buffer (SEB), ATM switches, and Assembly & Trigger Processor (ATP's). ATM is able to distribute and sort multi channel incoming data to multi channel outgoing data based on the tags attached on the data packets. The data have same tag is collected to one data stream. The SEB's attach the ATM tag on each packets. The packets which have the same tag numbers are collected to one of the ATP's. At this stage, an event is build to one complete data packet which includes all FEM's data. And the data is sent to the RCF (RHIC Computing Facility) via network and recorded in the HPSS system which is a large (a few hundred Tera bytes) tape robot system.

3.7.1 Front-end Modules

Since the front-end readout electronics for EMCal (EMCal FEM) is quite similar to the electronics for RICH (RICH FEM), and an author of the thesis developed the RICH FEM, some of the following descriptions are given for the RICH FEM[64, 65, 66].

The RICH FEM has been developed at CNS with the collaboration of University of Tokyo, Oak Ridge National Laboratory (ORNL), Waseda University, and Nagasaki Institute of Applied Science (NIAS).

Since the number of channels of RICH is 5,120 (it is 24,788 for EMCal), the special electronics system was developed. Sixteen channels pre-amplifiers is attached on the RICH vessel, and coaxial flat cables are fed into eight RICH FEM crates placed at the side of the central arm. Each crate is 9U-VME size crate and capable to read 640 PMT signals. RICH FEM receives timing/control information from MTS via GTM.

The pre-amplified signal of PMT is integrated in the Integrator chip specially made for RICH[67, 68, 69]. This chip has variable gain amplifier (VGA), charge integrator, discriminator, and time-to-analog converter (TAC). The amount of charge is converted to the voltage signal, and time difference relative to the beam collision timing is also converted to the voltage signal in the Integrator chip.

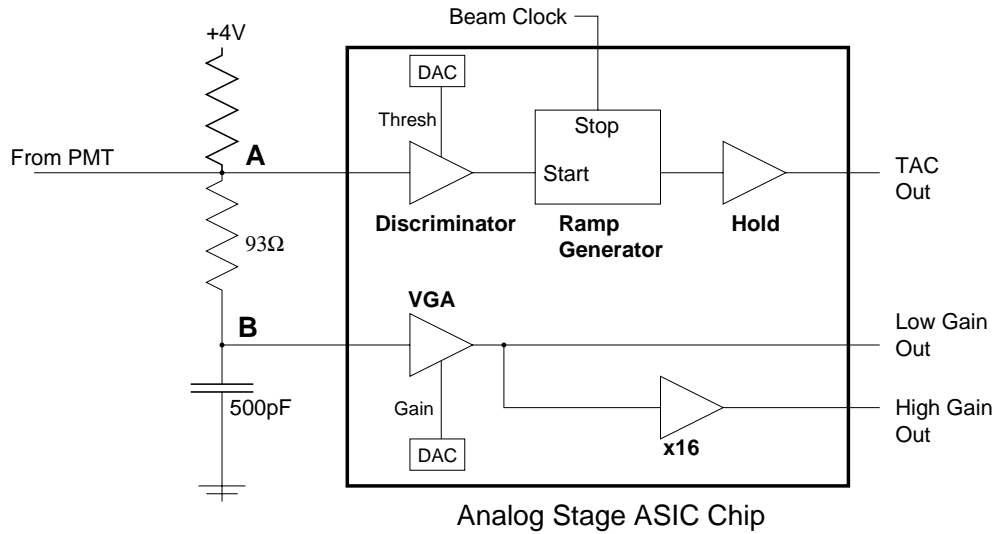


Figure 3.21: The block diagram of Integrator Chip of EMCAL (in a rectangle). The PMT signal is fed into a discriminator and a VGA. The discriminator starts the ramp generator and the timing is converted to analog signal. Amplified signal by the VGA is divided to two output signal. One is the direct output (low gain output), and the other is high gain output which is amplified signal by another amplifier with $\times 16$ gain. Both discriminator threshold and VGA gain are programmable by DAC's.

The different points of EMCAL FEM from the RICH FEM are mainly in the Integrator chip. The block diagram of the integrator chip used in EMCAL FEM is shown in Figure 3.21. The pulse from the PMT is fed into discriminator and VGA. Since the required dynamic range of the EMCAL is higher than RICH, each Integrator channel has two charge output, low gain output and high gain output. In Figure 3.21, amplified signal by VGA is divided to direct output for low gain and further amplifier with $\times 16$ gain for high gain. RICH Integrator has only direct output. The number of analog memory per channel for EMCAL FEM and following electronics resources for charge information are twice of RICH FEM.

Both charge and timing data are sent to the AMU/ADC chip which has AMU and Wilkinson type ADC. The AMU keeps the data of up to 64 beam crossing without considering whether physics event occurred or not at each beam crossing. Figure 3.22 shows the block diagram of the AMU/ADC chip. If the trigger signal is generated by Global Level 1 system outside FEM within ~ 30 beam crossing, the corresponding analog data in AMU are digitized by the ADC.

Timing diagram of RICH FEM is shown in Figure 3.23. The FEM is synchronized

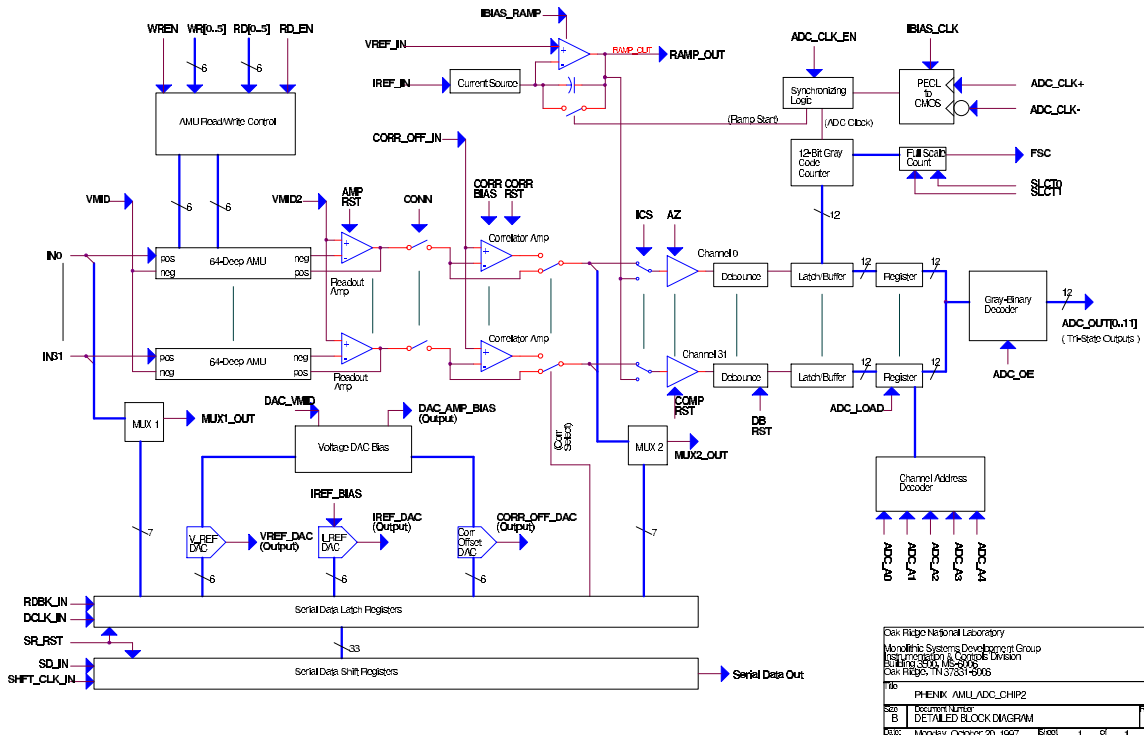


Figure 3.22: Detailed block diagram of the AMU/ADC ASIC. A chip has 32 channels AMU's. One AMU has 64 capacitor cells to keep data. The cell address to be written and read can be specified randomly. The analog data in read cell is converted to digital data by the Wilkinson type ADC. The ADC clock is commonly used for 32 channels.

to the RHIC clock. PMT output is continuously integrated. If the PMT fires, the discriminator fires and TAC starts. TAC is stopped by the next TAC clock which has the constant delay from RHIC clock. The integrator output and TAC output are copied to the AMU as charge data and timing data, respectively. Especially for charge data, two memory cells corresponding to pre-event and post-event are digitized because integrator is continuously integrating the charge from PMT. Those are subtracted in later stage of off-line analysis.

Other data in analog memory not triggered are discarded and the memory is continuously used for further beam crossings. During the AD conversion, the readout analog memory cell is occupied for a long time (few μ second), and can not be used for the coming beam crossing. Therefore the AMU is not a simple shift register. A complex

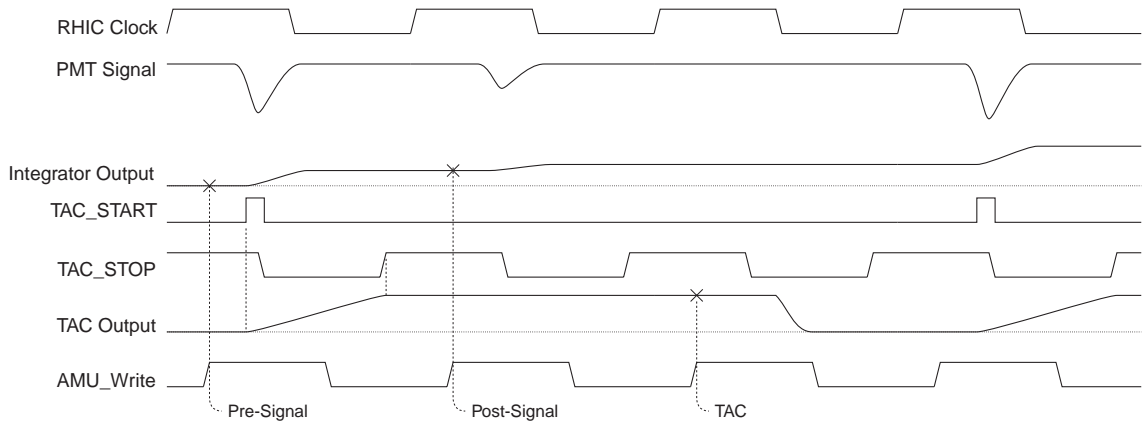


Figure 3.23: Timing diagram of RICH-FEM.

memory management system is required, and it was implemented in FPGA's[70].

Chapter 4

Run Conditions

4.1 Overview

This analysis is based on the experimental data taken in the first year RHIC run (Year-2000 run). The run began in May, 2000 and ended in September 5, 2000. Since it was the first run, the earlier half of the run period was dedicated for machine commissioning and studies. In the middle of June, the RHIC finally succeeded accelerating Au beams in both blue and yellow rings, and collisions were confirmed.

In the following sections, summary of experimental conditions and data statistics at the Year-2000 run are presented.

4.2 Beam Conditions

The RHIC provided Au+Au collisions at the Lorentz factor γ of 30 and 70 which correspond to 56 GeV and 130 GeV of center of momentum energy per nucleon pair ($\sqrt{s_{NN}}$), respectively. The data of $\sqrt{s_{NN}}=56$ GeV collisions was taken at only the early part of the Year-2000 run. The amount of data was a few ten thousand events. The data of $\sqrt{s_{NN}}=130$ GeV collisions was taken in ~ 1 month. A few millions of events at $\sqrt{s_{NN}}=130$ GeV were recorded. In this thesis, the data of $\sqrt{s_{NN}}=130$ GeV was used.

Figure 4.1 shows the transition record of the beam intensity and magnet current as a function of time at the beginning of a run¹ when the RHIC succeeded to ramp up the beam to $\sqrt{s_{NN}}=130$ GeV first on July 20, 2000. After the ramp started, the RHIC reached to $\sqrt{s_{NN}}=130$ in ~ 2 minutes, then collisions started.

Table 4.1 shows the summary of RHIC beam conditions in Year-2000 run. Beam luminosity was $\sim 10^{25}$ [cm⁻²s⁻¹]. With the maximum minimum bias event rate of ~ 100 [events/s], the luminosity is estimated to be $100/\sigma_{Au+Au} \sim 10^{25}$ [cm⁻²s⁻¹], where $\sigma_{Au+Au} \sim 7.2$ [barn] is the total hadronic interaction cross section of Au+Au collision.

¹Different from “Year-2000 run”, a word “run” represents a data taking period with a few ten minutes to several hours long.



Figure 4.1: First successful ramp of both RHIC beams to 65 GeV/u. The beam current of two rings are shown by lines (a) and (b), and a line (c) shows the magnet current. The ramp began at the time represented by a vertical line, and the magnet current reached maximum value in ~ 2 minutes. Both rings lost their beam current mainly at the beginning of the ramp. After the ramp, the beam intensity was kept long time typically several hours.

It is in the order of 1/10 of RHIC design luminosity (2×10^{26} [cm⁻²s⁻¹]), and this value is the goal of the Year-2000 run.

Once both yellow and blue rings succeeded to accelerate Au beams and start collisions, the state was kept for several hours. Beam intensity and event rate go down gradually, and after several hours, the beam was dumped and cycles of injections and accelerations were repeated.

Collision Ions	$^{197}_{97}\text{Au} + ^{197}_{97}\text{Au}$
Nominal γ (Lorentz factor)	70
Nominal \sqrt{s} per nucleon pair	130 GeV
Maximum beam current	$\sim 10^8$ Au ions / bunch
Maximum bunch count	55 bunches
Beam luminosity	$\sim 10^{25}$ ($\sim 1/10$ of design luminosity)

Table 4.1: RHIC Beam Conditions in Year-2000 run.

4.3 Detector Conditions

4.3.1 EMCal

In the Year-2000 run, two sectors of PbSc type Calorimeter (one sixth of all PbSc sectors) and one sector of PbGl type Calorimeter (one half of all PbGl sectors) were operational. Those are presented as shaded parts in Figure 3.3. Because only PbSc type calorimeter was used in the analysis for the thesis, only the status of the PbSc type calorimeter is described below.

In the two operated PbSc sectors, there were approximately 10 % of dead channels due to bad electronics modules or malfunctioning PMT's. Other part of PbSc sectors were functioning stably.

4.3.2 ZDC

Both north and south ZDC were fully operational. Due to the device characteristics study, the high voltage setting of the ZDC was not constant during the run. In the calibration stage, the differences of gain among those settings are normalized.

4.3.3 BBC

Both north and south BBC were operational in the Year-2000 run. Due to the electronics problem, the dynamic range of all pre-amplifiers for each BBC element were reduced to 1/10 of the expected value. For the events with many particles, the BBC total charge output saturated.

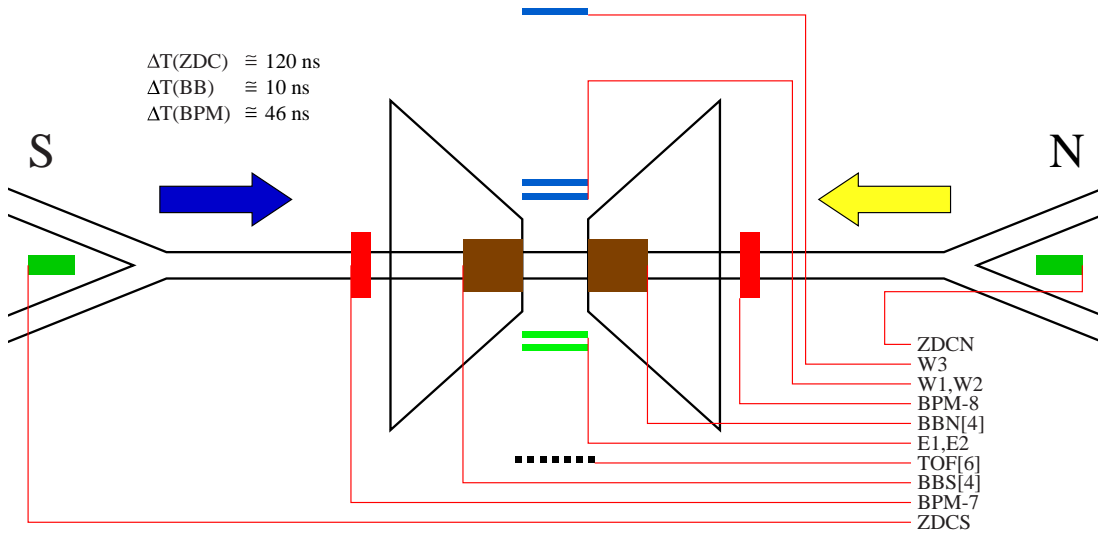


Figure 4.2: Schematic view of PHENIX trigger devices.

4.4 Trigger Settings

4.4.1 Raw Level Trigger

In the Year-2000 run, there were five sorts of trigger devices. Those are (1) North BBC (BBN[4]) and South BBC (BBS[4]), (2) North ZDC (ZDCN) and South ZDC (ZDCS), (3) Scintillators W1, W2, E1, and E2, (4) TOF, and (5) Beam profile monitor BPM-7 and BPM-8. Figure 4.2 shows schematic view of PHENIX trigger devices. Some of these trigger devices were used only for tests. Only BBN[4], BBS[4], ZDCN, and ZDCS were used for physics triggers. From these trigger devices, trigger logics were generated. The defined trigger logics are summarized in Table 4.2. Figure 4.3 shows the schematics of the circuits of physics triggers.

4.4.2 BBC Local Level 1 Trigger

With BBC-N and BBC-S timing information, the position of the event vertex along the beam line was roughly calculated, and BBC Local Level 1 trigger (BBC-LL1 trigger) was generated when the position of event vertex is within $\pm 20 \text{ cm}$ or $\pm 40 \text{ cm}$. The BBC-LL1 was not included in the early stage of Year-2000 run because it was under developed. After development of BBC-LL1 was completed, it was introduced instead of BBC-N \otimes S trigger bit.

Name	Definition
BBC-N	More than 2 hits of the four PMT's, 5 ns gate.
BBC-S	Same as above.
BBC-N \otimes S	Coincidence of all BBC-N, BBC-S trigger in 5 ns gate.
BBC-LL1	BBC Local Level 1 (see text).
ZDC-N	Linear sum of the 3 PMT's. Threshold is approximately 10 GeV.
ZDC-S	Same as above.
ZDC-N \otimes S	Coincidence of ZDC-N and ZDC-S.
W1 \otimes W2	100 ns coincidence of W1 and W2.
W1 \otimes W2 \otimes W3	100 ns coincidence of W1, W2, and W3.
E1 \otimes E2	100 ns coincidence of E1 and W2.
E1 \otimes E2 \otimes TOF	100 ns coincidence of E1, E2, and OR of 6 scintillator slats of TOF.
BPM-7	Delayed coincidence of BPM-7 signal with itself, provide a trigger when a Yellow and Blue ring bunches passed by the PHENIX.
BPM-8	Same as BPM-7 except that it is using BPM-8.
EMC-MUON	Internal EMCAL muon trigger aligned to BBC-LL1

Table 4.2: Trigger logic definitions. It includes triggers used only for test purposes. Only the BBC-N, BBC-S, BBC-N \otimes S, ZDC-N, ZDC-S, ZDC-N \otimes S and BBC-LL1 were used in the real data taking.

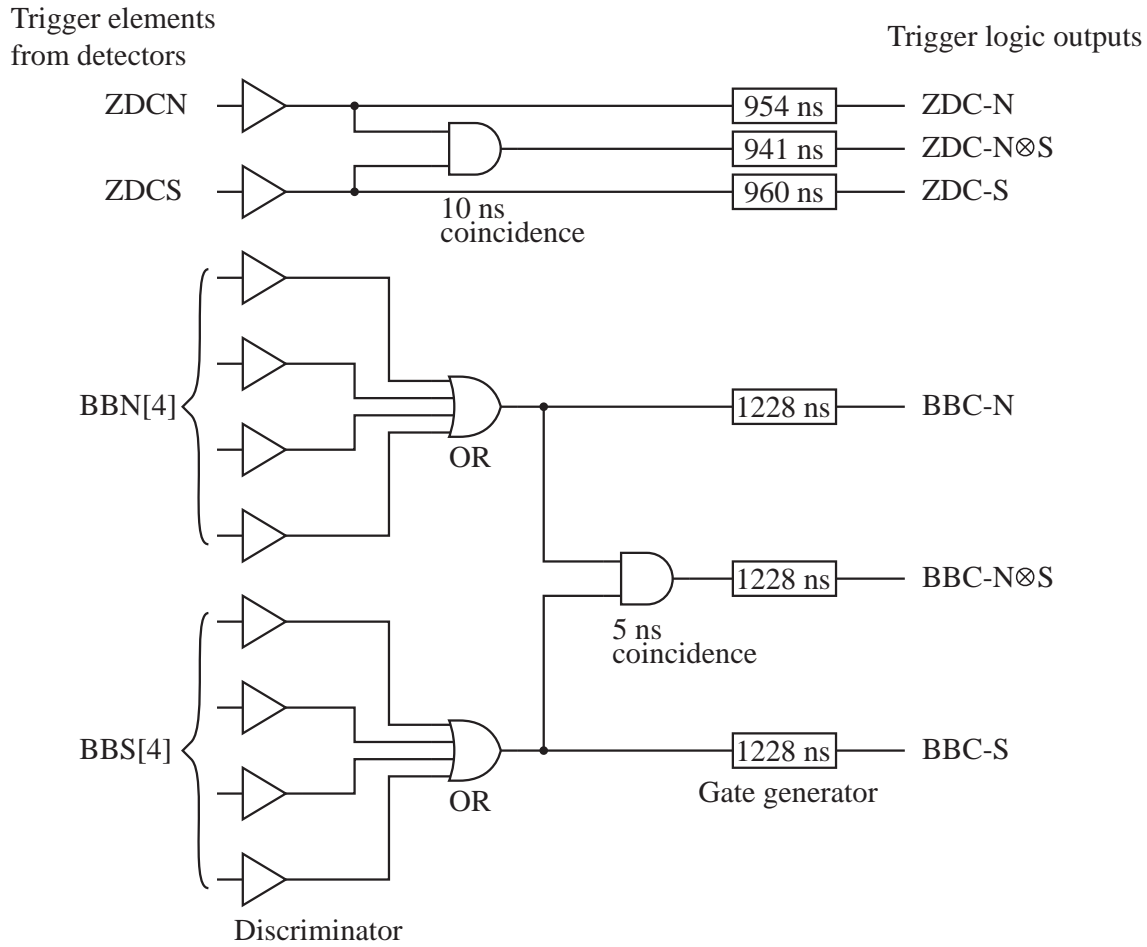


Figure 4.3: Schematics of PHENIX physics trigger logic used in Year-2000 run. Trigger elements from detectors were used to generate trigger logic outputs. The names of trigger elements corresponds to trigger devices shown in Figure 4.2. BBC-LL1 is not shown here.

4.5 Statistics

Figure 4.4 shows the integrated trigger rate during the run period from July 1 to September 5, 2000. The raw number of triggers counted by ZDC coincidence (ZDC-N \otimes S) was approximately 45 M events. And the number of ZDC triggered events acquired on the tape is approximately 1.9 M events. The raw number of triggers counted by BBC-LL1 or BBC-N \otimes S was approximately 6.1 M events, but the total number of acquired events on the tape was approximately 3.3 M events.

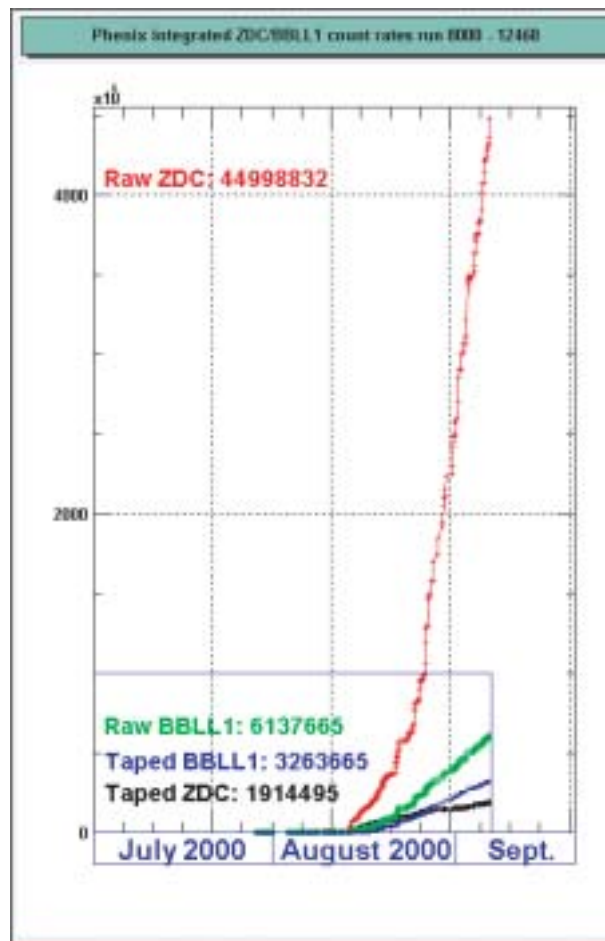


Figure 4.4: The integrated number of triggers in Year-2000 run.

Chapter 5

Data Analysis

5.1 Overview

In this chapter, the data analysis method and procedures used to obtain π^0 invariant yield are explained.

The analysis procedure is divided broadly into four steps. The first step is to select good events which fulfill the event selection criteria. The next step is to characterize the event according to the centralities determined from the BBC's and ZDC's information. Events are pigeonholed in order of centrality from head-on (central) collisions to non-central (peripheral) collisions. The third step is reconstruction of γ 's using EMCal. Energy and momentum vector of each γ are determined. The fourth step is to reconstruct π^0 from γ tracks by calculating invariant mass of daughter two γ 's. Efficiency, acceptance, and systematic errors are discussed when appropriate.

5.2 Invariant Yield

Before entering the analysis steps, the explanations about invariant yield is provided. The aim of this analysis is to obtain π^0 yield in each Au+Au collision in Lorentz invariant form i.e. "per event yield" because it is comparable to the theoretical calculations. The invariant (differential) yield is expressed by the form:

$$E \frac{d^3n}{dp^3} = \frac{d^3n}{p_T dy dp_T d\phi} \simeq \frac{d^2n}{2\pi p_T dy dp_T}, \quad (5.1)$$

where p is the momentum of the particle, y is the rapidity, $p_T = \sqrt{p_x^2 + p_y^2}$ is the transverse momentum, and ϕ is the angle to the x -axis. The $d^3n/p_T dy dp_T d\phi$ is averaged over full azimuth ($\phi = 0 \sim 2\pi$) in the last form of Eq. (5.1). The invariant yield Eq. (5.1) can be expressed using pseudorapidity η by

$$\frac{d^2n}{2\pi p_T dy dp_T} = \frac{\sqrt{p^2 + m^2}}{p} \frac{d^2n}{2\pi p_T d\eta dp_T} \simeq \frac{d^2n}{2\pi p_T d\eta dp_T}, \quad (5.2)$$

where m is the invariant mass of the particle. It was assumed that $p \gg m$ while deriving the last form. In the case of π^0 with momentum of $0.5 \text{ GeV}/c$, $\sqrt{p^2 + m^2}/p \sim 1.036$ and distinguish from 1 is negligible if the errors attached to experimental result is large enough. Furthermore η is more convenient than y because η is defined as $\eta = -\ln \tan(\theta/2)$ and θ is directly measured in the experiment. In the following discussions, therefore, η is usually used instead of y .

Eq. (5.2) can be rewritten using experimentally observed quantities by

$$\frac{d^3n}{2\pi p_T dy dp_T} = \frac{1}{2\pi p_T} \cdot \frac{1}{N_{ev}} \cdot \frac{1}{\epsilon(\eta, p_T)} \cdot \frac{N_{\pi}^{raw}(\eta, p_T)}{\Delta\eta \Delta p_T} [\text{GeV}^{-2}c^3], \quad (5.3)$$

where N_{ev} is the number of sampled events, $N_{\pi}^{raw}(\eta, p_T)$ is the number of π^0 's produced in a given phase space by η and p_T . Experimentally selected sizes of bins $\Delta\eta$ and Δp_T are used instead of $d\eta$ and dp_T . The quantity $\epsilon(\eta, p_T)$ is the detection efficiency depends on η and p_T . In the analysis, $\Delta p_T = 0.5 \text{ GeV}/c$ is taken. Due to limited statistics, η was not divided into bins. This does not cause problem because the η distribution of particles is expected to be almost flat in detector coverage ($-0.35 < \eta < 0.35$). The average in this η coverage is obtained.

Since π^0 is reconstructed from two photons, The π^0 detection efficiency depends on the geometrical acceptance and detection efficiency of photon, and expressed by

$$\epsilon(\eta, p_T) = \epsilon_{br}\epsilon_{pair}(\eta, p_T) \iint P(p_1, p_2) \cdot \epsilon_{\gamma}(p_1)\epsilon_{\gamma}(p_2) dp_1 dp_2, \quad (5.4)$$

where ϵ_{br} is the branching ratio of $\pi^0 \rightarrow 2\gamma$ which is $\sim 98.8\%$, $P(p_1, p_2)$ is the probability density that a π^0 decays to two γ with their four-momentum of p_1 and p_2 , $\epsilon_{\gamma}(p)$ is the detection efficiency of γ with four-momentum p , and $\epsilon_{pair}(\eta, p_T)$ is the efficiency of analysis cuts for γ pair.

The photon efficiency is expressed by products of finer elements:

1. detector geometrical acceptance,
2. γ identification (PID) efficiency,
3. detector fiducial volume (insensitivity in edge and dead towers), and
4. loss by $\gamma \rightarrow e^+e^-$ conversion.

To calculate Eq. (5.4), the Monte Carlo simulation is used. The full description about efficiency and acceptance calculations are provided in later sections.

After a completion of all analysis in this chapter, the set of $\epsilon(\eta, p_T)$ and N_{π}^{raw} for several bins of p_T are given. Then the shape of invariant yield is obtained in the form of Eq. (5.3). Those data are provided for several event classes from the central collisions to peripheral collisions.

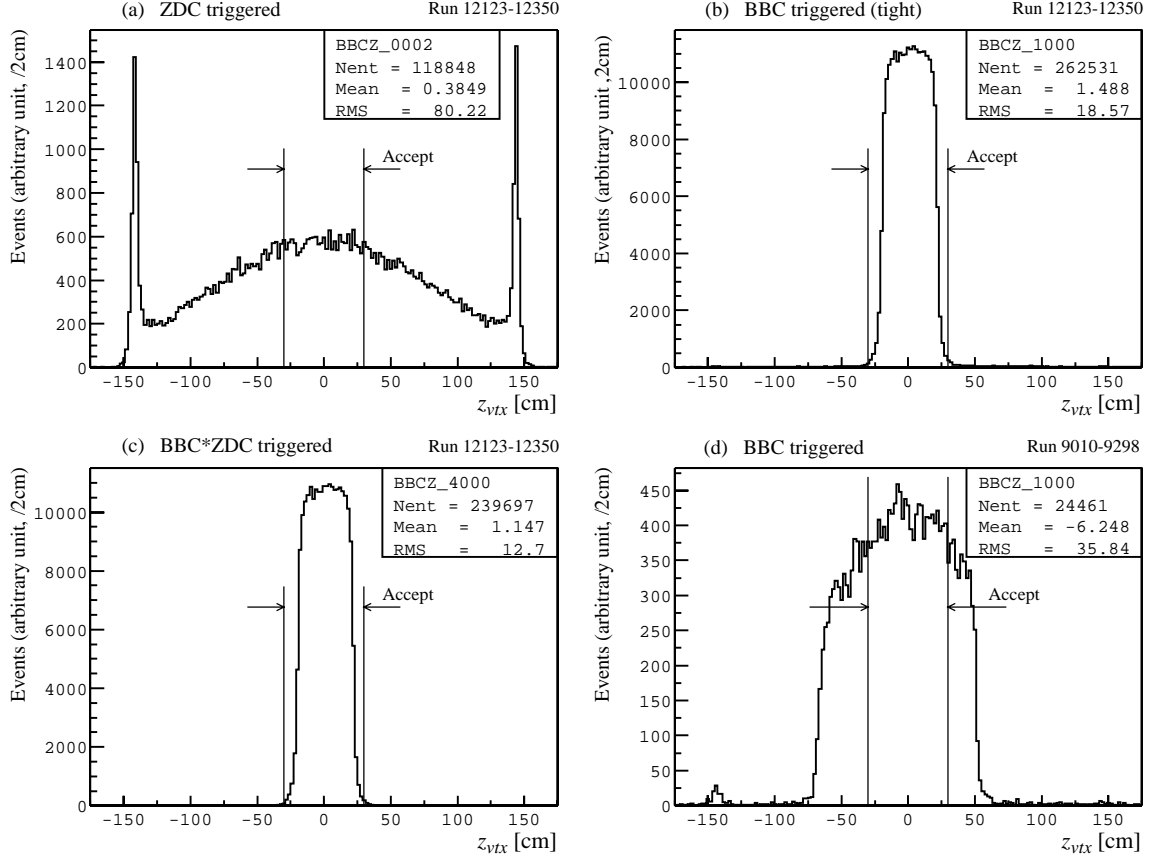


Figure 5.1: Vertex position z_{vtx} distribution measured by BBC's for events triggered by (a) ZDC-N \otimes S triggers, (b) BBC-LL1 triggers, (c) ZDC-N \otimes S and BBC-LL1 triggers coincidence, and (d) BBC-N \otimes S triggers.

5.3 Vertex and Collision Time Determination

5.3.1 Measurement of the Event Vertex Position

Since the Au beam has negligibly small (less than 1 mm) radius, event vertex position move along only z -axis, and expressed by $\mathbf{V} = (0, 0, z_{vtx})$. z_{vtx} is calculated from the time difference between the south and north BBC hits:

$$z_{vtx} = \frac{c}{2}(t_S - t_N), \quad (5.5)$$

where c is the speed of light, and t_S and t_N are the mean hit time of the south and north BBC arrays, respectively. Since the BBC timing resolution is ~ 50 ps, the resolution of vertex position is ~ 1 cm.

Figure 5.1(a) shows the measured z_{vtx} distribution of ZDC-N \otimes S triggered events. Since beam bunches have finite length and the collisions occur at any point in the region

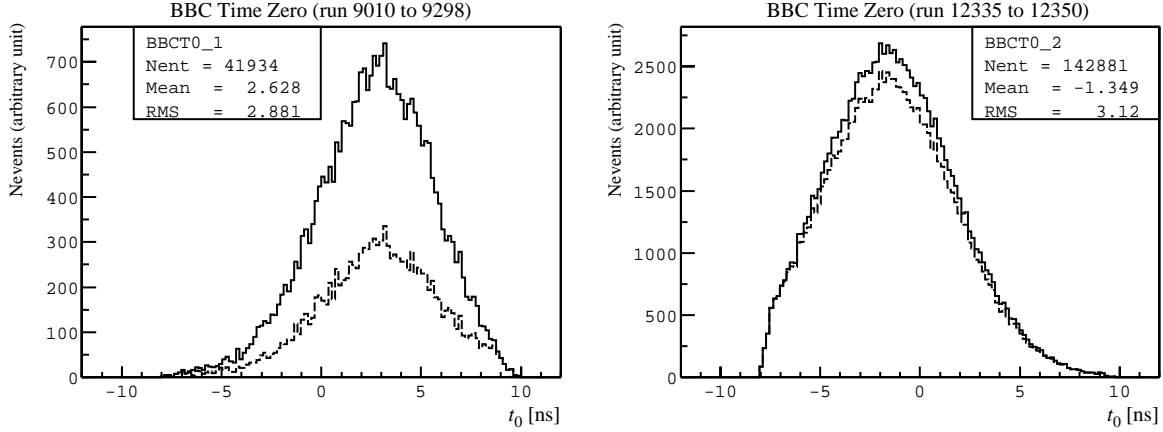


Figure 5.2: BBC t_0 distribution. Figures are placed in the same order as Figure 5.1. Solid lines are BBC t_0 distribution with only BBC and ZDC trigger selections. Dashed lines are the t_0 distribution after vertex selection.

where two bunches overlap, the z_{vtx} distribution is characterized by the bunch structure. From Figure 5.1(a), it is seen that the Au beams has bunch length of ~ 100 cm in FWHM which is significantly longer than the design value.

In order to check the absolute calibration, two sharp peaks seen in Figure 5.1(a) are used. The peaks correspond to the events occurred outside the BBC's and mainly from beam-gas interactions, and the positions should be ± 144 cm.

Other plots in Figure 5.1 show the z_{vtx} distribution for events triggered by (b) BBC-LL1, (c) ZDC-N \otimes S and BBC-LL1, and (d) BBC-N \otimes S triggers, respectively. By BBC-LL1 trigger, as seen in (b) and (c), the events occurred at outside of $|z| < \sim 30$ region are rejected.

5.3.2 Measurement of the Collision Time

The collision time t_0 is calculated from the mean time of south and north BBC hits:

$$t_0 = \frac{t_S + t_N}{2} - \frac{z_{bbc}}{c} + t_{off}, \quad (5.6)$$

where t_{off} is the time offset intrinsically included by devices and z_{bbc} is the $|z|$ of position of BBC's (144 cm). Figure 5.2 shows the distribution of t_0 from the two different run periods. The distribution of the t_0 apparently different between the two. This is because the offset t_{off} changes run-by-run. The origin of t_{off} is in the phase lock system of PHENIX master timing system. The beam crossing timing is provided as the clock which is a copy of signal of RF driver of RHIC. And PHENIX master timing system lock the phase to the RHIC clock at the beginning of run. Once the phase is locked to the

Analyzed Events	full field	4,384 K
	half field	73 K
	no field	917 K
	total	5,374 K
After trigger, vertex, and timing cut	full field	2,213 K
	half field	54 K
	no field	572 K
	total	2,839 K

Table 5.1: Statistics of the analyzed events. After trigger selection and event selection by z_{vtx} and t_0 , 2.2 millions full field data are remained.

RHIC clock, the relative time between RHIC clock and PHENIX clock is fixed during the run. But there is an ambiguity while finding phase position at the beginning of run and it causes finite t_{off} . This intrinsic offset due to phase lock system is common affect to the all PHENIX subsystem. By subtracting t_0 from any timing measurement in the PHENIX, t_{off} is removed.

Since t_N and t_S have each resolution of ~ 50 ps, the combined resolution of t_0 is ~ 35 ps. The distribution seen in Figure 5.2 spreading wider than 35 ps. This shape represent finite size bunch structure and is due to because the collision could occur at any time while two bunches are overlapping.

5.3.3 Event Selection

The trigger information, z_{vtx} , and t_0 were used for event selection.

The used trigger selection criteria is

$$[\text{Scaled down ZDC-N}\otimes\text{S}] \cup ([\text{ZDC-N}\otimes\text{S}] \cap [\text{BBC}]), \quad (5.7)$$

where BBC is one of the BBC-LL1 and BBC-N \otimes S triggers, depends on run. ZDC-N \otimes S is scaled down at the data taking and the scale-down factor is also depends on run.

Also trigger efficiency for the inelastic Au+Au collisions was found to be $\sim 92 \pm 2$ %. It is due to the number of charged particles per participant in one BBC is ~ 0.5 . In the last 8 % of peripheral events, trigger requirement of at least two particles in BBC's is not fulfilled.

The used vertex and timing criteria are

$$-30.0 \text{ cm} < z_{vtx} < 30.0 \text{ cm}, \quad (5.8)$$

$$\text{and } -8.0 \text{ ns} < t_0 < 10.0 \text{ ns}. \quad (5.9)$$

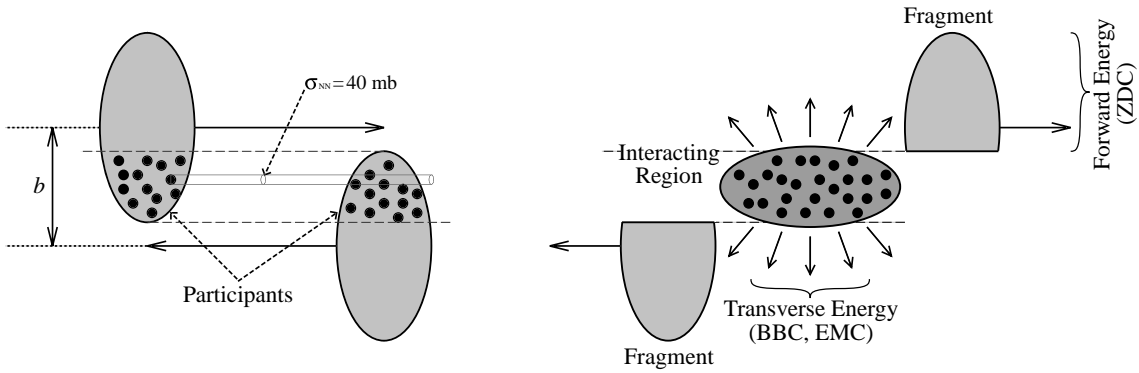


Figure 5.3: A schematic figure showing the participant-spectator model. The left figure shows colliding Au nuclei approaching with an impact parameter before the collision. The right figure shows states of the remnants of two nuclei after the collision. Nucleons which have interacted with other nucleons are called “participants” or wounded nucleons. Nucleons which have not interacted go straight with initial momenta. They are called “spectators”. The spectators are not stable nuclei but highly excited nuclei. The evaporated nucleons from spectators are measured by ZDC.

The $\pm 30 \text{ cm}$ of z_{vtx} limit was set because a significant fraction of emitted particles will hit material of the magnet pole pieces if the event vertex position is outside the region of $|z| < 40 \text{ cm}$. A 10 cm margin was taken. The t_0 window is defined as electronics is functional in this region.

The event statistics is summarized in Table 5.1. The number of analyzed events was 5.4 millions including three magnets settings. After event selection, total of 2.8 millions events survived. Approximately 2.2 millions events of full field data are used in the analysis below. The half field and no field data are not used.

5.4 Event Classification

In this section, a participant-spectator model and a Glauber model are described. The models are used to divide the events into event classes. Number of participants and number of collisions which characterize each event class, are calculated using the Glauber model.

5.4.1 Participant-Spectator Model

The global feature of the heavy ion collisions is described with the “participant-spectator model”. As is schematically shown in Figure 5.3, characteristics of the collision is determined by the impact parameter b . Nucleons in the overlap region are participants of the collision, and the others are spectators. If $b = 0$, all nucleons in the nuclei are the participants. The larger b is, the smaller nucleons participates. Collisions with small b are called “central collisions” and collisions with large b are called “peripheral collisions”.

After collision, the system is divided into mainly three sub systems. One is the system generated by participated nucleons. This may develop to high energy density medium such as QGP and it is the interesting system. The transverse energy observed as a particle is related to the deposited energy in the medium, as described in Section 2.2. The other two systems is spectator fragments. They are the lower excited systems, break into smaller nuclei by evaporating the nucleons and γ 's.

In the most central collisions ($b \approx 0$), almost all the nucleons in both nucleus participate the interactions. No fragments are detected at forward region and the highest transverse energy will be observed. In the peripheral collisions, relatively large number of neutrons are detected by ZDC's and small transverse energy is detected.

The participant-spectator model provides a basic view of nucleus-nucleus collisions. Based on the participant-spectator model, the Glauber model is used for quantitative calculations.

5.4.2 Glauber Model

The Glauber model[28] is a geometrical model of hadronic collisions which can be considered to be a microscopic participant-spectator model.

The nucleons in each colliding nucleus are randomly distributed according to a Woods-Saxon distribution:

$$\rho(r) = \rho_0 \cdot \frac{1}{1 + \exp\left(\frac{r-R}{a}\right)}, \quad (5.10)$$

where R is a radius of the Au nucleus. It is approximately represented by $R = (1.19A^{1/3} - 1.61A^{-1/3})$ fm. For the gold, $R \simeq 6.65$ fm, and $a \simeq 0.54$ fm. A collision of the nucleons are described by a constant $N+N$ cross section σ_{NN} , which is taken as the nucleon radius in the nuclei. In the calculation, the nucleons inelastic cross section of $\sigma_{NN} = 40$ mb is used. The nucleons pass through the other nucleus on straight trajectories. All nucleons in the opposite nucleus which have impact parameters less than two times of the nucleon radius interact without considering how many interactions a nucleon had before. Au+Au inelastic cross section is ~ 7.2 barn in this calculation.

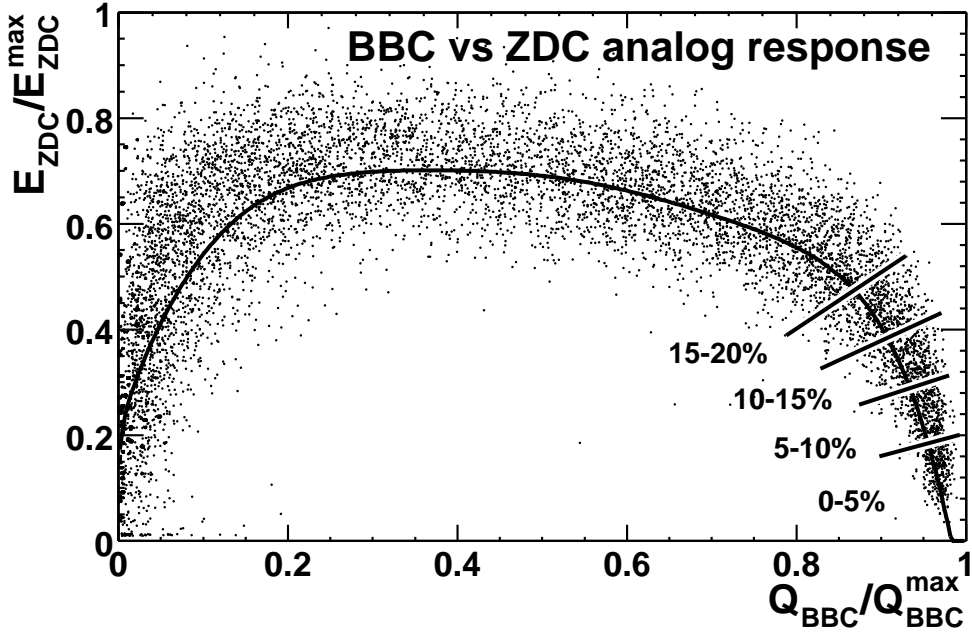


Figure 5.4: ZDC energy as a function of BBC charge. A horizontal axis is BBC total charge Q_{BBC} divided by maximum of it. A vertical axis is ZDC total energy E_{ZDC} divided by maximum of it.

Monte Carlo calculation is performed according to above assumptions and the number of nucleon+nucleon collisions (N_{coll}) is estimated. If a nucleon has at least one collision, it is counted as “participated nucleon”. The number of participated nucleons (N_{part}) is basically same as one explained in participant-spectator model. In general $N_{part} < N_{coll}$.

5.4.3 BBC and ZDC Responses

Figure 5.4 shows the observed response of ZDC and BBC for the events selected after Section 5.3. The total charge Q_{BBC} in BBC’s has the maximum value in the central collision. In the peripheral collision, since no transverse energy is generated, Q_{BBC} is small. If the neutrons in the fragments are all free, Q_{BBC} and E_{ZDC} should have inverse correlation and E_{ZDC} should be maximum at $Q_{BBC} = 0$. E_{ZDC} distribution has plateau at $Q_{BBC} = 0.2 \sim 0.5$ and becomes small at peripheral collision. This behavior was already seen in Pb+Pb collision at NA49 experiment in CERN[71]. In the peripheral collision, the total energy of fragments is large but the fraction of free neutrons is small due to coalescence.

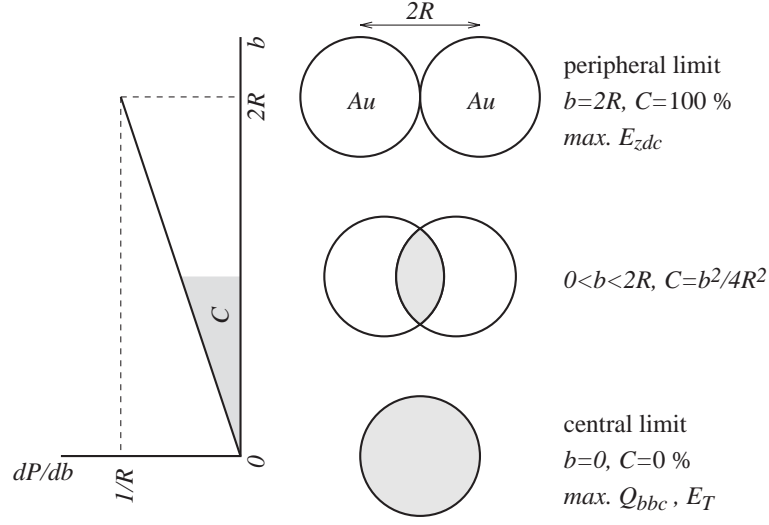


Figure 5.5: Relation between centrality (C) and impact parameter (b). C is defined to be the fraction of the total Au+Au cross section measured from the $b = 0$ event. The most central ($b = 0$) event corresponds to $C = 0$. $C=100\%$ corresponds to the total cross section including up to $b = 2R$ events.

5.4.4 Centrality

By using Figure 5.4, the events are divided into 20 centrality classes by straight lines perpendicular to the curve along the chine of the two dimensional distribution. And the centrality class C is defined as the fraction of the events between from the most central collision to the given events relative to total events. For example, $C=0-10\%$ means top 10% fraction of total cross section from the most central collision, and $C=60-80\%$ means top 80% events from the most central but excludes the top 60% fraction i.e. relatively peripheral events. Centrality span $\Delta C = 1\%$ corresponds to 1% of the total Au+Au cross section. Figure 5.5 shows the relation between the impact parameter b and the centrality.

The N_{part} for each class is obtained from the Glauber calculations considering the detector resolution, trigger efficiency, and systematics in the separation procedure, which are described below.

Simulation

The Au+Au collisions are simulated using Glauber model and N_{part} and N_{coll} were calculated for each simulated event. The responses of BBC and ZDC are simulated based on the following procedure.

The calculation of BBC response is based on the N_{part} scaling of charged particle

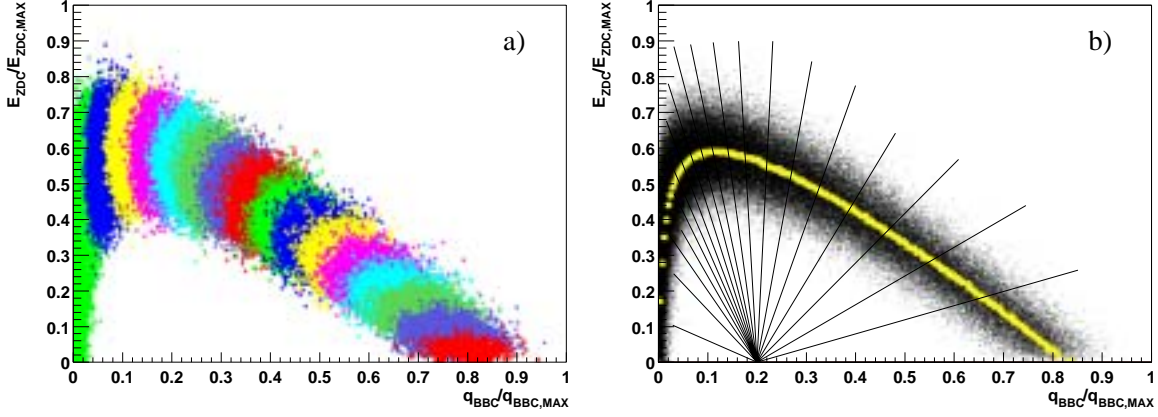


Figure 5.6: Simulated ZDC and BBC response (a) and demonstration of clockwise cut (b) used to estimate systematic uncertainty. Points in the plot (a) are grouped in the N_{part} period of 25.

density expressed by

$$\left\langle \frac{dN_{ch}}{d\eta} \right\rangle \propto N_{\text{part}}^{\alpha}. \quad (5.11)$$

In the WA80 experiment at CERN, the value α measured for the 158A GeV Pb+Pb collisions is 1.07 ± 0.04 for mid rapidity region. Under the assumption that number of particle in the Au+Au collision at RHIC has the same behavior as Eq. (5.11), the BBC response can be simulated using $\alpha = 1.00$. The average number of charged particles hit in each BBC are assumed to be 0.5 per participant. Those number of hits are distributed to all PMT's in BBC with the Poisson statistics where effective number of working PMT's of 40 is used. The amount of charge by each charged particle hit is simulated by Landau distribution with 75.0 pC of mean and 10.0 pC of the standard deviation. The total charges in BBC's are calculated by summing up the charges in all PMT's.

The number of spectator neutrons seen in the ZDC are estimated as the number of neutrons in the spectator in the first approximation. This number is at maximum for peripheral collision, and up to the number of neutrons in Au(118). But the number of free neutrons enter to the ZDC is suppressed because neutrons are bound in heavier nuclei. This neutron loss probability depends on centrality and bigger for the peripheral collisions. With the data of NA49 experiment at CERN SPS[71], the coalescence probability $P_{\text{coales}}(b)$ is set to be

$$P_{\text{coales}}(b) = 14.4 + 4.22 b \%. \quad (5.12)$$

The 30 % of neutron loss probability due to limited ZDC acceptance is taken into account. It is also assumed that 2 % of the participated nucleons enter into the ZDC. The energy

of each neutron is assumed to be the beam energy (65 GeV). The visible energy in the ZDC is smeared according to the intrinsic energy resolution expressed by Eq. (3.6).

Figure 5.6(a) shows the result of simulation. Qualitatively the behavior of ZDC and BBC responses are simulated. For the simulation data, the centrality selection is applied and the mean N_{coll} and mean N_{part} in each centrality class are calculated.

Figure 5.2 shows the estimated $\langle N_{\text{part}} \rangle$ and $\langle N_{\text{coll}} \rangle$ by Glauber model and number of events in each centrality bins obtained by applying the classification. An estimation method of attached systematic errors are discussed next.

5.4.5 Systematic Fluctuations of N_{part} and N_{coll}

The estimation of $\langle N_{\text{part}} \rangle$ and $\langle N_{\text{coll}} \rangle$ depends on the model parameters in the Glauber model, assumptions on response of BBC and ZDC, and the way to separate the events into centrality bins in the two-dimensional BBC and ZDC response plots. The systematic errors on $\langle N_{\text{part}} \rangle$ and $\langle N_{\text{coll}} \rangle$ were estimated by changing those parameters and methods. The different results of the N_{part} and N_{coll} calculations are shown in Figure 5.7. In this figure, eight sorts of different model settings are compared. For each model setting, the deviation from the mean of eight model settings is plotted. The list of model assumptions compared here are as follows:

- Reduced $N+N$ cross section of 35 mb.
- Different parameters for the Woods-Saxon distribution ($R=6.35$ fm and $a=0.35$ fm in Eq. (5.10)).
- Another parametrization of the neutron loss probability function in the ZDC simulation expressed by,

$$P_{\text{coales}}(b) = 33.1 + 1.3b + 100 \exp\left(\frac{b-17}{2}\right) \%.$$

- Turn on the simulations of the BBC saturation. Since BBC charge measurement had an upper limit of number of charged particle in each PMT in Year-2000 run, the PMT's with more than 150 pC are suppressed to have 150 pC.
- The additional statistical fluctuation in the BBC is simulated by smearing the number of hits in BBC's by the Gaussian with mean of square root of number of hits in BBC's. Also $\alpha = 1.2$ in Eq. (5.11) is taken.
- The different centrality bin definition is tested. Results of centrality selection based on the ‘‘clockwise’’ cut is tested. This method is schematically demonstrated in Figure 5.6 (b). $(Q_{\text{BBC}}, E_{\text{ZDC}}) = (0.2, 0)$ is taken as a center of the clock origin.

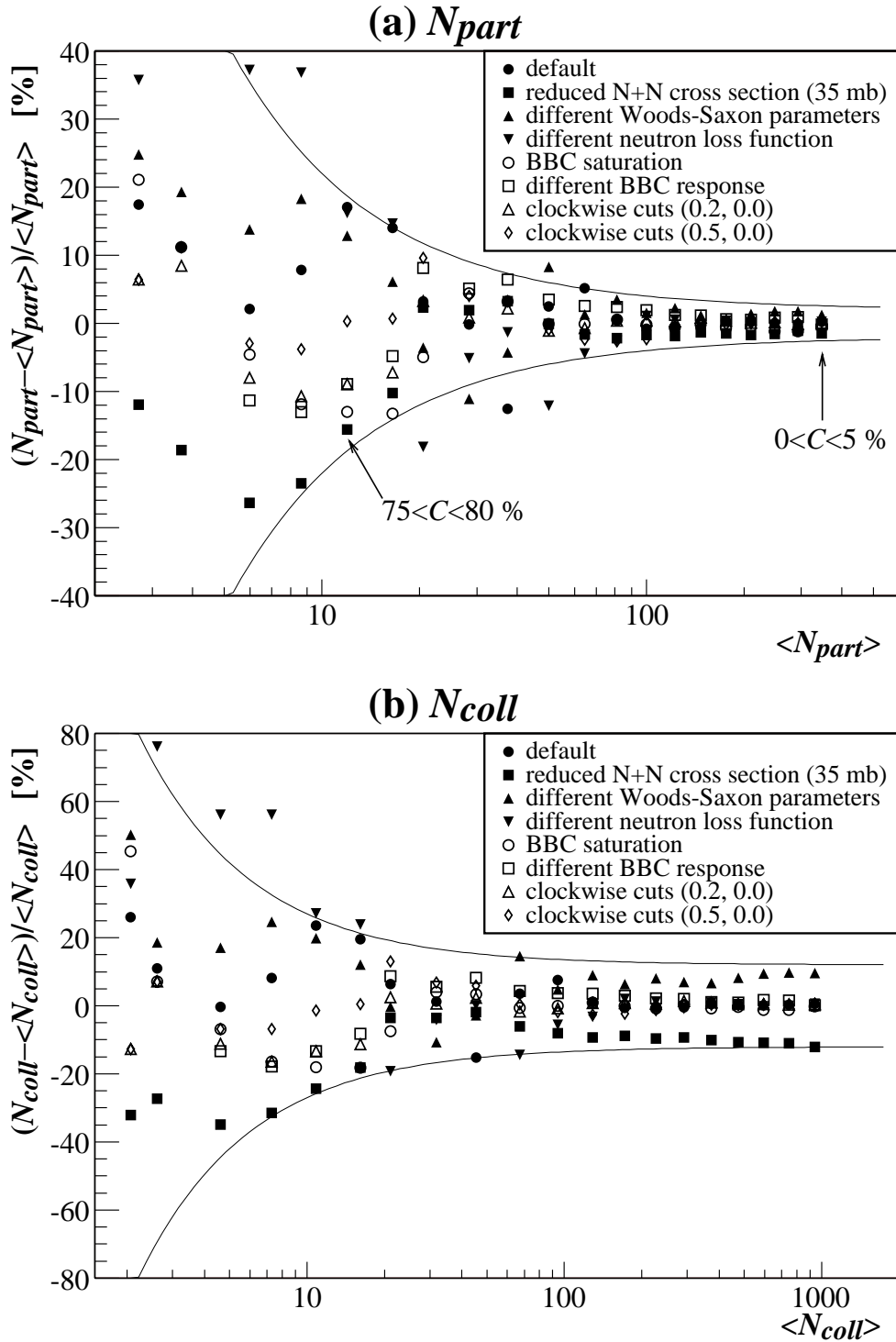


Figure 5.7: Systematic fluctuations of N_{part} (a) and N_{coll} (b). N_{part} and N_{coll} are calculated with eight variety of parameter settings of Glauber Monte Carlo. Solid curves show the estimated systematic uncertainties expressed by Eq. (5.13) and Eq. (5.14).

C	$\langle N_{\text{part}} \rangle$	$\langle N_{\text{coll}} \rangle$	N_{ev}
0–5	346.3 \pm 8.9	940.3 \pm 114.3	121,897
5–10	293.1 \pm 7.9	746.8 \pm 91.1	119,458
10–15	248.3 \pm 7.0	595.4 \pm 73.0	120,668
15–20	210.0 \pm 6.2	474.7 \pm 58.5	119,894
20–25	176.1 \pm 5.5	373.7 \pm 46.3	118,646
25–30	146.9 \pm 4.9	291.2 \pm 36.4	117,161
30–35	122.3 \pm 4.4	226.6 \pm 28.7	124,341
35–40	99.9 \pm 4.0	171.6 \pm 22.1	121,973
40–45	81.1 \pm 3.6	129.0 \pm 17.0	117,731
45–50	64.5 \pm 3.3	94.3 \pm 12.8	123,606
50–55	50.0 \pm 3.0	67.0 \pm 9.5	122,921
55–60	37.3 \pm 2.7	45.4 \pm 6.9	121,392
60–65	28.4 \pm 2.6	31.8 \pm 5.3	124,321
65–70	20.5 \pm 2.4	21.1 \pm 4.0	126,214
70–75	16.5 \pm 2.3	16.1 \pm 3.4	128,176
75–80	12.0 \pm 2.2	10.8 \pm 2.8	130,215
80–85	8.6 \pm 2.2	7.3 \pm 2.4	136,769
85–90	6.0 \pm 2.1	4.6 \pm 2.1	117,811

Table 5.2: The estimated mean number of participants $\langle N_{\text{part}} \rangle$ and mean number of collisions $\langle N_{\text{coll}} \rangle$, in each centrality bin. Associated errors are systematic fluctuations calculated by Eq. (5.13) and Eq. (5.14) with obtained $\langle N_{\text{part}} \rangle$ and $\langle N_{\text{coll}} \rangle$, respectively. The numbers of events in each centrality N_{ev} after applying the event classification to the real data are also shown. Numbers of events include only full field data which are used in the analysis. Events at $C > 90$ % region were not used because trigger efficiency drops at $C = 92 \pm 2$ %.

For a given point, the angle ϕ of a given (Q_{BBC}, E_{ZDC}) is calculated with respect to the clock origin. Then the centrality bins are defined to include equal fraction of total events.

- Also the other clock origin (0.5, 0.0) in clockwise cut is tested.

Based on results in Figure 5.7, the systematic uncertainties in N_{part} and N_{coll} are estimated to be

$$\frac{\delta N_{\text{part}}}{N_{\text{part}}} = 2 + \frac{200}{N_{\text{part}}} [\%], \quad (5.13)$$

$$\text{and } \frac{\delta N_{\text{coll}}}{N_{\text{coll}}} = 12 + \frac{150}{N_{\text{coll}}} [\%]. \quad (5.14)$$

The errors listed in Table 5.2 are calculated using Eq. (5.13) and Eq. (5.14), and also shown in Figure 5.7 by solid lines.

Ratio to Peripheral

In the following analysis, non-equal sizes of centrality bins, $C = 0-10\%$, $C = 10-20\%$, $C = 20-40\%$, $C = 40-60\%$, and $C = 60-80\%$ are used, and these are combined bins of fine bins shown in Table 5.2. The class $C = 60-80\%$ is, then, the “most peripheral” event class in the following analysis. The systematic uncertainties of the ratio:

$$R_{\text{part}} = \frac{N_{\text{part}}}{N_{\text{part}}|_{C=60-80\%}}, \quad (5.15)$$

$$\text{and } R_{\text{coll}} = \frac{N_{\text{coll}}}{N_{\text{coll}}|_{C=60-80\%}}, \quad (5.16)$$

are also estimated here, because those ratios are used for comparison in physics discussion.

Figure 5.8 shows the systematic uncertainties of the ratios R_{part} and R_{coll} . Results of the Glauber settings used in Figure 5.7 were plotted together. From the plot, the systematic uncertainty of R_{part} and R_{coll} are defined to be 7% and 10%, respectively.

5.5 EMCal Clustering and Photon Measurement

In this section, how to analyze the EMCal hit pattern and to obtain γ 's momentum are explained. The reconstruction of the γ 's momentum is realized by “clustering” [72].

Figure 5.9 shows a sample event recorded at one sector of the PbSc EMCal. The energetic photon and electron deposit their energy as electromagnetic shower. An electromagnetic shower forms a cluster of tower hits which consists of a tower with highest

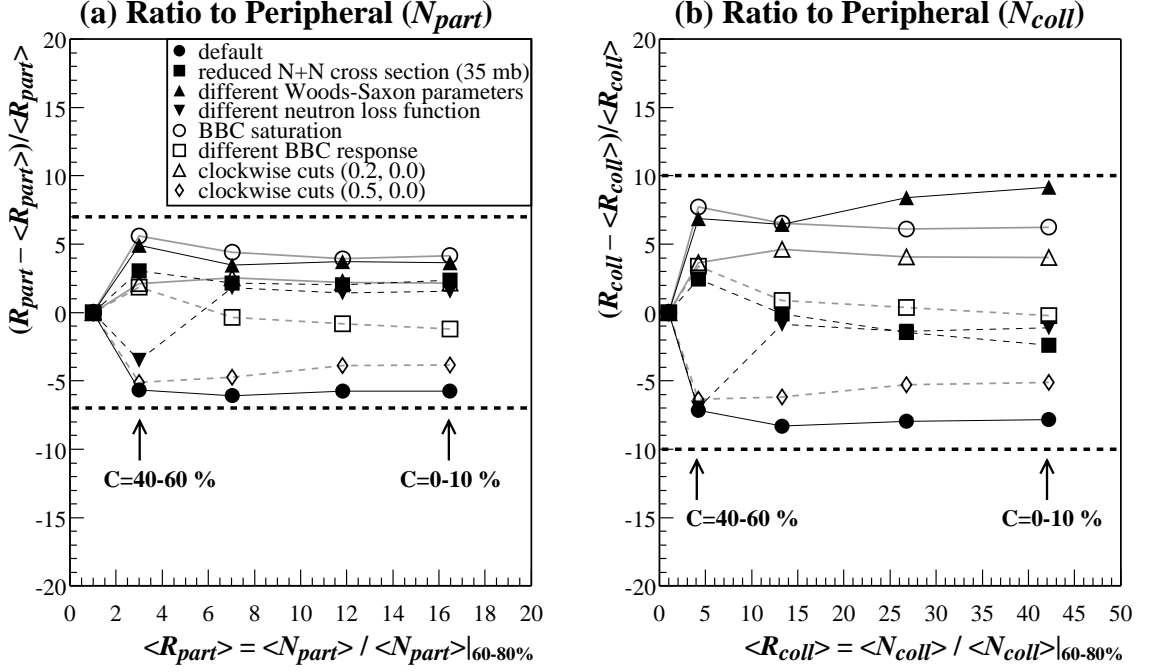


Figure 5.8: Fluctuation of $\langle N_{part} \rangle$ (a) and $\langle N_{coll} \rangle$ (b) divided by their values at $C = 60-80\%$ events among different Glauber calculations. Dashed lines at $\pm 7\%$ in (a) and $\pm 10\%$ in (b) show systematic upper and lower limits of the ratio.

energy deposit and a few surrounding towers with lower energy deposit. In the clustering, the entire towers of each EMCAL sector is scanned to find such clusters. Since the two-dimensional profile of the electromagnetic shower is well understood, a cluster candidate is compared to the predictions and γ PID is performed. Also since the γ 's are the fastest particles, the flash timing of highest energy deposited tower is useful to distinguish γ 's from other particles have non-zero mass.

5.5.1 Clustering Algorithm

The clustering of EMCAL is separated into three successive procedures, finding domain of hit towers, finding peaks, and shower recognitions. The procedures are explained below. The analysis is done for each sector independently.

Domain Finding

The energy deposit in a tower i is represented by E_i . A tower which fulfills the criteria:

$$E_i > 3 \text{ MeV}, \quad (5.17)$$

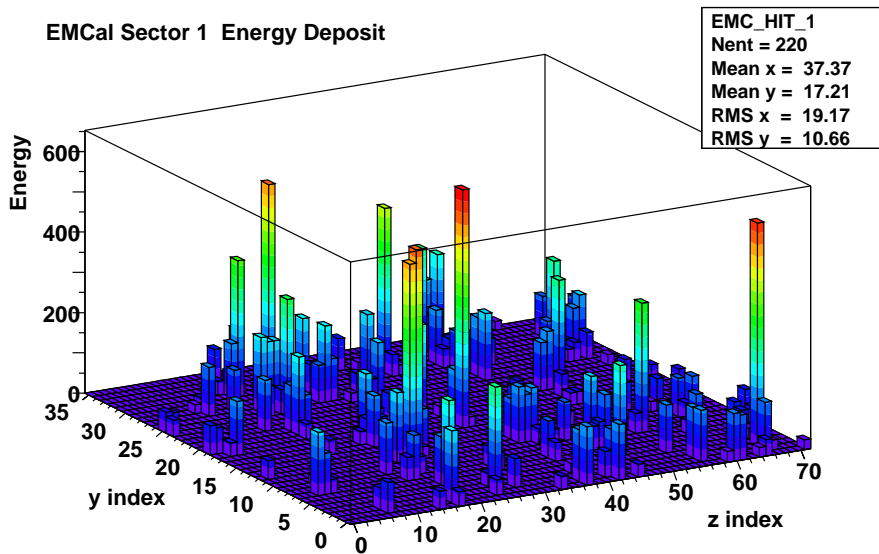


Figure 5.9: An example of event. The energy deposits in the towers are plotted.

are defined as a hit tower.

A domain is formed in the way that two neighboring hit towers belong to the same domain. A domain could have any number of towers from one to large number of towers.

Peak Finding

For each domain, the peak finding is performed. For the towers in the domain, if a tower has the highest energy of the nearest neighboring towers and the energy is more than 80 MeV, the tower is defined as a candidate of a peak.

For each peak candidate tower, the total energy and center of gravity of eight neighboring towers of the peak tower is calculated by energy and position of each tower. From the total energy and center of gravity position, the predicted energy deposit if the peak is generated by electromagnetic particle is calculated. The calculation is based on the test beam results.

At this stage, each tower could have contributions from multiple peaks so that the sum of those calculated contribution exceeds the measured energy deposit. Then, the fraction of energy deposits contributed by all peaks are obtained and this energy prediction is performed iteratively.

In the next step, the measured energy of each tower is shared by contributing peaks. The ratio of fractional energy of the currently evaluating peak divided by total energy deposit in the tower from all the peaks is used to calculate the total energy of the peak.

Six times iterations are performed. Then peaks are obtained. Each peak has the peak tower and associated towers. A tower could be associated to multiple peaks with fractional energy. In each peak, if the fractional energy of the tower is less than 2 MeV, it is neglected.

The next step “shower recognition” is performed for each peak independently from other peaks.

Shower Recognition

For each peak, the γ extraction is performed by using profile parameters of the peak.

If a peak consists of N towers located on $(x_0, y_0), (x_1, y_1), \dots, (x_{N-1}, y_{N-1})$, with their energy deposits of E_0, E_1, \dots, E_{N-1} , where x_i and y_i are position of the center of tower i . The peak total energy is then calculated by

$$E_{tot} = \sum_{i=0, \dots, N-1} E_i, \quad (5.18)$$

and center of peak is calculated by

$$(x_c, y_c) = \frac{1}{E_{tot}} \sum_{i=0, \dots, N-1} E_i \cdot (x_i, y_i). \quad (5.19)$$

In the ideal case, if the peak has no secondary contribution and has only an electromagnetic particle, the values (E_{tot}, x_c, y_c) are particle’s energy and hit position.

The shower shape parameter is calculated by

$$\delta^2 = \frac{1}{N} \sum_i \frac{(E_i - E_i^{pred})^2}{\sigma_i^2}, \quad (5.20)$$

where N is number of tower associated to the peak, E_i^{pred} is the predicted energy by assuming the peak is originated from an electromagnetic shower with energy E_{tot} , and σ_i is the variance of tower energy parametrized as a function of E_i^{pred} , E_{tot} , and position. The precise description of parametrization is given in Subsection 5.5.8. The center of shower position is obtained by searching the best δ^2 position in and around the peak tower. If the obtained δ^2 is too large, the cluster may contain more than one shower, so that 2γ hypothesis is tested. In 2γ hypothesis, the two best δ^2 positions with divided shower energy are looked up.

The two electromagnetic showers are extracted from the peak area at maximum. The clusters with $E_{tot} > 100$ MeV are used in this analysis.

5.5.2 Multiplicity

Figure 5.10 shows the distributions of number of clusters per event found in the two PbSc sectors. In the most peripheral event class (C=60–80 %) , the mean cluster multiplicity

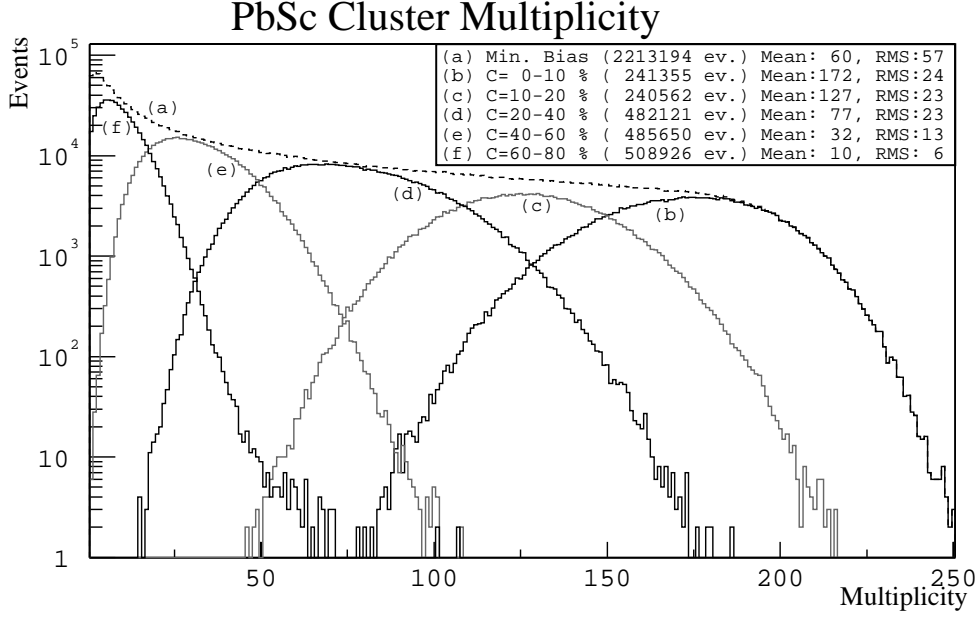


Figure 5.10: Cluster multiplicity distributions for selected centrality cuts. Dashed line is distribution of multiplicity for all full field events (minimum bias). Distributions for each centrality regions are shown by black or gray lines (see texts in the figure).

is ~ 10 . The probability P that arbitrary selected two clusters have distance less than r is, if there is no correlation, approximately given by

$$P = M \frac{\pi r^2}{S}, \quad (5.21)$$

where $S \sim 16 \text{ m}^2$ is the area of EMCal and M is the cluster multiplicity. Since 90 % of shower energy is deposited inside a cylinder with $\sim 6 \text{ cm}$ radius (Molière radius) and this radius depends little on shower energy, $r \sim 6 \text{ cm}$ can be taken as the limit of overlapping of two clusters. Then P is $\sim 0.7 \%$ for $M=10$ environment. In the low multiplicity events, overlap effect is not important. In the most central event class, the number of clusters reaches 250 at maximum. For $M=250$, P exceeds 18 %. It could cause not only modification (increasing) the cluster energy but also breakup of clusters.

As shown in later sections, the overlapping effect is seen in measured mass of π^0 and corrections were performed. Effect of cluster breakup and its effect to the efficiency is also discussed.

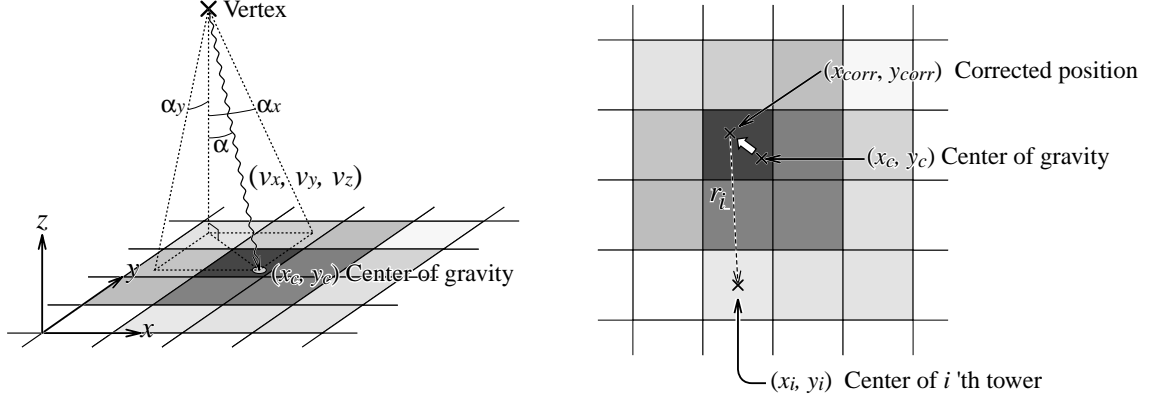


Figure 5.11: Definitions of impact angles (left) and impact position correction method (right). Matrices show the EMCAL tower and larger energy deposit is represented by dark gray.

5.5.3 Hit Position Correction

The cluster hit position measured as the center of gravity (x_c, y_c) in Eq.(5.19) is corrected by the hit angle. As is illustrated in Figure 5.11, the shower develops asymmetrically for the angle hit, and the center of gravity is not the impact position on the surface of EMCAL. The amount of the shift is estimated by the hit angle.

If the particle is a photon (or a neutral particle), the hit angle α at the EMCAL can be measured from the position of event vertex and the position of real hit position at EMCAL. While calculating the α , center of gravity (x_c, y_c) can be used instead of the real hit position. As shown in Figure 5.11, the vector (v_x, v_y, v_z) is obtained as a vector that points from the event vertex to the center of gravity. From the (v_x, v_y, v_z) , the impact angle α , α_x and α_y are calculated by

$$\sin \alpha = \frac{\sqrt{v_x^2 + v_y^2}}{\sqrt{v_x^2 + v_y^2 + v_z^2}}, \quad \sin \alpha_x = \frac{v_x}{\sqrt{v_x^2 + v_z^2}}, \quad \text{and} \quad \sin \alpha_y = \frac{v_y}{\sqrt{v_y^2 + v_z^2}}. \quad (5.22)$$

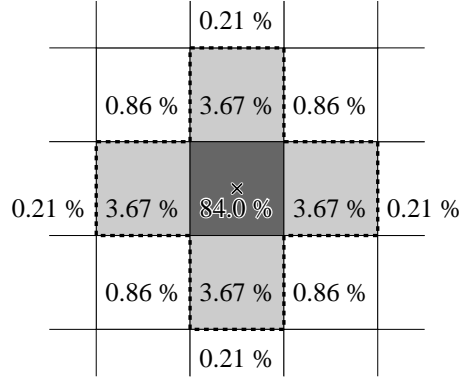
From the test beam result, the corrected position (x_{corr}, y_{corr}) are calculated by

$$\begin{bmatrix} x_{corr} \\ y_{corr} \end{bmatrix} = \begin{bmatrix} x_c - \pm(1.05 + 0.12 \ln E_{tot}) \sin^2 \alpha_x \\ y_c - \pm(1.05 + 0.12 \ln E_{tot}) \sin^2 \alpha_y \end{bmatrix}, \quad (5.23)$$

where positive signs are taken if the α_x or α_y are positive.

5.5.4 E_{core} Variable

The E_{core} variable was introduced to reduce shower overlap effect. For the cluster which has only an electromagnetic shower, the shower energy deposit in each tower can be



Perpendicular hit on the center of tower.

Figure 5.12: An example of predicted shower energy fraction in towers. This is the case of perpendicular hit of EM particle on the center of a tower. Surrounded five towers by dotted line is used for E_{core} calculation. Energy deposit from the secondary contamination to the towers except for the five towers do not modify the E_{core} value.

predicted from the beam test results, as already described. For a specific tower i included in the cluster, distance r_i between the position of tower center (x_i, y_i) and particle hit position (x_{corr}, y_{corr}) is calculated. Then the parametrized fraction of tower energy by the test beam result is presented by

$$F_i^p = P_1 \exp \left\{ -\frac{(r_i/r_0)^3}{P_2} \right\} + P_3 \exp \left\{ -\frac{(r_i/r_0)}{P_4} \right\}, \quad (5.24)$$

where r_0 is the size of EMCal tower (5.54 cm) and $P_i (i = 1, 2, 3, 4)$ are parametrized to be

$$P_1 = 0.59 - (1.45 + 0.13 \ln E_{tot}) \sin^2 \alpha, \quad (5.25)$$

$$P_2 = 0.265 + (0.80 + 0.32 \ln E_{tot}) \sin^2 \alpha, \quad (5.26)$$

$$P_3 = 0.25 + (0.45 - 0.036 \ln E_{tot}) \sin^2 \alpha, \quad (5.27)$$

$$\text{and } P_4 = 0.42. \quad (5.28)$$

As schematically shown in Figure 5.12, if a photon hits at the center of a tower perpendicularly, $P_1 + P_3 \sim 84\%$ of shower energy is deposited. And other towers have less than 4% energy.

By using the predicted fractions F_i^p , the shower core energy E_{core} is defined. If the F_i^p is less than 2%, the tower is not used in core energy measurement. Then the sum of those towers is defined by

$$E_{core} = \sum_{\text{for } F_i^p > 0.02} E_i, \quad (5.29)$$

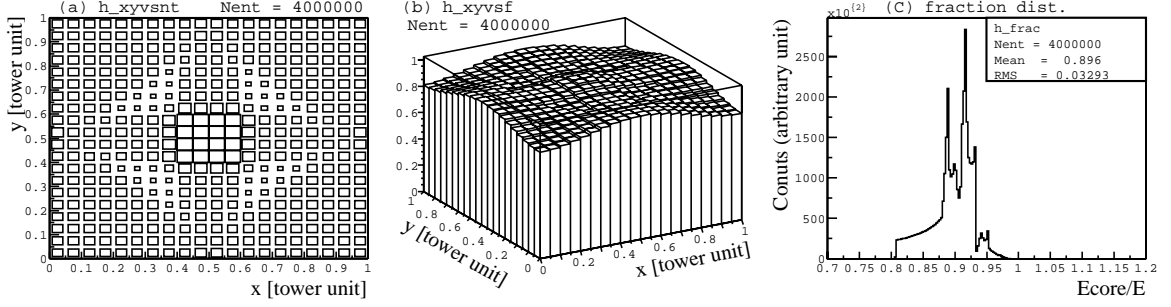


Figure 5.13: Number of towers in E_{core} and fraction of E_{core} estimated by the simulation. (a) shows the number of used towers in the E_{core} as a function of particle hit position in the tower. The smallest rectangle shows number of hit is 3. And the largest rectangles shows number of hit is 5. (b) shows the energy fraction E_{core}/E_{tot} as a function of particle hit position in the tower. (c) shows the distribution of energy fraction E_{core}/E_{tot} .

where E_i is the “measured” energy deposit in the tower i same as used in Eq. (5.18). In the Figure 5.12, the towers included in E_{core} calculation are towers in the region surrounded by dotted lines. E_{core} , is expected to be a more robust when the particle multiplicity is high. But it needs a correction to compensate for the unused towers. The correction factor is obtained with the following simulation study.

Correction for E_{core} and its Performance

With the definition of E_{core} , the number of towers used for E_{core} varies from three to five depending on the hit position on the tower surface as shown in Figure 5.13(a). The total energy fraction relative to the expected total energy are estimated for any point on a tower surface. Since E_{core} calculation is neglecting contribution from the shower tail, automatically causes deficit of shower energy, and the deficit depends on the particle hit position. For example, in the case of Figure 5.12, at least $4 \times 0.86\% + 4 \times 0.21\% \sim 4\%$ of shower energy is missing. The fraction of E_{core} relative to E_{tot} varies between $0.8 \sim 1$ as shown in Figure 5.13 (b) and (c). Then the correction is needed to return to total energy. If the particle hit the apex of the tower edges, the missing energy increase to 20%. The correction factor is 1.089% in average over the tower surface area.

The correction factor also depends on the hit angle α and slightly on the energy. From the Monte Carlo simulations, the corrected shower core energy is calculated by

$$E_{core}^{corr} = \frac{1.089}{1.0 - 1.35 \sin^4 \alpha (1.00 - 0.003 \cdot \ln E_{core})} \cdot E_{core}, \quad (5.30)$$

where 1.089 comes mainly from deficit seen in Figure 5.13.

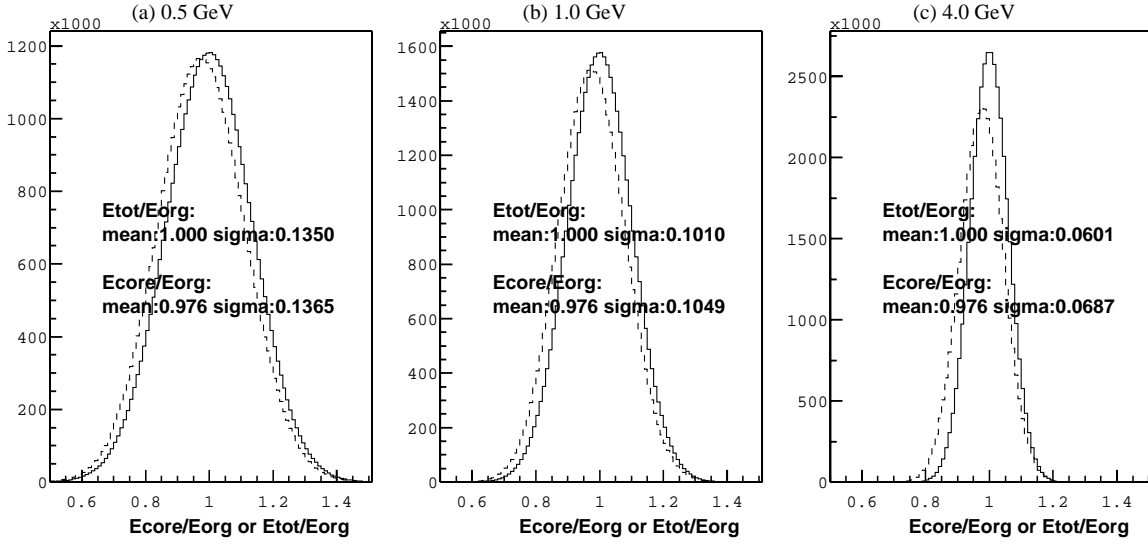


Figure 5.14: Effect of E_{core} algorithm. Simple Gaussian distributions with intrinsic EMCal energy resolution for 0.5, 1.0, and 4.0 GeV photons are convoluted by the fluctuations purely due to the algorithmic reason of E_{core} which was shown in Figure 5.13(c). Plots are demonstrating the E_{core} algorithm does not lose the intrinsic resolution of EMCal.

By using the results in Figure 5.13 (b) and (c), the resolution of the E_{core} is studied by a simple convolution of the energy by the fluctuation due to the E_{core} algorithm. The results are shown in Figure 5.14. The E_{core} algorithm causes a bit worth performance in energy resolution but the effect is small. In the following discussions, E_{core} means E_{core}^{corr} implicitly.

How the E_{core} is powerful is seen in the high particle multiplicity events. By using the GEANT simulation the E_{core} and E_{tot} are compared with the generated photon energy. Figure 5.15 shows the resolution of E_{tot} and E_{core} . (a) shows the E_{tot}/E_{org} distribution where E_{org} is the true photon energy produced in the simulation. (b) shows the E_{core}/E_{org} distribution. In both (a) and (b), the “dirty” cluster and the “clean” cluster are compared. The dirty cluster means the cluster has at least one secondary particle contamination. The clean cluster has no secondary contamination. Obviously the dirty clusters have higher average in energy than clean clusters and the distribution has longer tail at higher energy. The peak position of E_{core} the distributions is less affected by the secondary particles. There is still a long tail but with smaller magnitude compared with E_{tot} .

Finally the experimentally obtained E_{core} distributions of selected photon candidates are shown in Figure 5.16 for each centrality class.

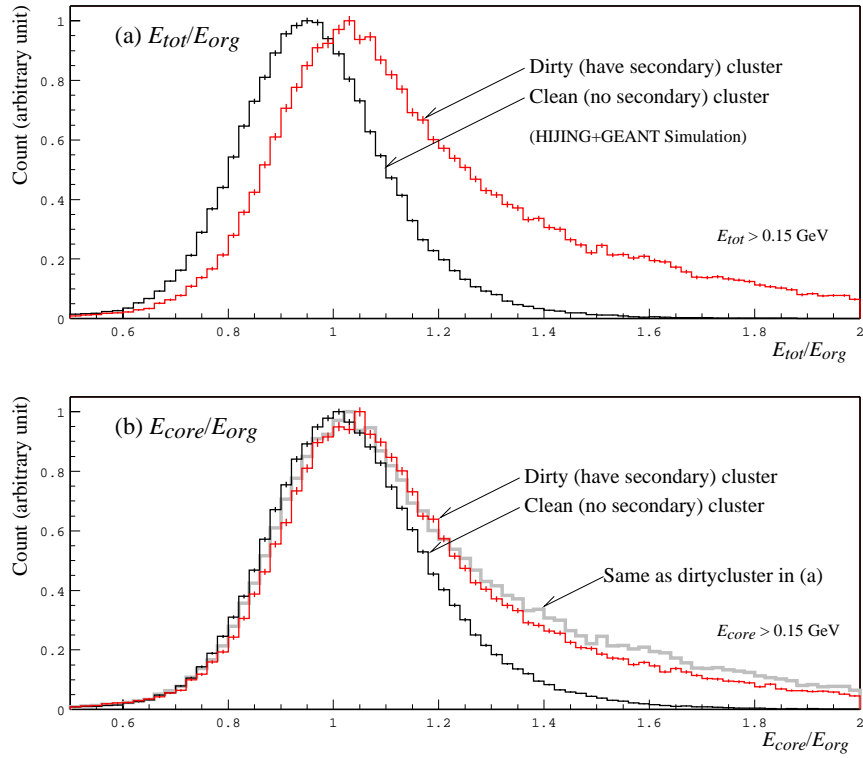


Figure 5.15: Simulated distributions of E_{tot}/E_{org} (a) and of E_{core}/E_{org} (b). Black lines are distribution of “clean” photon cluster without any secondary contribution to the cluster. Gray lines are distribution of “dirty” photon cluster have at least one secondary contribution to the cluster. The same distribution of dirty cluster’s distribution in (a) is plotted also in (b).

5.5.5 MIP Observation

The minimum ionization peak (MIP) by punch through energy deposition of muons and charged hadrons was used to confirm the absolute scale of EMCal energy measurement. The total energy deposit from a muon or a charged hadron is a function of the path length of the particle in the EMCal. From the simulation and beam test, the amount of MIP energy deposit is known to be ~ 270 MeV for the perpendicular hit on the EMCal and become large for skew hit. Per tower energy deposit gradually decreases for skew hits because total energy is distributed to several towers.

The MIP is already visible in Figure 5.16 at ~ 300 MeV position but it is broad and not clear. The clearer MIP can be seen in clusters with associate tracks reconstructed by DC and PC1. They are mainly charged pions.

Figure 5.17 shows the E_{core} distributions for the clusters with the track association.

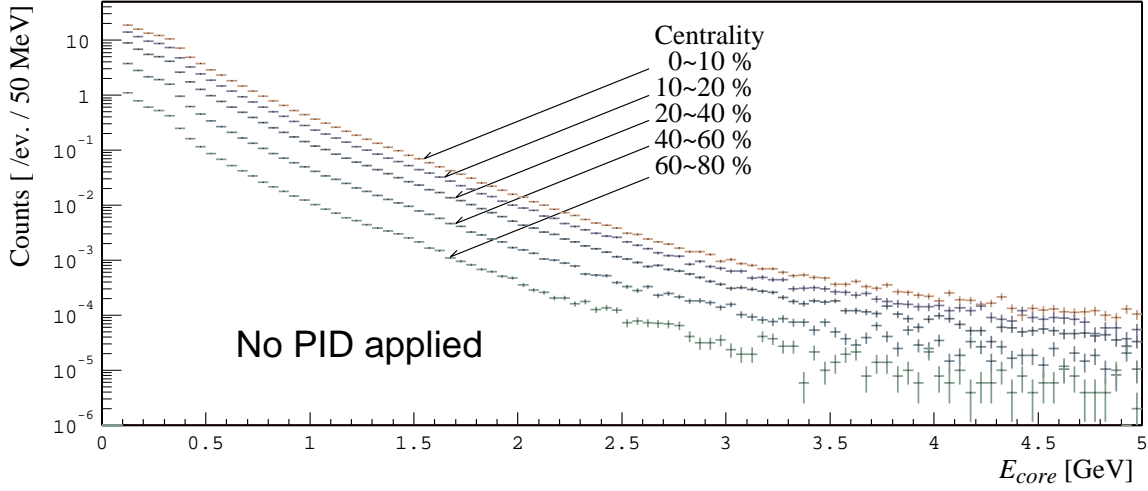


Figure 5.16: E_{core} distribution for several centrality bins. The distributions are scaled by the number of events in each centrality class.

Central and peripheral events are plotted. The MIP's are clearly seen. Then asymmetric Gaussian function associated by the exponential background is used to fitting the shape. The observed position of MIP is 304 ± 1 MeV and it is 10% higher than 270 MeV. There are several reasons in the difference. The path length is not corrected for the incident angle. The shower shape of the MIP is narrower than electromagnetic shower so that the correction with Eq. (5.30) is overestimated.

The observation of MIP supports the overall energy scale of EMCal is approximately correct. The precise energy correction is done by π^0 peak position measurement and will be discussed later.

5.5.6 Electron Observation

Electromagnetic shower shape for the electron is almost same as that of the photon except for the difference at the early stage of the shower development. Energy in EMCal can be compared with the momentum of the electrons measured and identified by tracking devices (DC and PC1) and RICH. Figure 5.18 shows the ratio of calorimeter energy divided by momentum measured by tracking (E/p) for identified tracks as electrons or positrons by RICH. The electron samples with momentum range between 0.3 and 1 GeV/c were plotted. Since β of electrons are unity in this momentum range. In the Figure 5.18, $E/p = 0.994 \pm 0.010$. This means energy scale of EMCal is approximately correct.

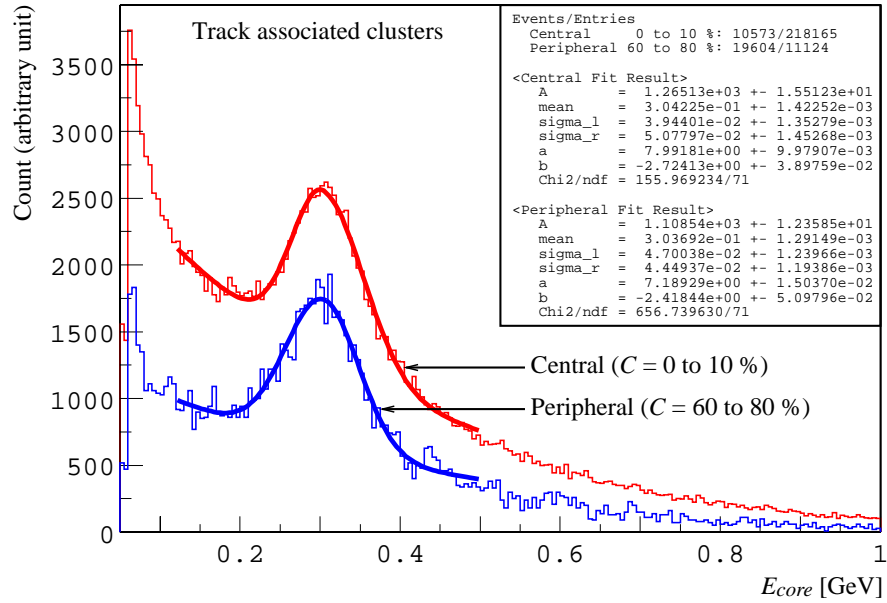


Figure 5.17: Energy distribution of clusters associated to the reconstruct tracks for most central events and peripheral events. The peripheral data is scaled by $\times 10$. Momentum lower limit of 0.5 GeV/c is applied. Approximately 10 K central events and 20 K peripheral events corresponding 4 % of full statistics were used in this plot.

5.5.7 Time of Flight Measurement with EMCal

Figure 5.19 shows the time-of-flight distribution obtained by EMCal. In the top plot of Figure 5.19, the EMCal time distribution before applying corrections is shown. It is widely spreading and has a broad peak at ~ -40 ns. In the Year-2000 run, run period was less than one day and calorimeter response does not change so much in a day. The reason why it fluctuates so much is in the clock synchronization part of electronics system.

Fitting for the peak were performed in each run and offset was obtained run-by-run. Gaussian function was used for the fitting. Figure 5.20 shows the mean peak position of EMCal time-of-flight as a function of run number. The size of vertical bars are standard deviation of the Gaussian function fitted to the TOF peak in each run. In each run, the TOF values are subtracted by the mean TOF value. All the mean TOF value in the all runs are then flattened and mean is collected to zero.

The time-of-flight peak position varies also tower-by-tower due to difference of characteristics of electronics. Fit by Gaussian function was applied again for time-of-flight peak at each tower separately.

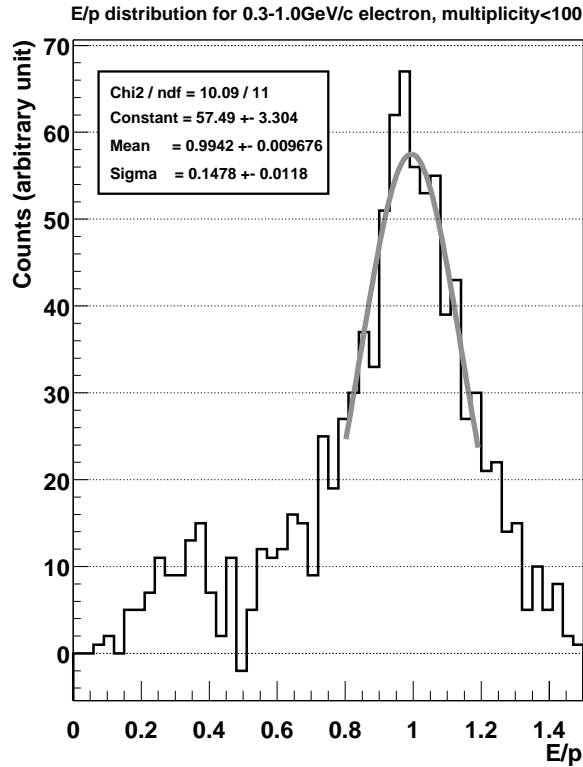


Figure 5.18: E/p ratio of electron samples identified by tracking devices and RICH.

After run-by-run and tower-by-tower calibration, as shown in middle figure in Figure 5.19, sharp peak at $t = 0$ was obtained.

As shown in bottom plots in Figure 5.19, Gaussian fittings are performed in the range approximately from -2σ to $+0.5\sigma$ of its fitting result (fitting was performed iteratively). The final timing resolutions for central and peripheral events are ~ 620 ps and 600 ps, respectively, after shower shape cut ($\delta^2 < 3$) described later in Section 5.5.8.

As shown in the Section 3.4, the intrinsic timing resolution of calorimeter towers is ~ 200 ps. The achieved timing resolution (~ 600 ps) is worse than intrinsic timing resolution. It still has potential to be improved future.

Ingredients of Timing Distribution and Timing Cut

In this analysis, to obtain as good as possible timing resolution is not the main issue, but it is required that photon efficiency for timing cut is stable and predictable. To do it, it is necessary to understand the ingredients in the timing distribution. For example, the right edge in the peak shown in Figure 5.19 is not the Gaussian and long tail exists. It is explained by contamination mainly from charged pions and other particles. To account

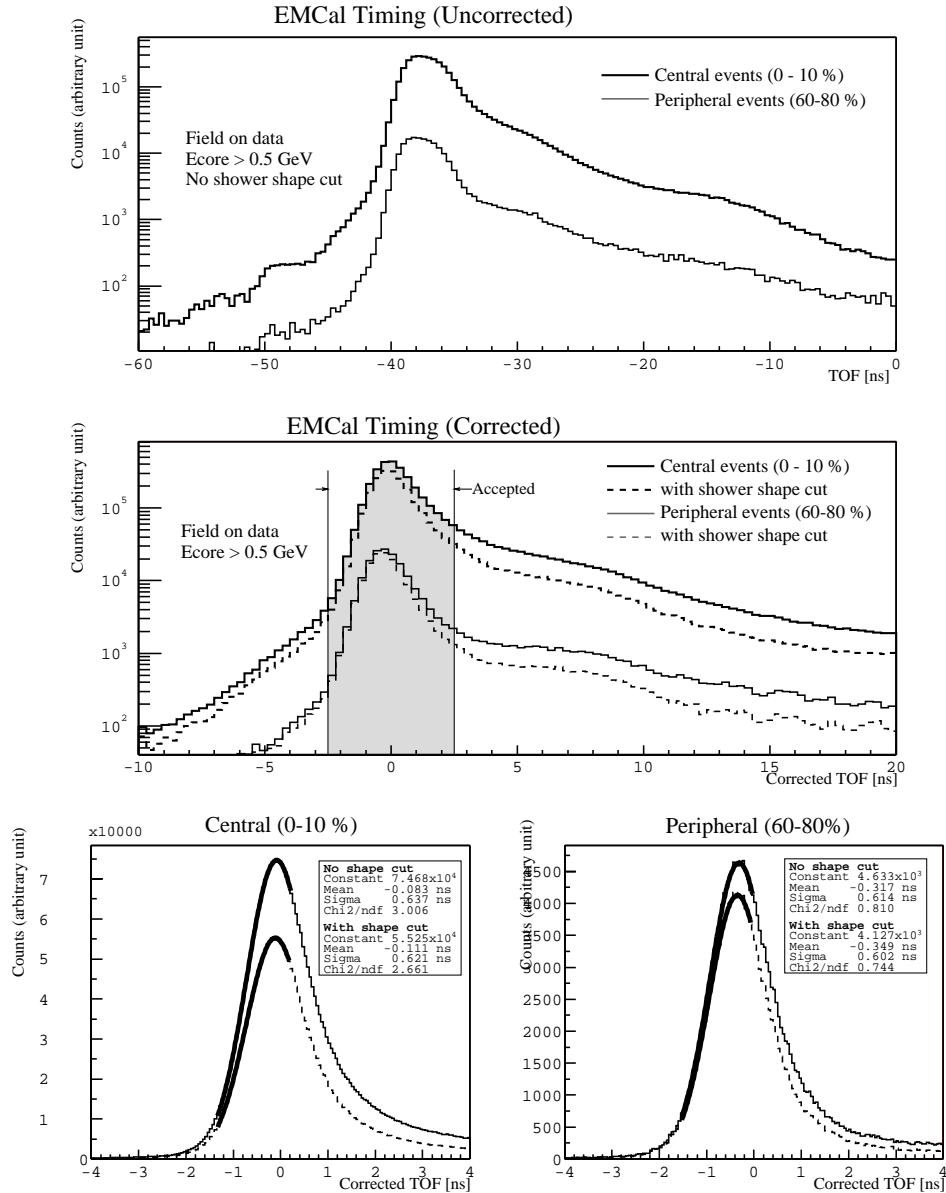


Figure 5.19: EMCAL timing distribution. Top figure is uncorrected flush time distribution of maximum energy deposited EMCAL towers in the clusters. A black line is for central events and a gray line is for peripheral events. Only cluster energy (E_{core}) above 0.5 GeV were selected. Middle figure is corrected time distribution also for central (black) and peripheral (gray). In the solid line, only $E_{core} > 0.5$ GeV threshold was applied and in the dashed line, also shower shape cut ($\chi^2 < 3$) was applied. Bottom figures are basically same as middle figure. Fit by Gaussian were performed. In these figures, every full field data was used.

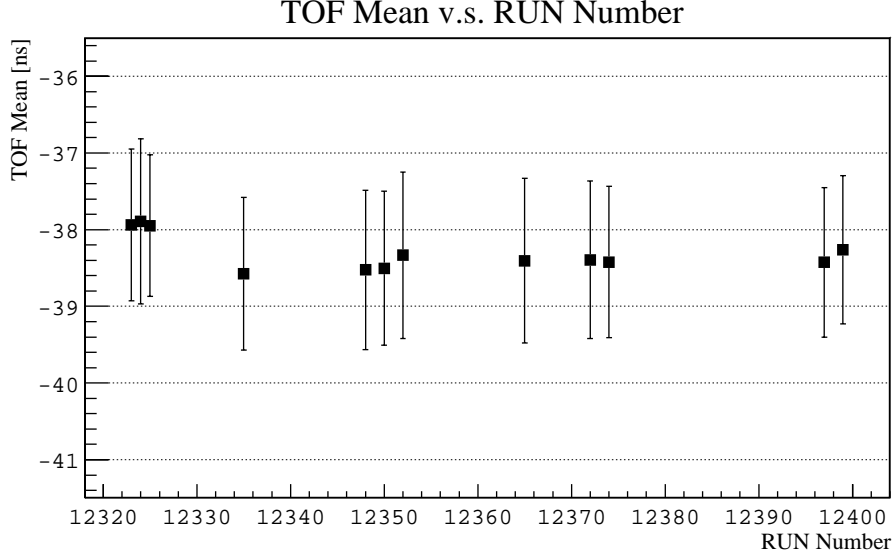


Figure 5.20: Example of EMCal-TOF run-by-run fluctuations before corrections. The mean values obtained by fitting Gaussian function to the prompt part of TOF distribution at each run are shown. Attached bars are not the error bars but standard deviation of fitted Gaussian which is TOF resolution.

for this tail, GEANT simulation is used.

Figure 5.21 shows the GEANT simulation results. Figure 5.21(a) is the simulated timing distribution for $E_{core} > 0.5$ GeV clusters and (b) is for $E_{core} > 1.0$ GeV clusters. In both plots, the main contamination is charged pions and next is electrons and positrons. The charged pion is seen as tail start from almost same position of photon peak. Also in higher momentum, \bar{p} and \bar{n} become dominant.

Here, enough large time window:

$$|t| < 2.5 \text{ ns} \quad (5.31)$$

is used as the timing cut to keep a large efficiency of the photon. Since the prompt peak has ~ 600 ps width, the cut Eq. (5.31) is enough large and 99 % photons are included in the window. But it also permit the contamination from other particles. The expected background ingredients in the 2.5 ns time window are calculated from the simulation and summarized in Table 5.3. The TOF cut keeps γ efficiency more than 98 %. The cut is effective in higher energy of clusters. In $E_{core} > 1$ GeV region, the γ purity become better than 50 without TOF cut. Also anti-baryons in $E_{core} > 1$ GeV region is significantly eliminated by the TOF cut.

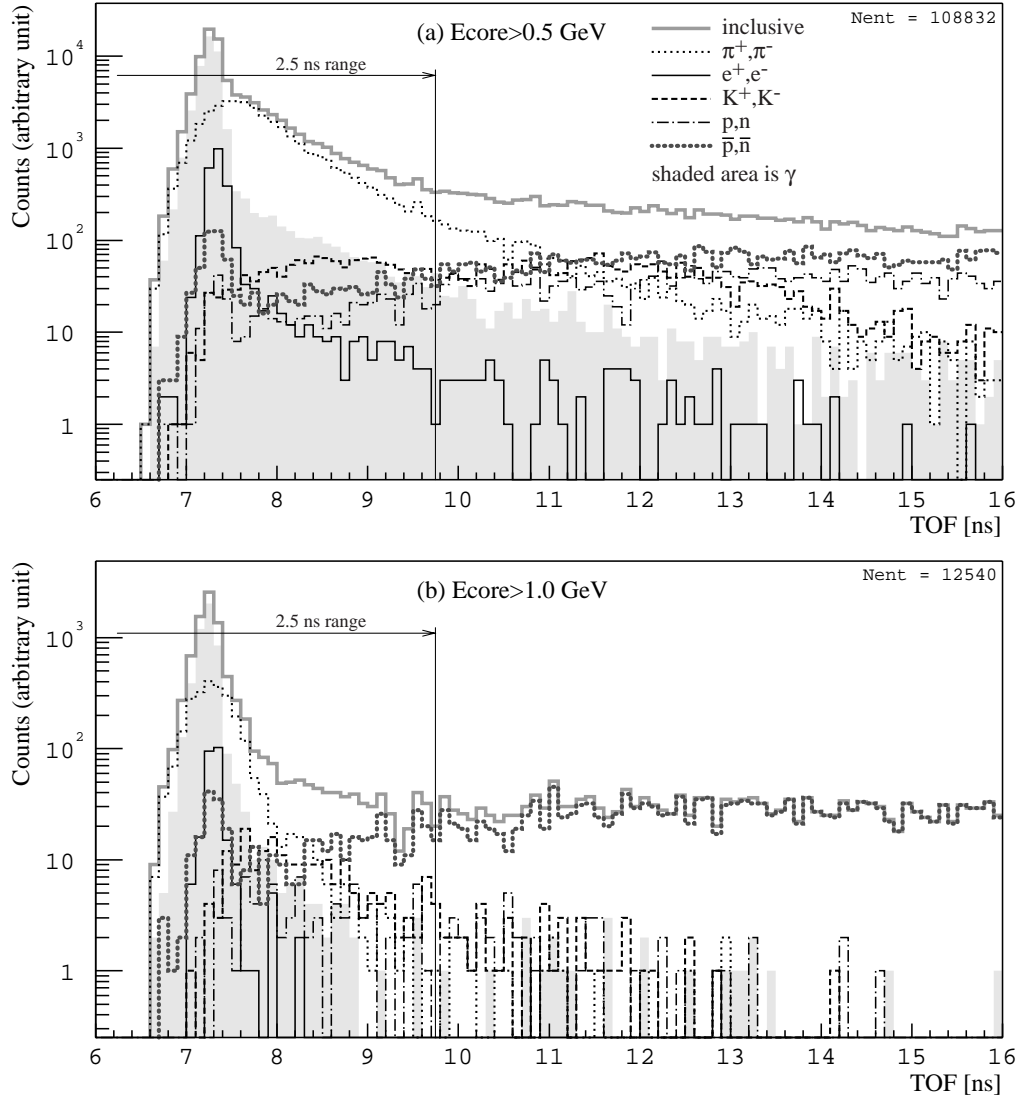


Figure 5.21: Simulated time of flight distributions for (a) $E_{core} > 0.5$ GeV clusters and (b) $E_{core} > 1.0$ GeV clusters. Inclusive TOF distribution is explained as admixture of several components.

(a) $E_{core} > 0.5$ GeV clusters.

particle species	without cut		with ± 2.5 ns TOF cut		
	count	yield	count	yield	efficiency
all	108,832	-	87,132	-	80.1 ± 0.4 %
γ	44,125	40.5 %	43,312	49.7 %	98.2 ± 0.7 %
e^+, e^-	2,555	2.3 %	2,454	2.9 %	96.1 ± 2.7 %
μ^+, μ^-	918	0.8 %	785	0.9 %	85.5 ± 4.2 %
π^+, π^-	39,568	36.4 %	36,991	42.5 %	93.5 ± 0.7 %
K_L^0	2,040	1.9 %	769	0.9 %	37.7 ± 1.6 %
K^+, K^-	3,491	3.2 %	1,267	1.4 %	36.3 ± 1.2 %
p	2,690	2.5 %	304	0.3 %	11.3 ± 0.7 %
n	675	0.6 %	188	0.2 %	27.9 ± 2.3 %
\bar{p}	6,837	6.3 %	508	0.6 %	7.4 ± 0.3 %
\bar{n}	5,933	5.5 %	554	0.6 %	9.3 ± 0.4 %

(b) $E_{core} > 1.0$ GeV clusters.

particle species	without cut		with ± 2.5 ns TOF cut		
	count	yield	count	yield	efficiency
all	12,540	-	8,363	-	66.7 ± 0.9 %
γ	4,867	38.8 %	4,840	57.9 %	99.5 ± 2.0 %
e^+, e^-	251	2.0 %	249	3.0 %	99.2 ± 8.9 %
π^+, π^-	2,474	19.8 %	2,451	29.3 %	99.1 ± 2.8 %
K_L^0	153	1.2 %	116	1.4 %	75.8 ± 9.3 %
K^+, K^-	242	2.0 %	194	2.3 %	80.2 ± 7.7 %
p	90	0.7 %	59	0.7 %	65.6 ± 11.0 %
n	42	0.3 %	30	0.4 %	71.4 ± 17.1 %
\bar{p}	2,646	21.1 %	211	2.5 %	8.0 ± 0.6 %
\bar{n}	1,774	14.1 %	212	2.5 %	12.0 ± 0.9 %

Table 5.3: Expected particle contamination within the ± 2.5 ns time of flight gates and efficiency calculated for (a) $E_{core} > 0.5$ GeV clusters and (b) $E_{core} > 1.0$ GeV clusters.

Timing Cut Efficiency

The efficiency of timing cut was checked by fitting TOF prompt peak for each E_{core} bin with 100 MeV step. The efficiency is estimated to be the area within the ± 2.5 ns TOF selection criteria divided by total area obtained by the Gaussian fitting.

Figure 5.22 (a) shows the peak position of TOF prompt peak obtained by fittings. The peak position is not constant and slightly walking. Figure 5.22 (b) shows the peak width of TOF prompt peak also obtained by fittings. From (a) and (b) of Figure 5.22, the efficiency of fixed TOF cut criteria was calculated and plotted in Figure 5.22 (c) as a function of E_{core} . Due to the walking of prompt peak position and width, the efficiency of fixed TOF cut slightly changes. Even though, 2.5 ns TOF cut criteria in Eq. (5.31) is wide enough and the efficiency of TOF cut is close to 100 %.

The efficiency distribution is well fit by a function:

$$\epsilon_{tof} = 1.0 - P_0 - P_1 E_{core} - P_2 E_{core}^2 - P_3 \exp(-P_4 E_{core}), \quad (5.32)$$

where,

$$P_0 = 3.6 \times 10^{-4} \pm 3.7 \times 10^{-4},$$

$$P_1 = -6.6 \times 10^{-4} \pm 8.4 \times 10^{-4},$$

$$P_2 = 3.9 \times 10^{-4} \pm 4.5 \times 10^{-4},$$

$$P_3 = 3.47 \times 10^{-2} \pm 0.92 \times 10^{-2},$$

$$\text{and } P_4 = 12.4 \pm 1.8.$$

For example, the efficiencies and propagated errors for 1 and 2 GeV photons are, 99.99 ± 0.10 % and 99.94 ± 0.25 %, respectively.

5.5.8 Shower Shape Parameter Cut

To identify clusters induced by photons, clusters are compared to the known photon cluster shape. For the electron, the cluster shape how the energy spreads in several towers are known by electron beam results and Monte Carlo simulations. Although there were no test results for photons, from the Monte Carlo simulations, the shower shape is known to be the same as electron except for that the photon shower starts at a few mm (\sim one radiation length) from the EMCAL surface. This difference between photons and electrons causes a small difference in the energy scale (~ 2 %) because of smaller attenuation in the WLS fiber for photons, and the correction was performed.

From the values (E, x_c, y_c) , the predicted energy distribution is calculated from the parametrization using the test beam results. To evaluate how the experimentally measured shower shape is close to the electromagnetic shower, δ^2 was defined by the same function as Eq. (5.20).

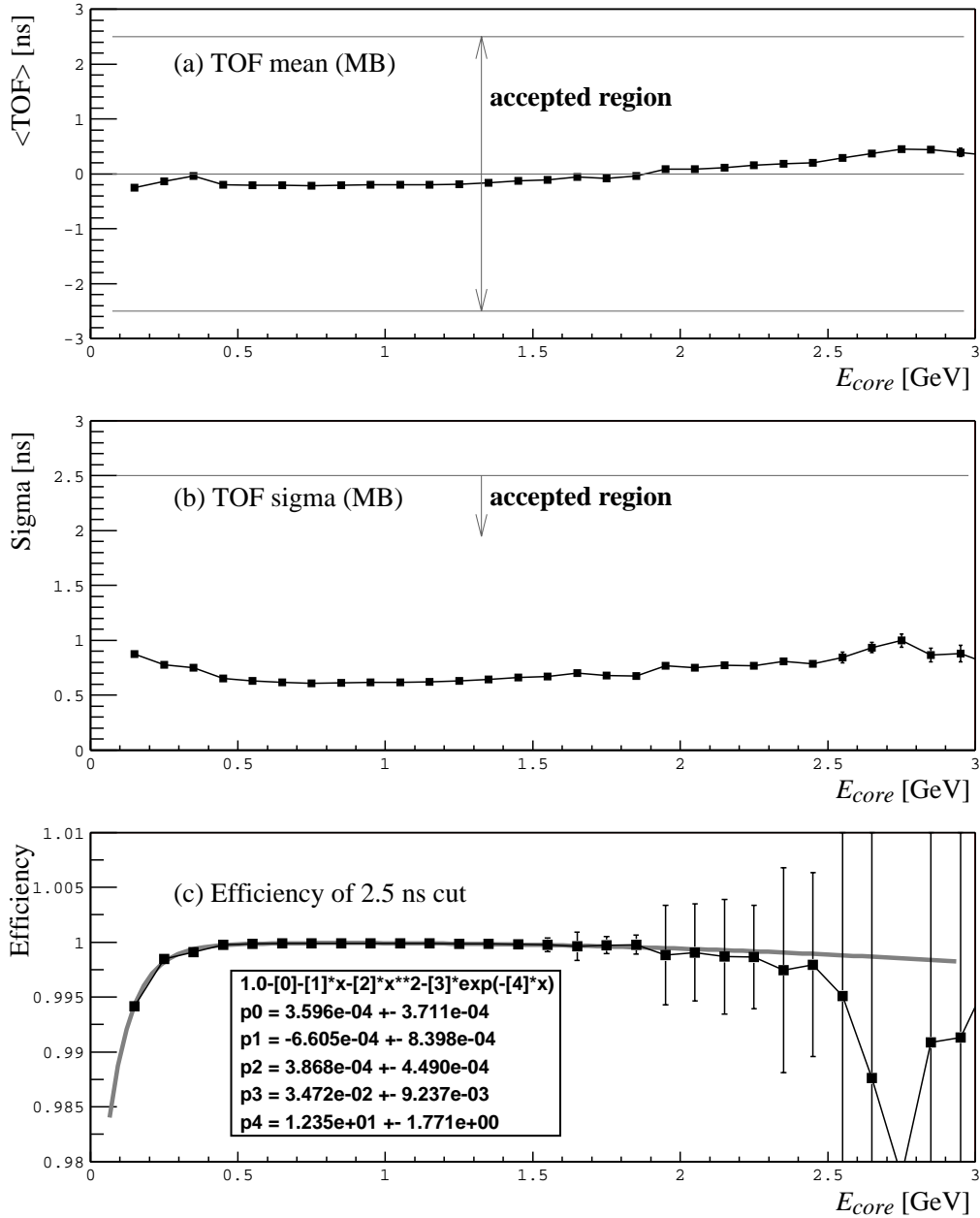


Figure 5.22: (a) shows the peak position of TOF prompt peak obtained by fittings. (b) shows the peak width of TOF prompt peak also obtained by fittings. (c) shows the efficiency of ± 2.5 ns cut calculated from (a) and (b).

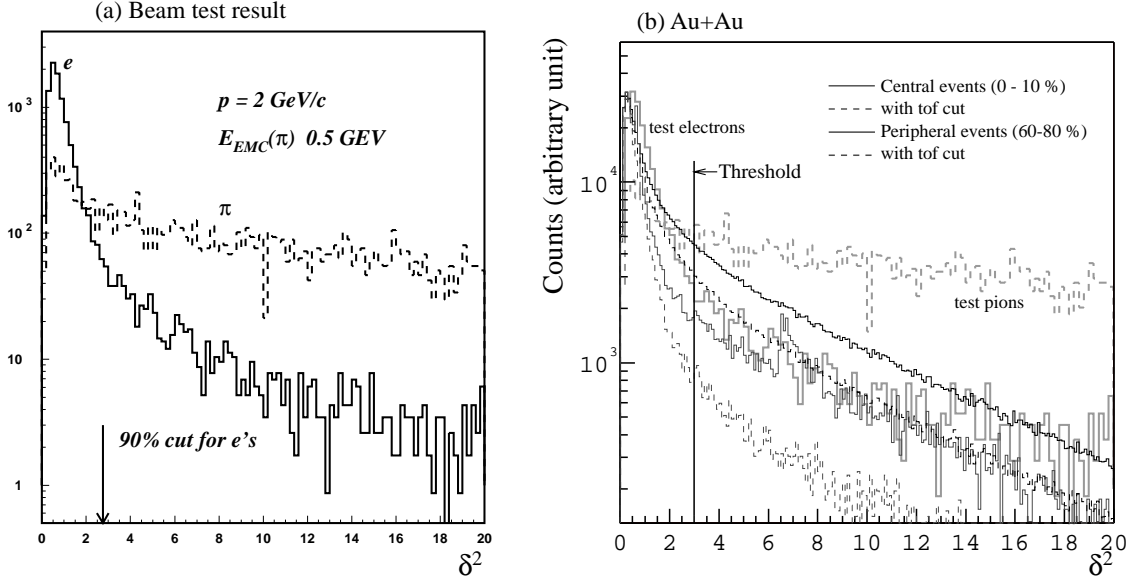


Figure 5.23: δ^2 distribution of EMCal clusters for photon candidates measured in test beam (a) and real events (b).

The variance σ_i is parametrized as the function of predicted energy E_i^{pred} in a specific tower, shower total energy, and the impact angle α of the tower. It is expressed by

$$\sigma_i^2 = \sigma_C^2 E_i^{pred} \left(1 + k \sqrt{E_{tot}} \sin^4 \alpha \right) \left(1 - \frac{E_i^{pred}}{E_{tot}} \right) + q_0^2 + q_1^2 E_{tot}^2, \quad (5.33)$$

where E_{tot} is the shower total energy expressed by Eq.(5.18), the constant $\sigma_C^2 = 0.03 \text{ GeV}^2$ is the scale for energy fluctuations in the shower measured from the test beam data, and the factor $(1 - E_i^{pred}/E_{tot})$ introduces the correlations between energies in the towers while keeping the covariance matrix diagonal. The parametrization for energy and impact angle dependence of the errors $k\sqrt{E_{tot}}\sin^4\alpha$ was chosen to fit test beam data where $k = 4.0/0.03 \sim 133$. Also constant coefficients q_0 and q_1 account for electronics noise; $q_0 \sim 5 \text{ MeV}$ and $q_1 \sim 0.0014$. For example, for the 1 GeV photon with perpendicular hit on the EMCal, if the hit position of the photon is the center of a tower and the predicted energy deposit on the central tower is $\sim 840 \text{ MeV}$ and this energy fluctuates with the variance $\sigma_i = 64 \text{ MeV}$ and $\sigma_i/E_i = 7.6 \%$.

The δ^2 characterizes how “electromagnetic” a particular shower is and it can be used to discriminate against hadrons and muons. The δ^2 distributions for 2 GeV/c electrons and charged pions (minimum ionization particle) are shown in Figure 5.23 (a). The arrow marks the $\delta^2 < 3.0$ cut corresponding to 90 % electron efficiency. In the region limited by $\delta^2 < 3.0$, the expected e/π ratio is more than 5 for 2 GeV/c electrons and pions.

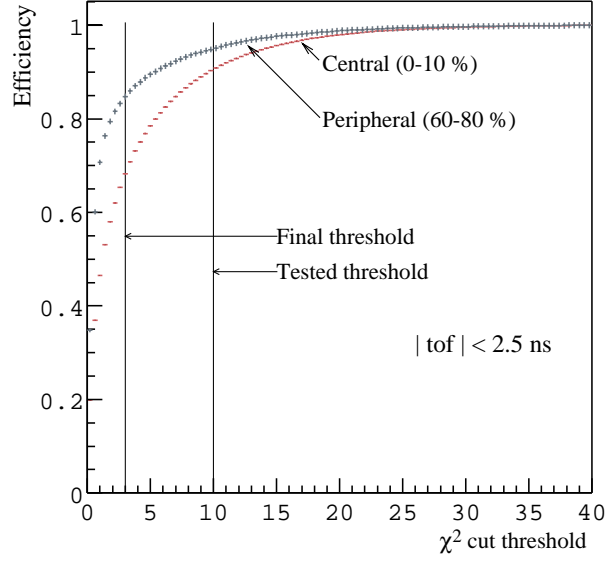


Figure 5.24: δ^2 cut threshold v.s. number of survived clusters. Horizontal axis is the upper limit of δ^2 and vertical axis is fraction of clusters included in the upper limit of δ^2 . Non-photon clusters are included.

For the high particle multiplicity environment, the δ^2 distribution of the electrons will become worse by the overlapping effects. Figure 5.23(b) shows the δ^2 distribution measured in real events. The shape of δ^2 distribution in the central Au+Au collision has longer tail at the high δ^2 because the showers in the central collision have strong effect of contamination. Even though, the 90% of showers are collected into $\delta^2 < 3.0$ region. And the δ^2 cut is fixed to be

$$\delta^2 < 3.0. \quad (5.34)$$

δ^2 Cut Efficiency

From Figure 5.23, efficiency of the δ^2 cut defined by Eq. (5.34) obviously depends on centrality. Figure 5.24 shows the cluster survival ratio of the δ^2 cut. Since the plot includes all the clusters including non-electromagnetic clusters, the survival ratio at $\delta^2 < 3.0$ is worth than 90 %. In the central, only 67 % showers remain. The true cut efficiency for the electromagnetic particle in central collision is probably between 67 and 90 %.

The only way to estimate the cut efficiency in the real condition is to measure the number of π^0 under various cut conditions because π^0 peak reconstructed from two clusters have no secondary contaminations. (The method of π^0 counting is explained in later section.)

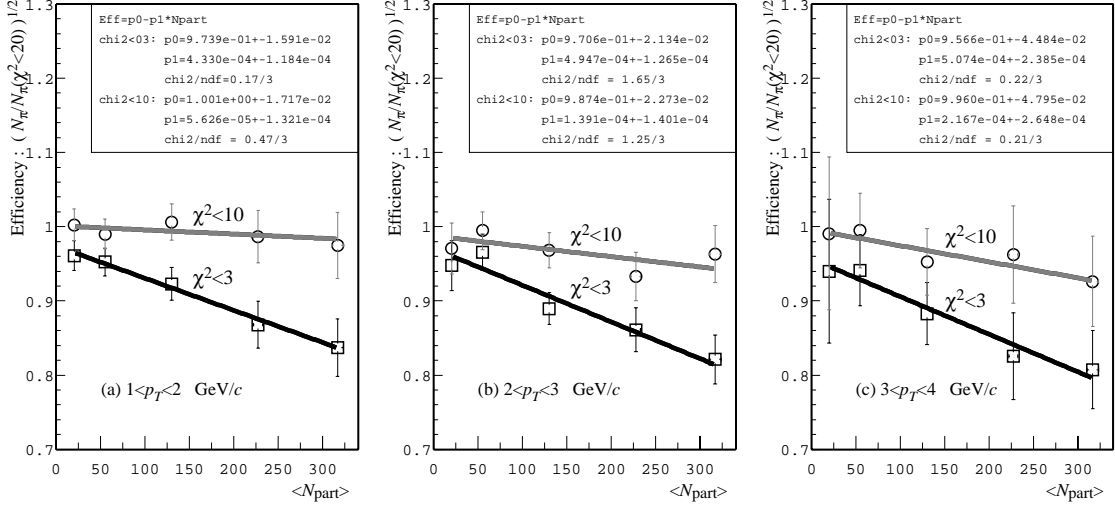


Figure 5.25: δ^2 cut efficiency calculated from number of π^0 . Square root of ratio of number of π^0 with δ^2 cut and without δ^2 cut was defined as the efficiency here.

As shown in Figure 5.25 Three δ^2 cuts (i) $\delta^2 < 3.0$, (ii) $\delta^2 < 10.0$, and (iii) $\delta^2 < 20.0$ are applied and the ratios of the number of π^0 are calculated for five centrality bins and three p_T bins. The ratios are plotted as functions of $\langle N_{\text{part}} \rangle$. A dependence is seen on $\langle N_{\text{part}} \rangle$. This dependence explains how the particle multiplicity effects the shower shape. No significant p_T dependence is observed.

The $\langle N_{\text{part}} \rangle$ dependent δ^2 cut efficiency are fitted by linear functions of $\langle N_{\text{part}} \rangle$, and expressed by

$$\sqrt{\frac{N_{\pi^0}^{(i)}(\langle N_{\text{part}} \rangle)}{N_{\pi^0}^{(iii)}(\langle N_{\text{part}} \rangle)}} = A - B \cdot \langle N_{\text{part}} \rangle, \quad (5.35)$$

where A and B are fit parameters and results are shown in Figure 5.25. The efficiency of δ^2 cut of Eq. (5.34) is then parameterized by

$$A = 0.97 \pm 0.016,$$

$$\text{and } B = (4.33 \pm 1.18) \times 10^{-4}.$$

These are values from Figure 5.25(a) corresponds to fit for $1 < p_T < 2$ region. Fit results on other regions are consistent within error bars. Corresponding systematic error for the efficiency derived from uncertainties in A and B is less than $\sim 4.8\%$.

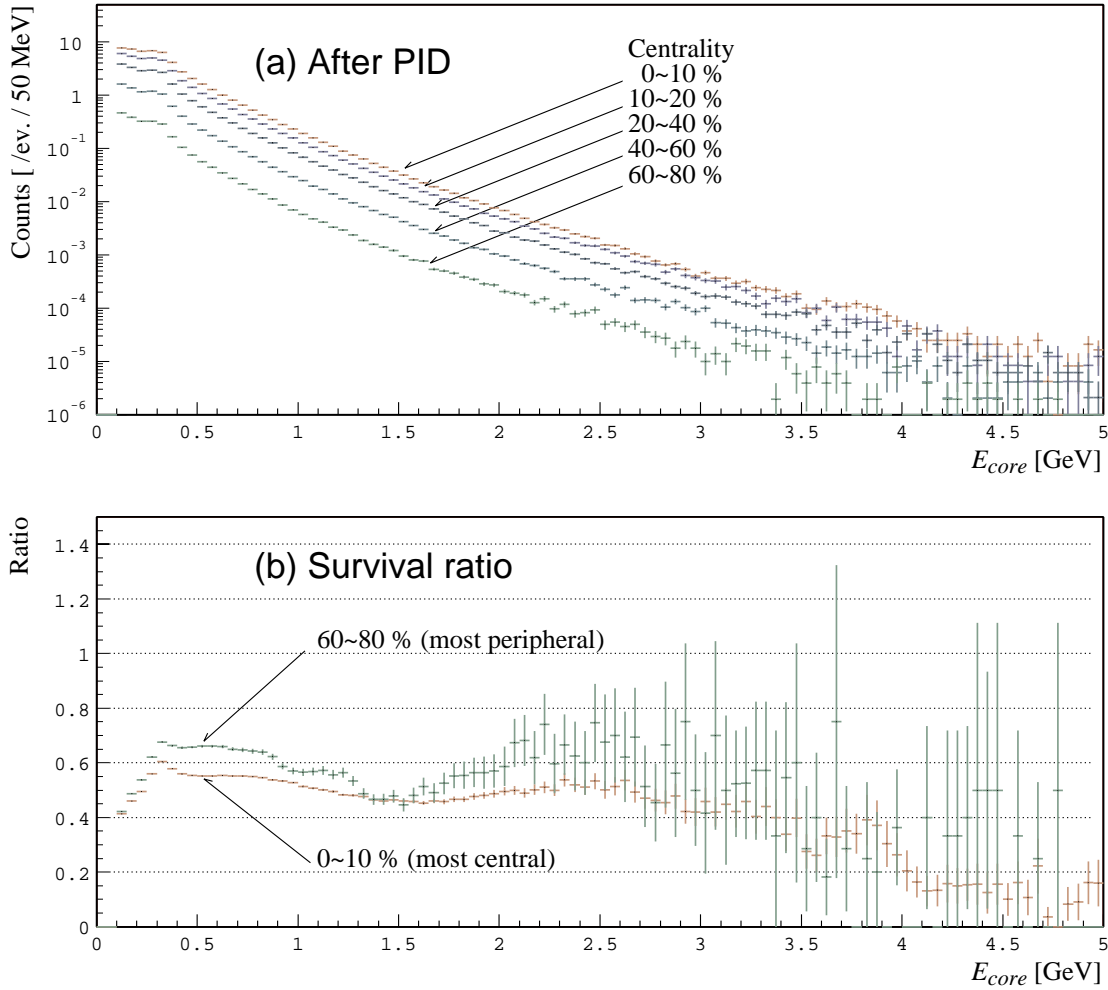


Figure 5.26: E_{core} distributions of the selected clusters.

5.5.9 Summary of γ PID

As for the γ PID, the timing selection of $|t| < 2.5$ ns and shower shape cut $\delta^2 < 3.0$ were applied. According to the simulation, the γ purity after the time of flight cut is better than 50 %. Efficiency of the timing cut is ~ 99 %. The δ^2 cut efficiency strongly depends on centrality. The dependence is checked by comparing π^0 yield among centralities. In the central events and peripheral events, the efficiency is 82 % and 92 %, respectively.

Figure 5.26(a) shows the E_{core} distributions of selected clusters. Figure 5.26(b) shows the ratio of number of clusters after PID divided by the number before PID shown in Figure 5.16. Only results of most central and peripheral event class are plotted. The bump at $1 < E_{core} < 2$ GeV probably shows that anti-neutrons or anti-protons are rejected. A small peak at $E_{core} \sim 0.3$ GeV means some of minimum ionization particle

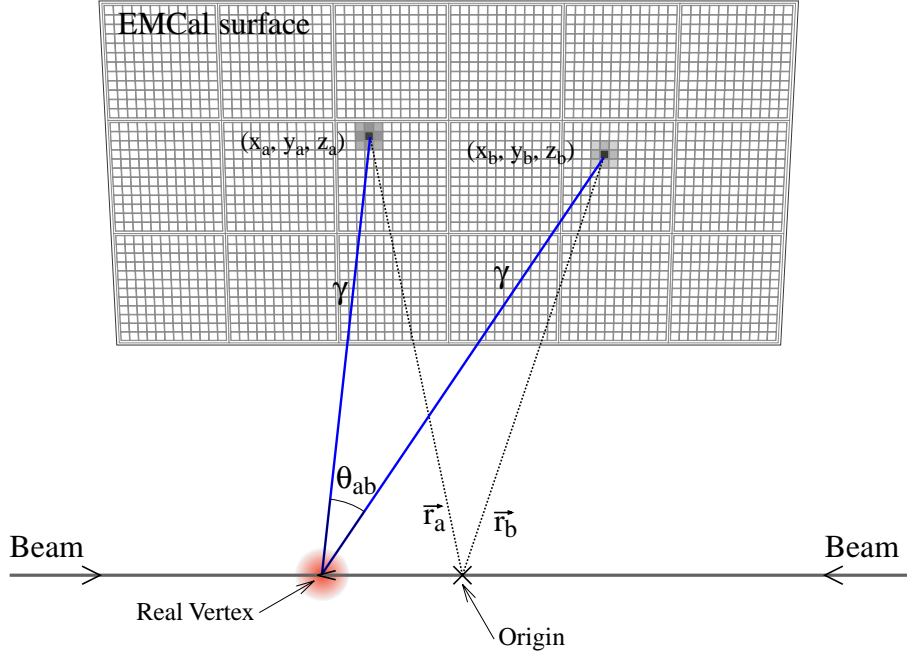


Figure 5.27: Schematic of π^0 reconstruction method.

could not be removed. In the central events, the mean reduction factor is $\sim 55\%$, and it corresponds to $\sim 70\%$ reduction of background in invariant mass spectra. All the clusters shown in Figure 5.26(a) are used to reconstruct π^0 as discussed from the next section.

5.6 π^0 Reconstruction

5.6.1 Invariant Mass and p_T of Photon Pair

The invariant mass of two γ 's is calculated by

$$m_{ab} = \sqrt{2E_a E_b (1 - \cos \theta_{ab})}, \quad (5.36)$$

where E_a and E_b are the energy of two γ 's, and θ_{ab} is the opening angle of two γ 's. The energy of each photon is measured by EMCal clustering and the corrected E_{core} discussed in Section 5.5.4 is used.

Figure 5.27 shows how π^0 's are reconstructed. The opening angle θ_{ab} is calculated by an internal product of two photon tracks:

$$\cos \theta_{ab} = \frac{(\mathbf{r}_a - \mathbf{V}) \cdot (\mathbf{r}_b - \mathbf{V})}{|\mathbf{r}_a - \mathbf{V}| |\mathbf{r}_b - \mathbf{V}|}, \quad (5.37)$$

where the vectors \mathbf{r}_a and \mathbf{r}_b are the corrected impact positions of two γ 's on the EMCal surface, and the vector \mathbf{V} is the collision vertex position measured by the BBC's. The \mathbf{r}_a and \mathbf{r}_b are calculated by translating the impact position on EMCal given by Eq. (5.23) which is represented in EMCal local coordinates system to the PHENIX global coordinates system. Since there are no γ tracking system in the PHENIX, it is impossible to get rid of photons with non-vertex origin. Then, it was assumed that every clusters of the EMCal identified as photon are from collision vertex. It was estimated with the Monte Carlo simulation that $\sim 10\%$ of non-vertex photons hit the EMCal. Such background effects are described in later sections. Also the life time of π^0 , $c\tau \sim 25.1$ nm can be neglected. Simultaneously, the momentum of two γ 's is reconstructed by

$$\mathbf{p}_{ab} = E_a \cdot \frac{\mathbf{r}_a}{|\mathbf{r}_a|} + E_b \cdot \frac{\mathbf{r}_b}{|\mathbf{r}_b|}. \quad (5.38)$$

Also transverse momentum p_T of the pair corresponds to transverse component of \mathbf{p}_{ab} .

Invariant mass and p_T are calculated for all the combinations of any two clusters in the events. If cluster multiplicity in one event is N , up to $N(N-1)/2$ pairs are calculated in one events. For entire events, the same calculations are performed and invariant mass distribution are made for each centrality. Only the combination of two γ 's from π^0 contribute the peak of π^0 in invariant mass distribution at $m_{ab} \sim 135$ MeV/ c^2 . Other fake combinations make combinatorial background. The solid line in Figure 5.28(a) shows the example of invariant mass distribution for some centralities. In the most peripheral events, clear π^0 peak is seen at $m_{ab} \sim 135$ MeV/ c^2 . The signal to noise ratio getting worth according to the centrality. In the most central events, it looks there is no π^0 peak. The subtraction of background from the invariant mass distribution is then necessary.

5.6.2 Combinatorial Background Calculation by Event Mixing

In the central events, the particle multiplicity is high and ~ 100 clusters are in each event. The number of possible combination of two γ 's reaches to $\sim 10^4$. This fact causes extremely huge combinatorial background in invariant mass spectra and real π^0 peak is almost hidden in the combinatorial background. The shape of combinatorial background is estimated by event mixing method and π^0 peak can be extracted even in the central events. The procedures of event mixing method and peak extraction are as following.

- (i) Select two different events X and Y with a criteria:

$$|M_X - M_Y| < 25, \quad (5.39)$$

where $M_X(M_Y)$ is the cluster multiplicity in the event $X(Y)$.

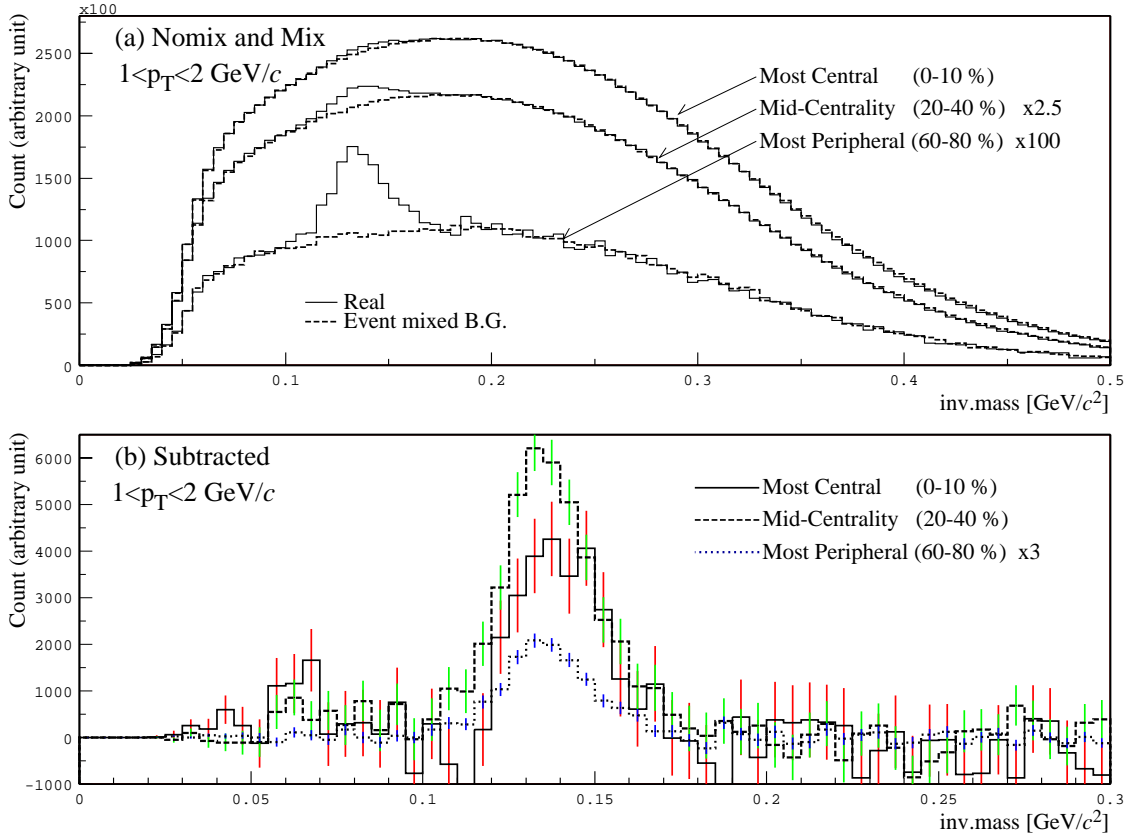


Figure 5.28: Typical Invariant mass spectra of $\gamma - \gamma$ combinations. (a) shows m_{ab} distributions for the most central events, mid-central events, and the most peripheral events. Solid lines are result of invariant mass calculation in the same event. Dashed lines are estimated background shape by the event mixing method. Background shapes are scaled arbitrary. (b) shows spectra after subtracting background from real distribution.

- (ii) Calculate invariant mass using i 'th cluster in the event X and j 'th cluster in the event Y . Calculation is performed for all possible combination of i and j . $M_X \times M_Y$ calculations are done and invariant mass histogram is made.
- (iii) The selections of events X and Y are repeated until enough statistics is obtained.
- (iv) Since the obtained invariant mass spectrum has different magnitude than real spectrum, the event-mixed spectrum is normalized by the sufficient normalization factor (see below).
- (iv) Subtract the normalized event-mixed spectrum from the real spectrum. If the event mixing method reproduces the shape of background in the real event and

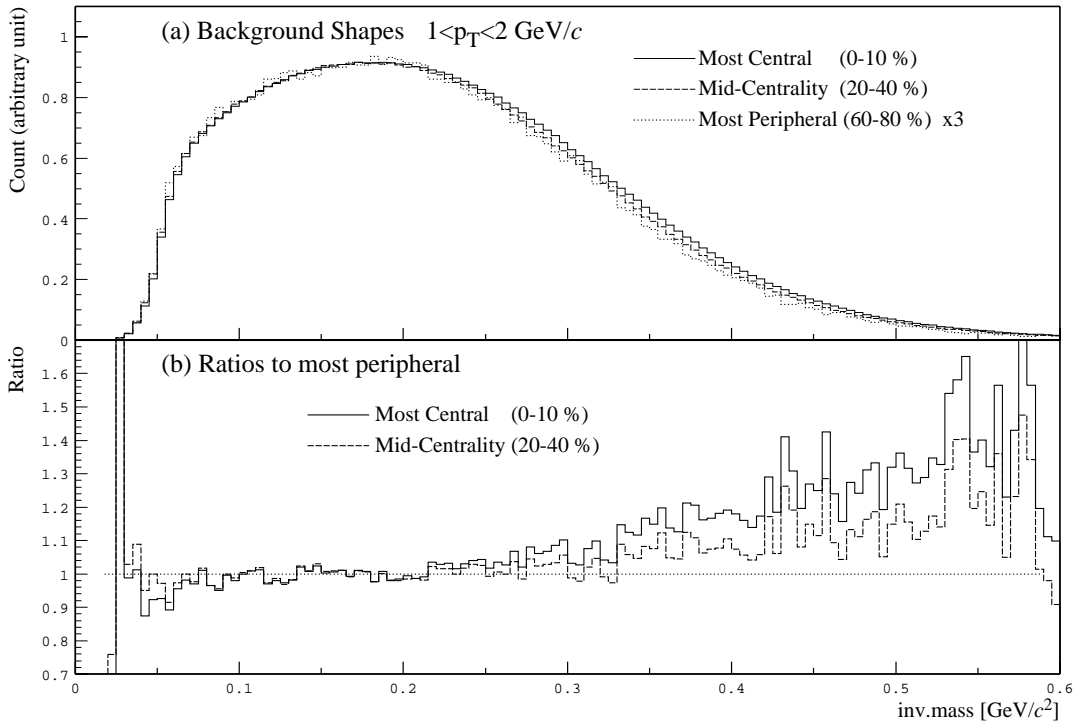


Figure 5.29: (a) The combinatorial background shapes for three centrality classes from the most central to the most peripheral events. Three shapes are arbitrary scaled as contents between 0.15 to 0.2 MeV/c² are same. (b) Ratio of the most central and mid-central events divided by the most peripheral events.

normalization is done correctly, only the π^0 peak remains.

The reproduced background is plotted in Figure 5.28(a) as dashed lines. As shown in Figure 5.28(b), the event mixing method works well.

The background shape is compared for different centralities. Figure 5.29 shows the shapes of background spectra in three centrality selections. The central events produces spectrum shifted slightly higher invariant mass than the peripheral events due to high particle multiplicity. This is the reason why the criteria Eq. (5.39) is used.

The normalization to the event-mixed spectra are done so that the number of entries around the expected π^0 peak become equal between event-mixed and real spectra.

Furthermore, to enrich the π^0 in the invariant mass distribution, the cut criteria of energy asymmetry and opening angle are applied while invariant mass calculation. Those are explained below.

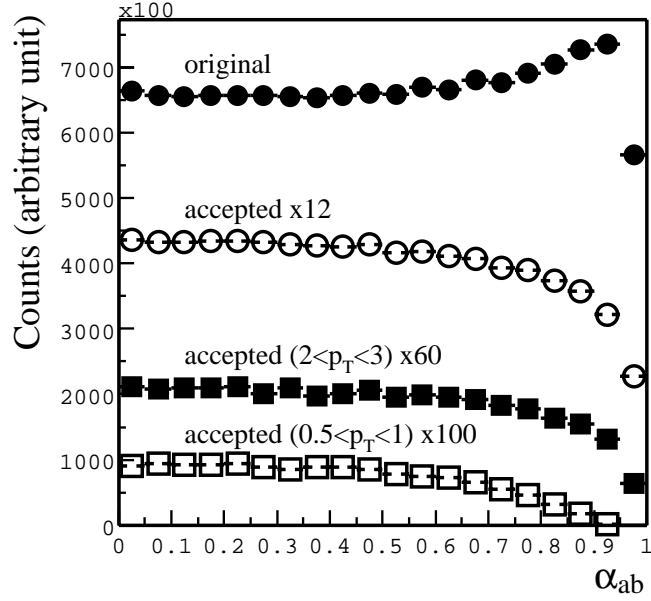


Figure 5.30: Asymmetry distributions of two γ 's obtained by simulation. The original distribution (solid circles) shows the α_{ab} distribution of two γ 's originated from π^0 without rejecting γ 's outside detector acceptance. Others show the α_{ab} distribution after rejecting γ 's outside detector acceptance, without momentum cut (open circles), with momentum cut for π^0 's (solid boxes and open boxes).

5.6.3 Asymmetry Cut

The energy asymmetry factor is defined by

$$\alpha_{ab} \equiv \left| \frac{E_a - E_b}{E_a + E_b} \right|. \quad (5.40)$$

Figure 5.30 shows the distribution of α_{ab} obtained by the simulation. Only γ 's from π^0 contributed to the plot. Since the π^0 decays isotropically in its rest frame, its asymmetry distribution is almost flat.

Figure 5.31 shows the distribution of α_{ab} of the real data. Asymmetry distribution has broad peak by the minimum ionization particles for low p_T sample and strong peak near $\alpha_{ab} = 1$. The latter is made by broken or mis-identified small energy clusters. Software gate for the α_{ab} was set to be

$$\alpha_{ab} < 0.8. \quad (5.41)$$

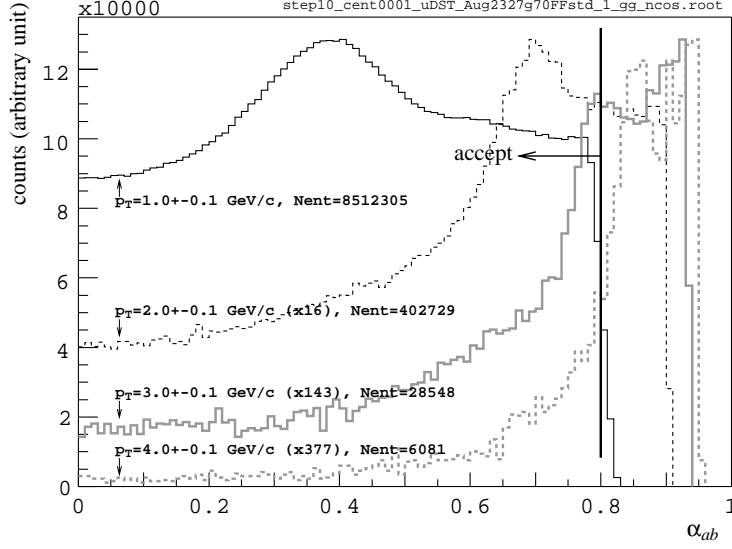


Figure 5.31: Asymmetry distributions of inclusive γ pairs in several p_T regions, 1.0 ± 0.1 (black solid line), 2.0 ± 0.1 (black dashed line), 3.0 ± 0.1 (gray solid line) and 4.0 ± 0.1 GeV/c (gray dashed line). Plots except for 1.0 ± 0.1 GeV/c are scaled as each plot has the same height with plot for 1.0 ± 0.1 .

5.6.4 Opening Angle Cut

As shown in previous sections, the randomly picked up pair of photon candidates form big combinatorial background but the shape of the background is reproduced by the event mixing method. But, as shown in two plots in upper half of Figure 5.32, the background shape calculated by event mixing method can not reproduce the shape of real combinatorial background in the low invariant mass region (≤ 50 MeV/ c^2).

The discrepancy at low mass region is made by small opening angle pairs of clusters. The opening angle θ_{ab} of two γ 's decayed from a true π^0 with mass of m_π is expressed using energy E_π and energy asymmetry α_{ab} by

$$\cos \theta_{ab} = 1 - 2 \cdot \frac{m_\pi^2}{E_\pi^2} \cdot \frac{1}{1 - \alpha_{ab}^2}. \quad (5.42)$$

For the completely asymmetric decay ($\alpha_{ab} = 0$), opening angle takes minimum:

$$\cos \theta_{min} = 1 - 2 \cdot \frac{m_\pi^2}{E_\pi^2}. \quad (5.43)$$

It is guessed that pairs with small opening angle contribute to this low mass region. If the clustering fails and a cluster is divided to two (or more numbers of) small cluster fragments, and if the invariant mass calculation is performed for such divided pair, the

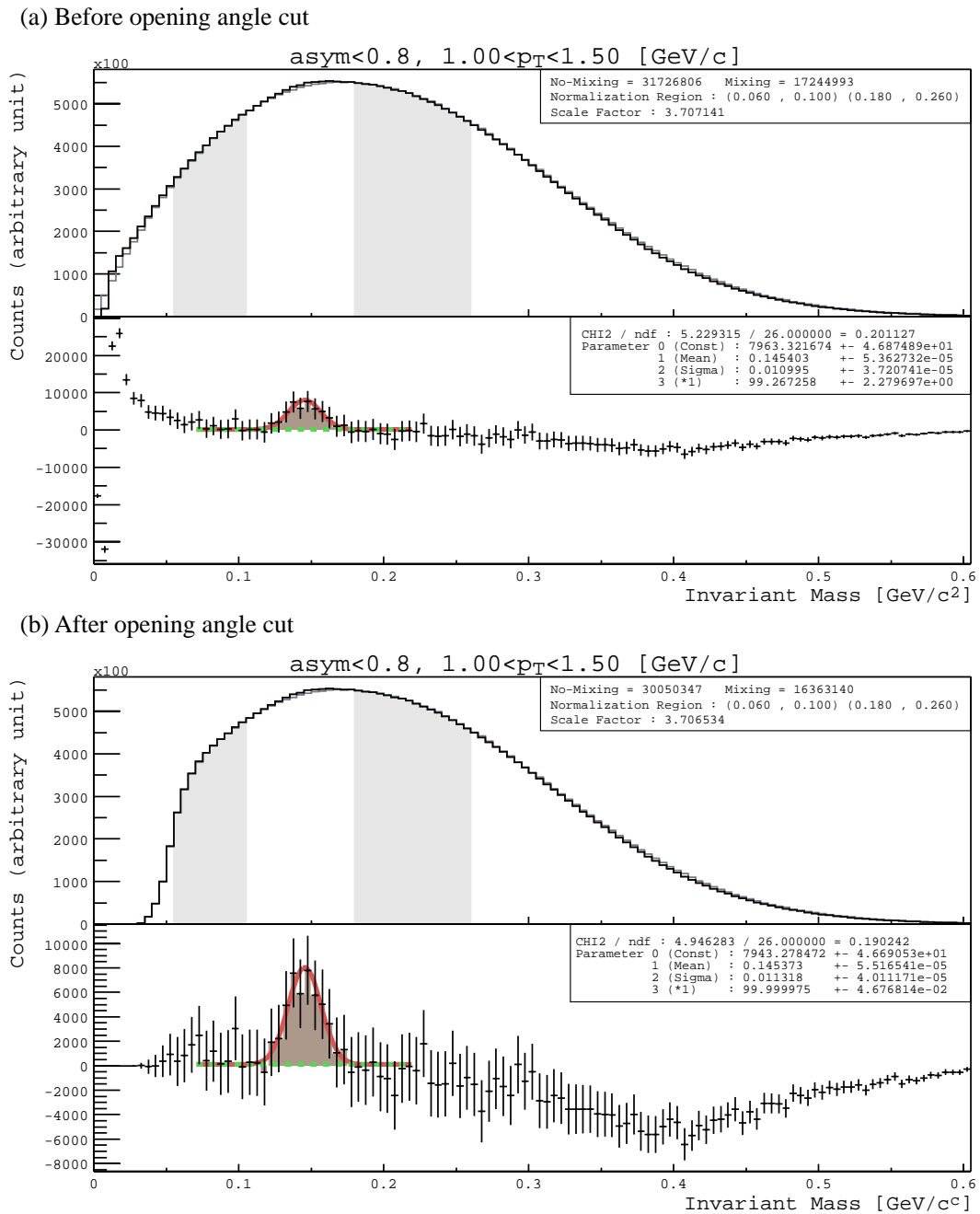


Figure 5.32: Before and after opening angle cut.

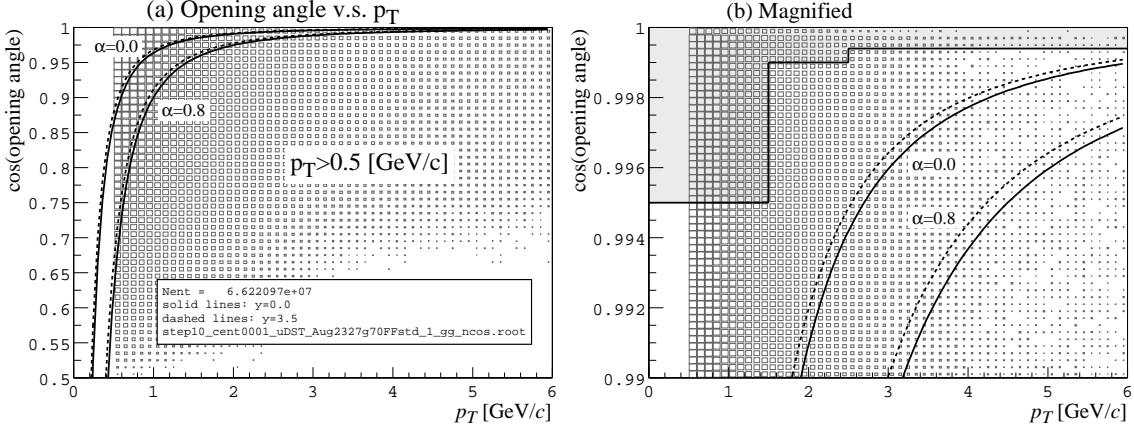


Figure 5.33: (a) shows p_T v.s. $\cos\theta_{ab}$ of 2γ combinations. (b) shows magnified figure of (a) at very small opening angle region ($\cos\theta_{ab} = 0.99 \sim 1.00$). Curves are opening angle calculated by Eq. (5.42) for two asymmetry parameters ($\alpha_{ab}=0.0$ or 0.8) and two rapidity parameters. Solid curves are for $y = 0.0$ and dashed curves are for 0.35 . A shaded area in the plot (b) represents rejected area by the opening angle cut.

invariant mass of them will be collected to low mass region. This correlation should be seen only while performing invariant mass calculations for randomly selected two clusters in an event. If invariant mass calculations are performed for two clusters, one is selected from an event and the other is selected from an other event, there will be no correlation at low mass region.

Another possible contribution to low invariant mass region is very high energy π^0 decay. For example, the calculated minimum opening angle for 10 GeV π^0 's is 1.6 degrees, and its corresponds to 14 cm distance at EMCal surface. Since the typical shower radius generated by photon in hit on EMCal is 6 cm, the showers of decayed two γ 's will overlap and disturb their measured energy each other if the π^0 energy is large enough. In the current analysis, this effect is negligible because the observed π^0 energy is less than 4 GeV.

To achieve rejection of such discrepancy due to correlation by cluster breakup, the opening angle cut for combinations of two γ 's are applied. To perform the opening angle cut safely without losing the π^0 , the threshold lower than minimum opening angle $\theta_{min}(E_\pi)$ was chosen as

$$\cos\theta < \begin{cases} 0.9950 & \text{if } p_T < 1.5 \text{ GeV}/c \\ 0.9990 & \text{if } p_T = 1.5 \sim 2.5 \text{ GeV}/c \\ 0.9994 & \text{if } p_T > 2.5 \text{ GeV}/c, \end{cases} \quad (5.44)$$

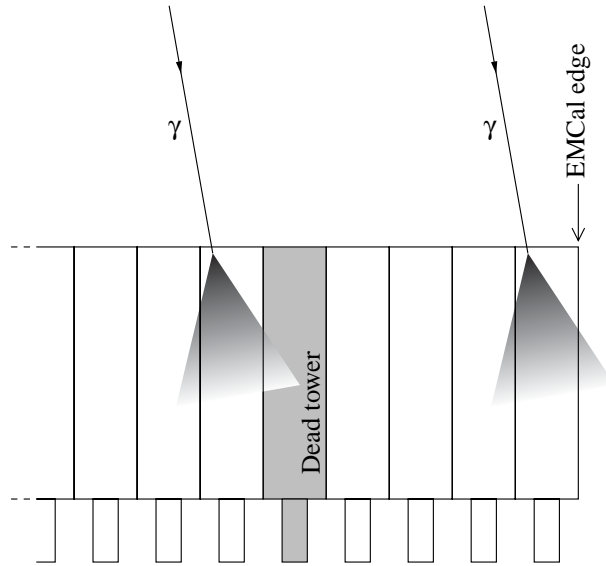


Figure 5.34: A schematic of idea of fiducial volume calculation.

where $p_T = \sqrt{E_\pi^2 - m_\pi^2 - p_{z\pi}^2}$ is measured transverse momentum of π^0 . Figure 5.33 shows the scatter plot of p_T and $\cos\theta$. The solid lines represent the upper limit of $\cos(\theta_{ab})$ expressed by Eq.(5.44). The curves show the minimum opening angle for several rapidity and asymmetry of π^0 . The black dashed curve ($y=3.5$ and $\alpha_{ab} = 0.0$) shows the kinematical limit of the PHENIX aperture, and any two γ 's originated from π^0 have less θ_{ab} value than this line and the cut by Eq. (5.44) does not have inefficiency of π^0 which have p_T less than 5 GeV/c .

Lower two plots in Figure 5.32 shows the invariant mass distribution after opening angle cut described above. By the opening angle cut, the low mass events are cut out well. In the Figure 5.32, the number of π^0 's before and after opening angle cut is $43,700 \pm 8,900$ and $44,600 \pm 8,900$, respectively, and these are consistent within statistical error.

Since the reconstructed π^0 in this thesis has less than 5 GeV/c transverse momentum, the true γ 's pair from π^0 is not dropped by this opening angle cut. Neither efficiency nor systematic error estimation is required.

5.6.5 Fiducial Area Cut

As schematically shown in Figure 5.34, if an electromagnetic particle hits somewhere in a tower at edge of the EMCal sector, the shower energy leak outside the EMCal and measured energy of the shower is smaller than real energy. Also the same effect happens around dead towers where the energy and position measurement are not possible.

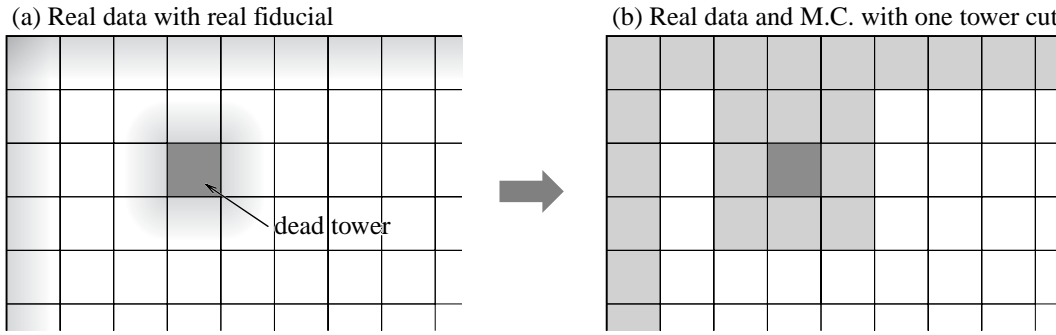


Figure 5.35: A schematic of one tower rejection. (a) is an imaginary picture of real fiducial. There is insensitive area around dead tower and edge of calorimeter. (b) shows that all the marginal regions are removed if towers surrounding dead tower or towers at edge are rejected.

The fiducial area of EMCal is, therefore, smaller than the area calculated by simply subtracting dead tower area from total area $4 \times 2 \text{ m}^2$.

As shown in Figure 5.35 (a), the border width of insensitive area around bad tower (or from edge) is unknown. But it is not bigger than one tower because only neighboring towers contribute to the E_{core} calculation as shown in previous sections. “One tower rejection” method was introduced. As shown in Figure 5.35 (b), the towers at edge of EMCal and all neighboring towers of dead tower are also defined as non-fiducial area. If the impact position of cluster is in the non-fiducial area, the cluster is discarded.

After dead and edge tower cut, furthermore, fiducial towers are defined by criteria based on: (i) hit probability (probability that the cluster center is in the tower), (ii) fluctuation of hit probability, (iii) energy distribution, and (iv) fluctuation of mean energy distribution. The towers passed these four checks were defined to be the fiducial area. Figure 5.36(a) ~ (h) shows the tower inspection histograms correspond to four check methods. The $\pm 3\sigma$ cut criteria were applied in all checks and towers outside the $\pm 3\sigma$ thresholds were defined as non-fiducial area.

After one tower rejection and inspection of towers, the dead region map was made. Figure 5.37 shows the dead region map. The number of tower passed all selection criteria is 1,704 towers in sector 0 and 1,736 towers in sector 1. The fraction of this tower area relative to all EMCal surface is $(1,704+1,736)/5,184=66.4 \%$, and it is equal to single γ efficiency.

The π^0 efficiency is worse than single γ efficiency because daughter two γ 's of π^0 must be detected. Figure 5.38 shows the result of Monte Carlo calculation. The efficiency is between single γ efficiency (66.4 %) and square of single γ efficiency (44.0 %).

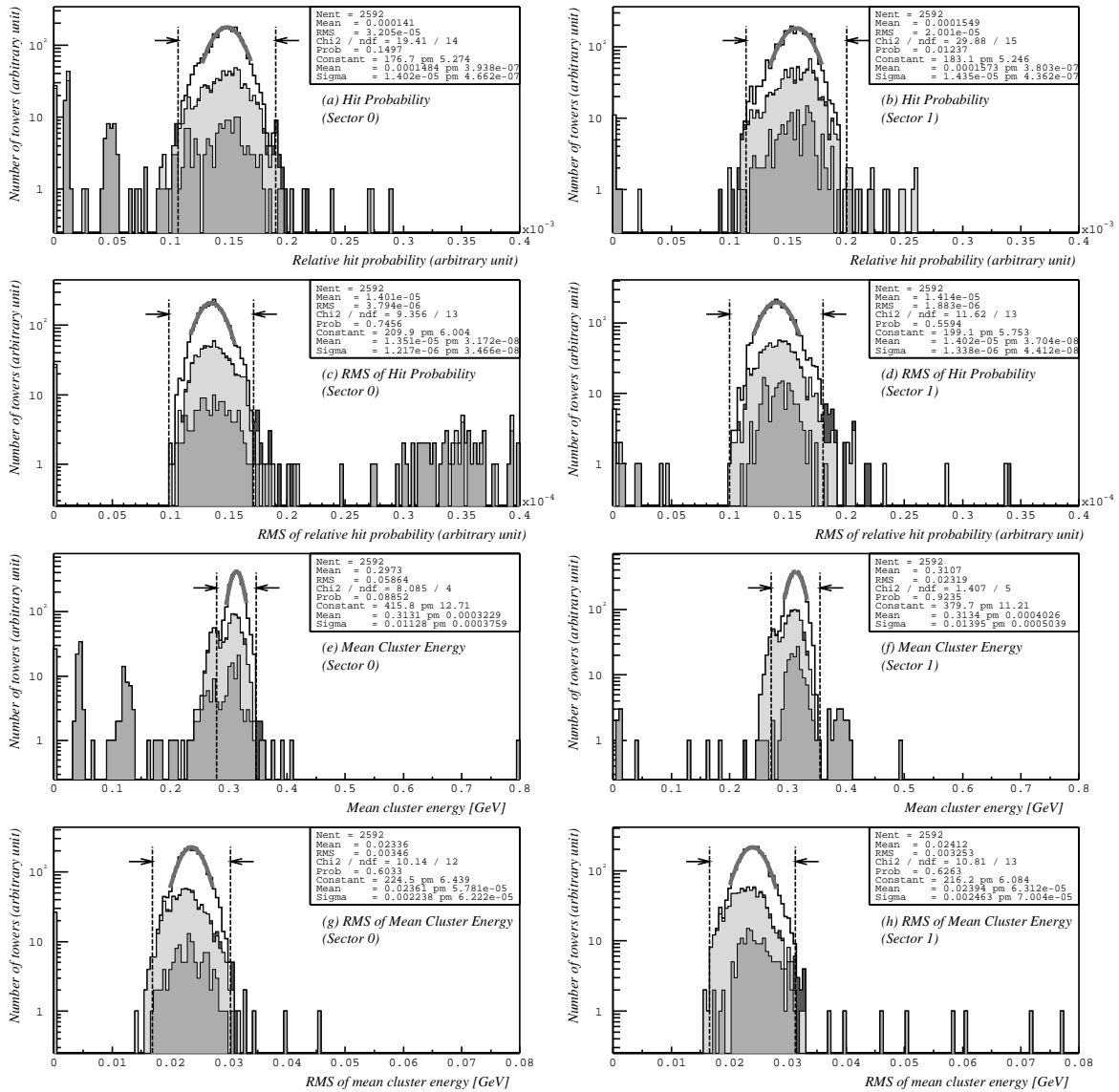


Figure 5.36: Tower inspection plots. Plots in left are plots of sector 0 and others are plots of sector 1. (a) and (b) are plot of hit probability. (c) and (d) are plots of RMS of hit probability. (e) and (f) are plots of mean energy distribution. (g) and (h) are plots of RMS of mean energy distribution. In all plots, non-colored histogram corresponds to all 2,592 towers. Filled histograms by gray, light-gray and dark-gray correspond to dead tower, around dead tower, and towers but by $\pm 3\sigma$ cut criteria, respectively.

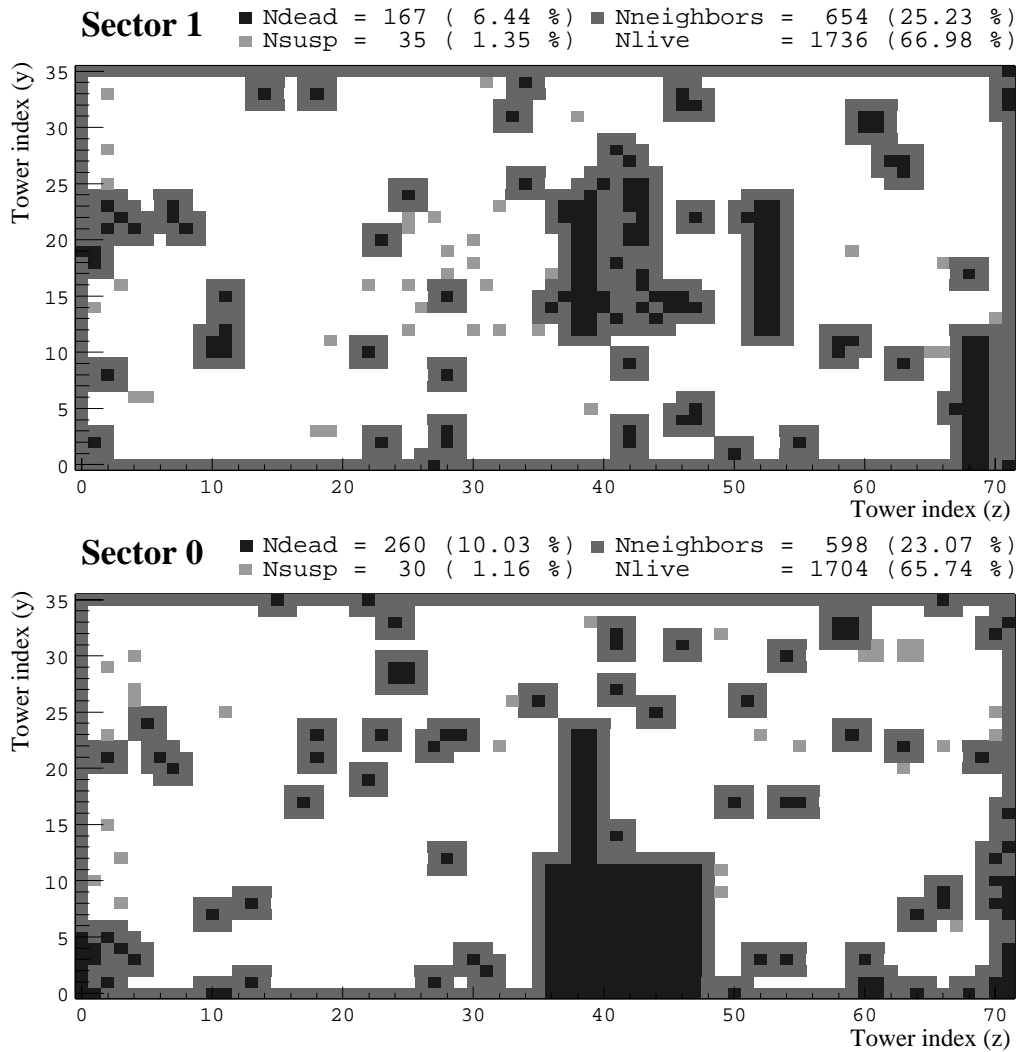


Figure 5.37: EMCal dead tower map. Black filled boxes are dead tower. Area filled by gray color is not dead towers but towers at the edge of sector or have dead tower as neighboring tower. The clusters in gray colored towers are rejected when “one tower rejection” is applied.

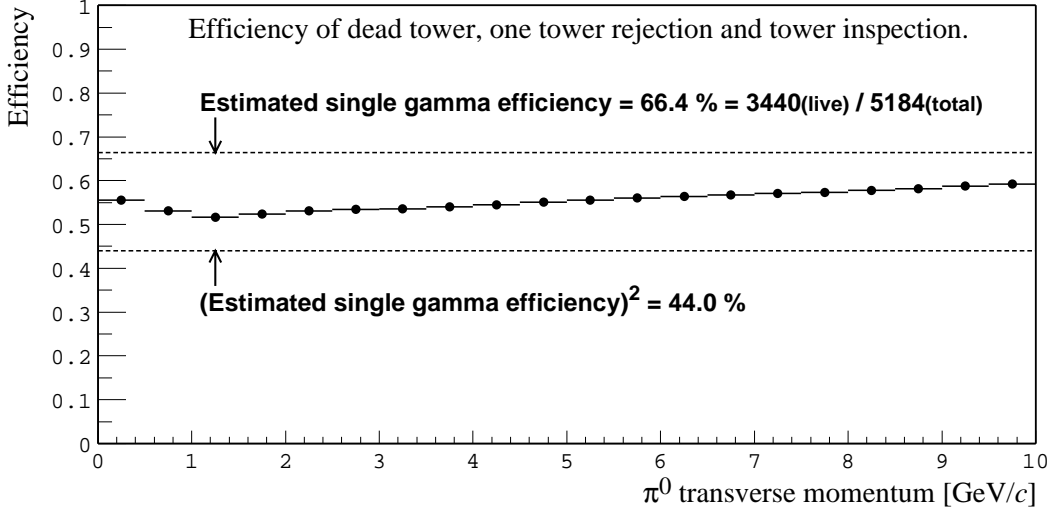


Figure 5.38: π^0 detection efficiency of fiducial area cut. The estimated efficiency calculated by number of live tower divided by total number of tower is 66.4 %. The calculated efficiency is between 66.4 % and $(66.4 \%)^2 = 44.0 \%$ because π^0 decays to two γ 's. And the efficiency asymptotically reaches 66.4 % at high p_T .

5.6.6 Counting π^0 's

With PID and cuts, and subtracting the background, a set of mass spectra for p_T bins are obtained for each centrality classes. Each mass spectrum has a peak corresponding to π^0 mass, and the number of π^0 's were calculated by fitting method and simple integration method.

Figure 5.39 shows the example of fitting for the central (left) and peripheral (right) events. The Gaussian function associated with a linear function:

$$F(m_{ab}) = NG_{m_0, \sigma}(m_{ab}) + n_0 + n_1 m_{ab}, \quad (5.45)$$

is used for fitting where m is the invariant mass, $G_{m_0, \sigma}$ is the normalized Gaussian function with mean m_0 and deviation σ , n_0 and n_1 are coefficients for associating linear function. The fitting mass region was typically 50 to 250 MeV/c^2 , and it was changed case-by-case to get stable fitting results.

If the calculated background shape by event mixing is perfectly simulating the real background shape, the subtracted mass distribution will be represented by a Gaussian shape and n_0 and n_1 will be zero. But there still remains small residues in the invariant spectrum even after background subtraction. One of the possible reason account for the residues are particle ($\pi^0 - \pi^0$ or $\gamma - \gamma$) correlation. But those are probably small factor.

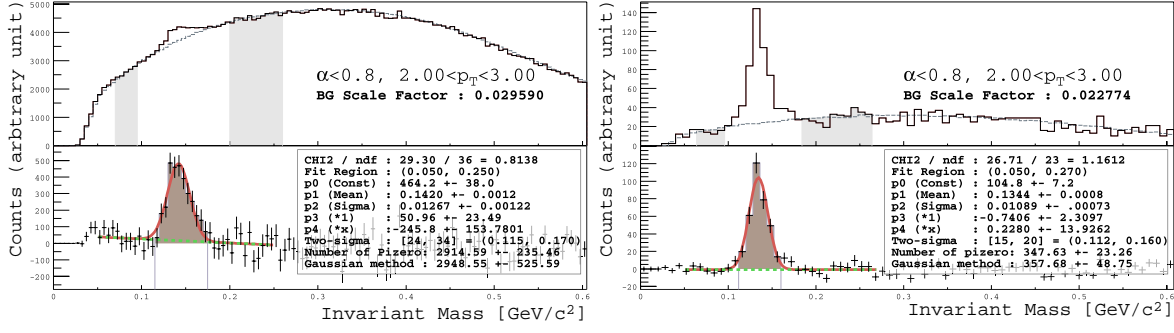


Figure 5.39: Example of counting π^0 's. The most central events (left) and peripheral events (right) are shown. Plots in top are the invariant mass distribution of 2γ 's in the same event (solid lines) and expected background shape by event mixing method (gray lines). The background shape was scaled so that the contents in the shaded regions is same for real distribution and event mixed distribution. Plots in bottom are after subtracting the background. Gaussian associated with linear function was used for fitting the peak and residual background.

The main factor of the difference is because the event characteristic, such as vertex position and particle multiplicity for two events (X) and (Y) used for event mixing are not same.

After fitting, the number of π^0 was estimated by following steps, (i) obtain actual bin contents N_{bin} in the window $m_0 - \sigma < m_{ab} < m_0 + \sigma$, (ii) obtain estimated residual background by integrating linear function in the same window, and (iii) subtract the residual background from N_{bin} .

The bin size of p_T is 0.5 GeV/c and it should be smaller than p_T resolution. The p_T resolution for π^0 is determined from the intrinsic energy and position resolution of EMCAL described in Section 3.4. Figure 5.40 shows the result of simulation using GEANT. p_T distributions of reconstructed π^0 's are plotted for 1 GeV/c (a) and 3 GeV/c (b) of original momentum of π^0 's. The calculated p_T resolution is 92 MeV/c and 165 MeV/c for 1 and 3 GeV/c π^0 's respectively. Both peaks have small tail in lower momentum region mainly due to the conversions in the materials. The effect of conversion loss is described in later Section 5.7.4.

The effect of finite p_T resolution causes contamination from different p_T region outside the certain p_T bin, and affect to the efficiency. This was simulated in the Monte Carlo when the efficiency is determined.

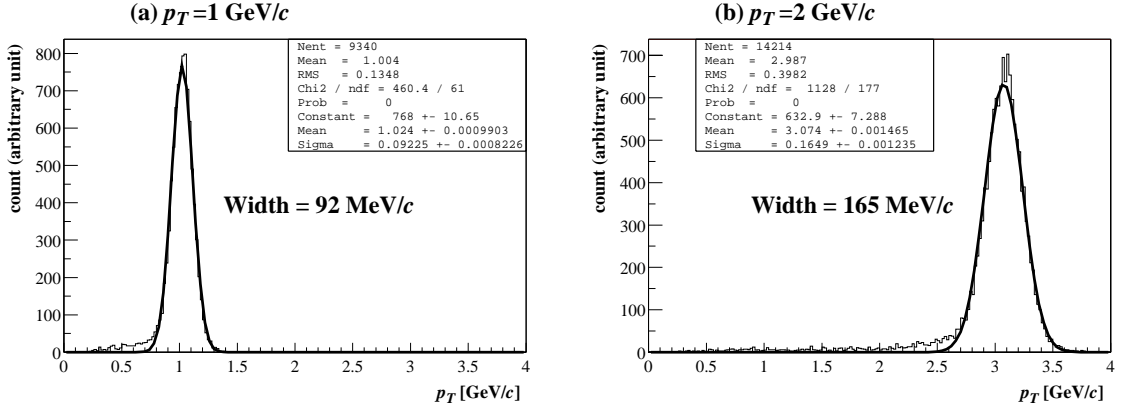


Figure 5.40: p_T resolution for π^0 's calculated by GEANT simulation. In (a) and (b), $p_T = 1.0$ GeV/ c and 3.0 GeV/ c π^0 's are simulated, and p_T resolutions of 92 MeV/ c and 165 MeV/ c were obtained, respectively. Peaks have tail in lower p_T region due to conversion.

Systematic Error in Counting

The Gaussian function associated with linear function was used to fit the π^0 peak. But the result of fitting and extracted number of π^0 depends on fitting methods. It always have to be considered as the systematic error in counting. The possible variations of method obtaining number of π^0 are, (i) using only Gaussian function for fitting function, (ii) using Gaussian associated with polynomial for fitting function, (iii) using different region to normalize event-mixed background, (iv) using different bin size, and (v) using different way of estimate number of π^0 after fitting. In method (v), it was attempted to get number of π^0 by only integrating the Gaussian function.

In any case above, the number of π^0 does not fluctuate more than 8 %, and it was considered as systematic error.

5.6.7 Energy Scale Correction Using π^0 Peaks

When the π^0 mass was reconstructed, the peak position of π^0 in the invariant mass spectrum should be 135 MeV/ c^2 if EMCAL is perfectly calibrated. In reality, the extracted mass came out more than 5 % too high relative to the known π^0 mass. With this peak position, the EMCAL energy scale is re-calibrated.

Figure 5.41 shows the measured π^0 peak position and width for various centrality regions. In spite of relatively large (~ 5 MeV/ c^2) fluctuations, the mass peak position is gradually increasing from the bottom (peripheral events) to top (central events) due

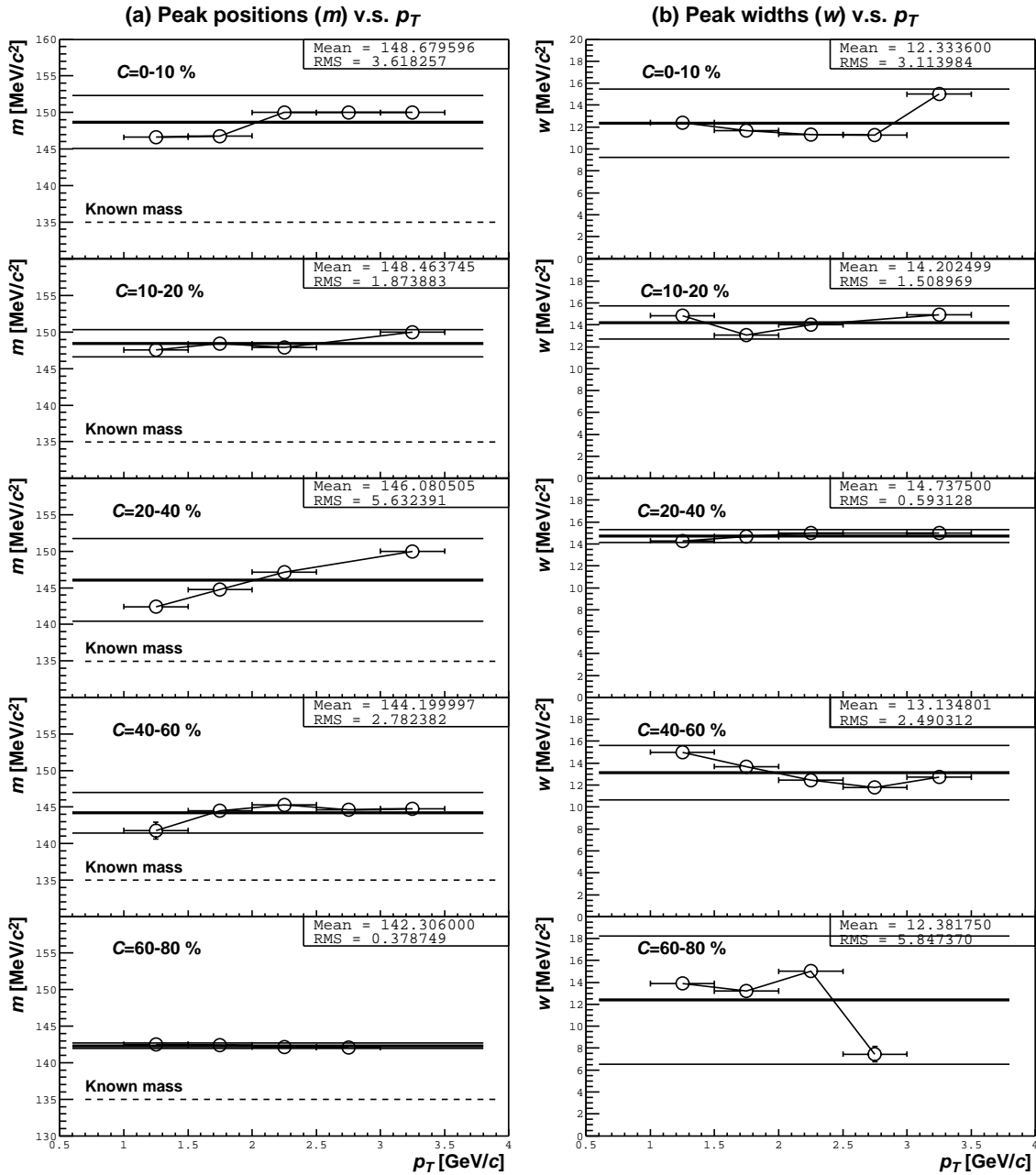


Figure 5.41: Measured π^0 peak position and width before the correction. Left figures are peak position v.s. transverse momentum. Right figures are peak width v.s. transverse momentum. The horizontal error bars are bin size. The vertical error bars (almost smaller than markers) are statistical error calculated while fitting π^0 peak in invariant mass spectrum of $\gamma - \gamma$ combinations.

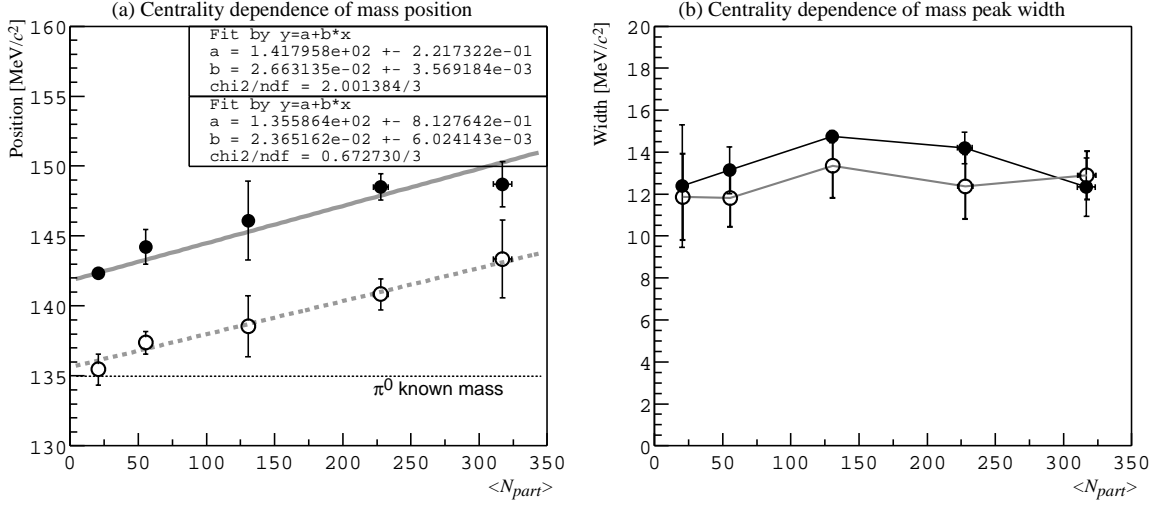


Figure 5.42: Centrality dependence of π^0 invariant mass peak position and width. (a) shows the mass peak position v.s. N_{part} . (b) shows the mass peak width v.s. N_{part} . In both (a) and (b), solid circles shows observed position or width before energy correction, and open circles shows observed position or width after correction. The horizontal error bars are systematic uncertainty of the N_{part} . The vertical error bars are RMS in mass and width distribution divided by square root of number of points shown in Figure 5.41. Fitting by linear function was applied for mass peak positions.

to overlapping effect. The peak width is stable between 12 and 16 MeV/c^2 .

Since the p_T dependence is small, the mean value of π^0 peak position and width are obtained for each centrality bins and those are plotted in Figure 5.42. This shows the centrality dependence of mass peak position and width.

The left of Figure 5.42 was fitted by linear function. The peak position m_{peak} is expressed by

$$m_{peak}(N_{part}) = \alpha + \beta N_{part}, \quad (5.46)$$

$$\text{where } \alpha = 141.8 \pm 0.2 \text{ MeV}/c^2,$$

$$\text{and } \beta = 0.0266 \pm 0.0036 \text{ MeV}/c^2.$$

Since the known π^0 mass m_{known} is $134.98 \text{ MeV}/c^2$, the Eq.(5.46) is expressed as $105.08 + 0.020047 N_{part}$ [%]. This means the peak position is $\sim 5\%$ too high at the limit of most peripheral collision. In the previous calibrations stages using MIP and E/p ratio, the calorimeter gain was set as it measure electron energy properly. Therefore, 2% of out of 5% is ascribed to the difference of shower profile between photons and electrons.

Remaining 3 % difference is due to incompleteness of calibrations. The calibration using π^0 gives the most precise result rather than using MIP observation which gives calibration only at low energy.

By Eq. (5.46), the calorimeter energy scale was trimmed as it measures proper energy at most peripheral event. Energy scale of the EMCal was globally corrected by

$$\frac{m_{known}}{m_{peak}(N_{part} = 2)} = 0.952 \pm 0.002. \quad (5.47)$$

The procedure of analysis from subtracting combinatorial background to the counting π^0 were performed again. The results are shown as open circles in Figure 5.42, and new fitting result is

$$m_{peak}^{corr}(N_{part}) = \alpha_{corr} + \beta_{corr} N_{part}, \quad (5.48)$$

$$\text{where } \alpha_{corr} = 135.6 \pm 0.8 \text{ MeV}/c^2 ,$$

$$\text{and } \beta_{corr} = 0.0237 \pm 0.0060 \text{ MeV}/c^2 .$$

The effect of a coefficient β_{corr} in Eq. (5.48) parametrizes gradual increasing of invariant mass peak position as a function of N_{part} . This is due to the particle multiplicity. The parametrization is used while the Monte Carlo calculations performed in the later section. From the fitting ambiguities due to the statistical fluctuations in the invariant mass measurement, also $m_{peak}^{corr}(N_{part})$ has N_{part} dependent systematic errors. In the peripheral event, $m_{peak}^{corr}(N_{part} \sim 20)$ has ~ 1 % uncertainty and while in the central event, $m_{peak}^{corr}(N_{part} \sim 300)$ has ~ 3 % uncertainty. This systematic error contributes to the uncertainties of efficiency correction factor, and it is explained later. Since the p_T distribution of π^0 has strong power-law dumping shape. This slightly affect to the observed π^0 mass. From the Monte Carlo analysis, it was found that the π^0 mass is $\sim 2 \pm 1 \text{ MeV}/c^2$ higher than original mass even if EMCal has infinitely good resolution of energy. Then the calibration using π^0 mass performed above gives $2 \text{ MeV}/c^2$ over correction. This effect was included in Monte Carlo by decreasing generated γ energy by $2 \text{ MeV}/c^2$.

Observed Peak Width

From the Figure 5.42 (b), the peak width of π^0 mass peak after energy scale correction is 12–13 MeV/c^2 that is ~ 5 % narrower than before correction, and it is consistent to the energy correction factor Eq. (5.47).

No significant dependence on $\langle N_{part} \rangle$ is seen in Figure 5.42 (b). According to Eq. (3.2), the intrinsic energy distribution of EMCal for 2 GeV and 1 GeV photons are 7.7 % and 10.1 %, respectively. If this values directly reflect mass peak width, from Eq. (5.36), corresponding mass peak width will be 10 to 14 MeV/c^2 . It is consistent with experimentally observed peak width.

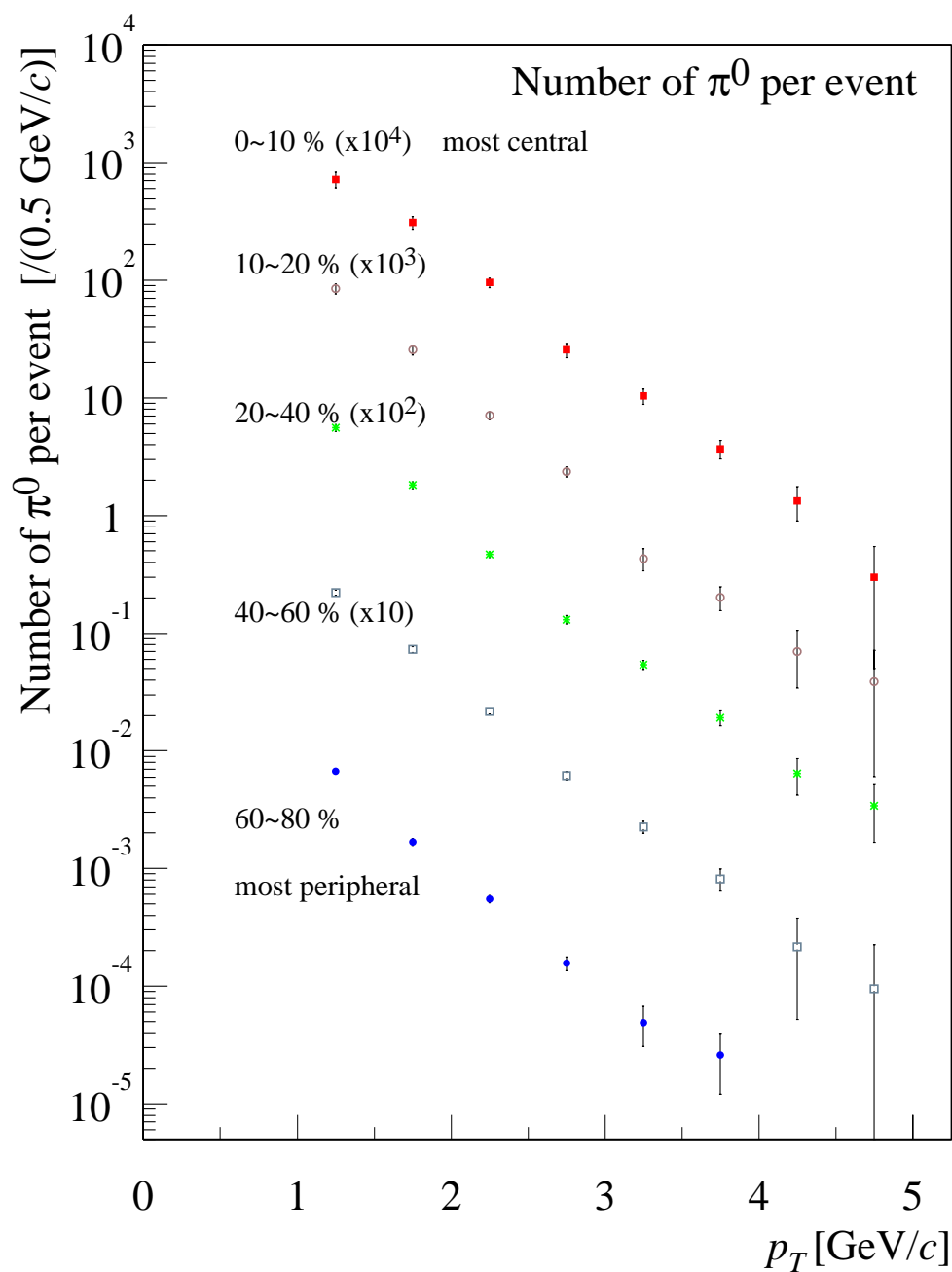


Figure 5.43: Raw numbers of extracted π^0 's divided by number of events extracted by cluster selection of $\delta^2 < 3.0$. Results of five centrality classes from most central (0–10 %) to peripheral (60–80 %) are overlaid. Associated error bars show only statistical errors. The number of events for each centrality classes are presented in Table 5.2. Raw numbers of π^0 's are listed on Table D.1 ~ D.5 too.

5.6.8 Raw Number of π^0 's

Figure 5.43 shows the results of counting π^0 's divided by number of events. Two plots show actual number of π^0 found in each p_T bins from 1.0 up to 5.0 GeV/ c in 0.5 GeV/ c step. In the plot, five slopes show results of centrality selections from most central events (C=0–10 %) and most peripheral events (C=60–80 %). The numbers used here are fully listed in Table D.1 ~ D.5. The number of events were taken from Table 5.2. The error bars in Figure 5.43 are only statistical errors.

5.7 Corrections and Systematic Uncertainties

The correction factor to reconstruct invariant yield of π^0 by Eq. (5.4) were calculated. The overall acceptance and efficiency for the π^0 depends on many factors. The possible factors are:

- (i) geometrical acceptance due to shape of detector,
- (ii) γ detection efficiency which is more precisely separated to:
 - EMCal clustering efficiency,
 - detector fiducial volume,
 - timing cut efficiency,
 - asymmetry cut efficiency,
 - opening angle cut efficiency,
 - δ^2 cut efficiency, and
 - loss by $\gamma \rightarrow e^+e^-$ conversion, and
- (iii) π^0 reconstruction efficiency which is more precisely separated to:
 - systematic ambiguity in counting π^0 ,
 - π^0 decay yield to 2γ channel, and
 - off vertex π^0 's.

Some of these are already given in previous sections. In the following sections, the acceptance and efficiency factors not explained yet are given and total efficiency and acceptance calculations are performed.

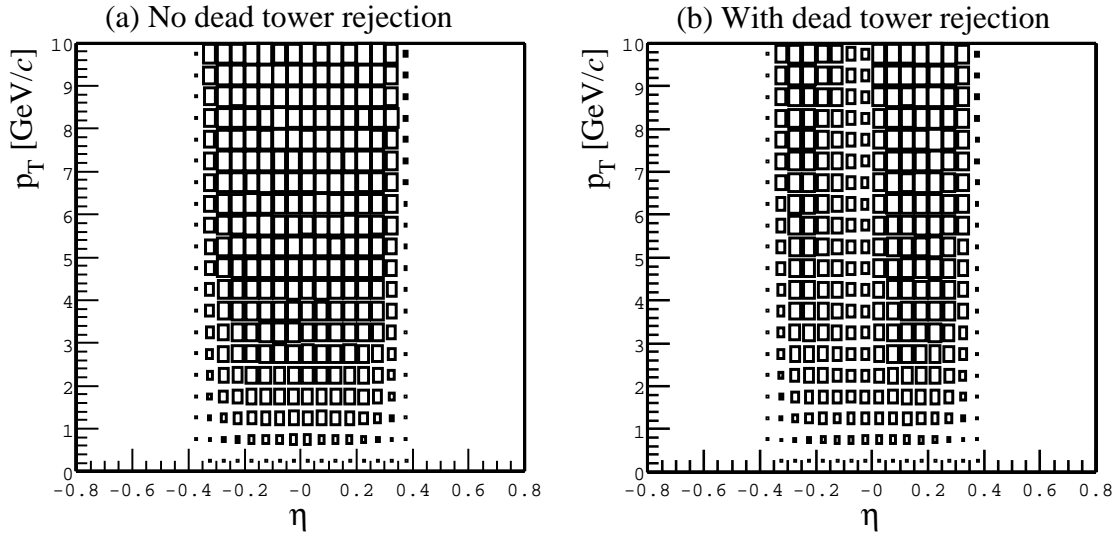


Figure 5.44: Geometrical acceptance of PbSc for π^0 's calculated by FMC. (a) shows the detection probability of π^0 if all the calorimeter towers are living. (b) shows the detection probability if dead towers are considered. The detector inefficiency due to reasons except for geometry, and inefficiency by analysis cuts are not considered yet.

5.7.1 Acceptance and Efficiency Corrections

Geometrical acceptance of the EMCal was calculated by the Fast Monte Carlo simulator (FMC)[73]. FMC simulates EMCal geometry and π^0 decays. In the FMC, π^0 's were initially generated and scattered into the phase space defined with

$$0 < p_T < 10 \text{ GeV}/c \quad \text{flat distribution,} \quad (5.49)$$

$$0 < \phi < 2\pi \quad \text{flat distribution and,} \quad (5.50)$$

$$\text{and} \quad -0.5 < \eta < 0.5 \quad \text{flat distribution.} \quad (5.51)$$

Then π^0 decays to two γ 's immediately at the origin (event vertex point) because its life time is negligible ($c\tau = 25.1$ nm). The orientation of decay axis of two γ 's is random in 4π solid angle in π^0 's rest frame. Then the probability of cases that both γ 's hit PbSc surface were calculated.

As the first step, the acceptance calculation without any inefficiency performed. The left plot in Figure 5.44 shows the acceptance of π^0 as a function of p_T and η . While calculating this plot, 100 % calorimeter towers are living and used. The effect of dead tower is also incorporated into the FMC. The right plot in Figure 5.44 shows the geometrical acceptance considering the dead towers.

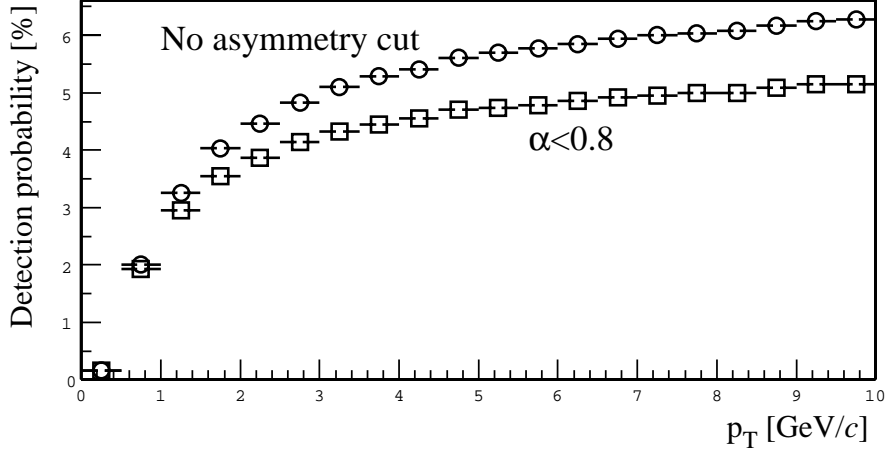


Figure 5.45: EMCAL geometrical acceptance v.s. p_T for π^0 's calculated by FMC.

Figure 5.45 shows the acceptance as a function of p_T with and without the $\alpha_{ab} < 0.8$ cut. Raw numbers of π^0 's are then corrected by the geometrical acceptance obtained by FMC. At this stage, no efficiency is considered yet.

Correction of p_T Bin Center

The p_T spectra has strong dumping shape. If the p_T bin size is small enough, the p_T positions can be represented by center of each bin. But due to the large bin size and steep slopes, the obtained numbers of π^0 's in the bin represent a bit lower position than bin center. The corrections for p_T positions are then needed. To obtain the shifted p_T position, a fitting of functions to acceptance corrected numbers are applied. The function used for fitting is power-law function represented by

$$\frac{1}{N_{ev}} \frac{dN_\pi}{2\pi p_T dp_T d\eta} = A \cdot \left(1 + \frac{p_T}{p_0}\right)^{-n}, \quad (5.52)$$

where A , p_0 and n are fitting parameters.

After the fitting, the p_T position where the number of π^0 in the bin size is equal to the height by Eq. (5.52) is obtained by solving the equation:

$$\int_{p_1}^{p_2} A \cdot \left(1 + \frac{p'_T}{p_0}\right)^{-n} dp'_T = A \cdot \left(1 + \frac{p_T}{p_0}\right)^{-n}, \quad (5.53)$$

where p_1 and p_2 are the lower and upper edges of a bin, respectively.

With the obtained corrected p_T position, the fitting and calculating p_T position were performed again. This iteration were performed until the p_T position and the fitting

Centrality	A	p_0	n	fit χ^2/ndf
0–10	2.916×10^2	2.441	1.194×10^1	15.66/5
10–20	1.482×10^2	4.638	1.844×10^1	5.833/6
20–40	7.680×10^1	5.390	2.018×10^1	15.54/6
40–60	3.191×10^1	4.448	1.724×10^1	10.21/5
60–80	1.049×10^1	3.736	1.558×10^1	6.801/4

Table 5.4: Result of fitting data by the power-law function. This is not the final result but result of the first step of the efficiency calculation using the FMC. This is used for as the parameter in the FMC at the second iteration.

function become stable. After three or four iterations the parameters were converged. The results are in Table 5.4.

Re-Calculation Using Fit Result and Efficiency

The p_T range discussed in this thesis is from 1 GeV/ c to 5 GeV/ c . In this range, the π^0 yield changes three order of magnitude as p_T changes. The input parameter defined by Eq. (5.49) is too much unrealistic.

By using the result of fitting shown in Table 5.4, π^0 's are generated again in the FMC and the efficiency is obtained again. At this stage, all the efficiencies, analysis cuts, and detector resolutions are simulated in the FMC using dice. The iterations are performed several times until the results converge.

Figure 5.46 shows the results of acceptance and efficiency calculations. The finally corrected π^0 yields and fitting results are shown in the next chapter.

5.7.2 Systematic Uncertainty in the Efficiency Correction

In the acceptance and efficiency calculation, the systematic uncertainties are estimated by modifying the simulation settings. The biggest uncertainty is due to the energy scale uncertainty. The cluster energy was corrected based on Eq. (5.48); i.e. the energy scale was increased as a function of N_{part} . In the most central events, ($N_{\text{part}} = 317$), the correction has $\sim 1.5\%$ uncertainty. It was checked in the FMC by replacing nominal correction factor to $\pm 1.5\%$.

Figure 5.47 shows the results of the FMC for (a) the most central and (b) the most peripheral events. In the central events, triangles placed in upper half of the plot are results by replacing the energy scale with 1.5% higher value, while the triangles in lower half are results of 1.5% lower energy scale. The same calculations are performed for

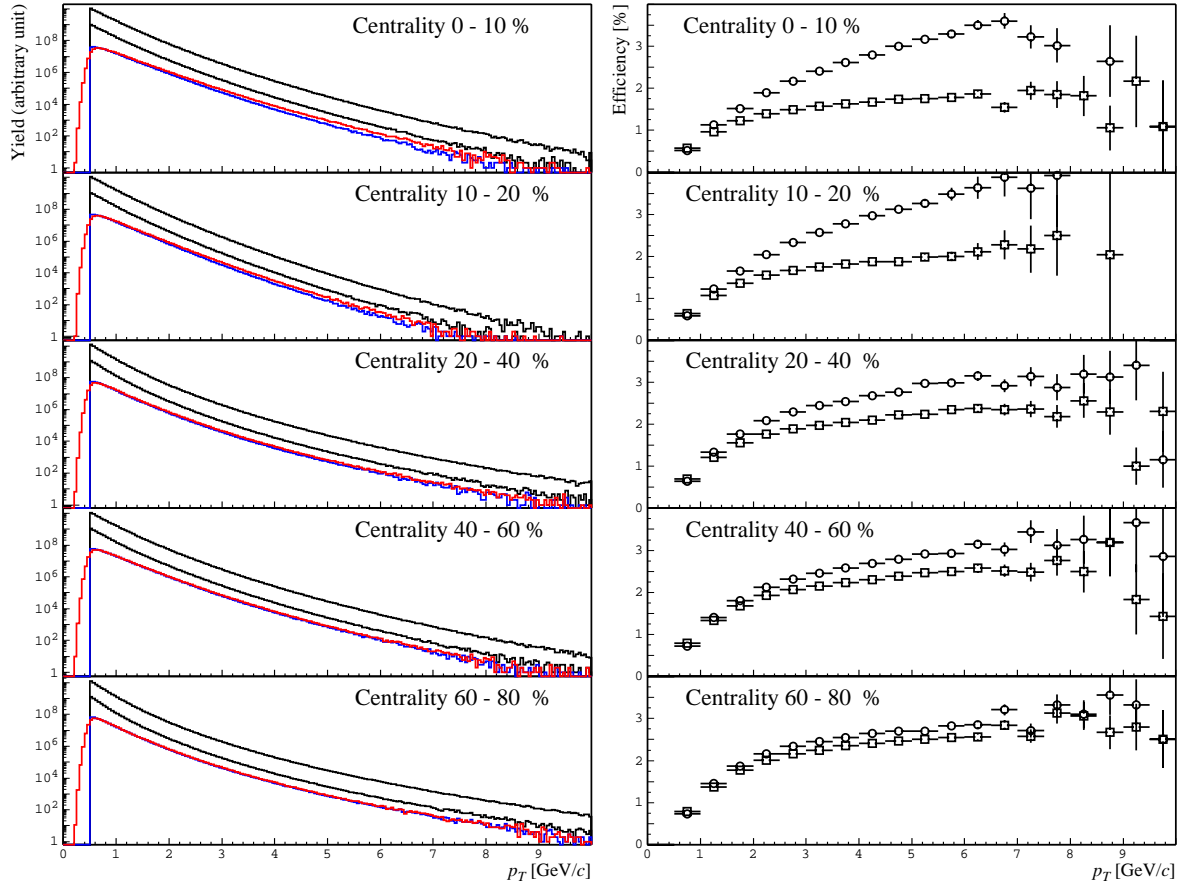


Figure 5.46: Left side plots are invariant distribution of simulated π^0 's for five centrality classes from most central (top) to most peripheral (bottom). Four lines in each plot show how the efficiency drops from highest magnitude histogram to lowest, correspond to original pions, pions toward EMCAL acceptance, pions those two photons hit the EMCAL, and pions both photons passed all the efficiency cut criteria, respectively. Right side plots are efficiency v.s. p_T for each centrality class. Open boxes are the efficiency without smearing and energy modification. Open circles are after including smearing and energy modification.

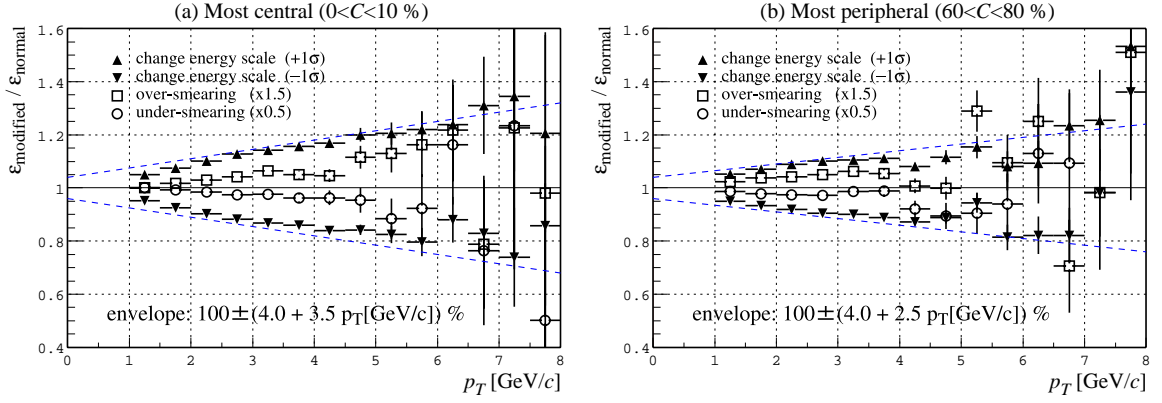


Figure 5.47: Efficiency based on different assumption of energy correction and smearing parameter divided by efficiency with normal condition for two cases of centrality (a) most central and (b) most peripheral. In both plots, open circles and open rectangles show the difference of efficiency by changing smearing parameter to be half and 1.5 times of nominal value, respectively. Triangles show results by changing energy correction parameter. In the over estimating points, the shift value is replaced by the nominal value plus standard deviation of it, and in the lower estimating points, the shift value is replaced by the nominal value minus standard deviation of it. The lines specifies one-sigma deviation due to shift value fluctuation.

the peripheral events where the systematic error for the correction value are $\pm 0.6\%$. In both (a) and (b), the effect is large for higher p_T .

From the results in Figure 5.47, the systematic error for the efficiency due to energy scale uncertainty are defined by

$$100 \pm (4.0 + 3.5 \cdot p_T) \% \quad (\text{for central events}), \quad (5.54)$$

$$\text{and } 100 \pm (4.0 + 2.5 \cdot p_T) \% \quad (\text{for peripheral events}), \quad (5.55)$$

where p_T is in the unit of GeV/c .

Other considerable systematic error in efficiency are uncertainty of EMCAL intrinsic resolution. The smearing of EMCAL is simulated using intrinsic resolution represented by Eq. (3.2). In Figure 5.47, also the results of changing the resolution to extreme cases (1) half of intrinsic resolution shown as open circles, and (2) 1.5 times of intrinsic resolution shown as open rectangles. Even such extreme cases, the efficiency does not change more than $\sim 5\%$. In the real case, the intrinsic resolution has much smaller uncertainty so that no systematic errors are needed to be assigned.

5.7.3 Shower Overlapping Effect

In addition to the cut efficiency for the clusters, the inefficiency to find clusters is essential especially in central events. In the central events, because particle multiplicity becomes large and the overlapping probability becomes large. If overlapping of two or more clusters occurred, merging of clusters or loss of a clustering may occur. Such effect is checked by the way of “raw data mixing”. In the raw data mixing, two different events are mixed into one artificial event before applying clustering software to the data.

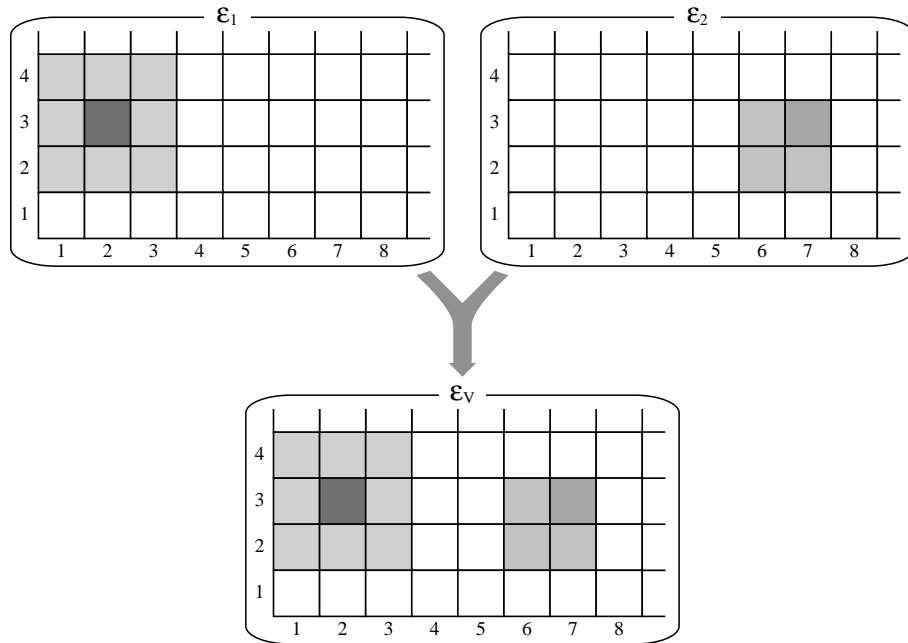


Figure 5.48: Conception of raw data mixing. \mathcal{E}_1 and \mathcal{E}_2 have hit towers of 9 and 4, respectively. After mixing, \mathcal{E}_V has 13 hit towers because there are no overlapping between \mathcal{E}_1 and \mathcal{E}_2 .

The basic procedure of raw data mixing is as follows. Two events \mathcal{E}_1 and \mathcal{E}_2 are arbitrary picked up. As schematically shown in Figure 5.48, both \mathcal{E}_1 and \mathcal{E}_2 has the tower indices of hit towers and their energy and timing information. Each tower energy was the sum of the two events. If \mathcal{E}_1 has N_1 hit towers and \mathcal{E}_2 has N_2 hit towers, and if there are completely no overlapping of hit towers, the mixed event \mathcal{E}_V has $M_{sum} = N_1 + N_2$ hit towers. If some overlap exists and cluster merging or breaking occurred, the number of cluster M_{mix} in \mathcal{E}_V becomes smaller. Once all the tower hits of the two events are merged, a new clustering is applied to the \mathcal{E}_V . The mixing is performed for arbitrary gathered two independent event sets each has several hundred events. And mixing software is looped over for all the combinations of events between two event sets.

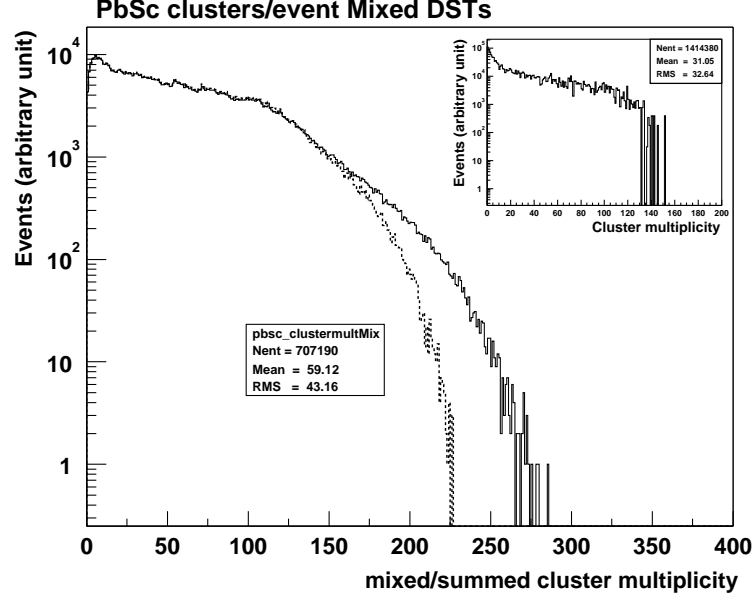


Figure 5.49: Cluster multiplicity distribution before/after mixing. Solid line shows the sum of multiplicity of the two events before mixing. Dashed line shows the multiplicity after mixing. The mixed multiplicity is less than the sum due to overlapping effect.

Figure 5.49 shows the result of the raw data mixing. The multiplicity distribution of original events is shown in small plot. About half area of EMCAL was used in this study. Since it has maximum multiplicity of ~ 140 , M_{sum} has maximum of ~ 280 . After the mixing, the maximum cluster multiplicity (M_{mix}) is reduced to ~ 230 . Both M_{mix} and M_{sum} distribution have very similar shape up to a multiplicity of ~ 120 where the effect of cluster overlapping begins.

Figure 5.50 (a) shows event-by-event plot of M_{mix} v.s. M_{sum} . Without shower losses, a perfect linear dependence between both variables is expected. Instead, the plot shows a separation from the linear dependence (solid line) above ~ 100 clusters, and it corresponds to a $\sim 10\%$ occupancy of the two PbSc sectors considering an average of 5.5 towers hit per cluster. This result suggests that the shower loss already present in the original (pre-merged) events. To minimize the effect of this shower loss, re-calculations for only events those have less than 100 clusters was performed. The result of the re-calculation is in Figure 5.50 (b). The result is fitted by a simple quadratic function:

$$M_{sum} = 0.994M_{mix} + 0.000412M_{mix}^2. \quad (5.56)$$

This relation is used to estimate the correction factor ($\epsilon_{overlap}^{-1}$) to compensate overlapping inefficiency.

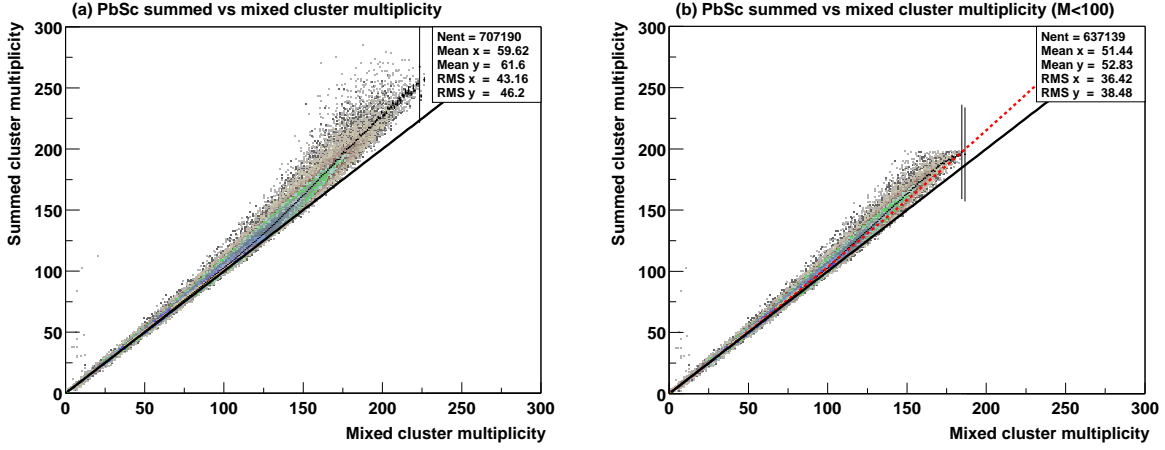


Figure 5.50: Summed v.s. mixed cluster multiplicity. (a) shows before selecting events. (b) shows after selecting events those clusters multiplicity is less than 100.

In the real experiment, M_{sum} corresponds to the real cluster multiplicity and M_{mix} corresponds to the observed cluster multiplicity. Then correction factor (inverse of efficiency) is expressed by

$$\begin{aligned}
 \epsilon_{overlap}^{-1} &= \frac{M_{sum}}{M_{mix}} \\
 &= 0.994 + 0.000412M_{mix} \\
 &= 0.994 + 0.000412 \cdot 0.56M_{obs},
 \end{aligned} \tag{5.57}$$

where M_{obs} is the observed cluster multiplicity. In the last form, the M_{obs} is multiplied by a ratio $140/250 = 0.56$ which is the multiplicity ratio between the limited acceptance (140) used in the present study of overlapping effect and full acceptance (250) used in this thesis, and used as M_{mix} .

The maximum multiplicity is $M_{obs} = 250$ and it corresponds to $\epsilon_{overlap} = 95\%$. The efficiency values for each centrality class were then calculated from Eq. (5.57) and mean multiplicity in Figure 5.10. Table 5.5 shows the $\epsilon_{overlap}$ for each centrality class.

5.7.4 Other Corrections

The following other corrections were applied.

Loss by Conversion in Material

Between event vertex and EMCAL, there are several materials which act as $\gamma \rightarrow e^+e^-$ converters. Those materials are listed in Table 5.6. The total radiation length between

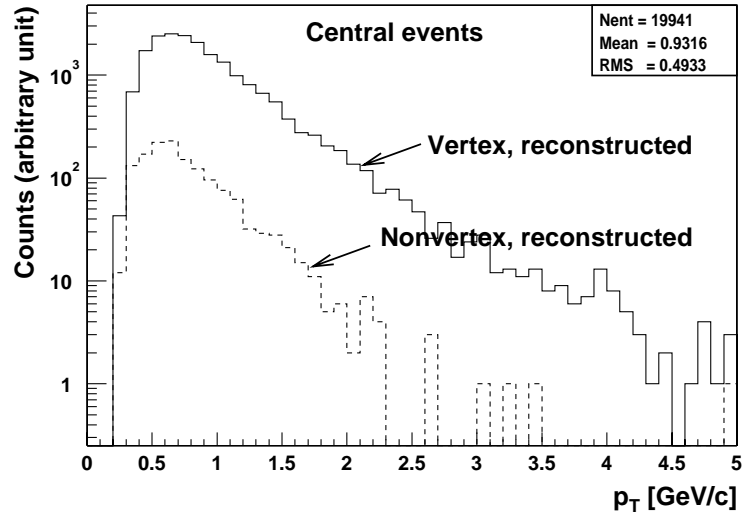


Figure 5.51: The amount of off vertex π^0 contamination estimated by GEANT simulation. Solid line shows the reconstructed π^0 's from the event vertex. Dashed line shows the π^0 's from off vertex but reconstructed.

the origin of the coordinate system and the center of EMCAL sector is $\sim 5.2\%$ where the distance from the origin to EMCAL surface is 507 cm. In the real case, photon hit positions spread entire EMCAL and event vertex also moves. The mean and RMS of photon path length is $523 \text{ cm} \pm 11.8 \text{ cm}$, and corresponding radiation length is $5.4 \pm 0.1\%$. Since each ingredient of radiation length in Table 5.6 has up to 0.1% uncertainties, the total radiation length also has 0.3% systematic error as a result of quadratic sum of them. Then the efficiency due to converter materials is

$$\epsilon_{conv} = 94.7 \pm 0.3\%. \quad (5.58)$$

C [%]	$\langle M_{obs} \rangle$	$\epsilon_{overlap}$ [%]
0 – 10	172	96.8
10 – 20	127	97.8
20 – 40	77	98.9
40 – 60	32	99.9
60 – 80	10	100.0

Table 5.5: Average multiplicity $\langle M_{obs} \rangle$ and $\epsilon_{overlap}$ for five centrality classes.

Part	Materials	X_0
Beam Pipe	Beryllium pipe (0.1 cm thickness and 7.6 cm outer diameter)	0.3 %
MVD	two Si strip (300 μm thickness each), support structure	1.0 %
RICH	150 cm CO_2 gas, two 125 μm Kapton windows, mirror	2.0 %
DC	two 0.2 mm mylar windows, 44 cm gas (1:1 Ar + Ethane)	0.2 %
PC1	FR4 structure, readout electronics, etc.	1.2 %
Others	~ 300 cm air	0.5 %
Total		5.2 %

Table 5.6: Materials between vertex and center of PbSc sector. The photon path length in the materials are shown in the unit of radiation length X_0 .

Off Vertex Contamination

The secondary π^0 's generated by conversions at structural materials of the detector decays into 2γ 's and reach to the EMCal. It is assumed that every clusters after PID are originated from the vertex measured by BBC's, the opening angle of 2γ 's from off vertex calculated by cluster position on EMCal is wrong. These γ 's will contribute to the background in the mass spectra. But it is sometime reconstructed as though it came from true vertex if the secondary π^0 is produced near the true event vertex.

Figure 5.51 shows effect of such non-vertex reconstructed π^0 's. The fraction of off vertex π^0 's in the reconstructed π^0 's is found to be 5 %, almost independent from the p_T .

5.7.5 Summary of Corrections and Systematic Uncertainties

The applied corrections and the associated systematic errors in the analysis are listed in Table 5.7. In the peripheral events, the overall systematic errors of the absolute values of π^0 yields are estimated to be 13 % at low transverse momentum (~ 1.2 GeV/ c) and 16 % at higher momentum (~ 3.2 GeV/ c). While in the central events, the estimated systematic errors are 14 % at low transverse momentum and exceeds 19 % at higher momentum. In any case, the statistical error exceeds the systematic error at $p_T = 2 \sim 3$ GeV/ c .

(a) Factors for single γ .

Factor	Typical efficiency or effect	Uncertainty	Reference
EMCal Fiducial Area	0.664	N.A.	5.6.5
TOF efficiency	> 0.99	~ 0	Eq. (5.32)
δ^2 cut efficiency	0.82 (C) – 0.95 (P)	5 %	Eq. (5.35)
Conversion	0.95	0 %	Eq. (5.58)
Overlap	0.97 (C) – 1.00 (P)	1 %	Table 5.5

(b) Factors for γ pair.

Geom. Acceptance	0.03 – 0.04	N.A.	Figure 5.45
Counting π^0	0.954 (2- σ window)	8 %	–
Energy smearing	modify p_T slope	~ 0	–
Energy correction	modify p_T slope	6 – 20 %	Eq. (5.54), (5.55)
Non-vertex π^0	1.05	N.A.	–
Branching ratio	0.988	0 %	[74]

(c) Other factors for comparison etc.

$\langle N_{\text{part}} \rangle$	N.A.	3 – 18 %	Table 5.2
$\langle N_{\text{coll}} \rangle$	N.A.	12 – 26 %	Table 5.2

Table 5.7: The applied corrections and the associated systematic errors in the analysis chain. (C) and (P) refer the most central event class and the most peripheral event class, respectively.

Chapter 6

Experimental Results

Figure 6.1 shows the results of analysis. The measured invariant yields of π^0 produced in Au+Au collisions at $\sqrt{s_{NN}} = 130$ GeV are plotted as a function of p_T . They are given as invariant yield per unit pseudorapidity at $\eta = 0$, per unit azimuth, and per event. The data are obtained for five centrality classes from $C = 0\text{--}10\%$ (top) to $C = 60\text{--}80\%$ (bottom). Data points of event classes except for the most peripheral are scaled by power of 10 as expressed in the figure. Also the same data are presented in tables from Table 6.2 to Table 6.6.

Associated error bars represented by solid vertical lines in the Figure 6.1 are statistical errors. Error bars represented by bold gray line show quadratic sum of all systematic uncertainties. Systematic error varies with respect to the p_T and typically 14 to 23 % in the central events and 12 to 17 % in the peripheral events. Statistical error varies from few % to 140 % with respect to the p_T . The statistical error exceeds systematic error at $p_T > 3$ GeV/ c region and is limiting maximum available p_T .

In Figure 6.1, data are fit by the power-law distribution function:

$$\begin{aligned} \frac{d^3n_\pi}{2\pi p_T dp_T d\eta} &= A \left(1 + \frac{p_T}{p_0}\right)^{-\mu} \\ &= S(\mu - 1)(p_0 + 1)^{\mu-1}(p_0 + p_T)^{-\mu}, \end{aligned} \quad (6.1)$$

where A , p_0 , and μ are the free parameters, and $S = Ap_0/(\mu - 1) \cdot (1 + 1/p_0)^{1-\mu}$ is the area of the function at p_T region from 1 GeV/ c to infinity. A combination of A , p_0 , and μ is usually used as fitting parameters but, in this case, the parameter A strongly correlate to the p_0 and μ . Fitting was therefore performed with free parameters of S , p_0 and μ . Results are shown as solid curves in Figure 6.1 and listed in Table 6.1.

In the fitting, only the statistical error of each data point are considered and propagated to the errors of S , p_0 and μ . Parameters p_0 and μ strongly correlate so that non diagonal coefficients of correlation matrix is close to unity.

The systematic errors to the fitted parameters are obtained by simultaneously shifting up or down the invariant yield spectra by systematic error for each data point. This is reasonable because all systematic errors except for the 8 % error due to π^0 counting are

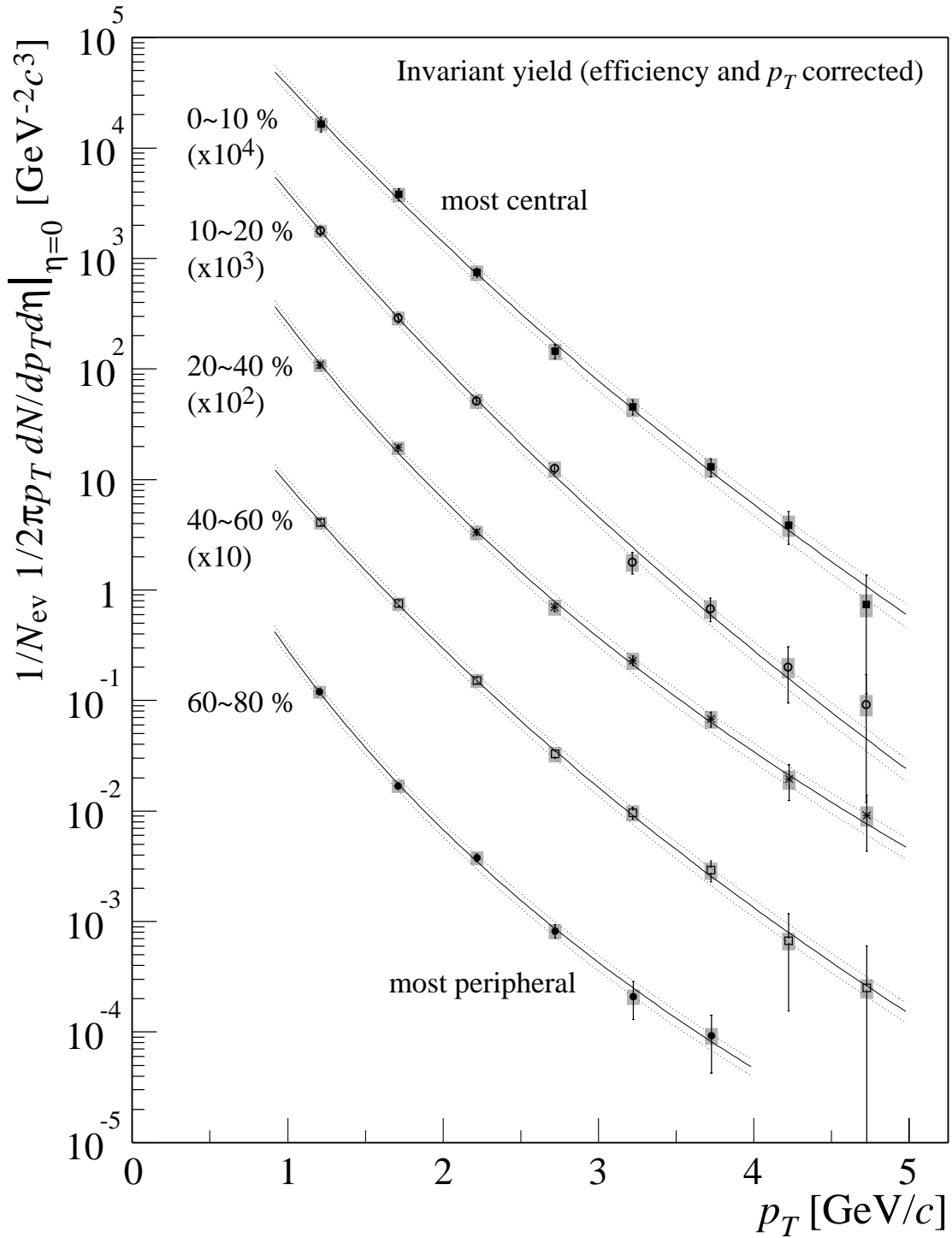


Figure 6.1: Points show the invariant p_T distributions of π^0 for five centrality classes. Statistical errors are expressed by solid lines and systematic errors are expressed by gray bold bars. Solid curves show the fit results by the power-law function. Each pair of dotted lines surrounding solid curve show the systematic upper or lower limits of the fit result.

C [%]	S	$\delta^{\text{stat.}}$ [GeV $^{-1}c^2$]	$\delta^{\text{sys.}}$	p_0	$\delta^{\text{stat.}}$	$\delta^{\text{sys.}}$	μ	$\delta^{\text{stat.}}$	$\delta^{\text{sys.}}$	χ^2/ndf
0–10	1.10	$\pm .13$	$^{+.15}_{-.16}$	5.98	± 3.35	$^{-.16}_{+.29}$	24.4	± 9.8	$^{-.7}_{+1.1}$	3.3/5
10–20	1.07	$\pm .09$	$^{+.15}_{-.15}$	5.33	± 2.91	$^{-.14}_{+.22}$	24.6	± 9.6	$^{-.6}_{+.9}$	5.4/5
20–40	.668	$\pm .038$	$^{+.090}_{-.090}$	2.24	$\pm .65$	$^{-.06}_{+.09}$	13.6	± 2.1	$^{-.3}_{+.4}$	6.1/5
40–60	.253	$\pm .012$	$^{+.034}_{-.034}$	4.02	± 1.50	$^{-.08}_{+.12}$	18.8	± 4.7	$^{-.3}_{+.5}$	1.5/5
60–80	.0705	$\pm .0035$	$^{+.0093}_{-.0093}$	1.40	$\pm .80$	$^{-.01}_{+.02}$	10.8	± 2.7	$^{-.1}_{+.1}$	1.9/3

Table 6.1: Fit results for π^0 invariant yields. Mean value of S , p_0 , and μ , and their statistical errors ($\delta^{\text{stat.}}$) obtained by fitting are shown. The systematic errors ($\delta^{\text{stat.}}$) are estimated by shifting all the data points to upper or lower limits within their systematic errors and fitting by the same function.

correlated among the data points. The differences between the central fit results and the shifted results are defined to be the systematic errors for the fit parameters.

p_T [GeV/c]	$\left. \frac{d^3 n_\pi}{2\pi p_T dp_T d\eta} \right _{\eta=0}$ [GeV ⁻² c ³]	\pm stat. error [GeV ⁻² c ³]	\pm sys. error [GeV ⁻² c ³]	\pm total error [GeV ⁻² c ³]
1.21	1.64	0.26	0.23	0.34
1.72	3.80×10^{-1}	0.48×10^{-1}	0.57×10^{-1}	0.74×10^{-1}
2.22	7.47×10^{-2}	0.71×10^{-2}	1.2×10^{-2}	1.4×10^{-2}
2.72	1.45×10^{-2}	0.21×10^{-2}	0.25×10^{-2}	0.33×10^{-2}
3.22	4.55×10^{-3}	0.69×10^{-3}	0.86×10^{-3}	1.1×10^{-3}
3.72	1.30×10^{-3}	0.24×10^{-3}	0.26×10^{-3}	0.36×10^{-3}
4.22	3.9×10^{-4}	1.3×10^{-4}	0.8×10^{-4}	1.5×10^{-4}
4.73	7.4×10^{-5}	6.3×10^{-5}	1.7×10^{-5}	6.5×10^{-5}

Table 6.2: Corrected invariant yield of π^0 per event for $C=0-10$ % events.

p_T [GeV/c]	$\left. \frac{d^3 n_\pi}{2\pi p_T dp_T d\eta} \right _{\eta=0}$ [GeV ⁻² c ³]	\pm stat. error [GeV ⁻² c ³]	\pm sys. error [GeV ⁻² c ³]	\pm total error [GeV ⁻² c ³]
1.21	1.78	0.18	0.24	0.30
1.71	2.89×10^{-1}	0.28×10^{-1}	0.42×10^{-1}	0.50×10^{-1}
2.22	5.16×10^{-2}	0.43×10^{-2}	0.81×10^{-2}	0.91×10^{-2}
2.72	1.25×10^{-2}	0.13×10^{-2}	0.21×10^{-2}	0.25×10^{-2}
3.22	1.78×10^{-3}	0.39×10^{-3}	0.32×10^{-3}	0.51×10^{-3}
3.72	6.8×10^{-4}	1.6×10^{-4}	1.3×10^{-4}	2.1×10^{-4}
4.22	2.0×10^{-4}	1.1×10^{-4}	0.4×10^{-4}	1.1×10^{-4}
4.72	9.2×10^{-5}	8.0×10^{-5}	2.0×10^{-5}	8.3×10^{-5}

Table 6.3: Corrected invariant yield of π^0 per event for $C=10-20$ % events.

p_T [GeV/c]	$\left. \frac{d^3 n_\pi}{2\pi p_T dp_T d\eta} \right _{\eta=0}$ [GeV ⁻² c ³]	\pm stat. error [GeV ⁻² c ³]	\pm sys. error [GeV ⁻² c ³]	\pm total error [GeV ⁻² c ³]
1.21	1.079	0.070	0.14	0.16
1.71	1.94×10^{-1}	0.13×10^{-1}	0.27×10^{-1}	0.30×10^{-1}
2.22	3.33×10^{-2}	0.19×10^{-2}	0.50×10^{-2}	0.54×10^{-2}
2.72	7.00×10^{-3}	0.59×10^{-3}	1.1×10^{-3}	1.3×10^{-3}
3.22	2.30×10^{-3}	0.22×10^{-3}	0.40×10^{-3}	0.45×10^{-3}
3.72	6.8×10^{-4}	1.0×10^{-4}	1.3×10^{-4}	1.6×10^{-4}
4.23	1.94×10^{-4}	0.69×10^{-4}	0.38×10^{-4}	0.79×10^{-4}
4.73	9.1×10^{-5}	4.8×10^{-5}	1.9×10^{-5}	5.2×10^{-5}

Table 6.4: Corrected invariant yield of π^0 per event for $C=20-40$ % events.

p_T [GeV/c]	$\left. \frac{d^3 n_\pi}{2\pi p_T dp_T d\eta} \right _{\eta=0}$ [GeV ⁻² c ³]	\pm stat. error [GeV ⁻² c ³]	\pm sys. error [GeV ⁻² c ³]	\pm total error [GeV ⁻² c ³]
1.21	4.08×10^{-1}	0.21×10^{-1}	0.54×10^{-1}	0.58×10^{-1}
1.71	7.53×10^{-2}	0.41×10^{-2}	1.1×10^{-2}	1.1×10^{-2}
2.22	1.517×10^{-2}	0.084×10^{-2}	0.22×10^{-2}	0.24×10^{-2}
2.72	3.28×10^{-3}	0.28×10^{-3}	0.51×10^{-3}	0.58×10^{-3}
3.22	9.6×10^{-4}	1.2×10^{-4}	1.6×10^{-4}	2.0×10^{-4}
3.72	2.91×10^{-4}	0.63×10^{-4}	0.51×10^{-4}	0.82×10^{-4}
4.23	6.7×10^{-5}	5.2×10^{-5}	1.3×10^{-5}	5.3×10^{-5}
4.73	2.5×10^{-5}	3.5×10^{-5}	0.50×10^{-5}	3.5×10^{-5}

Table 6.5: Corrected invariant yield of π^0 per event for $C=40-60$ % events.

p_T [GeV/c]	$\left. \frac{d^3 n_\pi}{2\pi p_T dp_T d\eta} \right _{\eta=0}$ [GeV ⁻² c ³]	\pm stat. error [GeV ⁻² c ³]	\pm sys. error [GeV ⁻² c ³]	\pm total error [GeV ⁻² c ³]
1.20	1.196×10^{-1}	0.059×10^{-1}	0.16×10^{-1}	0.17×10^{-1}
1.71	1.69×10^{-2}	0.11×10^{-2}	0.23×10^{-2}	0.26×10^{-2}
2.22	3.79×10^{-3}	0.29×10^{-3}	0.55×10^{-3}	0.62×10^{-3}
2.72	8.2×10^{-4}	1.1×10^{-4}	1.3×10^{-4}	1.7×10^{-4}
3.22	2.09×10^{-4}	0.79×10^{-4}	0.34×10^{-4}	0.86×10^{-4}
3.73	9.2×10^{-5}	5.0×10^{-5}	1.6×10^{-5}	5.2×10^{-5}

Table 6.6: Corrected invariant yield of π^0 per event for $C=60-80$ % events.

Chapter 7

Discussions

7.1 Overview

In this chapter, the physics based on the results shown in Chapter 6 is discussed. Based on the binary scaling introduced in Chapter 2, the obtained π^0 invariant p_T spectra are compared with the reference spectra of the scaled $N+N$ collisions. The presence of nuclear modification as well as the jet quenching effect are discussed. Data from other experiments at SPS and RHIC are referred and discussed. Finally, relation between the initial energy density and the nuclear modification factor is discussed.

7.2 Comparison to the $N+N$ Data

The first question is that whether the π^0 yields are described by superposition of $N+N$ collisions or not? If binary scaling is correct and no nuclear modification is there, the π^0 yield is proportional to $\langle N_{\text{coll}} \rangle$ for each centrality, and represented by

$$\frac{d^2 n_{AA \rightarrow \pi^0}}{2\pi p_T d\eta dp_T} = \frac{\langle N_{\text{coll}} \rangle}{\sigma_{in}} \frac{d^2 \sigma_{NN \rightarrow \pi^0}}{2\pi p_T d\eta dp_T}, \quad (7.1)$$

where $\sigma_{NN \rightarrow \pi^0}$ is the π^0 production cross section and $\sigma_{in} = 40$ mb is the $N+N$ inelastic cross section. The $\langle N_{\text{coll}} \rangle$ values for each centrality class are estimated from the Glauber model as described in Section 5.4. Since no $N+N$ reference data at $\sqrt{s}=130$ GeV is available, interpolation was made from the data points at ISR[26, 27, 20], $Spp\bar{p}S$ [75, 24, 23, 25], and Tevatron[22]. Details are described in Appendix B.

Figure 7.1 shows the comparison between the obtained π^0 spectra (points) and reference π^0 spectra by Eq. (7.1) (solid curves). The error bars for experimental data represented by solid lines are statistical error, and gray bar represents systematic uncertainties in π^0 yield. Pair of dotted curves surrounding each solid curve represents upper and lower limit of $N+N$ reference in systematic error. The systematic error consists of uncertainty of pion to hadron ratio and uncertainty in the hadron yields among referred

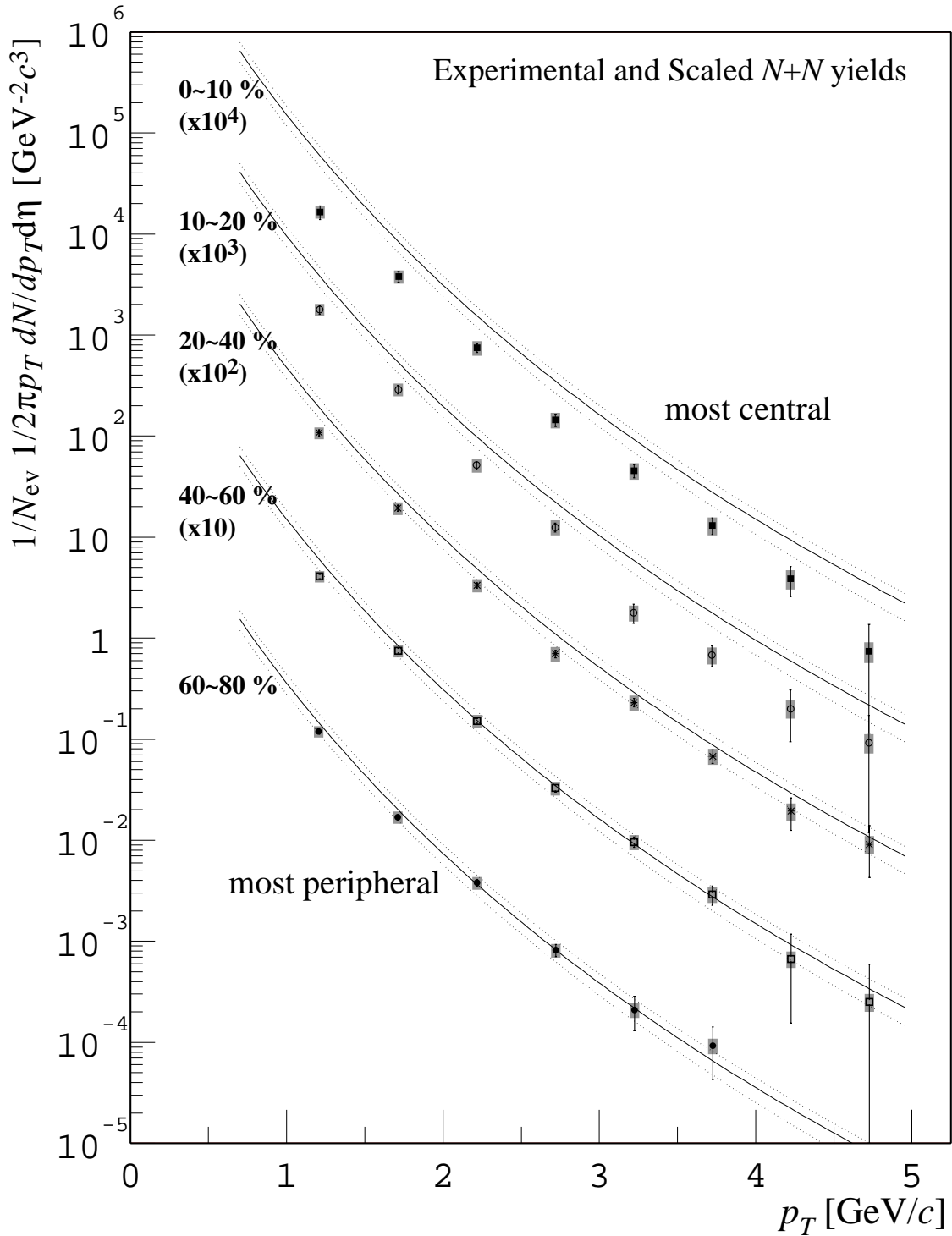


Figure 7.1: Comparison to scaled yield of π^0 in $N+N$ interactions. The solid lines are result of interpolation using ISR, $Spp\bar{S}$, and Tevatron data. The error bands are due to mainly systematic error in $\langle N_{\text{coll}} \rangle$. Data points are PHENIX data come directly from Figure 6.1. Lines and data points except for the most peripheral are scaled up by numbers shown in the plot.

experiments and interpolation methods (20 %). The uncertainty of $\langle N_{\text{coll}} \rangle$ is not included here and will be discussed later.

In the most peripheral events ($C = 60\text{--}80\%$), a scaled $N+N$ curve agrees with the experimental data within errors. But the agreements gradually becomes worse with the centrality. In the most central events ($C = 0\text{--}10\%$), the π^0 yield in Au+Au collisions is less than 50 % of scaled π^0 yield in $N+N$ collisions.

Compared to the SPS data described in Section 2.5 where strong Cronin enhancement was seen, the present result is quite different.

Modification Factor

Modification factor $R_{AA/NN}(p_T)$ defined by Eq. (2.14) was calculated for each centrality. The experimentally obtained π^0 yields were divided by the reference π^0 yields by Eq.(7.1). Figure 7.2 shows the result of calculation. The measured $R_{AA/NN}(p_T)$ are represented by points. Vertical solid lines attached to the points are statistical errors and vertical gray bars are systematic uncertainty. Horizontal straight lines are uncertainties in $\langle N_{\text{coll}} \rangle$ estimation among Glauber settings performed in Section 5.4. Gray horizontal bands show uncertainties in $N+N$ reference data same as the systematic error shown by dotted curves in Figure 7.1. These two sorts of uncertainties do not correlate each other.

If no nuclear modification exist and the binary scaling is correct, $R_{AA/NN}(p_T)$ should be unity. In $C = 60\text{--}80\%$ and $C = 40\text{--}60\%$ events, $R_{AA/NN}(p_T)$ is consistent to unity. It is apparent that the strongest suppression is seen in both $C = 10\text{--}20\%$ and $C = 0\text{--}10\%$ central events. For the next to the most peripheral events ($C = 40\text{--}60\%$), the Au+Au yield is still consistent to unity. No significant p_T dependence is seen beyond the statistical error in all centralities.

Centrality Dependence

From the Figure 7.2, the mean value of modification factor at $p_T > 2$ GeV/ c region were calculated in each centrality and plotted as a function of centrality variable C .

Figure 7.3 shows the obtained relation between obtained mean $R_{AA/NN}(p_T)$ and centrality. Closed circles represent the result of calculation using $\langle N_{\text{coll}} \rangle$. The vertical solid lines show the statistical errors. The vertical gray bars show the systematic uncertainties in the measurement. The systematic uncertainty in π^0 yield was estimated by shifting the data points to upper (or lower) limit of each systematic error simultaneously, because almost all systematic errors are correlated. Uncertainty of $N+N$ reference data is expressed by two horizontal solid lines at $1 \pm 25\%$. Represented by eight sorts of symbols are results of the $R_{AA/NN}(p_T)$ by the different model assumptions in N_{coll} calculations. The assumption used for each symbol is same as that of the same symbol in Figure 5.7.

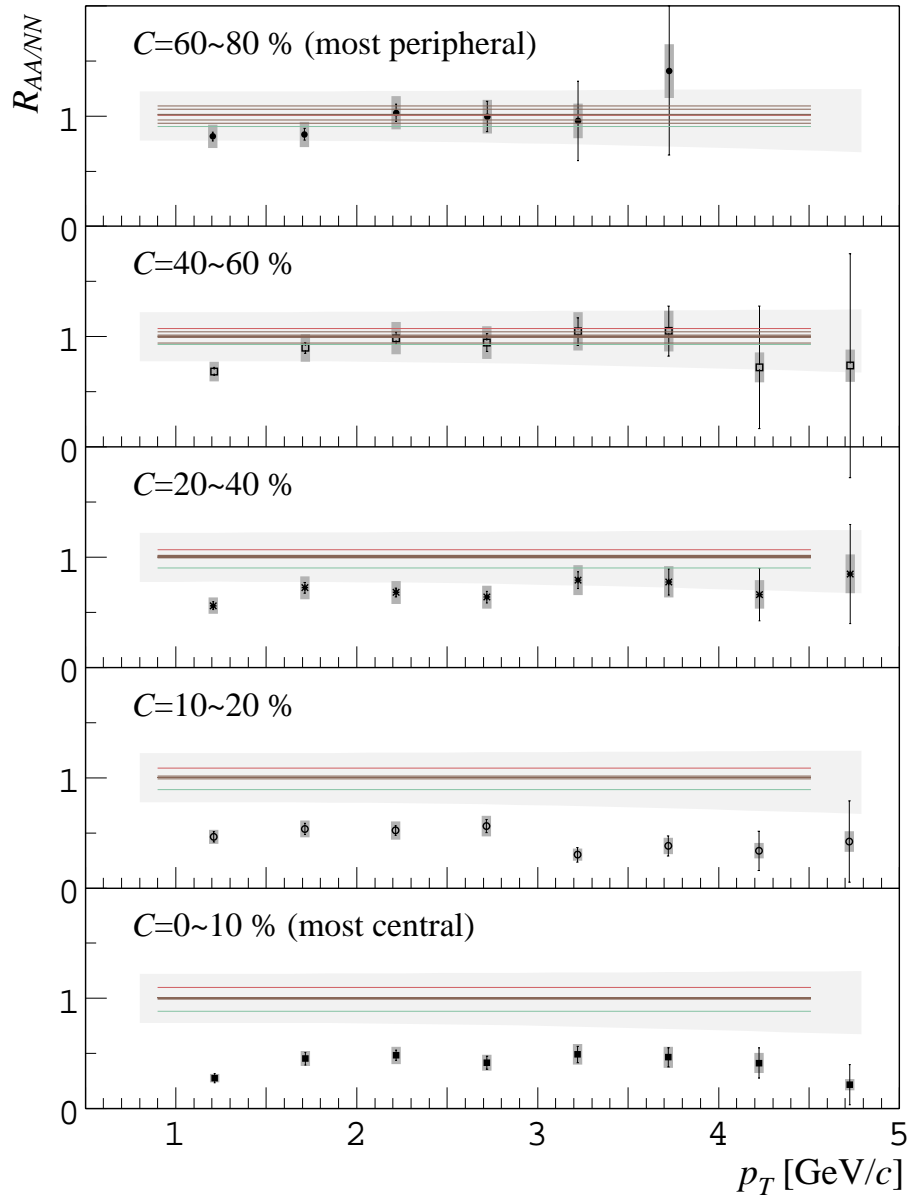


Figure 7.2: The ratio of π^0 yield divided by scaled yield of $N+N$ collisions are plotted for five centralities from the most peripheral events (top) to the most central events. Vertical solid lines and vertical gray bars are statistical and systematic uncertainties, respectively. Horizontal straight lines show the difference of unity definitions for Glauber settings. Gray horizontal bands show uncertainties in $N+N$ reference data.

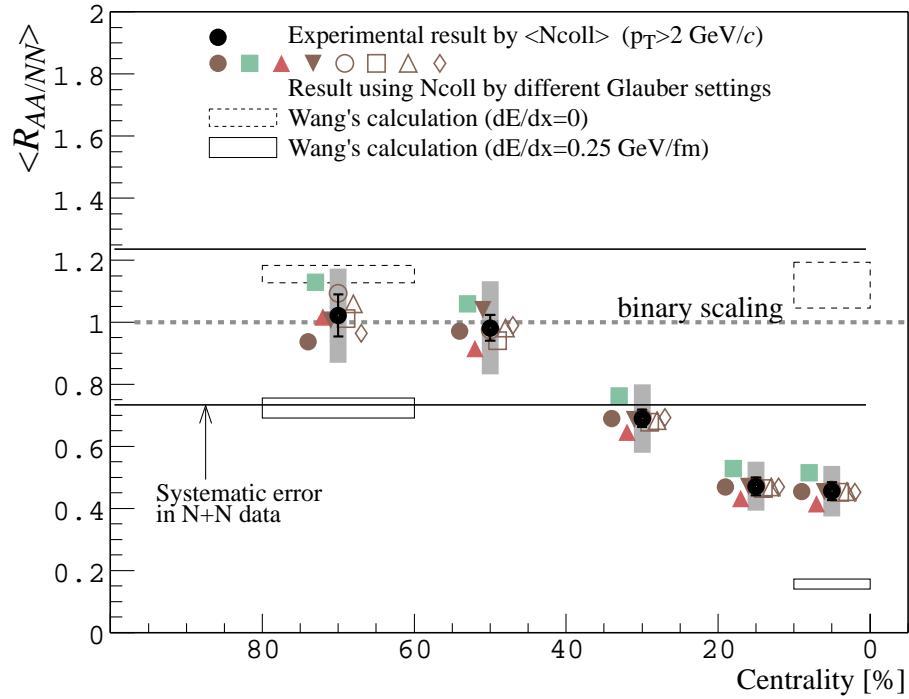


Figure 7.3: Averaged $R_{AA/NN}$ (solid marks) at $p_T > 2 \text{ GeV}/c$ v.s. centrality. Vertical solid and gray error bars are statistical and systematic uncertainties of π^0 yield, respectively. Horizontal lines at $\pm 25\%$ from unity represent uncertainties in π^0 yield in $N+N$ collisions. Other eight symbols are result of different Glauber settings, each corresponds to the same symbols in Figure 5.7. Solid and dashed rectangles are prediction of pQCD calculation by X.-N. Wang with and without assuming jet energy loss, respectively.

The symbols are horizontally displaced for the clearer presentation.

At the first two peripheral points, the modification factor is consistent to unity, and it significantly decreases at central collision. The decrease begins at $C \sim 50\%$ suddenly and suppression getting stronger until $C \sim 15\%$. Since uncertainties of $N+N$ data and π^0 yield make all the data points move up or down simultaneously but it does not change the tendency of decreasing of modification factor. Uncertainty of $\langle N_{\text{part}} \rangle$ also has no significant effect.

7.3 Comparison to the Peripheral Data

The comparison between the most peripheral events obtained in the measurement and other centrality classes are performed. Since π^0 yield in the most peripheral events ($C = 60\text{--}80\%$) is consistent with superposition of $N+N$ interactions as shown in the

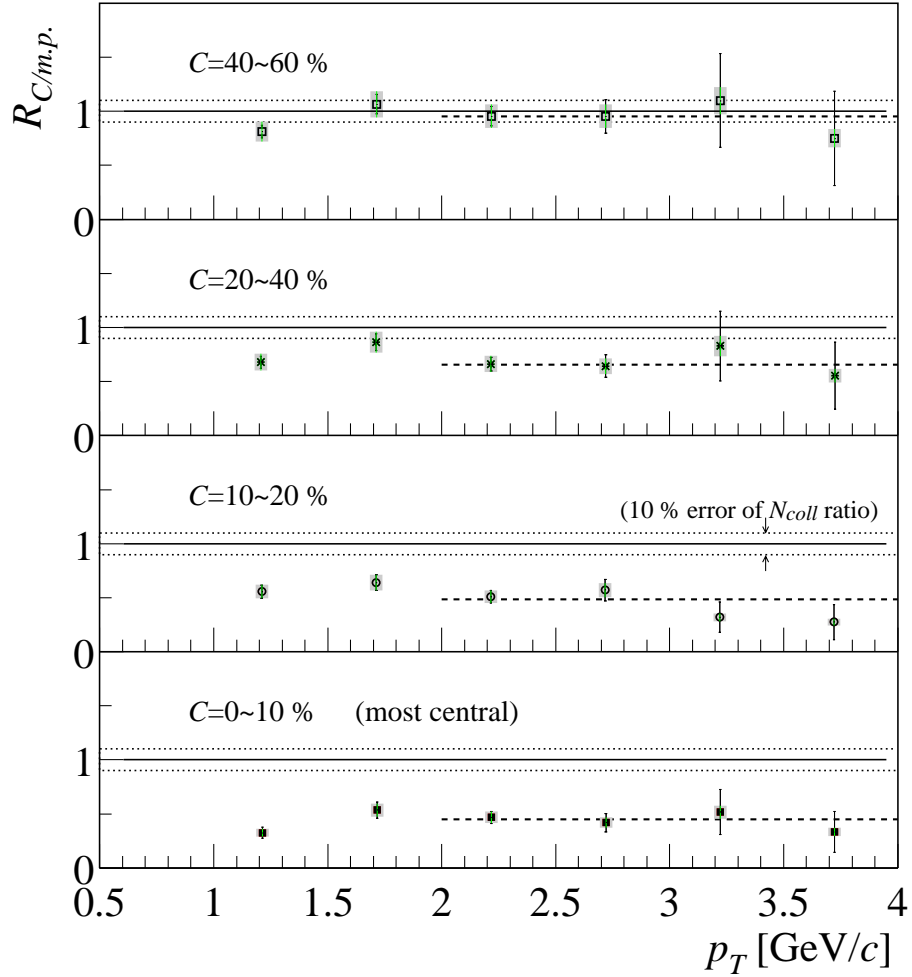


Figure 7.4: $R_{C/m.p.}$ as functions of p_T . Horizontal dotted lines show the systematic uncertainties of definition of unity due to the ratio $\langle N_{coll} \rangle^C / \langle N_{coll} \rangle^{(60-80\%)}$. Vertical solid lines and shaded bars show the statistical errors and systematic errors in π^0 yield. The solid line at $p_T > 2$ GeV/c show average at this region.

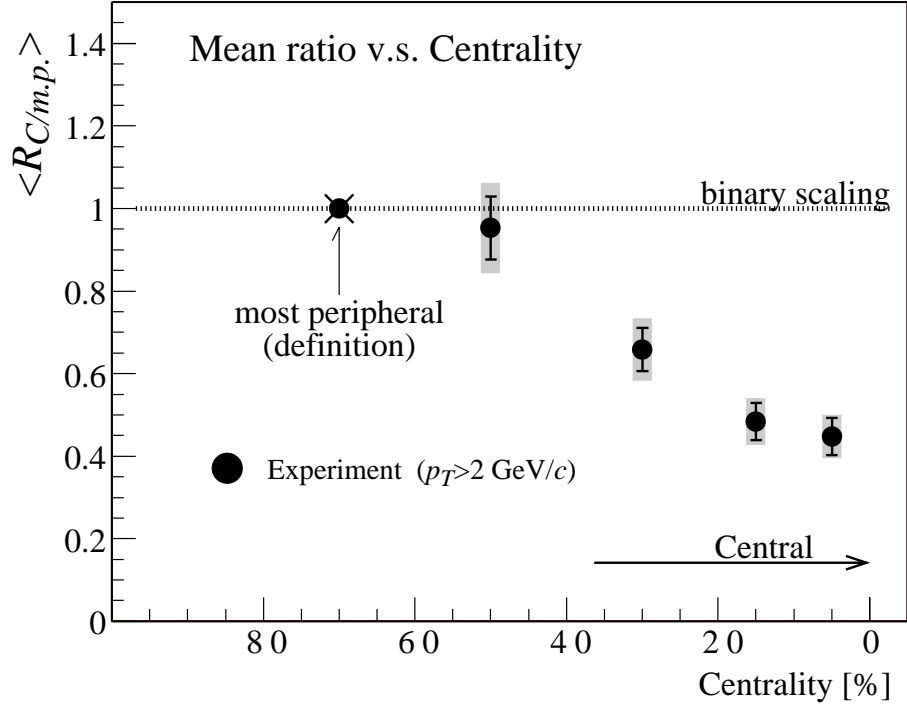


Figure 7.5: The averaged $R_{C/m.p.}$ as a function of centrality variable. Solid vertical lines show the statistical errors and vertical bars show the systematic uncertainties including uncertainties of $\langle N_{\text{coll}} \rangle^C / \langle N_{\text{coll}} \rangle^{(60-80\%)}$ and π^0 yields.

previous section, it can be used as reference instead of scaled $N+N$ data. Different from the comparison to the binary scaled $N+N$ data, some systematic uncertainties such as π^0 cross section in $N+N$ collision do not appear. Also substantial part of correlated systematic errors in π^0 yields cancels.

The modification factor $R_{C/m.p.}(p_T)$ is defined by

$$R_{C/m.p.}(p_T) = \frac{dn^C}{2\pi p_T d\eta dp_T} \bigg/ \frac{\langle N_{\text{coll}} \rangle^C}{\langle N_{\text{coll}} \rangle^{m.p.}} \cdot \frac{dn^{m.p.}}{2\pi p_T d\eta dp_T} \quad (7.2)$$

where $m.p.$ and C denote most peripheral ($C = 60-80\%$) class and other centrality classes, respectively. The values are obtained bin-by-bin of p_T . The central values of the bins are slightly different among centrality classes, but the affect is neglected. The uncertainty in the ratio $\langle N_{\text{coll}} \rangle^C / \langle N_{\text{coll}} \rangle^{(60-80\%)}$ was $\sim 10\%$ as described in Figure 5.8. The correlated systematic errors were estimated by shifting up or down the data simultaneously within the systematic error.

Figure 7.4 shows the calculated distributions of $R_{C/m.p.}(p_T)$. The 10% error in ratio of $\langle N_{\text{part}} \rangle$ is expressed by uncertainty of definition of unity, corresponds to dotted lines in the figure. Vertical solid lines are statistical error propagated from both a given centrality

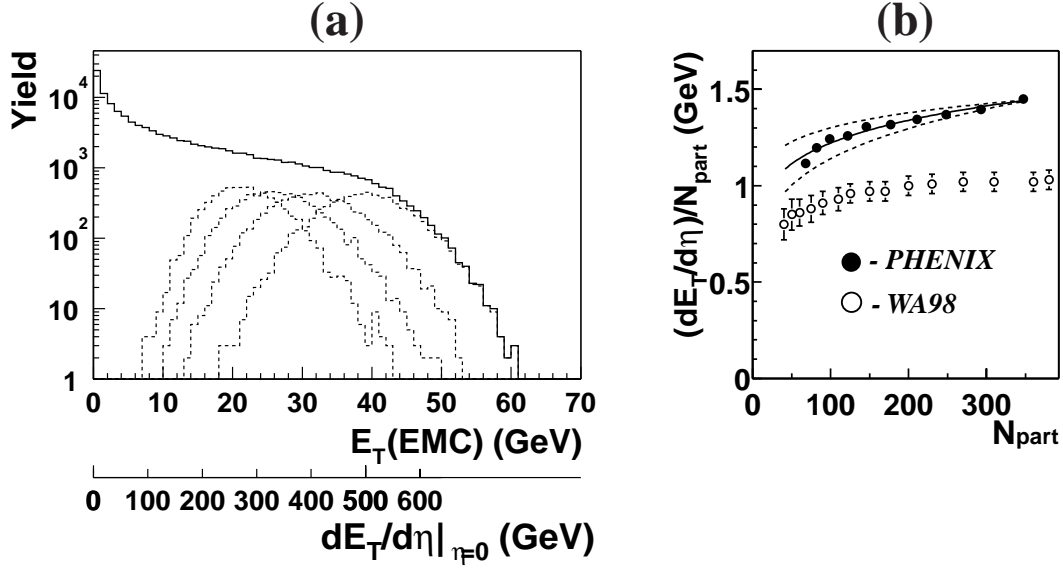


Figure 7.6: (a) E_T distribution measured from EMCAL for Au+Au at $\sqrt{s_{NN}}=130$ GeV (upper scale) and total hadronic $dE_T/d\eta|_{\eta=0}$ (lower scale). The solid line is the minimum bias distribution. The dashed lines from higher E_T to lower E_T correspond to events from $C=0-5\%$ to $C=15-20\%$ in 5% step, respectively. (b) Dependence of $dE_T/d\eta$ on N_{part} by PHENIX (Au+Au) and WA98 (Pb+Pb) experiments. The solid line is the N_{part}^α fit result for PHENIX data and the dashed lines are its systematic errors.

class and most peripheral class. Vertical gray bars are systematic errors. Almost all correlated systematic errors were canceled and up to 4% remained at high- p_T region in the most central class. Uncorrelated systematic errors ($8 \otimes 8 \sim 11\%$) remained in all data points. The tendency of the data is quite similar to $R_{AA/NN}(p_T)$.

As there is no significant p_T dependence, the averages of the modification factor at $p_T > 2$ GeV/ c region ($\langle R_{C/m.p.} \rangle$) were taken. Figure 7.5 shows the $R_{C/m.p.}(p_T)$ as a function of centrality. In the plot, all systematic errors are included in the error bars expressed by vertical gray bars. A decreasing behavior of modification factor as goes to the most central event is clearer than Figure 7.3.

7.4 ε_0 Dependence of $R_{AA/NN}$

Following Bjorken's scenario already discussed in Chapter 2, a spatial energy density ε_0 in a relativistic collision can be estimated from measurement of rapidity distribution of

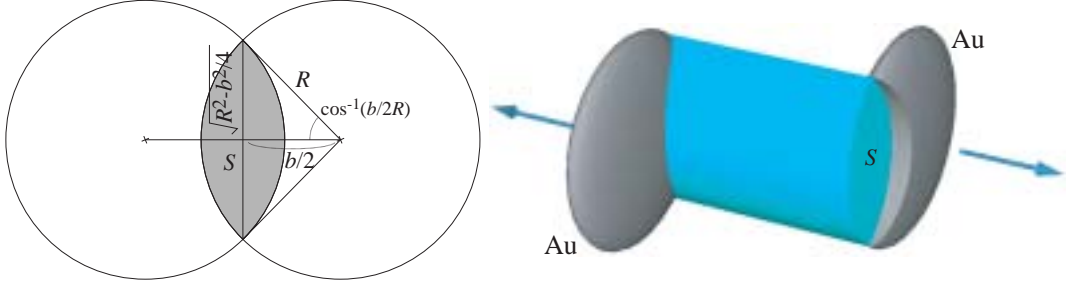


Figure 7.7: Calculation of the transverse area S .

transverse energy dE_T/dy by

$$\epsilon_0 = \frac{dE_T}{dy} \cdot \frac{1}{\tau_0 S}. \quad (7.3)$$

This is same as Eq. (2.7). The transverse energy E_T is measured by EMCAL and defined by

$$E_T = \sum_i E_i \sin \theta_i, \quad (7.4)$$

where E_i is the kinetic energy for nucleons and total energy for all other particles. θ_i is the polar angle, and the sum is taken over all particles emitted into a solid angle of the detector for each event.

The E_T measurement was performed by PHENIX experiment[76]. Figure 7.6(a) shows the distribution of E_T measured by EMCAL and Figure 7.6(b) shows its density per unit pseudo-rapidity divided by N_{part} as a function of N_{part} . WA98 data of Pb+Pb collisions at $\sqrt{s_{NN}}=17$ GeV are also shown for comparison. Both data are parametrized as $dE_T/d\eta|_{\eta=0} \propto N_{\text{part}}^\alpha$ where α is a free parameter. WA98 and PHENIX concluded that $\alpha = 1.08 \pm 0.06$ and $\alpha = 1.13 \pm 0.05$, respectively.

To estimate ϵ_0 , the transverse area S is also needed in Eq. (7.3). If the medium expands to only $\pm z$ direction, S is approximated by the overlapping area of two colliding nuclei, as shown in Figure 7.7. The transverse area (S) is expressed by

$$S = 2R^2 \cos^{-1} \left(\frac{b}{2R} \right) - bR \sqrt{1 - \left(\frac{b}{2R} \right)^2}, \quad (7.5)$$

where b is the impact parameter, and $R \sim 1.18A^{1/3}$ fm is the size of nucleus. For central Au+Au collision at $b = 0$, $S = \pi R^2 \sim 148$ fm². The impact parameter b and centrality variable C have the relation:

$$b = 2R\sqrt{C}. \quad (7.6)$$

From Eq. (7.5) and Eq. (7.6), S is expressed by

$$S = 2R^2 \left(\cos^{-1}(\sqrt{C}) - \sqrt{C(1-C)} \right). \quad (7.7)$$

Centrality [%]	$\langle N_{\text{part}} \rangle$	$\langle S \rangle$ [fm ²]	$\langle dE_T/d\eta _{\eta=0} \rangle$ [GeV]	$\langle \varepsilon_0 \rangle$ [GeV/fm ³]
0–10	319.7 ± 8.4	109	453 ± 29	5.0 ± 0.3
10–20	229.2 ± 6.6	77	311 ± 21	4.8 ± 0.3
20–40	136.3 ± 4.7	51	173 ± 13	4.1 ± 0.3
40–60	58.2 ± 3.2	27	66 ± 7	2.9 ± 0.3
60–80	19.4 ± 2.4	12	19 ± 4	1.9 ± 0.4

Table 7.1: Summary of centrality, $\langle N_{\text{part}} \rangle$, $\langle S \rangle$, $\langle dE_T/d\eta \rangle$, and ε_0 .

The formation time τ in Eq. (7.3) is assumed to be a constant value $\tau_0 = 1 \text{ fm}/c$.

The obtained Bjorken's initial energy density for each centrality class are summarized in Table 7.1. In Au+Au collisions at $\sqrt{s_{NN}}=130 \text{ GeV}$, the maximum energy density reaches near $5 \text{ GeV}/\text{fm}^3$, which is 68 % higher than that in Pb+Pb collision at CERN SPS ($\sim 3 \text{ GeV}/\text{fm}^3$).

Figure 7.8 shows the experimentally observed modification factors as a function of ε_0 . The uncertainties of $\langle N_{\text{coll}} \rangle$ is shown by vertical brackets here. Horizontal brackets show the uncertainties in ε_0 including systematic error for $\langle N_{\text{part}} \rangle$ (up to 12 %) and systematic error for $\langle dE_T/d\eta \rangle$ (up to 20 %).

In the peripheral and next to peripheral collision, the estimated ε_0 is 2 to 3 GeV/fm^3 and no significant suppression is observed in this region. It is noted that this energy density is close to that achieved at CERN SPS. And this suggests that the reason why the jet quenching was not observed at SPS is due to the smaller energy density ($\sim 2.9 \text{ GeV}/\text{fm}^3$) at the formation time of the equilibrated medium, and shorter life-time of the matter. The decreasing of modification factor begins at above $3 \text{ GeV}/\text{fm}^3$.

7.5 Result from STAR Experiment

Recently, STAR experiment at RHIC reported the result of measurement of inclusive hadron ($(h^+ + h^-)/2$) in Au+Au collisions at $\sqrt{s_{NN}} = 130 \text{ GeV}$ [77]. Figure 7.9 (a) shows the result from STAR experiment, and Figure 7.9 (b) is the present result same as shown in Figure 7.2. It can be argued that both results are reasonably consistent at high momentum region $p_T > 3 \text{ GeV}/c$ and strong suppression is seen in central event in both results. The centrality dependence of suppression is also similar between them. It should be remarked that the result of STAR is on the inclusive charged hadrons so that they contain protons and kaons.

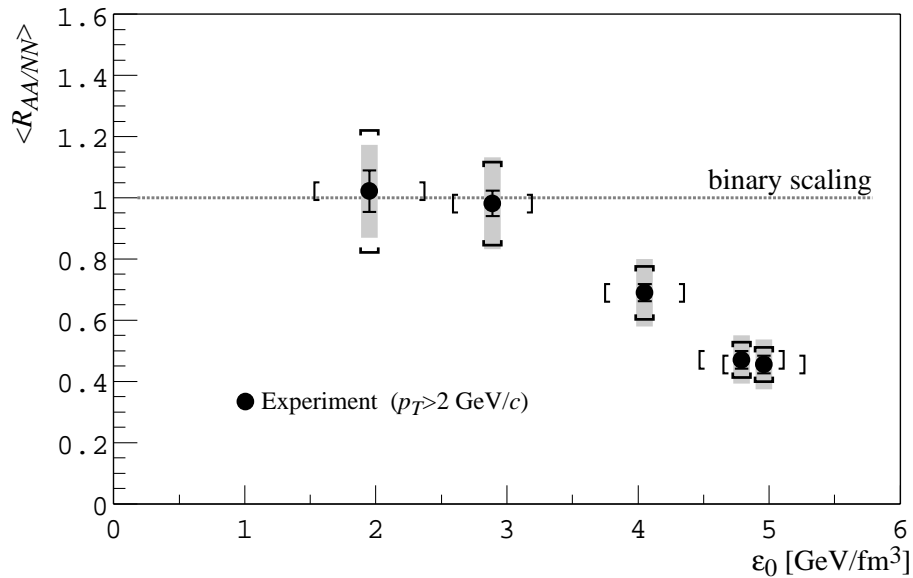


Figure 7.8: Average $R_{AA/NN}$ at $p_T > 2$ GeV/ c as a function of ϵ_0 . Solid vertical lines show error for π^0 yield, and gray bars show its systematic uncertainties. Brackets show the uncertainties of $\langle N_{\text{coll}} \rangle$ (vertical) and ϵ_0 (horizontal).

7.6 Comparison with the Theoretical Calculations

7.6.1 Perturbative QCD Calculation

X.-N. Wang performed theoretical predictions of π^0 spectra in the $\sqrt{s_{NN}} = 130$ GeV Au+Au collision[35], and it is compared to the present result here. His calculation is based upon a parton model with pQCD hard scattering which was described in Section 2.4. The model includes the intrinsic transverse momentum with broadening due to multiple parton scattering (Cronin effect), and jet quenching effect due to parton energy loss inside a dense medium. Result of comparison is shown in Figure 7.10. Experimental data are same as shown in Figure 7.1. The comparisons are done for only the most central ($C = 0-10$ %) data and the most peripheral data ($C = 60-80$ %). Three theoretical results are shown by dashed, dotted, and solid curves, those are described as following (i) to (iii), respectively.

- (i) A prediction of π^0 yield by Eq. (2.12) without any nuclear effect (dotted line in Figure 7.10). Scaling for $A+A$ collision is performed by integrating cross section of π^0 in $N+N$ interactions using a nuclear thickness function. This is equivalent to the $\langle N_{\text{coll}} \rangle$ scaling method.
- (ii) A prediction of π^0 yield modified by modeling the shadowing and Cronin effect

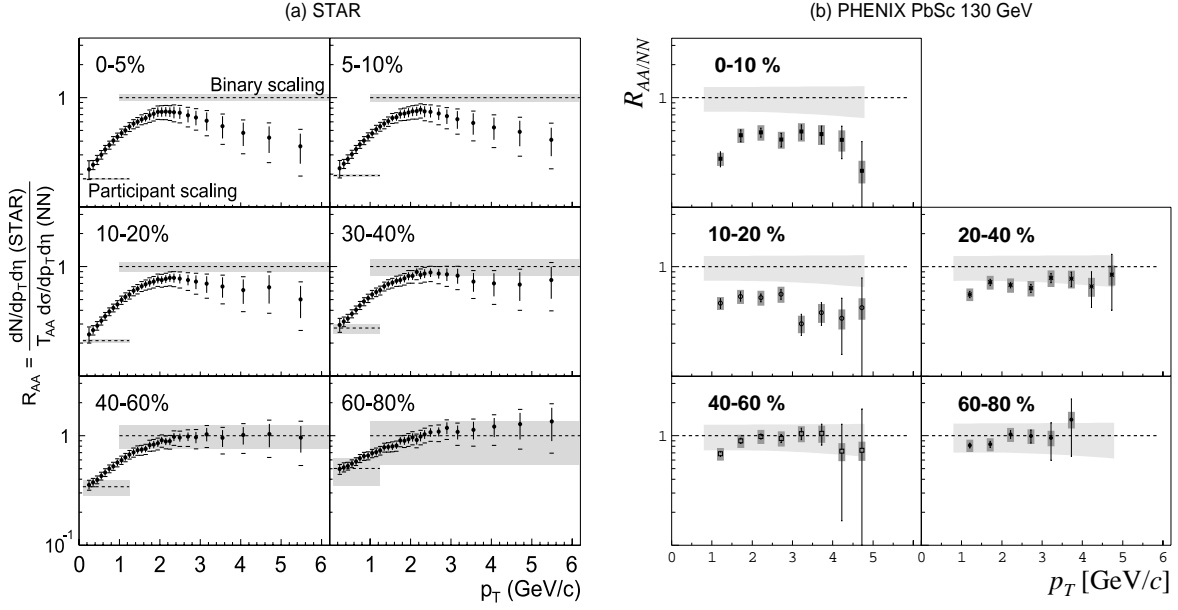


Figure 7.9: (a) High- p_T charged particle yields measured from STAR[77] at RHIC. (b) Present data π^0 same as Figure 7.2.

(dashed line in Figure 7.10). Shadowing effect was demonstrated by modifying the parton structure function by Eq. (2.16). And Cronin effect was demonstrated by smearing the parton fragmentation function by Eq. (2.19).

- (iii) In addition to (ii), “jet quenching” was introduced and modeled as an average energy loss of 0.25 GeV/fm for partons (solid line in Figure 7.10).

The peripheral data agrees reasonably well with all three scenarios. The central data is significantly below the calculations (i) and (ii). Shadowing effect causes weak suppression at $p_T < 2$ GeV/c but it can not explain the strong suppression at high- p_T . The calculation with 0.25 GeV/fm parton energy loss (iii) shows better agreement to the experimental data.

7.6.2 Hydrodynamical Calculation

Recently, T. Hirano and Y. Nara calculated the energy loss of partons in the medium with a three-dimensional hydrodynamical space-time evolution model[78, 79](Hydro+Jet). The hydrodynamical calculation treats the matter produced by $A+A$ collisions as a fluid. The fluid evolves according to the relativistic hydrodynamic equations:

$$\partial_\mu T^{\mu\nu} = 0, \quad T^{\mu\nu} = (\varepsilon + P)u^\mu u^\nu - P g^{\mu\nu}, \quad (7.8)$$

$$\partial_\mu n_B^\mu = 0, \quad n_B^\mu = n_B u^\mu, \quad (7.9)$$

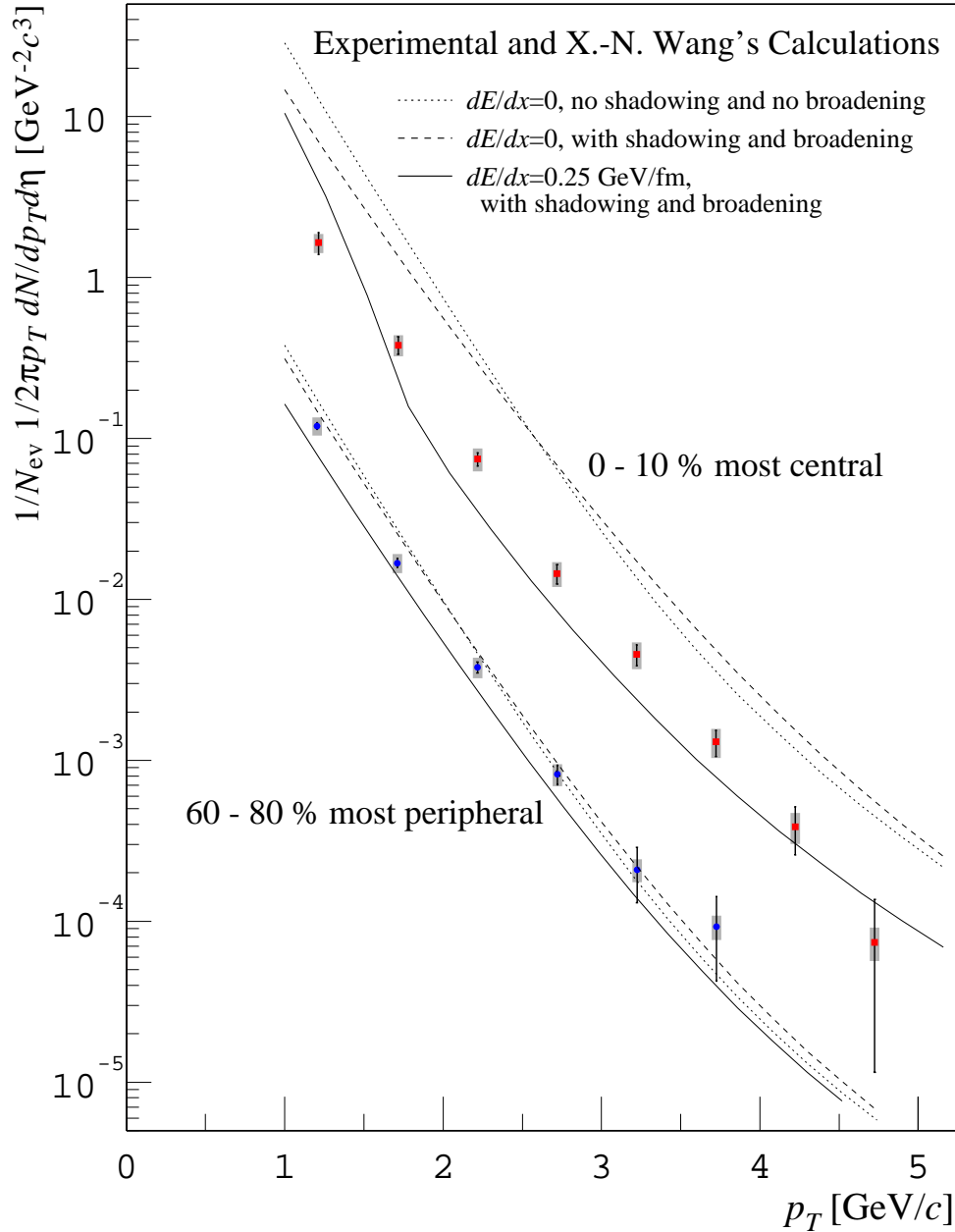


Figure 7.10: The most central event class and peripheral event class are compared to the pQCD calculations by X.-N. Wang[35]. Experimental data are shown as points with statistical errors (solid vertical lines) and systematic errors (gray bold bars). Solid curves are the result of calculation assuming constant $-dE/dx = 0.25$ GeV/fm and nuclear shadowing and broadening. Dashed curves are not assuming dE/dx but assuming nuclear shadowing and broadening. Dotted curves are assuming neither dE/dx nor any nuclear effect and this is same as $N+N$ superposition.

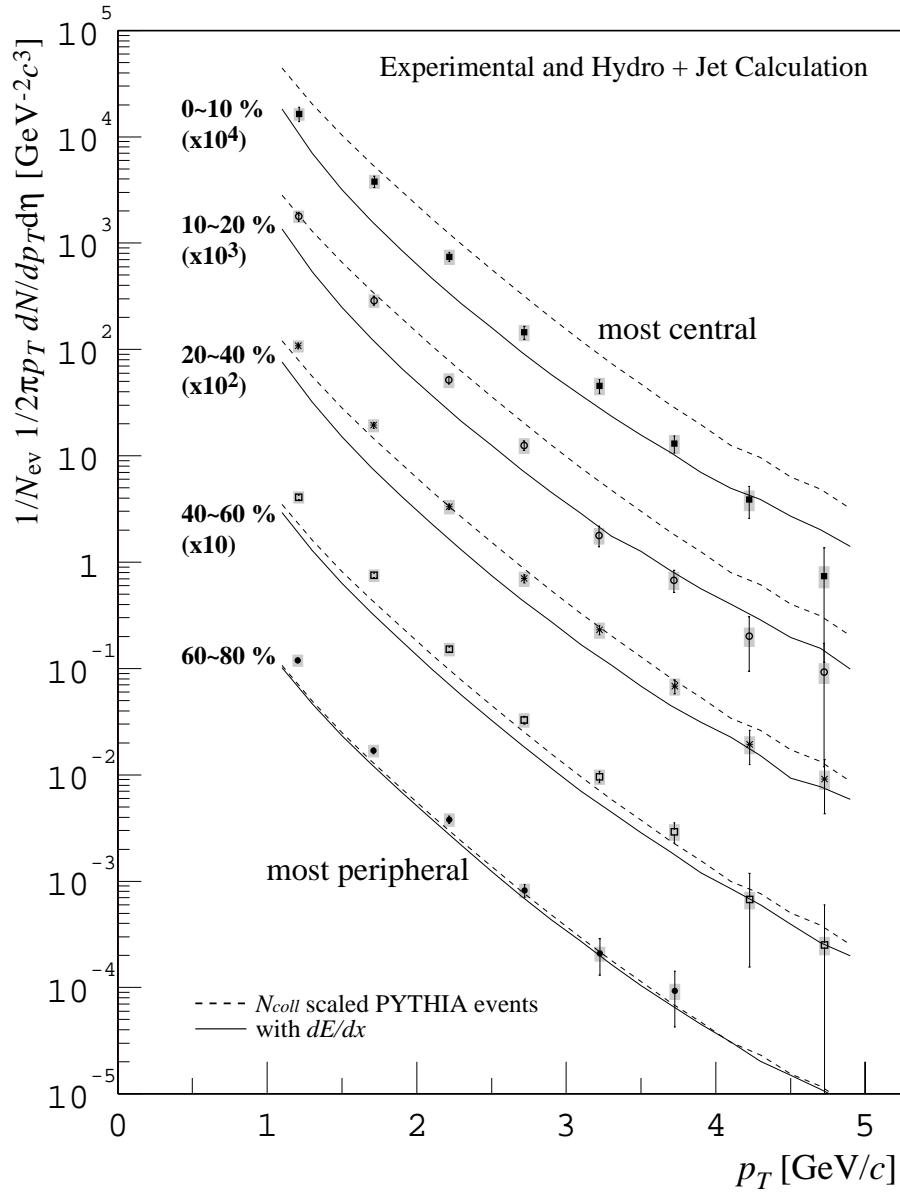


Figure 7.11: Comparison between PHENIX data and Hydro+Jet calculation[78, 79].

where $T^{\mu\nu}$ is the energy-momentum tensor, ε is the energy density of the medium, n_B is the baryon density, $u^\mu = \gamma(1, \beta_x, \beta_y, \beta_z)$ is four dimensional velocity. Eq. (7.8) represents energy and momentum conservation, and Eq. (7.9) represents the baryon number conservation.

The hydrodynamical model reproduces well particle spectra at soft region. Also the flow effect which is collective motion of particles in the $A+A$ collisions is explained as pressure gradients inside the equilibrated matter[80, 81].

PYTHIA was used to generate the hard partons. Then the hard partons were explicitly injected into the hydrodynamical fluid. The parton energy loss in the fluid is parametrized by

$$\frac{-dE}{dx} = \varepsilon\sigma\rho(\tau, \mathbf{r}), \quad (7.10)$$

where ε is an energy loss per scattering, σ is a parton-parton cross section, and $\rho(\tau, \mathbf{r})$ is the deconfined parton density at a given space-time position. Since $\varepsilon\sigma$ is unknown, it was taken to be a free parameter. The formation time of equilibrated fluid $\tau_0 \sim 0.6$ fm/ c and the first order phase transition at temperature $T_c = 170$ MeV were assumed. During the phase transition at $T = T_c$, the $\rho(\tau, \mathbf{r})$ is reduced by a fractional factor of QGP phase. $\rho(\tau, \mathbf{r})$ below T_c is set to zero. This means no energy loss is assumed in ordinary hadronic matter. After the parton energy loss is calculated, fragmentation of the parton into jet hadrons were simulated by PYTHIA.

Figure 7.11 shows the result of calculation and experimental data. The dashed lines are the results of PYTHIA Monte Carlo calculation scaled by number of binary collisions $\langle N_{\text{coll}} \rangle$, without including energy loss. No other normalization was performed. Solid lines are results of Hydro+Jet calculations with $\varepsilon\sigma = 0.06$ GeV fm². In the most peripheral events (bottom), experimental data are well reproduced by both calculations with and without dE/dx . Below 2 GeV/ c , the model slightly underestimates the data. This discrepancy at low p_T region is probably because no soft particles are added. In the most central and next to the most central events, the experimental data is below PYTHIA calculation and Hydro+Jet with dE/dx gives better prediction at high- p_T .

7.6.3 Comparison to a Simple Toy-Model

As the final discussion, an attempt was made to explain the relation between modification factor and centrality using a simple toy-model. The toy-model is based on the assumption that parton energy loss is proportional to the local energy density of the medium. The assumption is not unreasonable because in general the opacity of the medium is proportional to inverse of mean free path λ of the incident particle. The mean free path is calculated by $\lambda = \rho/\sigma$, where ρ is the number density of the medium and σ is scattering cross section. In the jet parton scattering, it is assumed that ρ is

proportional to the energy density of the medium, and jet parton loses some fractional energy per scattering.

After formation of the medium, the energy density of the medium is expected to decrease as a function of proper time τ with respect to the collision time. The energy density at proper time τ is expressed by

$$\varepsilon(\tau) = \varepsilon_0 \frac{1}{\tau/\tau_0}. \quad (7.11)$$

Since free streaming medium is assumed, the characteristics of thermalized medium such as pressure is ignored. If the pressure effect and transverse development of the medium is considered, $\varepsilon(\tau)$ decreases more rapidly.

Analog to the fact that dE/dx of a high energy electron traversing in the electromagnetic field is proportional to charge density, if the parton energy loss is proportional to the energy density and expressed by

$$-dE/dx = E_0 \varepsilon, \quad (7.12)$$

where E_0 is a constant value, the total jet energy loss in the medium is estimated to be

$$-\Delta E = \int_0^{x_{max}} \frac{dE}{dx} dx = E_0 \int_0^{x_{max}} \varepsilon_0 \frac{1}{\tau/\tau_0} dx, \quad (7.13)$$

where x is the transverse position of the parton. No parton energy dependent energy loss is considered here. In Eq. (7.13), only the partons at $x = 0$ at the formation time is considered and $x = \tau - \tau_0$ for high energy partons traversing at the speed of light. The integration upper limit x_{max} is defined as the position of parton at the ‘‘cut-off time’’ (τ_c) when energy loss vanishes by phase transition from QGP to ordinary hadron gas, as one of the possibilities. If one assume cut-off occur due to phase transition, τ_c relates to the phase transition energy density ε_c by $\tau_c = \tau_0(\varepsilon_0/\varepsilon_c)$ where Eq. (7.11) was used.

For the central collision, the estimated transverse area is $\sim 110 \text{ fm}^3$, the radius of the medium is $\sqrt{110 [\text{fm}^2]/\pi} \sim 6 \text{ fm}$. If this is larger than τ_c , the cut-off occur while the parton is still in the medium. If the τ_c is late enough, the parton particle reaches at the surface of medium before the system cool down to ε_c .

By the assumptions above, the x_{max} in Eq. (7.13) is replaced by τ_{PT} and ΔE would be

$$-\Delta E = E_0 \varepsilon_0 \tau_0 \int_{\tau_0}^{\tau_c} \frac{1}{\tau} d\tau = E_0 \varepsilon_0 \tau_0 \log \frac{\tau_c}{\tau_0}. \quad (7.14)$$

The shape of modification factor R_{AA} as a function of ε_0 is obtained by simply modifying the p_T to the $p_T - \Delta E$ and calculating ratio:

$$R_{AA} = \frac{1}{p_T'' - p_T'} \int_{p_T'}^{p_T''} \frac{d^2 n(p_T + \Delta E)}{p_T dp_T d\eta} \bigg/ \frac{d^2 n(p_T)}{p_T dp_T d\eta} dp_T, \quad (7.15)$$

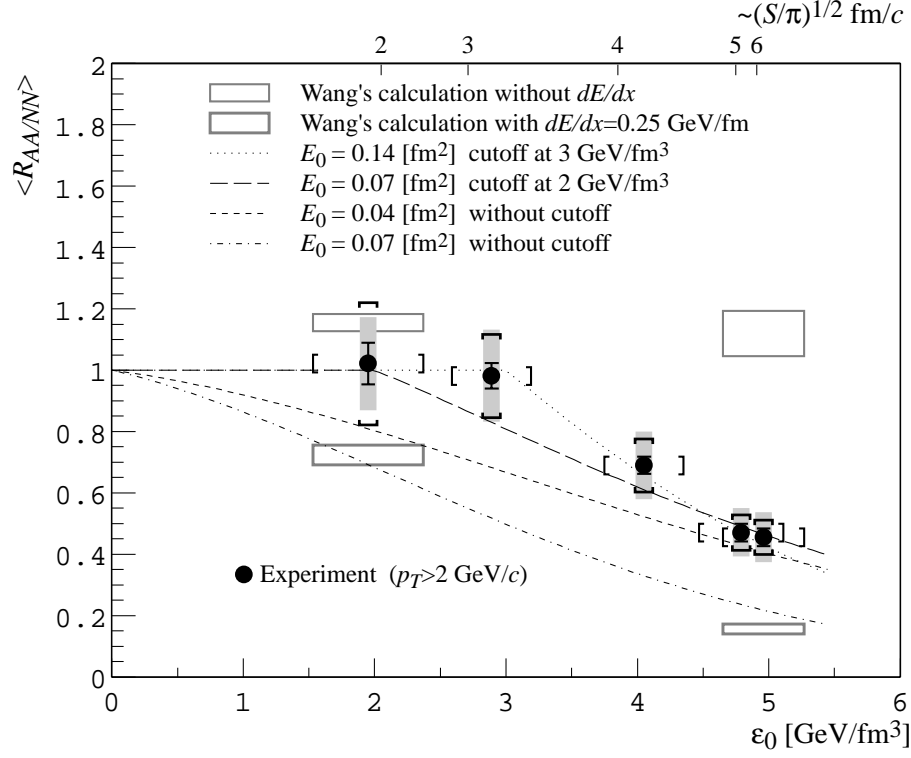


Figure 7.12: Average $R_{AA/NN}$ at $p_T > 2$ GeV/c as a function of ϵ_0 . Solid vertical lines show error for π^0 yield, and gray bars show its systematic uncertainties. Brackets show the uncertainties of $\langle N_{\text{coll}} \rangle$ (vertical) and ϵ_0 (horizontal). Two horizontal solid lines show the uncertainty of π^0 yield in $N+N$ reference. Results of toy-model calculation with or without assuming cut-off energy density and different energy loss strength E_0 are shown by curves (see text in the plot). Also the result of pQCD calculation by X.-N. Wang are shown again.

where the distribution $d^2n/p_T dp_T d\eta$ is the distribution without energy loss, and p'_T and p''_T are the p_T region of π^0 currently considering. The charged pion distribution of in $N+N$ collisions which was used in Section 7.2 was used here too.

Comparison with Data

Figure 7.12 shows the comparison between the toy-model calculation and measurement. The experimental data are same as in Figure 7.8. For comparison, the result of pQCD calculation by X.-N. Wang are shown again. Curves in Figure 7.12 shows the result of toy-model calculation. Results of four settings (i) $E_0 = 0.14$ fm² with $\epsilon_c = 3$ GeV/fm³, (ii) $E_0 = 0.07$ fm² with $\epsilon_c = 2$ GeV/fm³, (iii) $E_0 = 0.04$ fm² with $\epsilon_c = 0$ GeV/fm³, and (iv) $E_0 = 0.07$ fm² with $\epsilon_c = 0$ GeV/fm³ were shown.

Qualitatively the tendency of experimental data is consistent to the toy-model calculation with $\varepsilon_c = 3.0 \text{ GeV/fm}^3$ and $E_0 = 0.14 \text{ fm}^2$. Calculation with smaller ε_c ($= 2.0 \text{ GeV/fm}^3$) and weaker E_0 ($= 0.07 \text{ fm}^2$) also does not disagree to the data. The result of pQCD calculation assuming energy loss in both peripheral and central is close to the toy-model without assuming finite ε_c . But both the pQCD calculation and the toy-model without finite ε_c predict that there should be suppression already at peripheral collision, and they can not reproduce tendency of modification factor. It is more natural to introduce the cut-off at 2.0 to 3.0 GeV/fm^3 to account for the experimental data with this toy-model.

Chapter 8

Summary and Conclusions

The measurements of π^0 production from Au+Au collisions at $\sqrt{s_{NN}}=130$ GeV were carried out with the PHENIX detector system of RHIC, BNL.

Neutral pions were reconstructed from two photons measured with PHENIX lead-scintillator electromagnetic calorimeter. The kinematic region of measured π^0 's were approximately from 1.0 GeV/ c to 5.0 GeV/ c in the transverse momentum, and from -0.35 to 0.35 in rapidity. The p_T spectra of π^0 were measured for five centralities of event classes, from central to peripheral. From p_T spectra of π^0 and results of Glauber model calculation, the nuclear modification factor $R_{AA/NN}$ as a function of p_T and centrality was obtained.

The π^0 spectrum in peripheral ($C=60-80$ %) Au+Au collisions was consistent with the π^0 spectrum in $N+N$ collisions scaled by $\langle N_{\text{coll}} \rangle$. No suppression or enhancement was observed in the peripheral events. This was same for also the next to peripheral event class ($C=40-60$ %). The strong suppression of high- p_T π^0 was observed in the most central ($C=0-10$ %) collisions. It was also found the suppression is beginning at $C=20-40$ %. The result is quite different from the SPS result where strong enhancement was observed. The suppression is not explained by the nuclear shadowing and Cronin effect.

Data was compared with the perturbative QCD based calculation and Hydro+Jet calculation model. In both models, the results with assuming parton energy loss show better qualitative agreement to the experimental data than without assuming energy loss. While the Hydro+Jet calculation predicts more gradual suppression, the data indicates sudden suppression for $C < 40$ %.

From the measured E_T , the Bjorken's initial energy density were estimated for each centrality. In the picture, the suppression starts after $\varepsilon_0 > 3$ GeV/fm³. Since the estimated initial energy density at the SPS is less than 3 GeV/fm³, it is consistent that the suppression is not observed in the CERN experiments. Using a toy-model, the ε_0 dependence of the modification factor is qualitatively described by assuming that parton energy loss vanishes at certain cut-off energy density $\varepsilon_c \simeq 2$ GeV/fm³. Without cut-off energy density, the shape of $R_{AA/NN}$ as a function of ε_0 could not be explained.

Acknowledgments

It is a great pleasure to express my sincere gratitude to Prof. H. Hamagaki. I thank him for his encouragement and many peaces of valuable advice, and zealous support in many aspects. His abundant knowledge has always stimulated and guided me. Without his advice and discussions with him, I could not carry out my study at all. Special thanks are due to Prof. R.S. Hayano. Without his introduction, I would not even have my teeth into relativistic heavy ion experiment.

I wish to acknowledge all the collaborators of the PHENIX experiment. My work would never be completed without their great efforts and collaboration. I especially thank the Photon Working Group people of the PHENIX for their help and friendship. I am much obliged to Dr. G. David who is the team leader of our group, for his help in the data analysis and a great deal of valuable advice. I am under a special obligation to Dr. S. Mioduszewski, Dr. S. Botelho, and Dr. C. Woody for their efforts on the analysis and advice. I appreciate Dr. S. Nishimura for his introduction of the analysis technique. I am also grateful to Mr. H. Torii for his extensive calibration of the EMCal and valuable comments in the analysis. I would like to thank Dr. T. Sakaguchi for his development of excellent Fast Monte Carlo simulation software and contribution to the analysis.

I thank Dr. E. Kistenev, A. Bazilevsky and all the PHENIX EMCal group who constructed and maintained the EMCal, for their help and useful advice.

I acknowledge Prof. W.A. Zajc, the spokesperson of the PHENIX experiment, for his hospitality, various arrangements for my activity at BNL, and hearty encouragement. My sincere thanks are also due to Ms. D. Early, a very kind and able group secretary, for her hospitality and guidance for a stranger in Brookhaven. I would also like to thank Dr. Y. Akiba and Dr. K. Shigaki for their guidance, helps, and precious advices especially when I begin the study in Brookhaven.

I specially wish to acknowledge people in Nagasaki Institute of Applied Science, Waseda University, and Oak Ridge National Laboratory (ORNL). I am obliged to Prof. Y. Tanaka, Prof. J. Kikuchi, Prof. A.L. Wintenberg, Prof. G.R. Young, and all the people in their group who were the collaboration of the RICH FEE group. Without the successful completion of the development, I could not have a credit to write thesis

in the PHENIX collaboration. I thank Mr. H. Hara, Mr. M. Hibino, Mr. K. Ebisu, Mr. M. Tamai, and many people for their great efforts and collaboration.

I would like to acknowledge Mr. T. Matsumoto, Mr. K. Kato, and Mr. S. Kametani, for their technical support especially for their helps of off-line data analysis, operating the computer, and their efforts also in RICH FEE development.

Here I acknowledge all the members of the Center of Nuclear Study at the University of Tokyo. I express my special thanks to Dr. K. Ozawa and Dr. M. Inuzuka for giving me instructive and indispensable comments and advice. I thank institute secretaries, Ms. M. Hirano, Ms. K. Takeuchi, Ms. I. Yamamoto, Ms. H. Otsu, Ms. N. Suzuki, and Ms. T. Itagaki, for their daily helps and encouragements.

I wish to express my thanks to the staff of the RHIC project, Collider-Accelerator and Physics Department at BNL. The PHENIX experiment is supported by the U.S. Department of Energy under contracts with the U.S.-Japan High Energy Physics Collaboration Treaty. More than 450 scientists, engineers, and graduate students from 44 institutes in the world contributed to the PHENIX experiment. I thank everybody.

This analysis was mainly supported by the RIKEN PHENIX Computing Center in Japan (CCJ). I thank all the staff of the CCJ.

I am also grateful to Dr. T. Hirano who is one of the authors of Hydro+Jet simulation code, for fruitful discussions and comments. He gave me a very nice result by Hydro-Jet calculation.

I am grateful to Prof. K. Makishima, Prof. T. Matsui, Prof. H. Sakamoto, and Prof. S. Shimoura for their valuable advice. I am under a particular obligation to Prof. K. Tokushuku, for his truly relevant advice and proof-readings.

I thank Mr. Y. Kusakabe and Dr. H. Hukaya for their cooperate while I am writing the thesis and their friendship.

At last but not the least, I express my appreciation to my family members and Ms. I. Ushiba. It was entirely due to their support and encouragement that I could accomplish my study and have such precious experiences for my life.

Appendix A

QGP signatures

A.1 Overview

In this appendix, the possible signatures of deconfined matter currently proposed are briefly explained. Since so many signals are proposed until now, it is impossible to explain all of them. Only some representatives are explained. Those are summarized in Table A.1 and briefly explained below with the result in CERN. More detailed explanations are found in Ref. [15].

A.2 J/Ψ suppression

Matsui and Satz predicted that the formation of a QGP would screen the color binding potential, preventing the c and \bar{c} quarks to form charmonium state, and leading the measurable suppression of J/Ψ yield[82]. It is similar to the effect of Debye screening. In the high energy density medium, the $c\bar{c}$ interaction is screened. Then the linear term in the potential vanishes, and $c\bar{c}$ pair can not form J/Ψ .

At the CERN SPS, the NA38 and NA50 experiments have extensively studied the J/Ψ production in $A+A$ collisions. NA38 experiment reported the J/Ψ production yield is suppressed with respect to the Drell-Yan di-muons in S+U collisions. And the

Signals	Main observables
J/Ψ suppression (Debye screening)	depletion in J/Ψ yield
Jet quenching	depletion in high- p_T hadron spectra
Chiral symmetry restoration	modifications of $\rho, \omega, \phi \rightarrow e^+e^-$ spectra and charged/neutral fluctuation
Photon enhancement	direct γ production
Strangeness enhancement	K/π ratio and multi-strange baryon production

Table A.1: Some of the typical signatures of QGP and its observables.

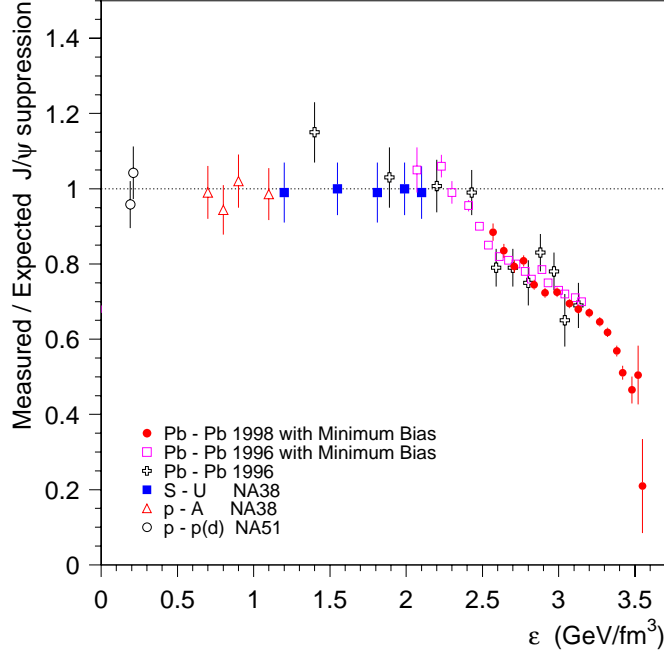


Figure A.1: The observed J/Ψ suppression in CERN SPS[83]. The measured J/Ψ yields are divided by the expected yields assuming only the nuclear absorption. The data is shown as a function of the energy density reached in the several collision systems.

suppression increases monotonically from $p+p$ to S+U[84]. The NA38 observation is understood in terms of nuclear absorption of the $c\bar{c}$ pair before it forms the J/Ψ state.

Based upon the results from the NA38 experiment, NA50 experiments tested the Pb+Pb collisions. NA50 experiment reported the production cross section in Pb+Pb collisions was found to be 77 % below the value expected on the basis of the normal nuclear absorption[83]. This anomalous suppression is studied precisely with higher statistics. Finally the observation resulted in that J/Ψ production is considerably suppressed in Pb+Pb collisions with an impact parameter.

Figure A.1 shows the results of NA50 experiment. The figure shows the ratio between the observed J/Ψ suppression pattern and the normal nuclear absorption curve, that reproduces $p+A$ and S+U results. The horizontal axis is expected energy densities reached in the collision systems. From the figure, it is deduced the first anomalous drop in the J/Ψ yield start at energy density of 2.3 GeV/fm^3 . Also the next anomalous drop looks beginning around 3.1 GeV/fm^3 of energy density. The first drop can be understood as due to the disappearance of the χ_c mesons, affect to the J/Ψ through its $\chi_c \rightarrow J/\Psi + \gamma$ decay. The second drop is probably dissolving the J/Ψ state.

The observation of anomalous J/Ψ suppressions in CERN can be considered as the

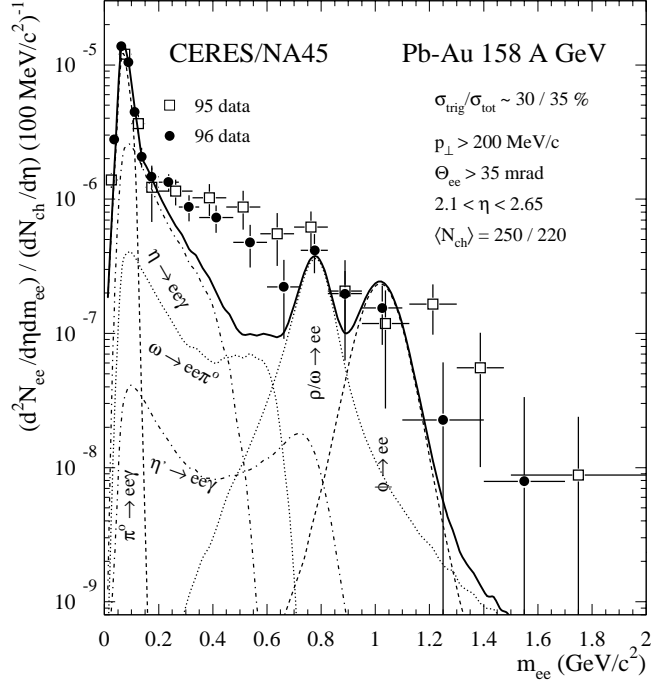


Figure A.2: Inclusive e^+e^- mass spectrum obtained from CERES experiment[85]. The data are compared to the sum of the expected contributions from hadron decays (solid line).

strong evidence of QGP. In RHIC, with the much higher energy density $\sim 5 \text{ GeV}/\text{fm}^3$, much stronger suppression might be observed. It is still under investigation.

A.3 Jet quenching

The momentum of hadrons originated from high- p_T jets decrease if the QGP has formed. The jets lose more energy in quark matter than in hadronic matter. Jet energy loss is observed as the depletion in the hadron p_T spectra and effectively jet yield looks suppressed. The “jet quenching” observation is the main subject of this thesis. It was not observed in CERN SPS. Further explanations are given already in this thesis, and the strong suppression of high- p_T hadrons were observed at RHIC.

A.4 Chiral Symmetry Restoration

Features of vector mesons (ρ, ω, ϕ , and etc.) production from the hadronic matter is sensitive to the restoration of the chiral symmetry[86, 87]. In the deconfined matter, chiral symmetry might be restored and it causes modifications in characteristics of those

resonances; their mass, width, and decay branching ratio, are expected to change from those values in the vacuum.

In CERES/NA45 experiment, the di-lepton invariant mass spectra were observed and large anomaly was found. The CERES/NA45 experiment performed measurement of low-mass di-electrons in the mass region below $2 \text{ GeV}/c^2$ in collisions of $158A \text{ GeV}$ Pb on Au[85]. A results of invariant mass spectra in the $158A \text{ GeV}$ Pb+Au collisions is shown in Figure A.2. In this mass region, there are known contributions from vector meson decays. But the observed data had strong enhancement in mass spectrum below ρ mass region and it can not be explained by the known contributions. Recently, CERES reported that larger enhancement than $158A \text{ GeV}$ was observed in Pb+Au collision at $40A \text{ GeV}$ [88].

More than 150 theoretical papers have appeared on the possible interpretation of the CERES results. There seems to be a general consensus that the observed enhancement is due to direct radiation from the fireball, dominated by annihilation process $\pi^+\pi^- \rightarrow \rho \rightarrow e^+e^-$. The shape of mass spectra requires strong medium modifications of the intermediate ρ , and it is interpreted as a precursor of the chiral symmetry restoration, where ρ mass is shifted lower and its width is spreading.

A.4.1 Disoriented Chiral Symmetry Restoration

The temporary restoration of the chiral symmetry in nuclear collisions may result in the formation of domains of disoriented chiral condensate (DCC)[89]. Such domain of DCC decays into neutral and charged pions and neutral to charge ratios substantially different from one third, and large fluctuation of the ratio maybe observed. No evidence of DCC is observed in past experiments yet.

A.5 Thermal photon enhancement

Another strong evidence of the quark matter is in an observation of the direct thermal photon [90]. Photons and leptons do not interact strongly and escape from the thermal equilibrating medium. Photons are produced in the hot initial state by the Compton scattering process of a quark and a gluon ($qg \rightarrow q\gamma$). Photons carry information on the initial state parameters, and bring the direct information about the temperature of the matter. The measurement of direct photon is difficult due to high multiplicity of background γ from π^0 and η decay.

SPS WA98 experiment group achieved this measurement and they reported the observation of the direct photons [91, 92, 93]. In the RHIC experiments, the same measurement will be possible in future.

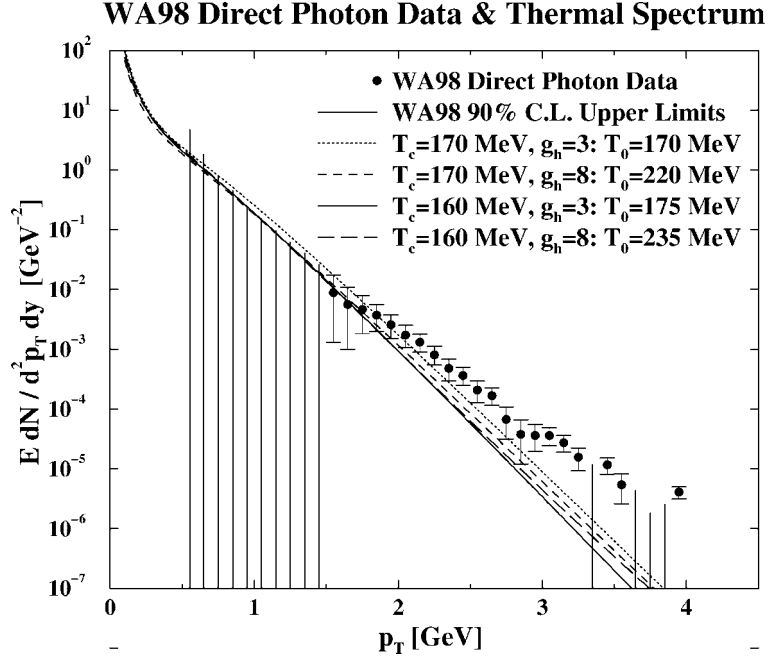


Figure A.3: WA98 direct photon data and upper limits on the initial temperature. The theoretical spectra supporting the phase transition from QGP to ordinary hadron gas (solid, short dashed, and long dashed lines) are compared with the experimental upper limits (vertical lines) and data (points).

A.6 Strangeness enhancement

In hadronic reactions, the production of hadrons containing s and \bar{s} quarks is normally less likely than the production of hadrons containing only u and d valence quarks. If QGP is formed and chemical equilibration is achieved, it is expected that the strange quarks yield will be enhanced [94, 95]. In the plasma, the dominant process of strangeness production is gluon scatterings ($gg \rightarrow s\bar{s}$) and quark-antiquark annihilations ($q\bar{q} \rightarrow s\bar{s}$). In the high temperature medium, production speed of $s\bar{s}$ pairs exceeds the speed of lighter quark pair creations because the further pair production of u and d are blocked by Pauli principle. If the chemical potential of light quarks exceeds mass of strange quarks ($\sim 150 \text{ MeV}/c^2$), the strangeness pair-creation become benefit. The situation continues until the productions and annihilations reaches chemical equilibrium. The equilibration time until chemical equilibration depends on the temperature T . For the plasma with $T = 160 \text{ MeV}$, the equilibration time is estimated to be $\sim 6 \text{ fm}/c$. If the long duration QGP is formed and the strangeness abundance saturates, the production of strange hadrons (Λ , Ω , and etc.) increases with respect to the ordinary nuclear matter. On the other hand, in the ordinary nuclear matter, the equilibration time exceeds 100 fm

due to small cross section of hadronic re-scattering such as $\pi^0 + p \rightarrow K^+ + \Lambda$. In addition, the production enhancement of multi-strange baryons will be prominent[96] in the high strangeness contents.

In the experiment of Pb+Pb collisions at SPS, a clear enhancements of $\bar{\Lambda}$, $\bar{\Xi}$, Ω^- and $\bar{\Omega}^+$ were observed compared to the p +Pb collisions[97]. The enhancements were stronger for multi-strangeness baryons, exceeded one order of magnitude in the case of Ω , and it can not be reproduced by only the hadronic re-scattering.

Appendix B

Hadron Spectra in $N+N$ Collisions at $\sqrt{s} = 130$ GeV

The comparison between Au+Au collision and $N+N$ collision requires p_T spectra of hadron productions in $N+N$ collisions at $\sqrt{s} = 130$ GeV, but no experimental data of $N+N$ collision is available at this energy. In this appendix, the inclusive charged hadron spectra in $p+p$ collision data measured by ISR[27], and $p+\bar{p}$ collisions at $Spp\bar{S}$ [23] and Tevatron[22] are referred, and the interpolation to the RHIC energy are performed[98, 99]. The collision energies and nuclear species used for interpolation are listed in Table B.1.

To generate a reference p_T distribution for the RHIC energy, the inclusive charged hadron data in Table B.1 were fitted with the empirical function form:

$$\frac{d\sigma^2}{2\pi p_T dp_T d\eta} = A \left(1 + \frac{p_T}{p_0}\right)^{-n}. \quad (\text{B.1})$$

The cross sections were interpolated to 130 GeV at several fixed p_T , and interpolated cross sections were fitted with the identical power-law function to obtain a smooth reference distribution. The fit parameters obtained are $A = 330 \text{ mb}\cdot\text{GeV}^{-2}c^3$, $p_0 = 1.72 \text{ GeV}/c$, and $n = 12.4$. Figure B.1(a) shows the past data in Table B.1(points), fit results for the past data (dotted lines) and fit result for the interpolation results (solid line). The dashed lines below and above a solid line indicate the systematic uncertainty. Systematic uncertainties include systematic discrepancies of data sets take by different experiment,

Experiment	Collisions	Reference
CERN ISR Brit.-Scan.	$p+p$ at $\sqrt{s} = 23, 53, \text{ and } 65$ GeV	[27]
CERN $Spp\bar{S}$ UA1	$p+\bar{p}$ at $\sqrt{s} = 200, 500, \text{ and } 900$ GeV	[23]
FNAL Tevatron CDF	$p+\bar{p}$ at $\sqrt{s} = 630 \text{ and } 1800$ GeV	[22]

Table B.1: $N+N$ collision data used to estimate the hadron spectra at RHIC energy.

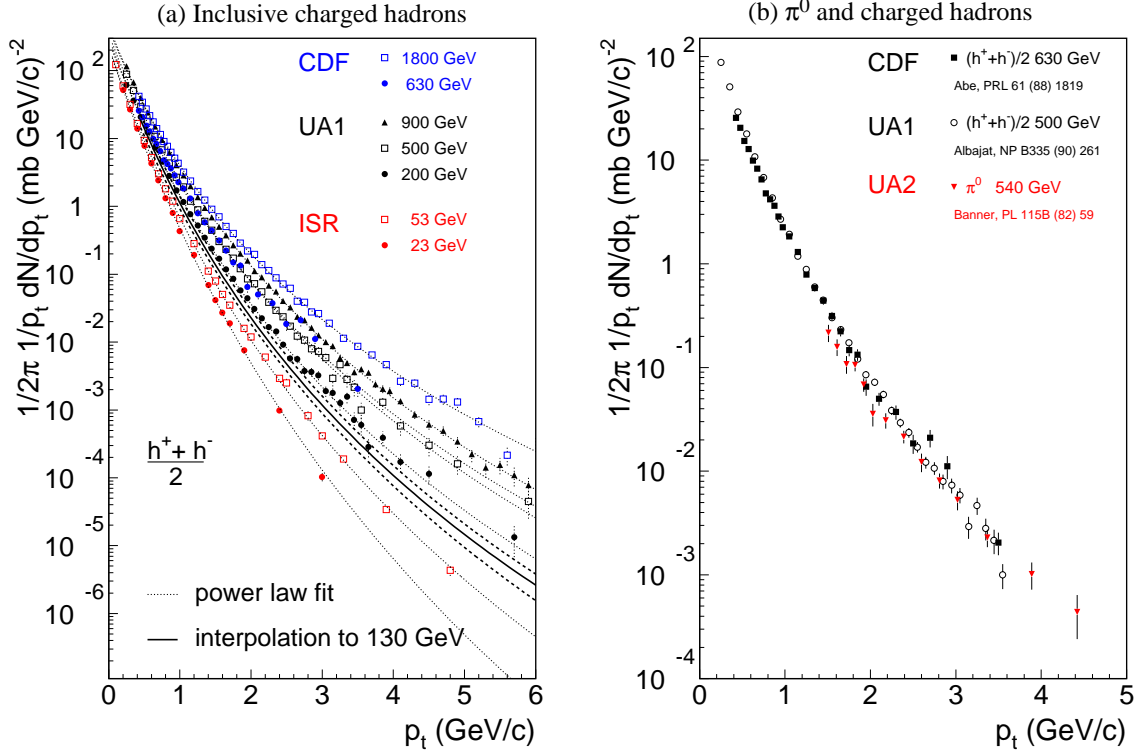


Figure B.1: (a) shows inclusive charged particle production for $N+N$ collisions. Points show the inclusive hadron spectra $(h^+ + h^-)/2$ obtained in the past experiments. Dotted lines show the fit results for the experimental data. Solid line is a obtained hadron spectra at $\sqrt{s} = 130$ GeV by interpolation. Dashed lines show the systematic uncertainties for the interpolation. (b) shows the example of systematic discrepancy between similar collision energy.

and uncertainties in the interpolation procedure. Former uncertainty was estimated to be about 20 % by comparing different data sets at similar \sqrt{s} collisions. An example is given in Figure B.1(b). The same systematic errors on $N+N$ collision is estimated by comparison to other extrapolations done by the STAR collaboration[100], by Wang, and other theoretical results (see [98] and references therein).

For π^0 's, the obtained inclusive charged hadron cross section was scaled by the charged pion to charged hadron ratio $\pi/h \sim 0.63 \pm 0.06$ observed at the ISR[27]. This is nearly independent of p_T at $p_T > 1.5$ GeV/c region within the error.

Appendix C

Supplements

C.1 Natural Units

In this thesis, the “natural units” are commonly used. This unit system is often used in high energy physics. Under the natural units, the Planck constant \hbar and speed of light in vacuum c is defined by

$$\hbar = 1, \tag{C.1}$$

$$\text{and } c = 1, \tag{C.2}$$

with implicit assumptions:

$$4\pi\epsilon_0 = 1, \tag{C.3}$$

$$\text{and } \alpha = \frac{e^2}{4\pi\epsilon_0\hbar c} = e^2 = \frac{1}{137}, \tag{C.4}$$

where ϵ_0 is the permittivity of free space, α is the fine structure constant, and e is the electron charge. Also

$$\hbar c = 1 = 197.3 \text{ [MeV fm]}. \tag{C.5}$$

C.2 Kinematic Variables

Choosing the beam direction as the z -axis, the rapidity variable y of a particle is defined as

$$y \equiv \frac{1}{2} \ln \left(\frac{E + p_z}{E - p_z} \right) = \tanh^{-1} \left(\frac{p_z}{E} \right), \tag{C.6}$$

where E is the total energy of the particle and p_z is the z -component of the momentum. The rapidity is transformed under the Lorentz boost in the z -direction with the velocity β as

$$y \rightarrow y + \tanh^{-1} \beta, \tag{C.7}$$

and shape of rapidity distribution is Lorentz invariant.

The transverse momentum p_T and the transverse mass m_T of a particle are defined by

$$p_T^2 \equiv p_x^2 + p_y^2, \quad (\text{C.8})$$

$$\text{and } m_T^2 \equiv m^2 + p_x^2 + p_y^2, \quad (\text{C.9})$$

respectively where m is the particle's rest mass and $p_{x(y)}$ is the $x(y)$ -directional component of particle momentum.

The relations:

$$E = m_T \cosh y, \quad (\text{C.10})$$

$$\text{and } p_z = m_T \sinh y, \quad (\text{C.11})$$

are useful.

Appendix D

Results of π^0 Extraction

D.1 Raw numbers, Mass, and Widths of π^0 's

Table D.1– D.5 give the result of counting raw number of π^0 's for five centrality classes from the most central ($C=0$ –10 %) to the most peripheral ($C=60$ –80 %).

The analysis cuts applied to clusters and pair of clusters are:

- (i) arrival timing cut for clusters ($|t| < 2.5$ ns),
- (ii) shower shape cut for clusters ($\delta^2 < 3.0$),
- (iii) fiducial area cut for dead towers, around dead towers, and edge of EMCal,
- (vi) p_T dependent opening angle cut for cluster pairs, and
- (v) asymmetry cut for cluster pairs ($\alpha < 0.8$).

The conditions of fitting (integration region in mass spectra, normalization region, and etc.) are shown in the next section. The fitting function is basically Gaussian associated with constant value or linear function. The resulted χ^2 values divided by number of degree of freedom in fittings are also shown in the tables.

In every tables, the numbers were obtained at several p_T bins. The maximum available p_T bins are limited by statistics. The errors associated to the numbers are only statistical errors. The numbers in 0.5–1.0 GeV/ c of p_T ranges are marginal since the combinatorial background shape estimation in the mass spectra for these region is collapsed.

D.2 Figures of π^0 Peaks

Figures D.1 ~ D.10 show the invariant mass spectra of 2γ combinations. Each has several panels each corresponds to p_T bin described in the panel. Each panel has original mass spectrum of 2γ combinations (solid line) and scaled mass spectrum by event mixing

$C=0-10\%$ (Number of events = 241,355)

p_T [GeV/c]	$N_{\pi^0} \pm \delta N_{\pi^0}$ (total number)	$n_{\pi^0} \pm \delta n_{\pi^0}$ (per event)	$m \pm \delta m$ [MeV/c ²]	$w \pm \delta w$ [MeV/c ²]	$\chi^2/$ ndf
0.5–1.0	$(30.9 \pm 3.1) \times 10^4$	$(12.8 \pm 1.3) \times 10^{-1}$	140.3 ± 3.0	26.5 ± 3.4	10.8/33
1.0–1.5	$(17.4 \pm 2.7) \times 10^3$	$(7.2 \pm 1.1) \times 10^{-2}$	139.5 ± 2.1	11.3 ± 1.8	32.9/36
1.5–2.0	$(74.8 \pm 9.4) \times 10^2$	$(31.0 \pm 3.9) \times 10^{-3}$	141.2 ± 1.6	12.2 ± 1.5	21.3/36
2.0–2.5	$(23.0 \pm 2.2) \times 10^2$	$(95.5 \pm 9.1) \times 10^{-4}$	141.9 ± 1.5	12.7 ± 1.4	33.6/36
2.5–3.0	$(61.8 \pm 8.7) \times 10^1$	$(25.6 \pm 3.6) \times 10^{-4}$	142.1 ± 2.0	12.6 ± 2.5	23.4/36
3.0–3.5	$(25.1 \pm 3.7) \times 10^1$	$(10.4 \pm 1.5) \times 10^{-4}$	141.9 ± 3.5	16.1 ± 2.8	50.1/28
3.5–4.0	$(8.9 \pm 1.6) \times 10^1$	$(37.0 \pm 6.7) \times 10^{-5}$	137.2 ± 3.2	12.9 ± 3.1	13.8/19
4.0–4.5	$(3.2 \pm 1.0) \times 10^1$	$(13.3 \pm 4.3) \times 10^{-5}$	137.2 ± 5.9	14.7 ± 4.0	10.7/15
4.5–5.0	7.2 ± 6.0	$(3.0 \pm 2.5) \times 10^{-5}$	133.4 ± 7.4	6.2 ± 8.4	0.9/09

Table D.1: Raw π^0 numbers detected in $C=0-10\%$ events. N_{π^0} is the total number of π^0 in the invariant mass peak. n_{π^0} is the N_{π^0} divided by number of events (241,355) in this centrality class. Neither acceptance nor efficiency corrections for n are applied yet. m is the mass peak position and w is the mass peak width. Associated errors are only statistical errors.

$C=10-20\%$ (Number of events = 240,562)

p_T [GeV/c]	$N_{\pi^0} \pm \delta N_{\pi^0}$ (total number)	$n_{\pi^0} \pm \delta n_{\pi^0}$ (per event)	$m \pm \delta m$ [MeV/c ²]	$w \pm \delta w$ [MeV/c ²]	$\chi^2/$ ndf
0.5–1.0	$(14.2 \pm 1.8) \times 10^4$	$(59.1 \pm 7.5) \times 10^{-2}$	139.7 ± 2.5	18.6 ± 2.9	5.0/32
1.0–1.5	$(20.4 \pm 2.0) \times 10^3$	$(84.8 \pm 8.3) \times 10^{-3}$	139.6 ± 1.6	13.4 ± 1.5	27.7/40
1.5–2.0	$(61.5 \pm 5.9) \times 10^2$	$(25.6 \pm 2.4) \times 10^{-3}$	137.8 ± 1.1	10.6 ± 1.4	23.7/36
2.0–2.5	$(17.0 \pm 1.4) \times 10^2$	$(70.7 \pm 5.8) \times 10^{-4}$	137.9 ± 1.0	10.7 ± 1.0	39.8/36
2.5–3.0	$(56.7 \pm 5.7) \times 10^1$	$(23.6 \pm 2.4) \times 10^{-4}$	138.7 ± 1.2	10.4 ± 0.2	40.5/36
3.0–3.5	$(10.3 \pm 2.2) \times 10^1$	$(43.0 \pm 9.3) \times 10^{-5}$	139.1 ± 24.4	9.6 ± 56.1	11.3/12
3.5–4.0	$(4.9 \pm 1.1) \times 10^1$	$(20.2 \pm 4.6) \times 10^{-5}$	133.2 ± 2.4	9.1 ± 2.2	8.5/14
4.0–4.5	16.9 ± 8.7	$(7.0 \pm 3.6) \times 10^{-5}$	140.2 ± 4.5	7.3 ± 6.5	3.7/16
4.5–5.0	9.3 ± 7.9	$(3.9 \pm 3.3) \times 10^{-5}$	132.1 ± 8.5	9.5 ± 7.2	1.8/10

Table D.2: Raw π^0 numbers detected in $C=10-20\%$ events. N_{π^0} is the total number of π^0 in the invariant mass peak. n_{π^0} is the N_{π^0} divided by number of events (240,562) in this centrality class. Neither acceptance nor efficiency corrections for n are applied yet. m is the mass peak position and w is the mass peak width. Associated errors are only statistical errors.

$C=20-40\%$ (Number of events = 482,121)

p_T [GeV/c]	$N_{\pi^0} \pm \delta N_{\pi^0}$ (total number)	$n_{\pi^0} \pm \delta n_{\pi^0}$ (per event)	$m \pm \delta m$ [MeV/c ²]	$w \pm \delta w$ [MeV/c ²]	$\chi^2/$ ndf
0.5–1.0	$(12.3 \pm 1.6) \times 10^4$	$(25.6 \pm 3.3) \times 10^{-2}$	137.3 ± 2.6	18.2 ± 3.3	7.3/32
1.0–1.5	$(26.8 \pm 1.7) \times 10^3$	$(55.6 \pm 3.6) \times 10^{-3}$	135.8 ± 0.9	12.4 ± 1.0	16.2/33
1.5–2.0	$(87.5 \pm 5.7) \times 10^2$	$(18.2 \pm 1.2) \times 10^{-3}$	137.4 ± 0.9	13.2 ± 1.1	25.4/36
2.0–2.5	$(22.5 \pm 1.3) \times 10^2$	$(46.7 \pm 2.6) \times 10^{-4}$	137.7 ± 0.7	11.3 ± 0.7	29.0/36
2.5–3.0	$(63.0 \pm 5.2) \times 10^1$	$(13.1 \pm 1.1) \times 10^{-4}$	139.6 ± 1.2	12.1 ± 1.4	55.9/40
3.0–3.5	$(26.0 \pm 2.4) \times 10^1$	$(53.9 \pm 5.0) \times 10^{-5}$	139.5 ± 1.2	11.8 ± 1.3	45.6/40
3.5–4.0	$(9.2 \pm 1.3) \times 10^1$	$(19.1 \pm 2.8) \times 10^{-5}$	139.4 ± 2.2	13.7 ± 2.1	13.2/23
4.0–4.5	$(3.1 \pm 1.1) \times 10^1$	$(6.4 \pm 2.2) \times 10^{-5}$	139.6 ± 3.4	10.9 ± 2.8	4.9/16
4.5–5.0	16.5 ± 8.4	$(3.4 \pm 1.7) \times 10^{-5}$	141.5 ± 3.9	8.0 ± 5.5	0.9/16

Table D.3: Raw π^0 numbers detected in $C=20-40\%$ events. N_{π^0} is the total number of π^0 in the invariant mass peak. n_{π^0} is the N_{π^0} divided by number of events (482,121) in this centrality class. Neither acceptance nor efficiency corrections for n are applied yet. m is the mass peak position and w is the mass peak width. Associated errors are only statistical errors.

$C=40-60\%$ (Number of events = 485,650)

p_T [GeV/c]	$N_{\pi^0} \pm \delta N_{\pi^0}$ (total number)	$n_{\pi^0} \pm \delta n_{\pi^0}$ (per event)	$m \pm \delta m$ [MeV/c ²]	$w \pm \delta w$ [MeV/c ²]	$\chi^2/$ ndf
0.5–1.0	$(43.4 \pm 4.9) \times 10^3$	$(8.9 \pm 1.0) \times 10^{-2}$	135.3 ± 2.2	18.4 ± 2.6	9.8/33
1.0–1.5	$(107.5 \pm 5.6) \times 10^2$	$(22.1 \pm 1.2) \times 10^{-3}$	136.1 ± 0.7	12.2 ± 0.8	25.2/36
1.5–2.0	$(35.2 \pm 1.9) \times 10^2$	$(72.5 \pm 3.9) \times 10^{-4}$	136.3 ± 0.8	13.0 ± 0.8	16.1/36
2.0–2.5	$(105.3 \pm 5.7) \times 10^1$	$(21.7 \pm 1.2) \times 10^{-4}$	136.8 ± 0.8	12.3 ± 0.7	40.5/36
2.5–3.0	$(30.0 \pm 2.5) \times 10^1$	$(61.8 \pm 5.1) \times 10^{-5}$	138.1 ± 1.0	11.1 ± 0.8	29.2/36
3.0–3.5	$(11.0 \pm 1.3) \times 10^1$	$(22.6 \pm 2.6) \times 10^{-5}$	135.9 ± 1.3	8.8 ± 0.6	32.2/36
3.5–4.0	39.8 ± 8.4	$(8.2 \pm 1.7) \times 10^{-5}$	134.5 ± 0.7	7.8 ± 10.4	8.9/36
4.0–4.5	10.5 ± 7.9	$(2.2 \pm 1.6) \times 10^{-5}$	134.1 ± 5.1	6.5 ± 4.5	0.9/12
4.5–5.0	4.6 ± 6.3	$(1.0 \pm 1.3) \times 10^{-5}$	131.7 ± 20.8	8.5 ± 9.8	0.1/11

Table D.4: Raw π^0 numbers detected in $C=40-60\%$ events. N_{π^0} is the total number of π^0 in the invariant mass peak. n_{π^0} is the N_{π^0} divided by number of events (485,650) in this centrality class. Neither acceptance nor efficiency corrections for n are applied yet. m is the mass peak position and w is the mass peak width. Associated errors are only statistical errors.

$C = 60\text{--}80\%$ (Number of events = 508,926)

p_T [GeV/c]	$N_{\pi^0} \pm \delta N_{\pi^0}$ (total number)	$n_{\pi^0} \pm \delta n_{\pi^0}$ (per event)	$m \pm \delta m$ [MeV/c ²]	$w \pm \delta w$ [MeV/c ²]	$\chi^2/$ ndf
0.5–1.0	$(11.2 \pm 1.2) \times 10^3$	$(21.9 \pm 2.4) \times 10^{-3}$	133.8 ± 2.0	15.9 ± 2.2	16.0/40
1.0–1.5	$(34.0 \pm 1.7) \times 10^2$	$(66.7 \pm 3.3) \times 10^{-4}$	135.7 ± 0.8	13.7 ± 0.9	38.8/40
1.5–2.0	$(85.4 \pm 5.4) \times 10^1$	$(16.8 \pm 1.1) \times 10^{-4}$	136.6 ± 0.8	11.5 ± 0.7	32.8/40
2.0–2.5	$(28.0 \pm 2.2) \times 10^1$	$(55.1 \pm 4.2) \times 10^{-5}$	133.6 ± 0.5	11.1 ± 0.8	22.1/23
2.5–3.0	$(8.0 \pm 1.1) \times 10^1$	$(15.6 \pm 2.1) \times 10^{-5}$	137.6 ± 1.7	10.1 ± 1.3	29.6/40
3.0–3.5	25.0 ± 9.3	$(4.9 \pm 1.8) \times 10^{-5}$	136.7 ± 3.1	9.1 ± 2.8	1.4/18
3.5–4.0	13.2 ± 7.1	$(2.6 \pm 1.4) \times 10^{-5}$	135.5 ± 6.8	11.3 ± 5.0	0.8/20

Table D.5: Raw π^0 numbers detected in $C = 60\text{--}80\%$ events. N_{π^0} is the total number of π^0 in the invariant mass peak. n_{π^0} is the N_{π^0} divided by number of events (508,926) in this centrality class. Neither acceptance nor efficiency corrections for n are applied yet. m is the mass peak position and w is the mass peak width. Associated errors are only statistical errors.

method (dotted line) in the left upper sub panel, subtracted spectrum and fitting result in the left lower sub panel, and explanations in the right panel. The error bars in the subtracted mass spectra are only statistical error. The normalization region, scale factor of event mixed spectrum, fitting region, function used for fitting, fitting results, the region used for counting π^0 's, and number of π^0 's counted by three different ways are shown in the right panel. The fitting regions are also expressed by light shaded region in the original mass spectra. Dark shaded region in each fit function represents the region consists of bins in 2σ width of Gaussian function.

The three different result of counting π^0 are, (i) $N_{(2sigma)}$ which is sum of the number of entries contained in the bins in the 2σ region defined by Gaussian part of fitting function without considering residual background, (ii) $N_{(2sigma-pol.)} = N_{(2sigma)} - N_{(pol.)}$ where $N_{(pol.)}$ is the region under the polynomial function, and (iii) $N_{(Gauss)}$ which is the numerical integration of Gaussian part of fitting function. Due to the finite bin size, the width of bins in 2σ region is little different from 2σ width of Gaussian. It was corrected in the calculation of $N_{(2sigma)}$. In the analysis, the value $N_{(2sigma-pol.)}$ were taken as the final number N_{π^0} .

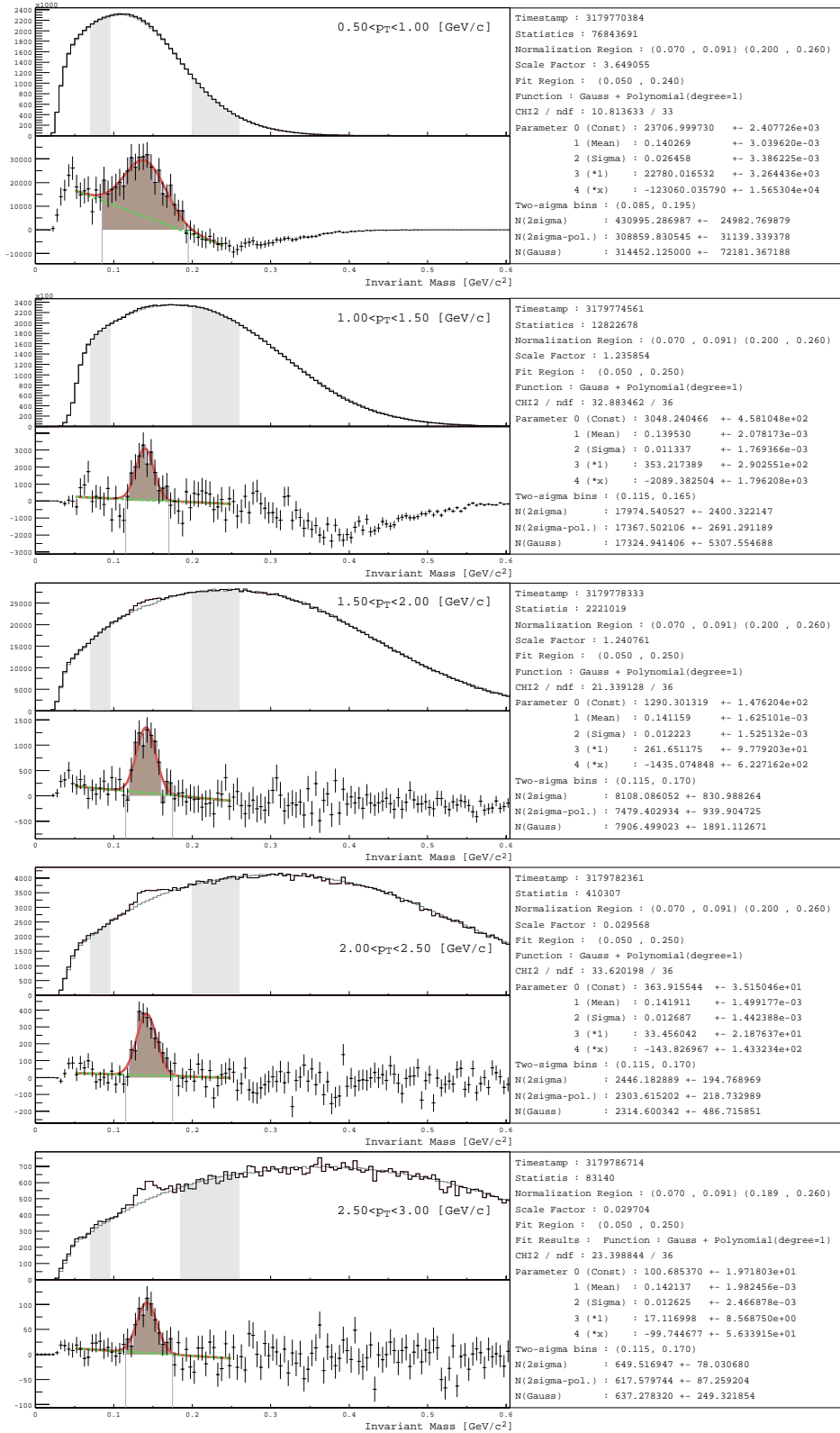


Figure D.1: Fitting results of π^0 peaks for $C=0-10\%$ events. p_T bins of 0.5 – 1.0 GeV/c, 1.0 – 1.5 GeV/c, 1.5 – 2.0 GeV/c, 2.0 – 2.5 GeV/c, and 2.5 – 3.0 GeV/c are shown.

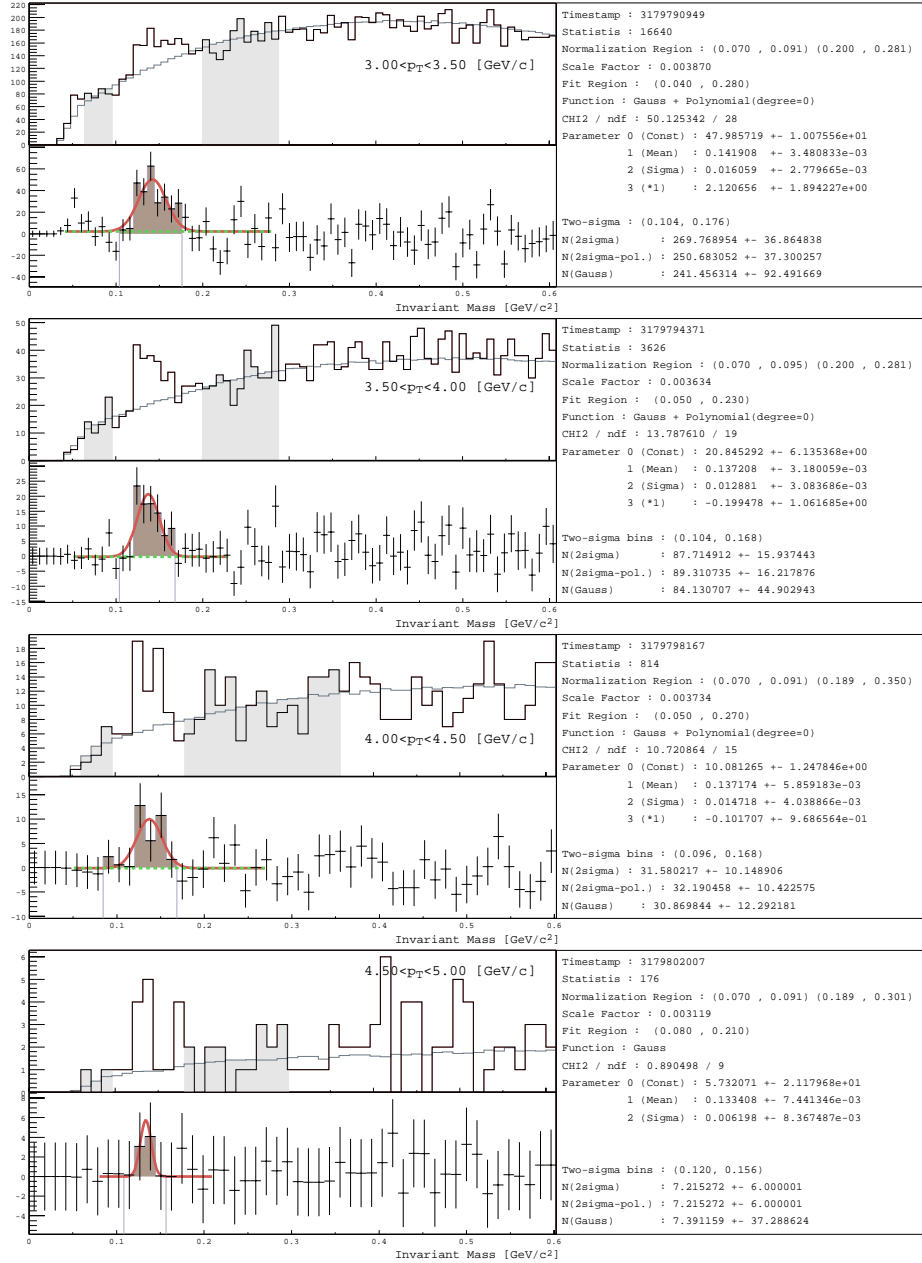


Figure D.2: Fitting results of π^0 peaks for $C=0-10\%$ events. p_T bins of $3.0 - 3.5$ GeV/c, $3.5 - 4.0$ GeV/c, $4.0 - 4.5$ GeV/c, and $4.5 - 5.0$ GeV/c are shown.

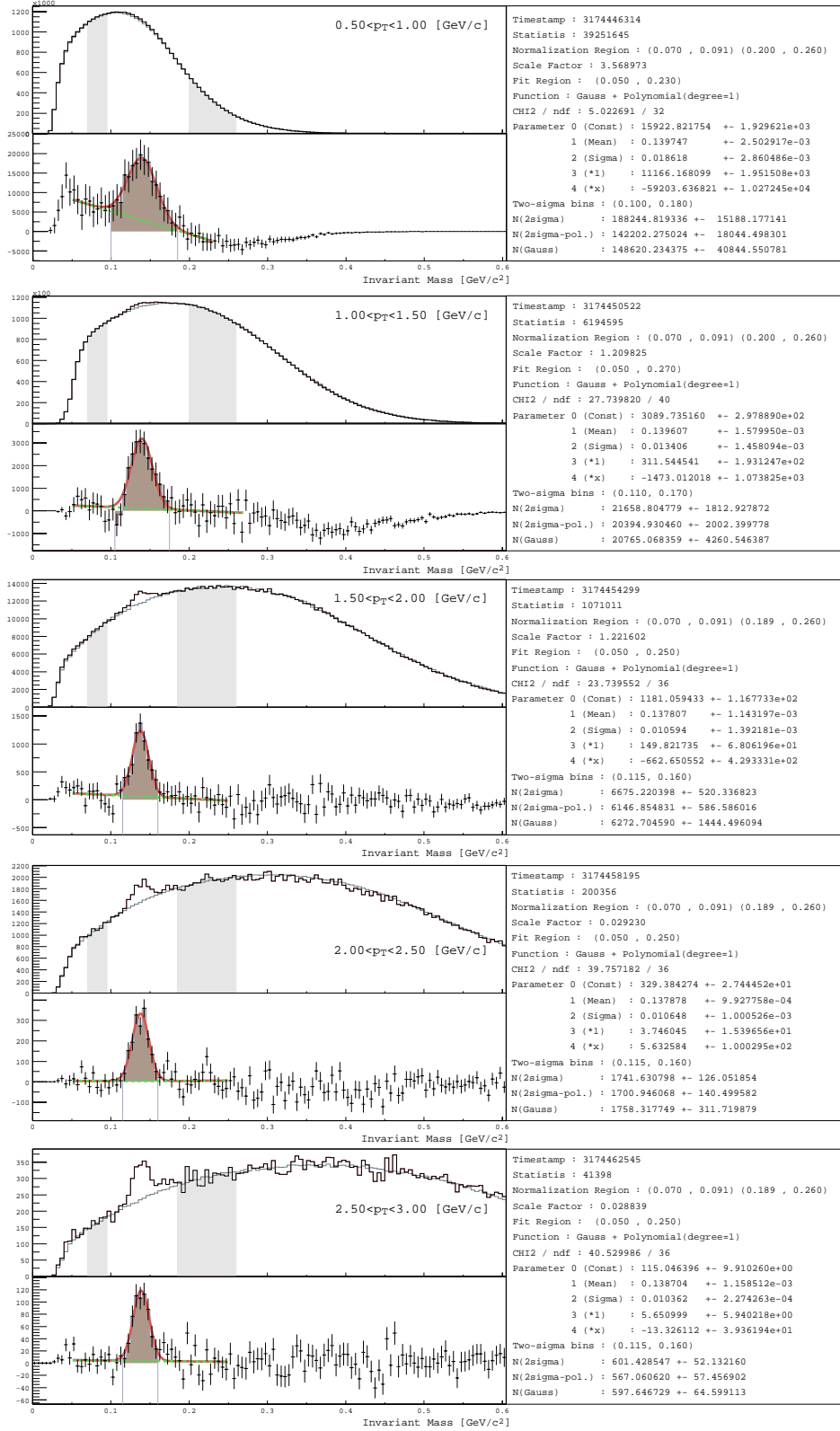


Figure D.3: Fitting results of π^0 peaks for $C = 10-20\%$ events. p_T bins of $0.5 - 1.0$ GeV/c, $1.0 - 1.5$ GeV/c, $1.5 - 2.0$ GeV/c, $2.0 - 2.5$ GeV/c, and $2.5 - 3.0$ GeV/c are shown.

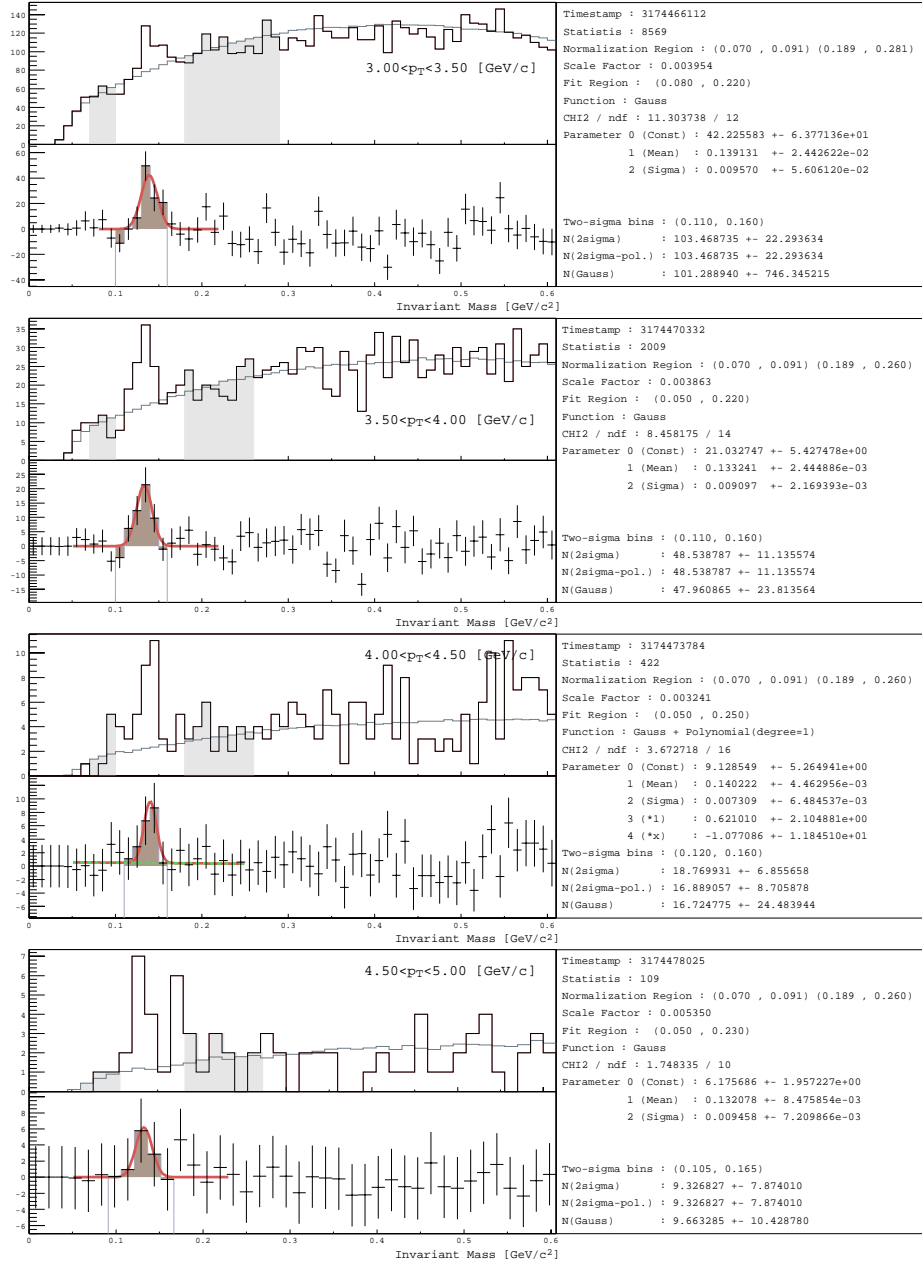


Figure D.4: Fitting results of π^0 peaks for $C = 10\text{--}20\%$ events. p_T bins of $3.0 - 3.5$ GeV/c, $3.5 - 4.0$ GeV/c, $4.0 - 4.5$ GeV/c, and $4.5 - 5.0$ GeV/c are shown.

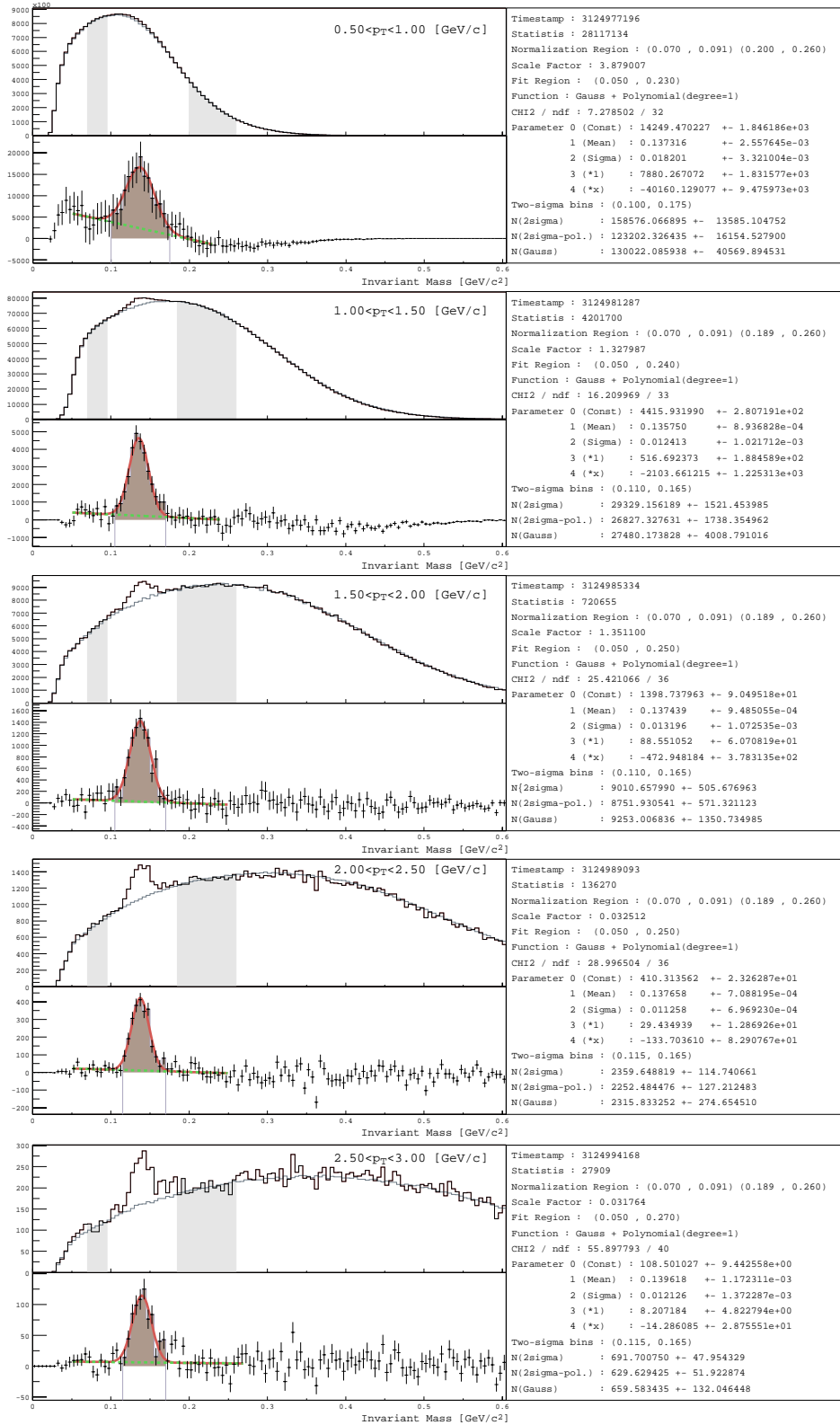


Figure D.5: Fitting results of π^0 peaks for $C=20-40\%$ events. p_T bins of $0.5 - 1.0 \text{ GeV}/c$, $1.0 - 1.5 \text{ GeV}/c$, $1.5 - 2.0 \text{ GeV}/c$, $2.0 - 2.5 \text{ GeV}/c$, and $2.5 - 3.0 \text{ GeV}/c$ are shown.

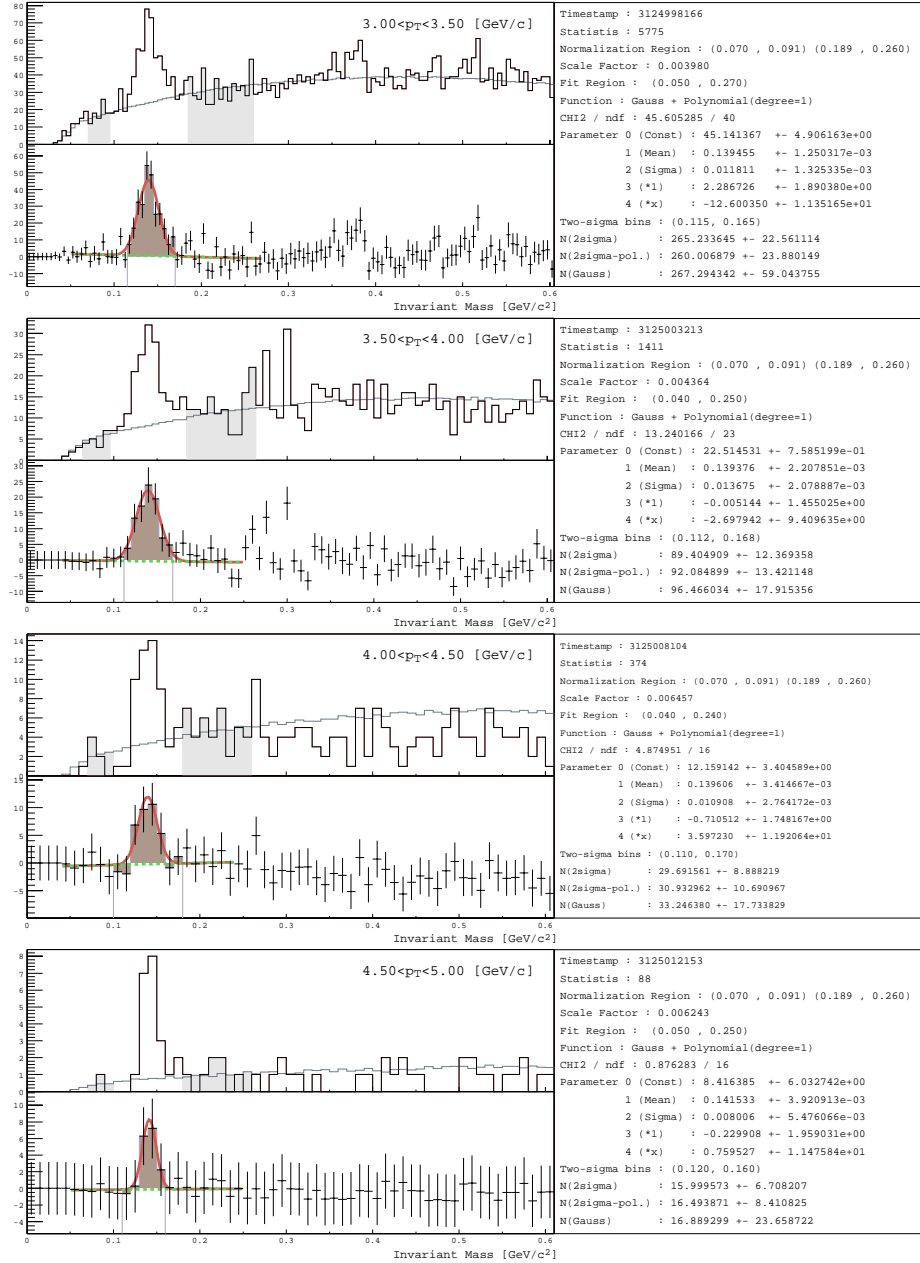


Figure D.6: Fitting results of π^0 peaks for $C = 20\text{--}40\%$ events. p_T bins of 3.0 – 3.5 GeV/c, 3.5 – 4.0 GeV/c, 4.0 – 4.5 GeV/c, and 4.5 – 5.0 GeV/c are shown.

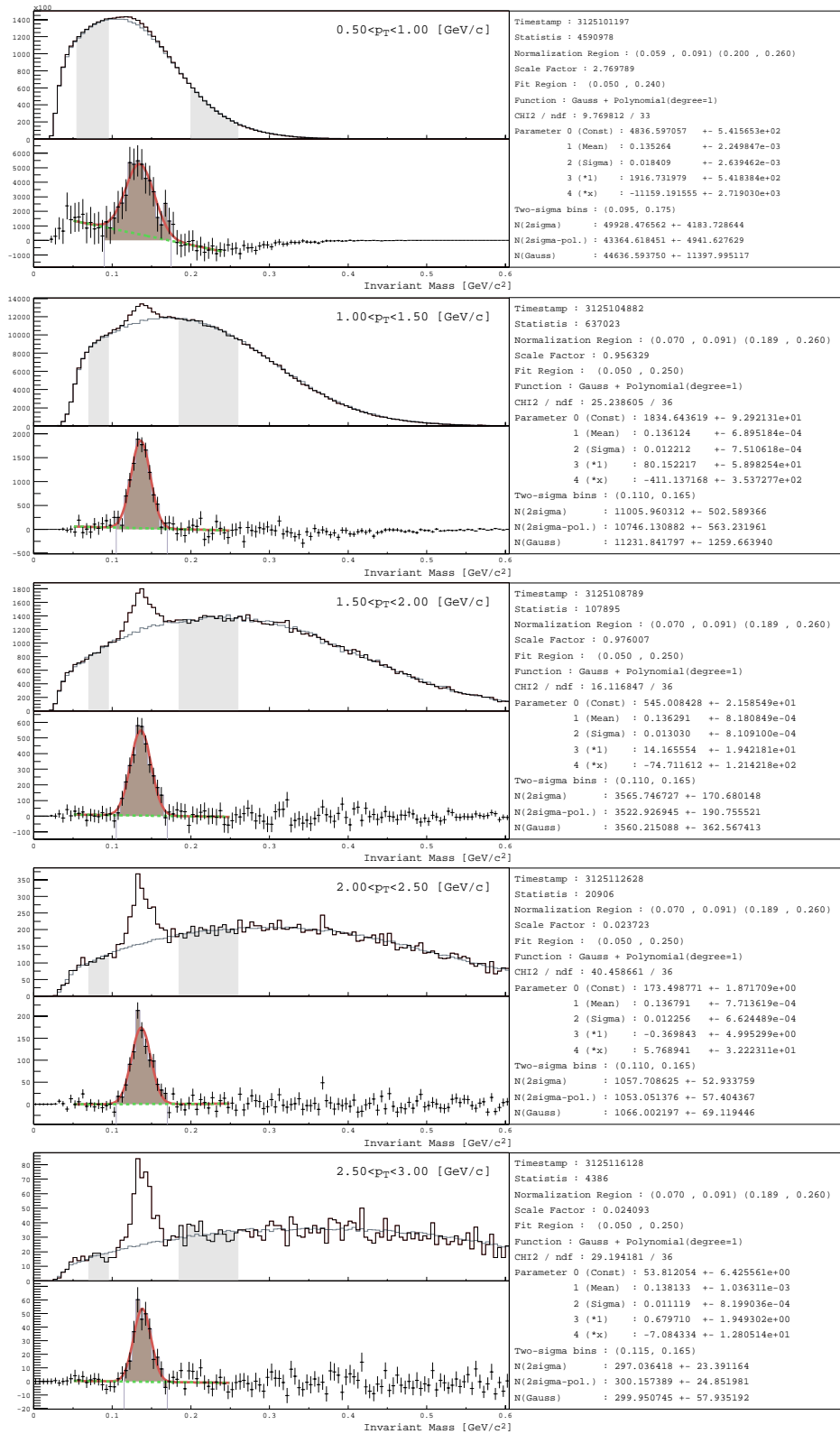


Figure D.7: Fitting results of π^0 peaks for $C=40-60\%$ events. p_T bins of $0.5 - 1.0$ GeV/c, $1.0 - 1.5$ GeV/c, $1.5 - 2.0$ GeV/c, $2.0 - 2.5$ GeV/c, and $2.5 - 3.0$ GeV/c are shown.

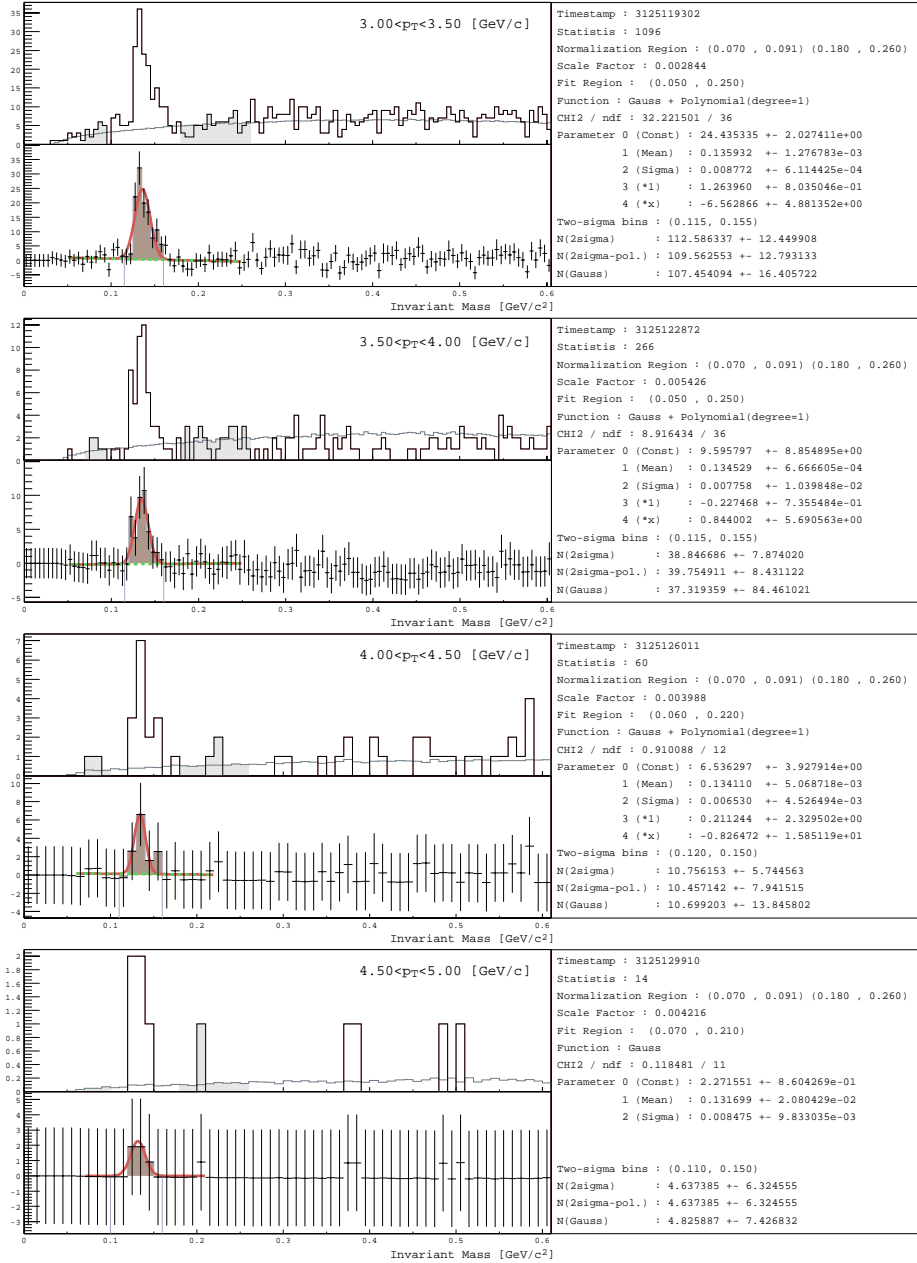


Figure D.8: Fitting results of π^0 peaks for $C=40-60\%$ events. p_T bins of 3.0 – 3.5 GeV/c , 3.5 – 4.0 GeV/c , 4.0 – 4.5 GeV/c , and 4.5 – 5.0 GeV/c are shown.

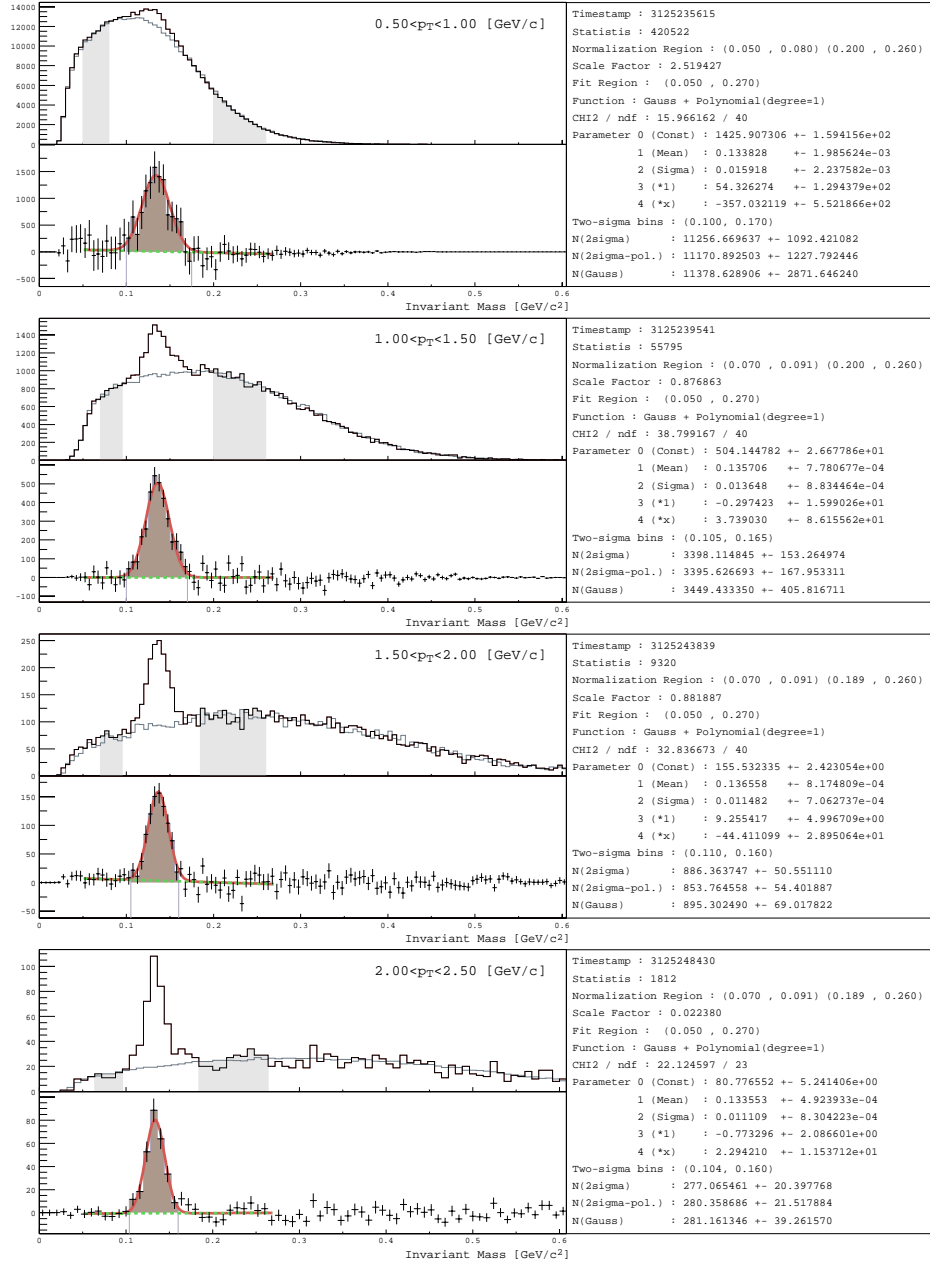


Figure D.9: Fitting results of π^0 peaks for $C=60-80\%$ events. p_T bins of 0.5 – 1.0 GeV/c , 1.0 – 1.5 GeV/c , 1.5 – 2.0 GeV/c , and 2.0 – 2.5 GeV/c are shown.

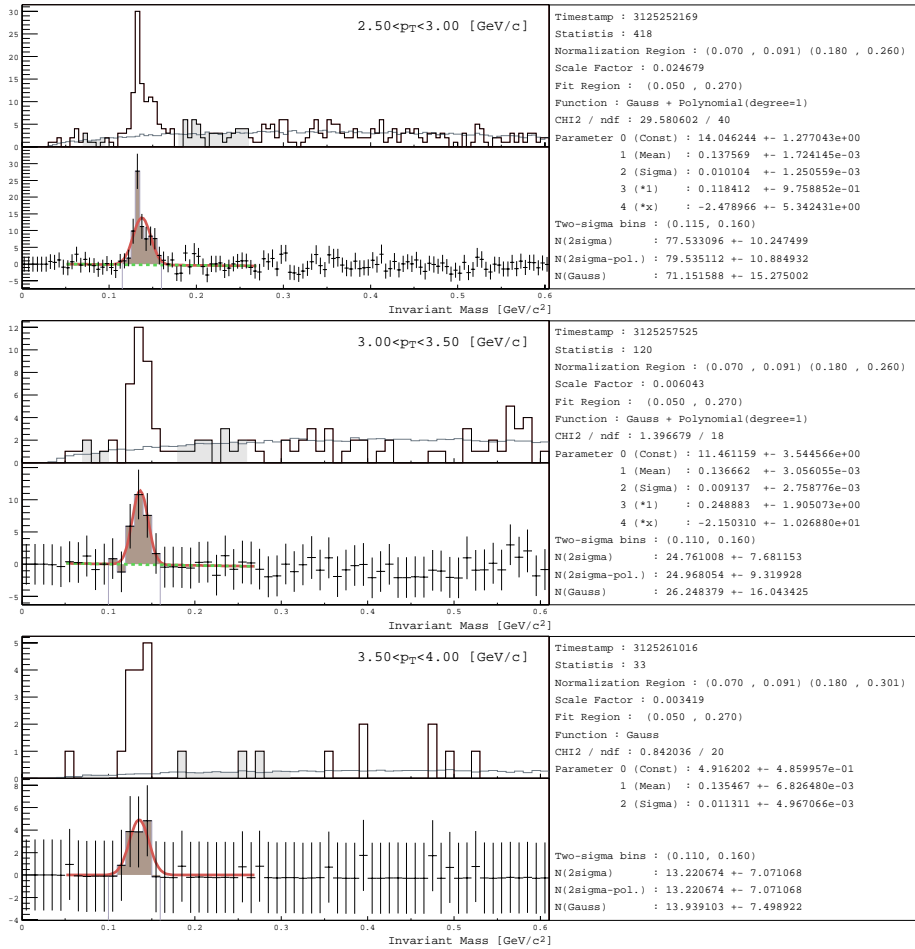


Figure D.10: Fitting results of π^0 peaks for $C=60-80\%$ events. p_T bins of $2.5 - 3.0$ GeV/c, $3.0 - 3.5$ GeV/c, and $3.5 - 4.0$ GeV/c are shown.

Appendix E

Correction Factors

Correction factors (ϵ) used to calculate π^0 invariant yields are given in Table E.1. The invariant yield of π^0 is calculated by dividing raw number of π^0 found in a certain p_T range by the correction factors of the same p_T range. The p_T bin width is fixed to 0.5 GeV/ c .

The uncertainties ($\delta\epsilon$) in the table are statistical errors in the Monte Carlo calculations and this is negligibly small for yield calculation compared to statistical errors of raw number of π^0 . No systematic uncertainties are shown here.

p_T [GeV/ c]	$\epsilon \pm \delta\epsilon$ [$\times 10^{-2}$]				
	$C=0-10$ %	$C=10-20$ %	$C=20-40$ %	$C=40-60$ %	$C=60-80$ %
1.0 – 1.5	1.087 \pm .000	1.182 \pm .000	1.280 \pm .000	1.348 \pm .000	1.386 \pm .000
1.5 – 2.0	1.446 \pm .000	1.569 \pm .001	1.663 \pm .001	1.709 \pm .001	1.765 \pm .001
2.0 – 2.5	1.766 \pm .001	1.892 \pm .002	1.936 \pm .002	1.972 \pm .002	2.008 \pm .002
2.5 – 3.0	1.997 \pm .003	2.124 \pm .004	2.105 \pm .004	2.127 \pm .003	2.153 \pm .004
3.0 – 3.5	2.181 \pm .005	2.303 \pm .009	2.238 \pm .008	2.241 \pm .007	2.245 \pm .007
3.5 – 4.0	2.355 \pm .010	2.457 \pm .019	2.325 \pm .015	2.329 \pm .013	2.326 \pm .012
4.0 – 4.5	2.518 \pm .019	2.551 \pm .037	2.418 \pm .027	2.346 \pm .022	2.434 \pm .021
4.5 – 5.0	2.640 \pm .034	2.749 \pm .072	2.452 \pm .045	2.490 \pm .040	2.466 \pm .034

Table E.1: Correction factors for each p_T and centrality bin. Uncertainties represents the statistical errors due to limited statistics in Monte Carlo.

References

- [1] M. Althoff *et al.* (TASSO Collaboration), *Z. Phys. C* **22**, 307 (1984).
- [2] D.J. Gross, R.D. Pisarski, L.G. Yaffe, *Rev. of Mod. Phys.* **53**, 43 (1981).
- [3] L. McLerran, *Rev. of Mod. Phys.* **58**, 1021 (1986).
- [4] A. Ukawa, *Nucl. Phys. A* **638**, 339c (1998).
- [5] T. Schäfer, *Nucl. Phys. A* **642**, 45c (1998).
- [6] K. Langfeld and M. Rho, *Nucl. Phys. A* **660**, 475 (1999).
- [7] N.K. Glendenning *et al.*, *Phys. Rev. C* **60**, 25803 (1999).
- [8] E. Witten, *Phys. Rev. D* **30**, 272 (1984).
- [9] J.H. Applegate, C.J. Hogan, and R.J. Scherrer, *Phys. Rev. D* **35**, 1151 (1987).
- [10] C.L. Bennet *et al.*, *Astrophys. J. A* **464**, L1 (1996).
- [11] C. Schmid, D.J. Schwarz, and P. Widerin, *Phys. Rev. D* **59**, 43517 (1999).
- [12] D.J. Schwarz, *Mod. Phys. Lett. A* **13**, 2771 (1998).
- [13] J.J. Drake *et al.*, *Astrophys. J. A* **572**, 996 (2002).
- [14] CERN press release, Feb. 2002.
- [15] J.W. Harris and B. Müller, *Annu. Rev. Nucl. Part. Sci.* **46**, 71 (1996).
- [16] X.-N. Wang, *Phys. Rev. C* **63**, 54902 (2001).
- [17] J.D. Bjorken, *Phys. Rev. D* **27**, 140 (1983).
- [18] X.-N. Wang, *Phys. Rev. C* **58**, 2321 (1998).
- [19] R. Baier, Yu.L. Dokshitzer, S. Peigné, and D. Schiff, *Phys. Lett. B* **345**, 277 (1995).

- [20] W. Thomé *et al.*, Nucl. Phys. B **129**, 365 (1977).
- [21] C.-Y. Wong and R.-C. Wang, Phys. Rev. D **44**, 679 (1991).
- [22] F. Abe *et al.*, Phys. Rev. Lett. **61**, 1819 (1988).
- [23] C. Albajar *et al.* (UA1 Collaboration), Nucl. Phys. B **335**, 261 (1990).
- [24] G. Arnison *et al.* (UA1 Collaboration), Phys. Lett. B **172**, 461 (1986).
- [25] C. Albajar *et al.* (UA1 Collaboration), Nucl. Phys. B **309**, 405 (1998).
- [26] B. Alper *et al.* (British-Scandinavian Collaboration), Nucl. Phys. B **87**, BS (1975).
- [27] B. Alper *et al.* (British-Scandinavian Collaboration), Nucl. Phys. B **100**, BS (1975).
- [28] R.J. Glauber and G. Matthiae, Nucl. Phys. B **21**, 135 (1970).
- [29] X.-N. Wang and M. Gyulassy, Phys. Rev. D **44**, 3501 (1991).
- [30] J. Ashman *et al.* (European Muon Collaboration), Phys. Lett. B **202**, 603 (1988).
- [31] J. Ashman *et al.* (European Muon Collaboration), Phys. Lett. B **211**, 492 (1988).
- [32] S.J. Brodsky and H.J. Lu, Phys. Rev. Lett. **64**, 1342 (1990).
- [33] D. Antreasyan, J. W. Cronin *et al.*, Phys. Rev. D **19**, 764 (1979).
- [34] J.W. Cronin *et al.*, Phys. Rev. D **11**, 3105 (1975).
- [35] X.-N. Wang, Phys. Rev. C **61**, 64910 (2000).
- [36] A.B. Migdal, Phys. Rev. **103**, 1811 (1956).
- [37] R. Baier, Y.L.Dokshitzer, A.H. Mueller , and D. Schiff, Phys. Rev. C **58**, 1706 (1998).
- [38] R. Albrecht *et al.* (WA80 Collaboration), Eur. Phys. J. C **5**, 255 (1998).
- [39] M.M. Aggarwal *et al.* (WA98 Collaboration), Preprint nucl-ex/9806004 (1998).
- [40] M.M. Aggarwal *et al.* (WA98 Collaboration), Eur. Phys. J. C **23**, 225 (2002).
- [41] X.-N. Wang, Phys. Rev. Lett. **81**, 2655 (1998).
- [42] BNL, BNL51801 (1984).
- [43] BNL, BNL51932 (1986).

- [44] K.H. Ackermann *et al.* (STAR Collaboration), Nucl. Phys. A **661**, 681c (1999).
- [45] R. Pak *et al.* (PHOBOS collaboration), Nucl. Phys. A **698**, 416 (2002).
- [46] F. Videbaek *et al.* (BRAHMS collaboration), Nucl. Phys. A **566**, 299 (1994).
- [47] F. Videbaek *et al.* (BRAHMS collaboration), Nucl. Phys. A **698**, 29 (2002).
- [48] N. Saito for the PHENIX Collaboration, Nucl. Phys. A **638**, 575c (1998).
- [49] J. Kiryluk for the STAR Collaboration, Preprint hep-ex/0201276 (2002).
- [50] D.P. Morrison *et al.* (PHENIX Collaboration), Nucl. Phys. A **638**, 565 (1998).
- [51] J. Barrette *et al.* for the PHENIX pad chamber group, Nucl. Phys. A **661**, 665 (1999).
- [52] Y. Akiba *et al.*, Nucl. Instr. and Meth. in Phys. Res. A **433**, 143 (1999).
- [53] Y. Akiba *et al.*, Nucl. Instr. and Meth. in Phys. Res. A **453**, 279 (2000).
- [54] G. David *et al.*, IEEE Transactions on Nuclear Science, Vol. 43, 1491 (1996).
- [55] M. Rosati *et al.* for the Time Expansion Chamber Group, Nucl. Phys. A **661**, 669 (1999).
- [56] K. Ikematsu *et al.*, Nucl. Instr. and Meth. in Phys. Res. A **411**, 238 (1998).
- [57] C. Adler *et al.*, Nucl. Instr. and Meth. in Phys. Res. A **461**, 337 (2001).
- [58] C. Adler *et al.*, Nucl. Instr. and Meth. in Phys. Res. A **470**, 488 (2001).
- [59] C. Fabjan and T. Ludlam, adapted with permission from the Annual Review of Nuclear and Particle Science, Vol.32, ©1982 by Annual Reviews, Inc.
- [60] G. David *et al.*, IEEE Transactions on Nuclear Science, Vol. 42, 4 (1995).
- [61] T.C. Awes *et al.*, Preprint nucl-ex/0202009 (2002).
- [62] S. Kametani *et al.*, CNS Ann. Rep. **23**, 34 (1999).
- [63] M.S. Emery *et al.*, IEEE Transactions on Nuclear Science, Vol. 44, 374 (1997).
- [64] K. Oyama *et al.*, CNS Ann. Rep. **23**, 27 (1999).
- [65] Y. Tanaka *et al.*, Nucl. Instr. and Meth. in Phys. Res. A **455**, 576 (2000).
- [66] T. Sakaguchi *et al.*, Nucl. Instr. and Meth. in Phys. Res. A **453**, 382 (2000).

- [67] A.L. Wintenberg *et al.*, IEEE Transactions on Nuclear Science, Vol. 45, 758 (1998).
- [68] M. Hibino *et al.*, CNS Ann. Rep. **13**, 23 (1998).
- [69] T. Matsumoto *et al.*, CNS Ann. Rep. **23**, 29 (1999).
- [70] H. Hara *et al.*, CNS Ann. Rep. **13**, 31 (1998).
- [71] H. Appelshauser *et al.*, Eur. Phys. J. A **2**, 383 (1998).
- [72] A. Bazilevsky, private communications.
- [73] T. Sakaguchi *et al.*, CNS Ann. Rep. **36**, 35 (2001).
- [74] Particle Data Group, Eur. Phys. J. C **15**, 1 (2000).
- [75] G. Arnison *et al.* (UA1 Collaboration), Phys. Lett. B **118**, 167 (1986).
- [76] K. Adcox *et al.* (PHENIX Collaboration), Phys. Rev. Lett. **87**, 52301 (2001).
- [77] C. Adler *et al.* (STAR Collaboration), Preprint nucl-ex/0206011 (2002).
- [78] T. Hirano and Y. Nara, Preprint hep-ph/0208029 (2002).
- [79] T. Hirano, private communications.
- [80] T. Hirano, Phys. Rev. Lett. **86**, 2754 (2001).
- [81] D. Teaney, J. Lauret, and E.V. Shuryak, Phys. Rev. Lett. **86**, 4783 (2001).
- [82] T. Matsui and H. Satz, Phys. Lett. B **178**, 416 (1986).
- [83] M.C. Abreu *et al.* (NA50 Collaboration), Phys. Lett. B **477**, 28 (2000).
- [84] M.C. Abreu *et al.* (NA38 Collaboration), Phys. Lett. B **449**, 128 (1999).
- [85] B. Lenkeit for the CERES Collaboration, Nucl. Phys. A **661**, 23 (1999).
- [86] R.J. Furnstahl, T. Hatsuda, and Su H. Lee, Phys. Rev. D **42**, 1744 (1990).
- [87] K.L. Haglin and C. Gale, Nucl. Phys. B **421**, 613 (1994).
- [88] S. Damjanovic and K. Filimonov for the CERES Collaboration, (Int. Europhys. Conf. on HEP) PrHEP-hep2001/250 (2001).
- [89] A.A. Anselm and M.G. Ryskin, Phys. Lett. B **266**, 482 (1991).
- [90] F.D. Steffen and M.H. Thoma, Phys. Lett. B **510**, 98 (2001).

- [91] M.M. Aggarwal *et al.* (WA98 Collaboration), Phys. Rev. Lett. **85**, 03595 (2000).
- [92] M.M. Aggarwal *et al.* (WA98 Collaboration), Preprint nucl-ex/0006007 (2000).
- [93] A. Lebedev for the WA98 Collaboration, Nucl. Phys. A **698**, 135 (2002).
- [94] J. Rafelski and Berndt Muller, Phys. Rev. Lett. **48**, 1066 (1982).
- [95] J. Rafelski and Berndt Muller, Phys. Rev. Lett. **56**, 2334 (1986).
- [96] J. Rafelski, Phys. Lett. B **262**, 333 (1991).
- [97] E. Andersen *et al.* (WA97 Collaboration), Phys. Lett. B **449**, 401 (1999).
- [98] A. Drees, Nucl. Phys. A **698**, 331c (2002).
- [99] K. Adcox *et al.* (PHENIX Collaboration), Phys. Rev. Lett. **88**, 22301 (2002).
- [100] J.C. Dunlop for the STAR Collaboration, Nucl. Phys. A **698**, 515 (2002).



PHENIX Major Facility Hall (Building 1008) at RHIC BNL in N.Y. on January 8, 2001.